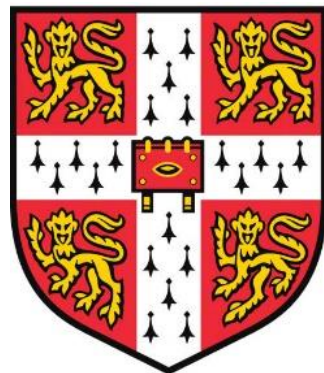


# **Design and Synthesis of Molecularly Encapsulated Conjugated Materials for Organic Electronics.**

Jeroen Royakkers  
St. Catharine's College

Supervisor: Dr. Hugo Bronstein



Thesis submitted for the degree of  
Doctor of Philosophy  
in Chemistry

University of Cambridge

April 2021

## **Declaration**

I hereby declare that my thesis/dissertation is the result of my own work and includes nothing which is the outcome of work done in collaboration except as declared in the Contributions. I further state that no substantial part of my dissertation has already been submitted, or is being concurrently submitted for a degree, diploma or other qualification at the University of Cambridge or any other University. Where information has been derived from other sources, I confirm that this has been indicated in the thesis. This dissertation does not exceed the prescribed word limit.

Name: Jeroen Royakkers

Signature:

Date: April 2021

Place: Cambridge, United Kingdom.

## **Copyright**

The copyright of this thesis rests with the author. Any information used or derived from it should be acknowledged. © Copyright Jeroen Royakkers, University of Cambridge, 2021.

## Abstract

The (photo)physical properties of polymers are predominantly attributed to their intermolecular and intramolecular interactions. In conjugated polymers, charges or excitons can transport either along the conjugated backbone or intermolecularly via  $\pi$ -stacking interactions. Yet, our understanding of what each type of interaction contributes, is still rather limited. Moreover, independently studying the effects of either inter or intramolecular interactions is often not possible in traditional conjugated polymers or materials. Therefore, it is important to develop new materials or polymers, in which there is control over these interactions, and which in turn can afford desirable properties or improved device performance. Encapsulated conjugated materials are an attractive class of materials that could potentially improve our fundamental understanding in these areas. In this thesis, we will therefore discuss how molecular encapsulation influences interactions within or between polymer chains/materials as well as their (photo)physical properties, and/or device performance.

The first chapter explains some of the key concepts in organic electronics and introduces important background information on conjugated polymers or materials and why they are of interest to both research and industry. Furthermore, it discusses some of the most important discoveries in the field of (non)covalent encapsulated conjugated polymers, their applications, and why researchers might prefer to work with covalent versus noncovalent encapsulated conjugated materials (and vice versa).

The second chapter starts with a short summary of our own, previous work, outlining the overall concept of encapsulation and the most important findings. It serves as an introduction for the research conducted in this PhD degree. In brief, our previous work demonstrates a series of novel, red-emitting and encapsulated conjugated polymers based on DPP and compares them to their naked (reference) counterparts. The study shows that molecular encapsulation can suppress intermolecular interactions, generate polymers with a lower degree of energetic disorder and conformational defects, and enhance backbone co-linearity. Furthermore, the suppression of inter and intramolecular interactions led to a remarkable (3 to 4-fold) increase in solution and solid-state PLQYs compared to the naked counterparts, and thereby allowed DPP polymers to be used, for the first time, as an emissive solid-state material. Therefore, these initial, promising results, led to further exploration of the concept, which will be discussed in this thesis.

To further understand the effects of molecular encapsulation, we therefore designed a novel series of encapsulated DPP-based conjugated polymers (in chapter II) in which the encapsulation density is varied. Here, the variation in encapsulation density is correlated to the photoluminescence quantum yields (in solution and film), and solution to solid-state quenching behaviour. Therefore, this chapter explores how molecular encapsulation can potentially be used

to further optimize the optoelectronic properties of DPP-based conjugated polymers. The novel polymer series demonstrates that through control over density of encapsulation it is possible to greatly suppress aggregation-caused quenching (ACQ) in our red-emitting conjugated polymers. Furthermore, we report the most emissive red conjugated polymers in the solid state, to date.

Chapter III focusses on the use of encapsulation to molecularly engineer/alter the aggregation and packing behaviour of (relatively) planar conjugated polymers based on naphthalene diimide (NDI). Through comparison of the naked reference polymer with both a bulky and encapsulated NDI polymer, it is possible to investigate how structural changes affect the polymer's morphology, packing, photophysical properties and device performance, and establish a structure-property relationship. The study reveals, for the first time, that the famous, reference polymer (**P(NDI-2OD-T)**) undergoes aggregation induced emission; an effect that is suppressed upon encapsulation due to an increasing pi-stacking distance. In other words, the naked, reference polymer has a higher thin film photoluminescence quantum yield compared to the encapsulated one, which might give a clue as to why their performance has been so superior. Therefore, the study suggests that AIE through pi-stacking may be an attractive method to enhance the radiative properties of conjugated polymers, in contrast to the current paradigm where it is viewed as a potential source of optical quenching.

In chapter IV, the aim was to prepare an encapsulated PDI molecule and investigate how the structural influence of molecular encapsulation affects the photophysical properties of the PDI chromophore. Our strategy proved successful at suppressing intermolecular  $\pi$ - $\pi$  interactions in both solution and the solid-state. However, bright, PDI-based solid-state emitters could not be obtained due to the use of electron-rich peripheral aryls, which introduced charge transfer character into our molecule and thus photoluminescence quenching. Nevertheless, it was found that covalent encapsulation can be used to rigidify molecular architectures and potentially direct solid-state packing or 3D crystal growth. This work therefore highlights both the power of encapsulation as a synthetic tool for chromophore control but also their potential non-innocence with regards to underlying photophysical properties.

In the final chapter (chapter V), we propose that the encapsulation concept can be used as a powerful, synthetic tool to control the distance or orientation between two different building blocks. This is of great interest in the field of organic photovoltaics, as it can provide structural control over the exact configuration of the donor-acceptor interface. This model system can therefore be used to study, for the first time, how subtle changes in the structure or D-A orientation can influence the optoelectronic properties and overall OPV device performance. Furthermore, it can potentially be used to investigate how certain distances between the donor and acceptor interface or rigidifications of the straps alter their performance. Having great control over the

donor-acceptor interface should therefore provide lots of fundamental understanding, which can help pave the way towards next-generation photovoltaic materials or devices.

## Motivations

In today's world, cutting-edge (opto)electronic technologies are often limited by the availability of materials.<sup>1</sup> Therefore, the design and manipulation of novel functional materials remains extremely important and has a profound impact on emerging applications, the way we interact with it and our quality of life.

To date, the world's energy demand has been met primarily by burning fossil fuels like coal and petroleum oil.<sup>2</sup> However, due to the threat of global warming and depletion of these fossil fuels, it has become increasingly important to meet our energy demands through the use of alternative and renewable energy sources.<sup>3</sup> Solar energy is particularly promising as the energy provided by one hour of solar irradiation equates to the world energy consumption in a year.<sup>3</sup> Capturing all this "free" energy would therefore be extremely beneficial to the world.

While conventional silicon solar cells are very efficient and largely dominate the solar energy market, conjugated polymers can offer a more cost-effective fabrication of certain optoelectronic devices (or parts of them), or enable completely new device functionalities (e.g., mechanical flexibility, optical transparency, and impact resistance).<sup>4</sup> Therefore, rather than replacing inorganic silicon, organic polymers are expected to fulfil different or complementary functions, which are difficult to obtain with silicon alone. Besides organic photovoltaics, conjugated polymers are also expected to have enormous potential for the development of disruptive, cutting-edge wearable electronics or biocompatible devices.<sup>5-7</sup>

In other words, conjugated polymers are projected to expand the functionality and accessibility of electronics, provide more eco-friendly and sustainable alternatives and result in devices that are prepared via resource-friendly and energy-efficient processes.<sup>8</sup>

Through the development of novel conjugated polymers, this dissertation should therefore contribute to 1) devices with a better optoelectronic performance and/or 2) a deeper fundamental understanding, which can hopefully bring us closer to improved or next-generation devices.

## Table of Content

Declaration .....	2
Copyright.....	2
Abstract .....	3
Motivations.....	5
Table of Content .....	6
Contributions .....	8
Acknowledgements.....	9
Publications .....	10
List of Abbreviations .....	11
<b>Chapter I: Introduction .....</b>	<b>18</b>
1.1 Organic Conjugated Materials .....	18
1.2 The Origin of Narrow Bandgaps .....	18
1.3 Molecular Bandgap Engineering.....	19
1.4 Traditional Methods for Preparing Conjugated Materials .....	25
1.5 Absorption and Emission of Electromagnetic Radiation.....	34
1.6 Device Fundamentals: OPVs and OLEDs .....	40
1.7 Polymer Definition, Molecular Weights and Polydispersity .....	45
1.8 Introduction to Macrocyclic Encapsulated Conjugated Polymers.....	46
1.9 Dissertation Scope and Objectives .....	58
<b>Chapter II: Molecularly Encapsulated DPP-Based Conjugated Polymers.....</b>	<b>61</b>
Introduction .....	61
Previous Work .....	61
Project Objectives .....	61
Synthetic Design .....	62
Optical and (Photo)Physical Properties.....	65
Conclusions .....	68
Final Notes.....	68
<b>Chapter III: Molecularly Encapsulated NDI Polymers .....</b>	<b>69</b>
Background Information.....	69
Introduction .....	70
Project Objectives .....	77
Synthetic Design .....	77
Results & Discussion .....	83
Conclusions .....	88
<b>Chapter IV: Molecularly Encapsulated PDI Molecules .....</b>	<b>89</b>
Introduction .....	89

Project Objectives .....	90
Synthetic Design & Characterization .....	90
Results & Discussion .....	94
Conclusions .....	101
<b>Chapter V: Through-Space Polymers.....</b>	<b>102</b>
Through-Space Polymers: Part 1 .....	102
Introduction .....	102
Project Objectives .....	108
Synthetic Design & Characterization .....	109
Results & Discussion .....	112
Through-Space Polymers: Part 2 .....	115
Synthetic Design & Characterization .....	115
Results & Discussion .....	117
Conclusions .....	121
<b>Thesis Summary .....</b>	<b>123</b>
<b>Experimental Section.....</b>	<b>125</b>
<b>References .....</b>	<b>162</b>
<b>Appendix.....</b>	<b>177</b>
Chapter II.....	177
Chapter III .....	179
Chapter IV .....	188
Chapter V .....	196

## Contributions

Most of the research projects presented in this thesis have had a very collaborative nature. Therefore, I would like to this opportunity to acknowledge the contributions of other researchers.

### Chapter II:

- X-ray crystallography was performed by Mérina K. Corpinot from Dr. Dejan-Krešimir Bučar's group at University College London.
- The UV-Vis spectra and PLQY data were taken by Alessandro Minotto and Ali Hassan from Prof. Franco Cacialli's group at University College London.
- The encapsulated anthracene monomer (II-6) was prepared by Dr. Daniel Congrave from Dr. Hugo Bronstein's group at the University of Cambridge.

### Chapter III:

- X-ray crystallography was performed by Dr. Andrew D. Bond from the University of Cambridge.
- The UV-Vis spectra, PLQY data and lifetimes were measured by Kunping Guo and Alessandro Minotto from Prof. Franco Cacialli's group at University College London.
- The GIWAXS data was collected by Dr. Daniel T. W. Toolan at the University of Sheffield.
- PESA measurements were performed by Dr. Rajendar Sheelamanthula from Prof. Iain McCulloch's group at the King Abdullah University of Science and Technology.

### Chapter IV:

- X-ray crystallography was performed by Dr. Andrew D. Bond from the University of Cambridge and further analyzed by Dr. Dejan-Krešimir Bučar from University College London.
- The UV-Vis spectra, PLQY data and lifetimes were measured by Alessandro Minotto and Adil Patel from Prof. Franco Cacialli's group at University College London.

### Chapter V:

- X-ray crystallography was performed by Dr. Andrew D. Bond from the University of Cambridge.
- Minor synthetic help was provided by Dr. Daniel Congrave and Dr. Anastasia Leventis from Dr. Hugo Bronstein's group at the University of Cambridge.
- UV-Vis spectra were measured by Dr. Daniel Congrave and me (Jeroen Royakers) from Dr. Hugo Bronstein's group at the University of Cambridge, and Dr. Flurin Eisner from Prof. Jenny Nelson's group at Imperial College London.

## Acknowledgements

Thanks to the Winton Programme for the Physics of Sustainability for funding this research.

I would like to express special thanks to my supervisor, Dr. Hugo Bronstein, for the opportunity to work in his group and challenging me with various, interesting research projects. I have learnt a great deal and enjoyed myself a lot.

I am also extremely grateful to all the members of his group, in particular Anastasia and Dan. Anastasia, thank you for always being there, helping everyone out and making the Bronstein group a real family. Dan, thanks a lot for passing down your knowledge, all our fruitful discussions, spending more time in the lab (listening to Scooter) than at home, and of course all the fun nights out. I would also like to thank Christina, Dave, Niall, and Alex. Their presence has made any (social) setting, a lot more entertaining and fun (and yes Niall, this includes your trash-talk sessions during bowling).

Thank you to my friends, Moriam, Luke, Eric and Pooj for treating me to an occasional food baby, brightening up almost any day, and all the crazy days/nights we spent together. You have made my journey very joyful.

Finally, I am extremely grateful to my family and girlfriend for their unconditional support, strength, love, and patience. You have been amazing throughout.

## Publications

### Chapter I:

- J. Royakkers, H. Bronstein. “Macrocyclic Encapsulated Conjugated Polymers.” *Macromolecules* **2021**, *54*, 3, 1083–1094.

### Chapter II:

- A. Leventis, J. Royakkers, A. G. Rapidis, N. Goodeal, M. K. Corpinot, J. M. Frost, D.-K. K. Bučar, M. O. Blunt, F. Cacialli and H. Bronstein. “Highly Luminescent Encapsulated Narrow Bandgap Polymers Based on Diketopyrrolopyrrole.” *J. Am. Chem. Soc.* **2018**, *140*, 5, 1622–1626. (Obtained during MSc project, 1<sup>st</sup> co-author, used for previous work section in chapter II).
- J. Royakkers, A. Minotto, D. G. Congrave, W. Zeng, A. Hassan, A. Leventis, F. Cacialli and H. Bronstein. “Suppressing Solid-State Quenching in Red Conjugated Polymers.” *Chem. Mater.* **2020**, *32*, 23, 10140–10145.

### Chapter III:

- J. Royakkers, K. Guo, D. Toolan, L. Wen, A. Minotto, A. D. Bond, M. Al-Hashimi, T. Marks, A. Facchetti, F. Cacialli and H. Bronstein. “Synthesis and Optical Properties of Molecularly Encapsulated Naphthalene Diimide (NDI) Based  $\pi$ -Conjugated Polymers” Manuscript in preparation.

### Chapter IV:

- J. Royakkers, A. Minotto, D. G. Congrave, W. Zeng, A. Patel, A. D. Bond, D. K. Bučar, F. Cacialli and H. Bronstein. “Doubly Encapsulated Perylene Diimides: Effect of Molecular Encapsulation on Photophysical Properties.” *J. Org. Chem.* **2020**, *85*, 1, 207–214.

### Chapter V:

- Through Space Conjugated Polymers Give Insight into the Donor-Acceptor Interface. Manuscript in preparation, some results pending.

## List of Abbreviations

$\epsilon$	Extinction coefficient
$\kappa_R$	Radiative decay
$\kappa_{NR}$	Non-radiative decay
$\lambda$	Wavelength
$\lambda_{max}$	Maximum absorption wavelength
$\mu_h$ or $\mu_0$	Hole mobility
$\mu_e$	Electron mobility
$\mu_w$	Microwave
$\nu$	Wavenumber
$\rho_{Enc.}$	Density of encapsulation
$\tau$	Lifetime
$\tau_{AVG}$	Average lifetime
$\Phi_F, \Phi_{PL}$	Photoluminescence/ fluorescence quantum yield
$\Phi_R$	Photoluminescence/ fluorescence quantum yield ratio
$^\circ$	Degrees
$\propto$	Proportional to
1,5-COD	1,5-cyclooctadiene
3D	Three-dimensional
A	Absorbance
A	Acceptor
$\text{\AA}$	Angstrom
Abs	Absorption
ACQ	Aggregation caused quenching
AIE	Aggregation induced emission
Ar	Aromatic substituent
$BBr_3$	Boron tribromide
BDT	Benzodithiophene
BLA	Bond length alternation
$Br_2$	Bromine
BT	Bithiophene
BTOR	3,3'-dialkoxy-2,2'-bithiophene
BTR	3,3'-dialkyl-2,2'-bithiophene
C	Carbon

c	Concentration
c	Speed of light
CB	Chlorobenzene
CB	Conduction band
CBPQT4+	Cyclobis(paraquat- <i>p</i> -phenylene)
CD	Cyclodextrin
$\text{CDCl}_3$	Deuterated chloroform
$\text{CHCl}_3$	Chloroform
CIExy	Commission Internationale de l'Éclairage coordinates
cm	Centimeters
COSY	homonuclear correlation spectroscopy
CPL	Circularly polarized light
CPs	Conjugated polymers
CT	Charge transfer
Cu	Copper
C-X	Carbon-halogen
D	Donor
DAP	Direct arylation polymerization
DBH	1,3-Dibromo-5,5-dimethylhydantoin
DBI	Dibromoisoxyuric acid
DCM	Dichloromethane
DEPT	Distortionless Enhancement of Polarization Transfer
DFF	Diketofurofuran
DFT	Density functional theory
Disp.	Disproportionation
DMF	Dimethylformamide
DMSO	Dimethyl sulfoxide
DPP	Diketopyrrolopyrrole
DT	2-decyldtetradecyl
E	Electric field strength
$e^-$	Electron
e	Electron charge
EA	Electroabsorption
ECL	Effective conjugation length

EDG	Electron donating group
EDOT	Ethylenedioxathiophene
EDTT	Ethylenedithiathiophene
Eg	Band gap energy (optical band gap)
EH	2-ethylhexyl
EI	Electron ionization
Em	Emission
EL	Electroluminescence
Et <sub>2</sub> NH	Diethylamine
Et <sub>3</sub> NH	Triethylamine
EtOAc	Ethyl acetate
EtOH	Ethanol
eV	Electron volts
EWG	Electron withdrawing group
EQE	External quantum efficiency
<i>f</i>	Oscillator strength
FMOs	Frontier molecular orbitals
GPC, SEC	Gel permeation chromatography/Size exclusion chromatography
GRIM	Grignard metathesis
h <sup>+</sup>	Hole
Ha	Hartrees
HD	2-hexyldecyl
H-H	Head-to-head
HMBC	Heteronuclear Multiple Bond Correlation Spectroscopy
HOMO	Highest occupied molecular orbital
HRMS	High resolution mass spectrometry
HSQC	Heteronuclear single quantum coherence spectroscopy
H-T	Head-to-tail
hν <sub>A</sub>	Absorbed photon
hν <sub>E</sub>	Emitted photon
I <sub>2</sub>	Iodine
ICT	Intramolecular charge transfer
IMWs	Insulated molecular wires
<sup>i</sup> PrOH	Isopropanol

IQE	Internal quantum efficiency
IR	Infrared
ISC	Intersystem crossing
K <sub>2</sub> CO <sub>3</sub>	Potassium carbonate
K <sub>3</sub> PO <sub>4</sub>	Potassium phosphate
kDa	Kilo Daltons
l	Path length
LCMS	Liquid chromatography–mass spectrometry
LDA	Lithium diisopropylamide
LRMS	Low resolution mass spectrometry
LUMO	Lowest unoccupied molecular orbital
m	Mass of an electron
M	Molarity
M	Molecular weight
MAEs	Masked alkyne equivalents
MALDI	Matrix-assisted laser desorption/ionization
MeOH	Methanol
mg	Milligrams
MgSO <sub>4</sub>	Magnesium sulphate
MHz	Megahertz
mL	Millilitre
M <sub>n</sub>	Number average molecular weight
MOs	Molecular orbitals
M <sub>w</sub>	Weight average molecular weight
N	Number of molecules
n	Number of monomer units
n	Refractive index of the medium
N	Nitrogen
N <sub>A</sub>	Avogadro's number
N <sub>A</sub>	Number of photons absorbed
Na <sub>2</sub> CO <sub>3</sub>	Sodium carbonate
NaHCO <sub>3</sub>	Sodium hydrogen carbonate
NaSEt	Sodium ethanethiol
NBS	N-bromosuccinimide

NDA	Naphthalene dianhydride
NDIs	Naphthalene diimides
$N_E$	Number of photons emitted
NFA	Nonfullerene acceptor
Ni	Nickel
$\text{Ni}(\text{COD})_2$	Bis(cyclooctadiene)nickel(0)
$\text{Ni}(\text{dppe})\text{Cl}_2$	Dichloro(1,2-bis(diphenylphosphino)ethane)nickel
$\text{Ni}(\text{dppp})\text{Cl}_2$	Dichloro(1,3-bis(diphenylphosphino)propane)nickel
nm	Nanometres
NMR	Nuclear magnetic resonance
ns	Nanosecond
n-type	Negative charge carrier
o	Ortho
O	Oxygen
OA	Oxidative addition
OD	2-octyldodecyl
OFETs	Organic field-effect transistors
OLEDs	Organic light emitting diodes
OLETs	Organic light-emitting transistors
OPVs	Organic photovoltaics
OSCs	Organic solar cells
OTFTs	Organic thin film transistors
p	Para
$\text{P}(\text{o-tol})_3$	Tri(o-tolyl)phosphine
P3AT	Poly-3-alkylthiophene
P3HT	Poly-3-hexylthiophene
PCE	Power conversion efficiency
Pd	Palladium
$\text{Pd}(\text{PPh}_3)_2\text{Cl}_2$	Bis(triphenylphosphine)palladium(II) dichloride
$\text{Pd}(\text{PPh}_3)_4$	Tetrakis(triphenylphosphine)palladium(0)
Pd/C	Palladium on carbon
$\text{Pd}_2\text{dba}_3$	Tris(dibenzylideneacetone)dipalladium(0)
PDA	Perylene Dianhydride
PDI	Perylene diimide

PDI	Polydispersity index
PESA	Photoelectron spectroscopy in air
Ph-DPP	Phenyl-diketopyrrolopyrrole
PIA	Photo-induced absorption
PITN	Poly-isothianaphthene
PivOH	Pivalic acid
PL	Photoluminescence
PLQY	Photoluminescence quantum yields
PPh <sub>3</sub>	Triphenylphosphine
ppm	Parts per million
PPP	Poly(p-phenylene)
PPV	Polyphenylenevinylene
PS	Polystyrene
PSCs	Polymer solar cells
PT	Polythiophene
p-type	Positive charge carrier
RE	Reductive elimination
rr	Regioregular
RW	Ring walking
s	Second
SE	Stimulated emission
S <sub>N</sub> Ar	Nucleophilic aromatic substitution
SPhos	2-Dicyclohexylphosphino-2',6'-dimethoxybiphenyl
STM	Scanning tunnelling microscopy
TD-DFT	Time-dependent density functional theory
Th-DPP	Thiophene-diketopyrrolopyrrole
THF	Tetrahydrofuran
THP	Tetrahydropyran
TICT	Twisted intramolecular charge transfer
TM	Transmetallation
TMEDA	Tetramethylethylenediamine
TOF-MS	Time-of-flight-mass spectrometry
Tr*	Super trityl
Ts	Toluenesulfonyl (Tosyl)

TT	Tail-to-tail
UV-Vis	Ultraviolet-visible
V	Volt
VB	Valence band
VMs	Vibration modes
W	Weight

# Chapter I

## Introduction

### 1.1 Organic Conjugated Materials

Until nearly half a century ago, conjugated polymers were regarded as electrically insulating plastics, having an impressive range of applications, spanning from performance materials in the construction or automotive industry, to more specialized fields such as pharmaceuticals. However, it was not until 1977 that conjugated polymers were truly revolutionized.<sup>9</sup> For the first time, Nobel Laureates Heeger, McDiarmid and Shirakawa proved that “plastics” such as polyacetylene, could display metallic conductivity whilst maintaining favorable mechanical properties; a remarkable discovery which led to the rapid expansion of this field.

In the 1980s, considerable progress has been made through the development of a library of various conducting polymers (**Figure 1**). The produced polymers, such as polyaniline, polypyrrole, polythiophene and polyphenylene were soluble in organic solvents and could therefore be processed according to the demands of the application.

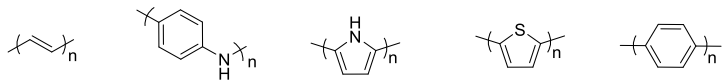


**Figure 1.** Early examples of conjugated polymers. From left to right you can see polyacetylene, polyaniline, polypyrrole, polythiophene and polyphenylene.

Presently, conjugated polymers are of high commercial importance in organic electronics with major applications in organic photovoltaics<sup>4,10,11</sup>, light-emitting diodes<sup>4,11</sup>, transistors<sup>4,11</sup> and even lasing<sup>12,13</sup>. Their excellent optoelectronic performance can be mainly attributed to their  $\pi$ -conjugated backbone, which allows for good charge transport, and/or their absorption or emission of electromagnetic radiation.<sup>4</sup> In particular, narrow bandgap materials are of high interest because they can harness light in the (near-) infrared region allowing capture of a greater proportion of incident photons (in the case of a solar cell) or emission in biologically relevant optical windows.<sup>14</sup>

### 1.2 The Origin of Narrow Bandgaps

The origin of narrow bandgaps in conjugated polymers originates from the effect of conjugation (i.e., alternating double and single bonds, **Figure 2**).<sup>15</sup> For small molecules such as ethylene or 1,3-butadiene, the bonding ( $\pi$ ) and antibonding ( $\pi^*$ ) energy levels are discrete and relatively far apart (**Figure 3**).<sup>16</sup> When the conjugation length of the system increases (e.g., in oligomers or polymers), more  $p_z$  orbitals will overlap, which gives rise to an increased number of energy levels. This consequently brings the HOMO and LUMO closer in energy and reduces the gap between the energy levels until they eventually are no more discrete and become continua of energy levels

or bands.<sup>17</sup> In other words, by increasing the effective conjugation length (ECL) of the polymer, less energy is needed to excite electrons from the HOMO (valence band) to the LUMO (conduction band) and thus the polymer's absorption will be more red-shifted (longer wavelengths). Continuous overlap of  $\pi$ -bonding  $p_z$  orbitals therefore leads to semiconductor behaviour and is essential to create a pathway for charge transport or conduction along the polymer backbone.

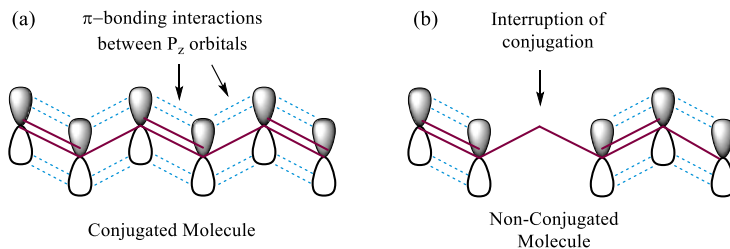


**Figure 2.**  $\pi$ -bonding orbital interactions in a conjugated (a) and non-conjugated molecule (b).

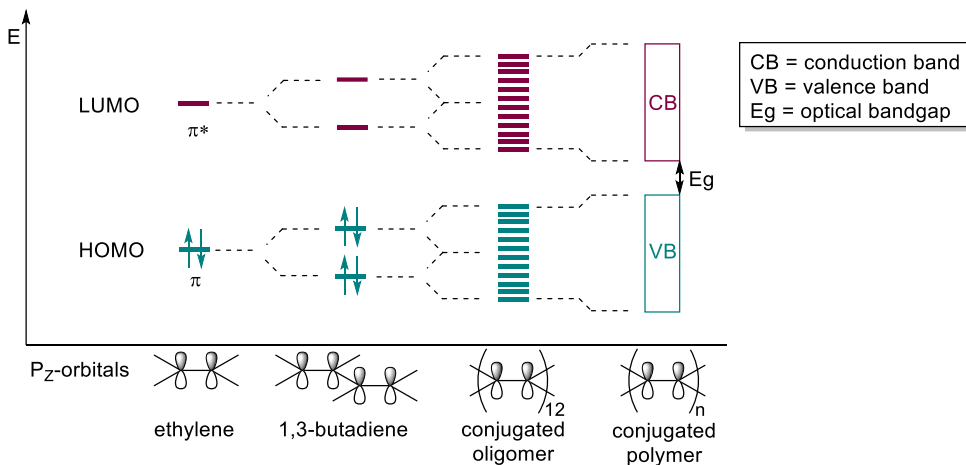


**Figure 3:** Energy diagram demonstrating the origin of narrow bandgaps in conjugated polymers, with increasing  $P_z(\pi)$  orbital overlap or conjugation length.

Typical organic semiconductors exhibit an optical bandgap ( $E_g$ ) of between 1.0 – 3.0 eV (~400 – 1200 nm), which allows them to absorb incident photons in the ultraviolet, visible light (UV-Vis) and near-infrared (near-IR) regions of the electromagnetic spectrum.<sup>18–20</sup> Hence, besides conduction, alternating single and double bonds are also responsible for why conjugated materials can harness incident photons and be used as the active layer in light-harvesting applications (e.g., OPVs) or to generate light (e.g., in OLEDs).

### 1.3 Molecular Bandgap Engineering

The optical bandgap of an organic semiconductor greatly determines its optoelectronic properties. Developing a better understanding on how to molecularly engineer or control this crucial parameter is therefore of extreme importance. Typical methods used to engineer the bandgap will be discussed in the following sections.

### 1.3.1 Aromatic and Quinoidal Resonance Structures

The bond length alternation (BLA)<sup>21</sup> is the average of the difference in C-C bond lengths in a polyene backbone and constitutes the major contribution to the magnitude of  $E_g$ . When the conjugated backbone predominantly has a quinoid character in the ground state, more carbon-carbon double bonds will be present in adjacent rings, thereby decreasing the bond-length alternation and the bandgap. Therefore, the less the aromatic units are stabilized, the more likely they will adopt a quinoid resonance and hence the better the delocalization along the conjugated backbone. Avoiding or diluting strong aromatic character of the building blocks is therefore very important to obtain a narrower bandgap.

For aromatic conjugated polymers, it is important to realize that there are two different non-degenerate ground state resonance forms.<sup>19</sup> The aromatic resonance is the form in which each aromatic unit maintains its aromaticity; that is all  $\pi$ -electrons are confined within the rings. Alternatively, a molecule can also adopt the quinoidal form. Here, the  $\pi$ -electrons are conjugated along the conjugated chains and all the double bonds are converted into single bonds and *vice versa*. Both resonance forms are in competition with each other. However, since the aromatic form is still fully aromatic, it is more energetically stable and has a bigger bandgap than the quinoid form.<sup>19</sup>

In general, the quinoid form is more likely to occur with decreasing aromatic character, as can be demonstrated by a series of examples (**Figure 4**).<sup>11</sup> Polyphenylene has a high aromatic character due to the stable nature of the benzene rings and hence has a relatively large bandgap of ~3.2 eV. When introducing more double bond character (like in PPV), the aromatic nature of the polymer is diluted and thus the bandgap reduces to ~2.4 eV. When moving to heteroaromatics such as polythiophenes, the inherent aromaticity is already lower than for polyphenylene and hence it is more likely to adopt a quinoidal resonance. Again, this results in a smaller bandgap of ~2 eV. The quinoid character can be even further increased by fusing thiophene on top of a phenyl ring, as in the case of poly-isothianaphthene (PITN). This design strategy is very clever as the phenyl ring is so stable, it essentially bullies the thiophene part to become quinoidal, which consequently results in very narrow bandgap of only ~1.1 eV.

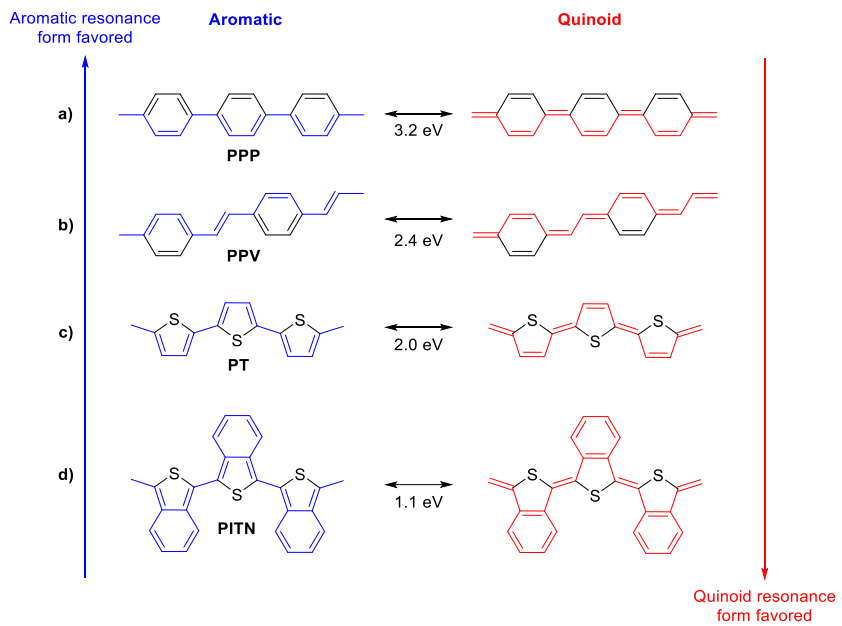


**Figure 4.** Several materials demonstrating the effect of aromatic and quinoidal resonance. As observed, molecules with increased quinoid resonance tend to have a lower bandgap.

### 1.3.2 Electron-Withdrawing and Donating Groups

Alternatively, the HOMO and LUMO levels can also be influenced by incorporating electron-withdrawing or donating groups onto the polymer backbone. In 1994, Bredas and Heeger researched how various electron-withdrawing and donating substituents on poly(p-phenylene vinylene) (PPV) and poly(p-phenylene) (PPP) affected the energy levels of the polymer.<sup>22</sup> They show that the use of electron-donating or withdrawing effects can both reduce the bandgap.

Incorporation of electron donating groups (EDGs) result in an upwards shift of both the HOMO and LUMO, however the HOMO energy level shifts slightly more (through destabilization of the frontier orbitals) and consequently the bandgap decreases.<sup>19</sup> In contrast, electron-withdrawal does the exact opposite, with the LUMO level shifting more down than the HOMO (through stabilization of the electronic levels), which again results in a smaller bandgap.<sup>19</sup> Throughout the years, incorporating electron-donating or withdrawing substituents onto the polymer backbone has become a useful and simple tool for developing materials with a narrower bandgap.

### 1.3.3 Rigidifying the $\pi$ -Conjugated System

In theory, extending (or shortening) the conjugation length gives rise to a narrower (or wider) band gap. However, in real life this is not always the case. Instead, if the dihedral angle between two consecutive units is too distorted (or large), the conjugation length gets interrupted, which affects the (opto)electronic properties of the material (**Figure 5**).<sup>15</sup> Therefore, by reducing the effective conjugation length, the bandgap will be wider and hence the material will absorb shorter wavelengths.<sup>15</sup>

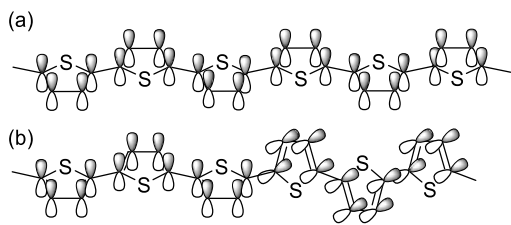


**Figure 5.** Planar conjugated polythiophene backbone (a) versus twisted polythiophene backbone (b).

One way to overcome backbone twisting is to covalently rigidify the  $\pi$ -conjugated system in order to suppress rotational disorder and maintain planarity (**Figure 6**).<sup>15</sup> In the past, this technique has been applied successfully to a series of molecules<sup>23–26</sup>, typically resulting in smaller bandgaps or greater electron delocalization. However, due to the chemical complexity this often requires additional synthetic steps.

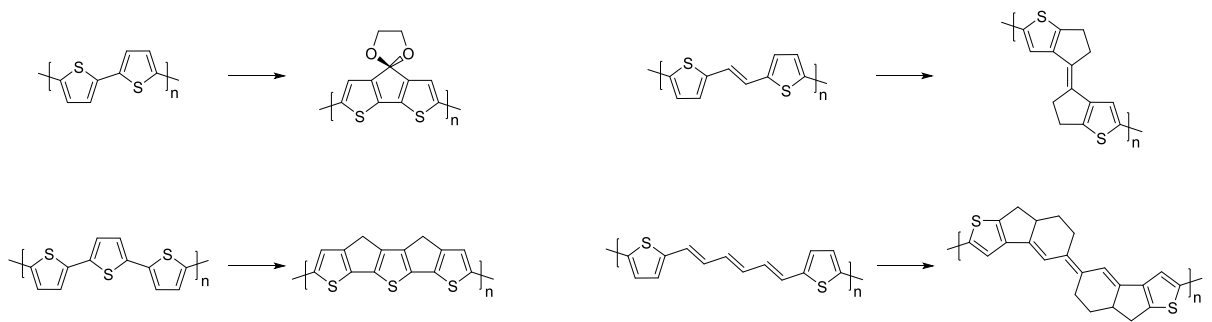


**Figure 6:** Rigidification of various  $\pi$ -conjugated systems to increase backbone planarity.<sup>23–26</sup>

### 1.3.4 Donor-acceptor push-pull polymers

One of the most powerful methods to create narrow bandgaps in conjugated polymers is to alternate electron-rich donor (D) and electron-deficient acceptor (A) building blocks to form an inherent push and pull system. The push and pull effects between D and A building blocks (**Figure 7a**), facilitates delocalization of the  $\pi$ -electrons and the formation of quinoid mesomers along the polymer backbone (**Figure 7b**). This consequently reduces the bond length alternation and hence distortions or structural defects are less likely.<sup>19</sup> Furthermore, as the D and A orbitals interact, they form hybridized D-A orbitals which consequently gives rise to a higher-lying HOMO level and a lower-lying LUMO level and thus a narrower optical bandgap (**Figure 8**). By carefully selecting both the donor and acceptor component, it is therefore possible to control the bandgap.<sup>19</sup>

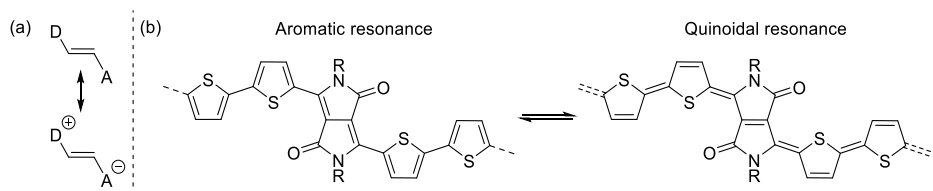


**Figure 7.** (a) The push-pull effect in a D-A system. (b) Aromatic and quinoidal resonance structures of a DPP polymer.

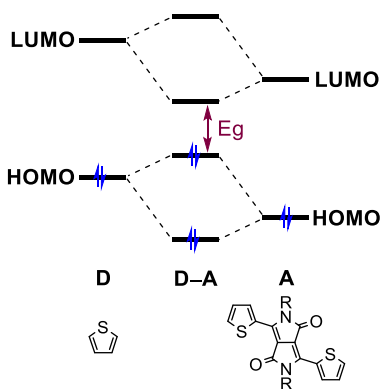


**Figure 8.** Molecular orbital hybridization of a donor-acceptor system, demonstrating narrowing of the optical bandgap.

### 1.3.5 Conformational Locking

Lastly, the bandgap can also be modified using noncovalent intramolecular interactions to increase backbone co-linearity of the polymer.<sup>27</sup> This method is commonly referred to as “conformational locking”. In literature, molecular conformations have often been stabilized using X···S (X=halide), O···S, N···S or hydrogen-bonding interactions as they promote molecular organization of crystallization.<sup>27–30</sup> As a result, the device morphology, polymer size domains and structural ordering of polymer strands can be tuned and thereby result in enhanced optoelectronic performance.<sup>27,31,32</sup>

Two great examples that demonstrate the effect of heteroatom interactions are the polymers PEDOT and PEDTT (**Figure 9**).<sup>33</sup> As observed, PEDOT is largely dominated by noncovalent S···O interactions (conformational locks), which give the polymer a rigid and planar structure and a relatively narrow bandgap of 1.53 eV.<sup>29</sup> In contrast, the polymer analogue “PEDTT” has a much wider bandgap of 2.49 eV due to the increased backbone twisting caused by non-cooperative S···S interactions.<sup>34</sup> The large dihedral angle between neighboring monomer units of 87° is also responsible for reducing the effective conjugation length. In fact, the polymer backbone is so twisted, the bandgap is almost identical to that of the monomer.

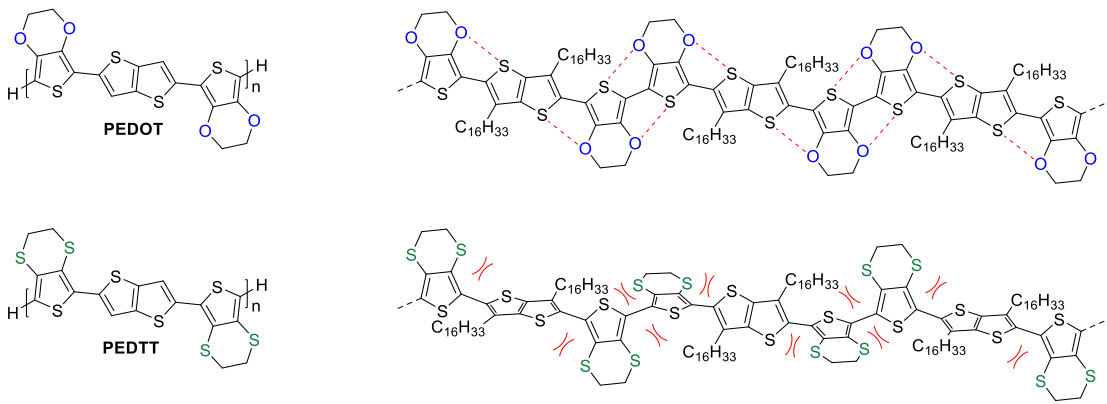


**Figure 9.** The difference in heteroatom interactions between PEDOT and PEDTT. As seen, PEDOT displays a more planar conjugated backbone due to favourable Coulombic heteroatom interactions, whereas PEDTT is more twisted.<sup>33</sup>

A few other noteworthy studies that demonstrate the importance of noncovalent interactions in polymers were reported by Guo and coworkers.<sup>35–39</sup> One of their first studies demonstrates that by simply replacing the two alkyl chains of 3,3'-dialkyl-2,2'-bithiophene (BTR) with two alkoxy chains (BTOR), the conjugated backbone is exposed to less steric repulsion and hence planarizes (**Figure 10**).<sup>35</sup> This can be attributed to the favorable noncovalent Coulombic S···O interactions, which lock the conjugated backbone in place and thereby stimulate interchain packing and self-planarization in thin films.<sup>40,41</sup> As a result, their BTOR-phthalimide donor acceptor polymers exhibited enhanced hole mobilities ( $\mu_h$ ) of up to  $0.28 \text{ cm}^2 \text{ V}^{-1} \text{ s}^{-1}$  in organic thin film transistors (OTFTs).<sup>35</sup> However, as they incorporated strongly electron-donating alkoxy chains into their system, their polymers suffered from high-lying HOMO levels which can be detrimental to the ambient material or device stability.

Therefore, to lower the HOMO level of the polymers, the BTOR unit was further optimized through insertion of difluorobenzene in between the adjacent BTOR thiophenes (**Figure 10**).<sup>36</sup> Besides lowering the HOMO levels (due to the electron withdrawing fluorophenyl units), difluorobenzene also maintains the planar polymer backbone (through F···S interactions) and results in compact interpolymer packing.<sup>36</sup> The novel building block 1,4-di(3-alkoxy-2-thienyl)-2,5-difluorophenylene (DOTFP) was polymerized again with phthalimide (PhI), leading to enhanced carrier mobilities in OTFTs (up to  $1.20 \text{ cm}^2 \text{ V}^{-1} \text{ s}^{-1}$ , a fourfold increase) and an excellent power conversion efficiencies of up to 10.65%.<sup>36</sup>

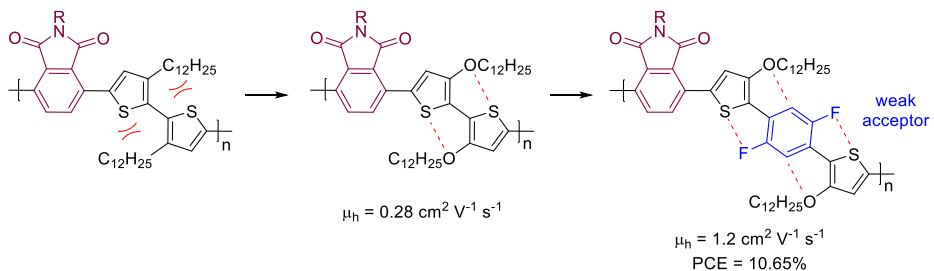


**Figure 10.** Research conducted by the Guo group shows that it is possible to take advantage of conformational locking to enhance the planarity phthalimide based conjugated polymers and their device performance.<sup>35,36</sup>

A similar trend was also observed when they polymerized BTOR and DOTFP with difluorinated benzothiadiazole (ffBT) instead of phthalimide, as the PCE increased from an initial 2.6% for BTOR-ffBT to an impressive 8.7% for DOTFP-ffBT (**Figure 11**).<sup>37</sup> These studies therefore demonstrate that noncovalent interactions, such as conformational locking can be used as an effective strategy to design or modify optoelectronic materials and thereby enhance their device performance.<sup>28,29,42,43</sup>

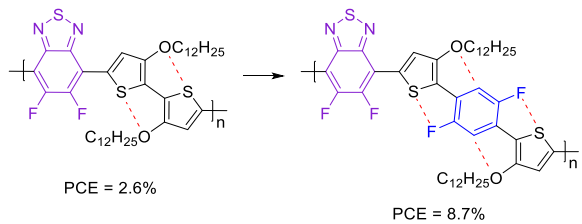


**Figure 11.** Favourable conformational locking leads to enhanced backbone planarity and improved PCE values in benzothiadiazole polymers.<sup>37</sup>

#### 1.4 Traditional Methods for Preparing Conjugated Materials

The preparation of conjugated materials or polymers relies on efficient construction of C–C bonds between two unsaturated carbons.<sup>18</sup> Besides electrochemical<sup>44,45</sup> or chemical oxidative polymerization methods<sup>46</sup>, the use of transition metals has become particularly powerful for forming Csp<sup>2</sup>–Csp<sup>2</sup> or Csp<sup>2</sup>–Csp bonds between aromatic systems.<sup>18,47</sup> The importance of transition-metal catalyzed C–C bond formation has been recognized with a Nobel prize in 2010.<sup>48</sup> Typically, transition-metal catalyzed cross-couplings proceed through 1) oxidative addition where the electron-rich catalyst inserts into an electron-withdrawn C–X bond, 2) transmetalation with an organometallic nucleophile and 3) reductive elimination, which results in the formation of the C–C bond and regenerates the active catalyst (**Figure 12**).<sup>18</sup> For polymers, the more the cycle repeats itself, the more the conjugation length is extended.

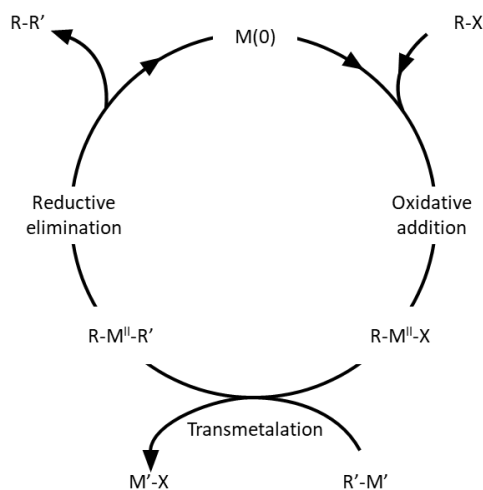


**Figure 12.** Overall reaction pathway for transition metal catalysed cross coupling reactions.

The most common transition-metal catalysts are Palladium (Pd) or Nickel (Ni) complexes, although other options are also available.<sup>18</sup> Typical C-C bond forming reactions include the coupling of organohalides or triflates with Grignard reagents (Kumada-Corriu),<sup>49</sup> alkenes (Heck-Mizoroki),<sup>50-52</sup> organozinc species (Negishi)<sup>53</sup>, tin reagents (Stille)<sup>54</sup>, boronic acids/esters (Suzuki-Miyaura)<sup>55</sup> or the coupling of alkynes with organocupper reagents (Sonogashira).<sup>56</sup> Lastly, it is also possible to *homo*-polymerize a single dihalogenated monomer through a Nickel-mediated dehalogenative coupling reaction (Yamamoto).<sup>57</sup> The application of these popular cross-coupling reactions in conjugated polymer synthesis will be illustrated with various literature examples, below.

#### 1.4.1 Kumada-Corriu & Negishi

In a Kumada-Corriu reaction, Grignard reagents are coupled with alkyl, vinyl or aryl halides using Pd or most commonly Ni. Using this method, McCullough prepared head-to-tail regioregular poly(3-hexyl thiophene) (rr-P3HT).<sup>58</sup> As observed, 2-bromo-3-alkylthiophene was treated with lithium diisopropylamide (LDA) and quenched with magnesium bromide to yield the organomagnesium intermediate, which then polymerized through the use of Ni(dppp)Cl<sub>2</sub> to afford P3HT with 90% head-to-tail regioselectivity and in 44-69% yield (**Figure 13, top**).<sup>59</sup>

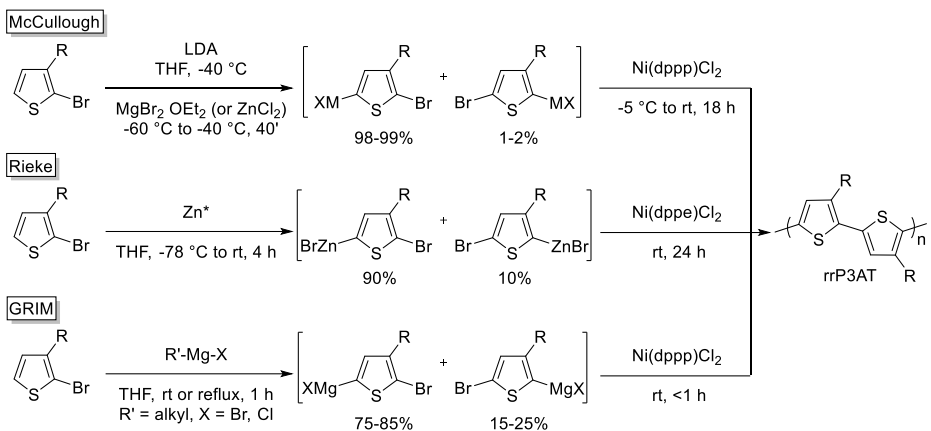


**Figure 13.** McCullough, Rieke and GRIM methods for the synthesis of regioregular polythiophenes.

The intrinsic asymmetry of 3-alkyl thiophenes (P3ATs) can result in three types of coupling products, namely: 2→5' head-to-tail (HT), 2→2' head-to-head (HH) and 5→5' tail-to-tail (TT) (**Figure 14**).<sup>60</sup> Due to the steric interactions of the C3 alkyl groups (with each other or with a sulfur lone pair) any contamination with HH couplings results in a twisted, non-planar backbone conformation.<sup>60–62</sup> This consequently gives rise to an interrupted π-conjugation and hence widens the bandgap and decreases carrier mobility on the polymer backbone. Therefore, research has been primarily focused on the synthesis of regioregular P3ATs with continuous HT couplings.<sup>60–62</sup>

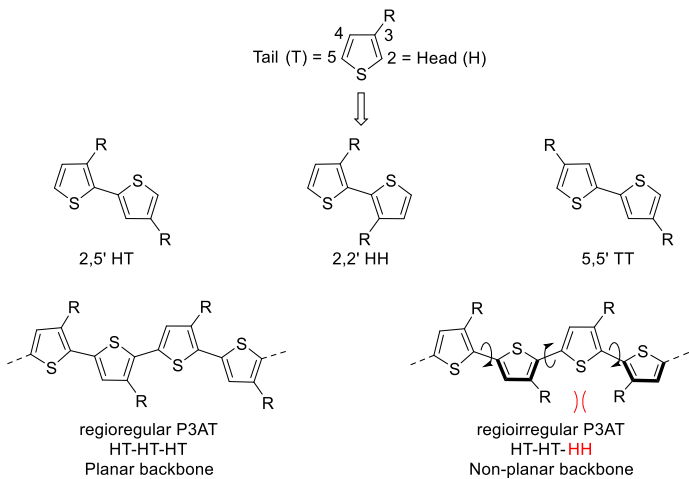


**Figure 14.** Possible coupling products of 3-alkylated thiophenes.

Soon after McCullough's work, a novel Negishi-type Rieke method was reported (**Figure 13, middle**).<sup>61,63–65</sup> In a Negishi cross coupling, organic halides or triflates are reacted with organozinc (or sometimes aluminium or zirconium reagents) to form a C-C bond.<sup>66</sup> In the Rieke method, highly reactive zerovalent zinc (Rieke Zinc) performs an oxidative addition reaction with 2,5-dibromo-3-alkylthiophenes to form zinc bromide intermediates in a 9:1 ratio, which later polymerizes upon introduction of Ni(dppe)Cl<sub>2</sub> to yield rr-P3ATs in ~75% yield and 98-100% regioregularity.

Later, McCullough further optimized the reaction conditions through the development of new and economical Kumada-type method, namely: Grignard metathesis (GRIM) (**Figure 13, bottom**).<sup>67,68</sup> In this strategy, 2,5-dibromo-3-hexylthiophene was reacted with one equivalent of a Grignard reagent, thereby affording metalated regioisomers in a ratio between 85:15 and 75:25.<sup>59</sup> Although, the ratio between the wanted and unwanted isomers is worse than either the McCullough or Rieke method, polymerization with catalytic Ni(dppp)Cl<sub>2</sub> afforded rr-P3ATs with 99% regioregularity.<sup>59</sup>

Yokozawa and coworkers proposed that Ni-catalyzed polymerization (e.g., McCullough and GRIM methods) occurs through chain growth with a catalyst transfer mechanism.<sup>69–72</sup> The proposed mechanism for regioregular P3AT synthesis is demonstrated in **figure 15**.<sup>73–75</sup> First, two equivalents of starting material (**1** or **2**) react with Ni(dppp)Cl<sub>2</sub> by displacement of chlorine (transmetalation; TM) to form organonickel complex **3**, which immediately undergoes a reductive elimination (RE) to generate the associated pair of 2,2-dibromo-5,5-bithiophene and Ni(0).<sup>59</sup> During the associated phase, the catalyst ring-walks (RW) closer towards one of the C-X bonds (from **4** to **4'**) so that it can perform an “intramolecular” oxidative addition (OA) and thereby insert into the respective C-X bond.<sup>71</sup> Next, the generated nickel complex **5** transmetalates with another equivalent of the starting material **1**, generating compound **6**. Reductive elimination then yields the associated pair of terthiophene (**7** and **7'**) and Ni(0). The polymer backbone keeps growing upon insertion of one monomer at a time (**7'** to **10**). As observed in the reaction cycle, the Ni(dpp) unit always incorporates as an end group in the polymer chain through formation of a π-complex (ring walking).<sup>59</sup> Therefore, Ni(dppp)Cl<sub>2</sub> is thought to behave as an initiator (rather than a catalyst), which restricts chain growth to only one end of the polymer. Further experiments supported that this reaction is a living polymerization<sup>74,75</sup> as 1) the degree of polymerization increases with monomer conversion and 2) adding Grignard reagents (R-MgX) at the end of the reaction leads to end-capping with R.<sup>76,77</sup> Therefore, the nature of living polymerizations offers great control over the molecular weights (M<sub>n</sub> and M<sub>w</sub>) and polydispersity (PDI) of the material<sup>78,79</sup> and thus allows systematic, structure-property relationship studies and a better overall understanding on polythiophene chemistry.<sup>59,80</sup>

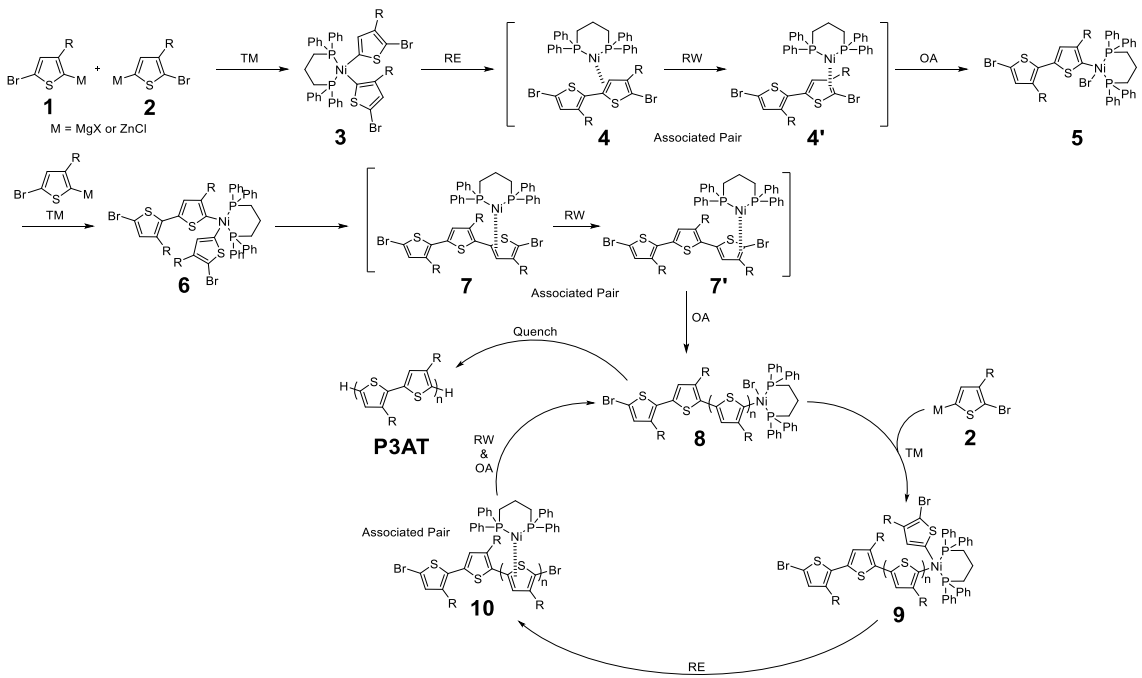


**Figure 15.** Proposed reaction mechanism for the Nickel mediated cross coupling of 3-alkyl thiophenes.

#### 1.4.2 Yamamoto

Yamamoto dehalogenative reactions rely on the homo-polymerization of dihalogenated monomers and are typically promoted by a stoichiometric amount of  $Ni(0)$ .<sup>60</sup> The detailed mechanism of this reaction is still poorly understood, however Yamamoto and coworkers propose the following overall pathway (**Figure 16**).<sup>81,82</sup> As seen,  $Ni(COD)_2$  undergoes a ligand exchange, followed by two oxidative additions (OAs) to form the nickel(II) complex  $[(bpy)Ni(Ph)_2]$ . This in turn undergoes a disproportionation (Disp.) with itself to afford  $[(bpy)NiBr_2]$  and  $[(bpy)Ni(Ph)_2]$ .<sup>81,82</sup> The latter species then undergoes a rapid reductive elimination, generating the coupled product (Ph-Ph). This method was used by Müllen and coworkers in 2006 for the preparation of a polycarbazole (**Figure 17**).<sup>83</sup>

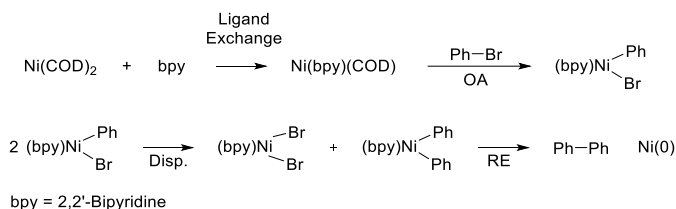


**Figure 16.** Proposed reaction pathway for Yamamoto coupling reactions by Yamamoto.<sup>81,82</sup>

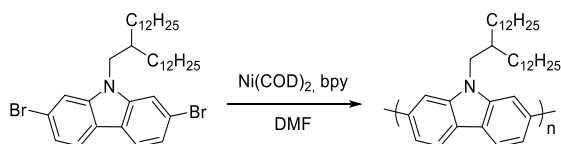


**Figure 17.** Synthesis of polycarbazole using Yamamoto conditions.<sup>83</sup>

### 1.4.3 Heck-Mizoroki

The Heck reaction relies on the Pd-catalyzed cross-coupling of aryl halides with alkenes to form an aryl-vinyl bond<sup>84-87</sup> and is therefore particularly attractive to generate vinyl-containing polymers, such as polyphenylenevinylanes (PPVs).<sup>59</sup> As with most Palladium catalyzed cross-coupling reactions, the initial step of the catalytic cycle requires pre-activation of the Pd catalyst.<sup>85</sup> The active Pd<sup>0</sup> catalyst can be either prepared *in situ* from cheaper, commercially available Pd<sup>II</sup> salts with the use of ligands, through transmetalation of Pd<sup>II</sup>L<sub>2</sub>X<sub>2</sub> with 2 equivalents of an organometallic reagent to form Pd<sup>0</sup>L<sub>2</sub>, or by going from a coordinatively saturated Pd<sup>0</sup>L<sub>4</sub> complex to the coordinatively unsaturated Pd<sup>0</sup>L<sub>2</sub> via ligand dissociation or reductive elimination of the ligands. An example mechanism for each process is provided in **figure 18**.

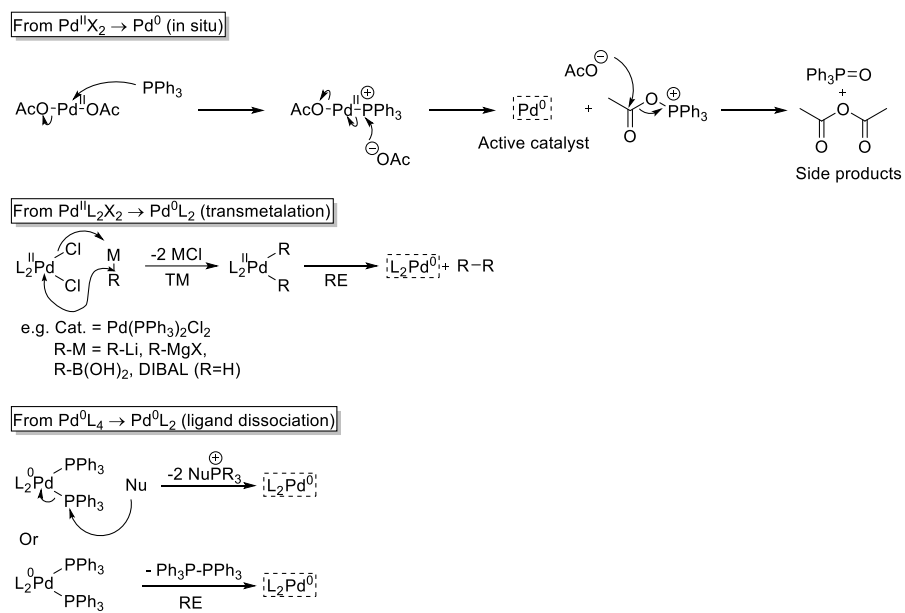


**Figure 18.** Overall methods to generate the active Pd<sup>0</sup> catalyst from the Pd<sup>II</sup> pre-catalyst.

The mechanism of the Heck cross-coupling reaction is shown in **figure 19**.<sup>85</sup> Once the active catalyst is formed, it can enter into the catalytic cycle by performing an oxidative addition into the electrophilic C-X bond.<sup>85</sup> Due to the nucleophilic nature of Pd<sup>0</sup>, the concerted oxidative addition process is promoted by electron-rich, sterically hindered ligands. The C and X groups are placed “*trans*” to each other. The proposed transition state and process is shown in **figure 19**. Next, the terminal alkene ( $\pi$ -electrons) coordinates to the electrophilic Pd<sup>II</sup> complex, thereby undergoing a migratory insertion (or carbopalladation).<sup>85</sup> The carbopalladation follows an asynchronous concerted pathway (syn-addition). As seen, the electrophilic Pd<sup>II</sup> species adds to the end of the alkene that is more electron-rich, whereas R<sup>1</sup> attacks the more electron-positive side. The resulting Pd<sup>II</sup> complex then undergoes a  $\beta$ -H elimination (syn-fashion) and thereby generates the alkene-containing product. Lastly, the active catalyst is regenerated and ready to

enter the next cycle. A few polymers prepared through the Heck reaction are demonstrated in **figure 20**.<sup>88</sup>

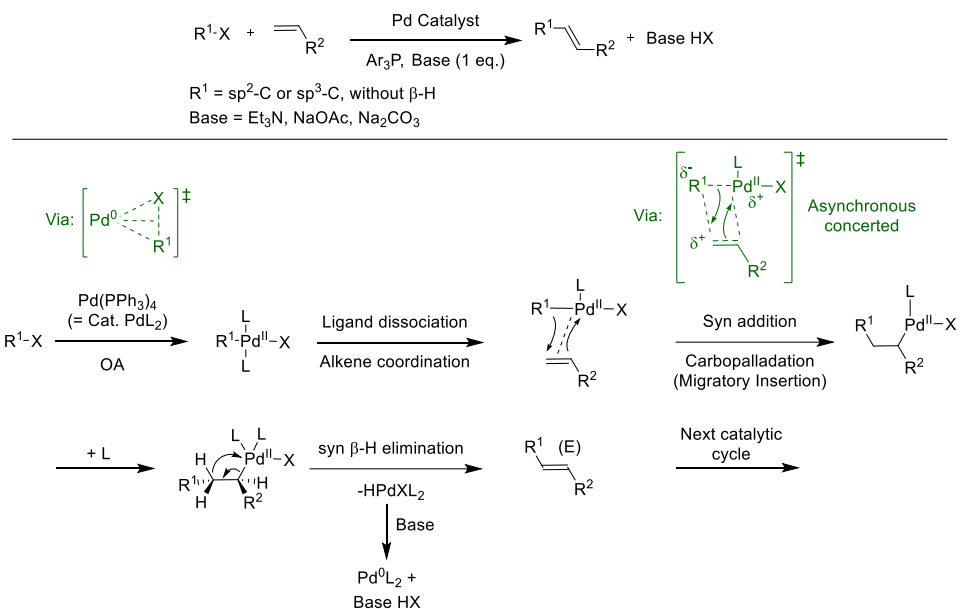


**Figure 19.** Heck-Mizoroki cross coupling reaction mechanism.

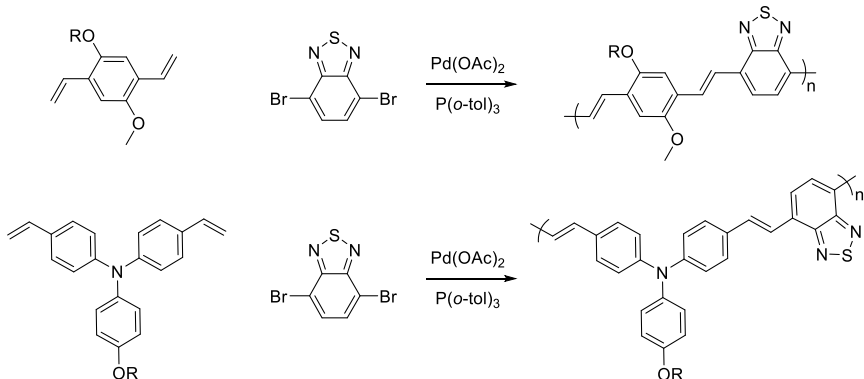


**Figure 20.** Example polymers prepared via a Heck-Mizoroki cross coupling reaction.<sup>88</sup>

#### 1.4.4 Sonogashira

The most popular choice to construct polyarylethylenes (PAEs) is probably the Sonogashira cross-coupling reaction. In this reaction, a C-C bond is formed between a terminal alkyne and an organohalide with the help of Pd and Cu catalysis. As observed from **figure 21**, the Pd<sup>0</sup> complex inserts into the electrophilic C-X bond through oxidative addition.<sup>89</sup> The resulting Pd<sup>II</sup> complex then undergoes a transmetalation with the copper acetylide, followed by *trans*-to-*cis* isomerism and reductive elimination to form the alkyne coupled product and regenerate the active Pd catalyst.<sup>89</sup> During the process, Cu also gets used and recycled. As seen, the Cu catalyst first coordinates to the alkyne. This makes the alkyne C-H acidic enough to be deprotonated by base (Et<sub>2</sub>NH) and forms the copper acetylide, which then gets used in the transmetalation step (as

explained before) and regenerates the Cu<sup>I</sup> catalyst.<sup>89</sup> Examples that use the Sonogashira method to construct PAEs are shown in **figure 22**.<sup>89,90</sup>

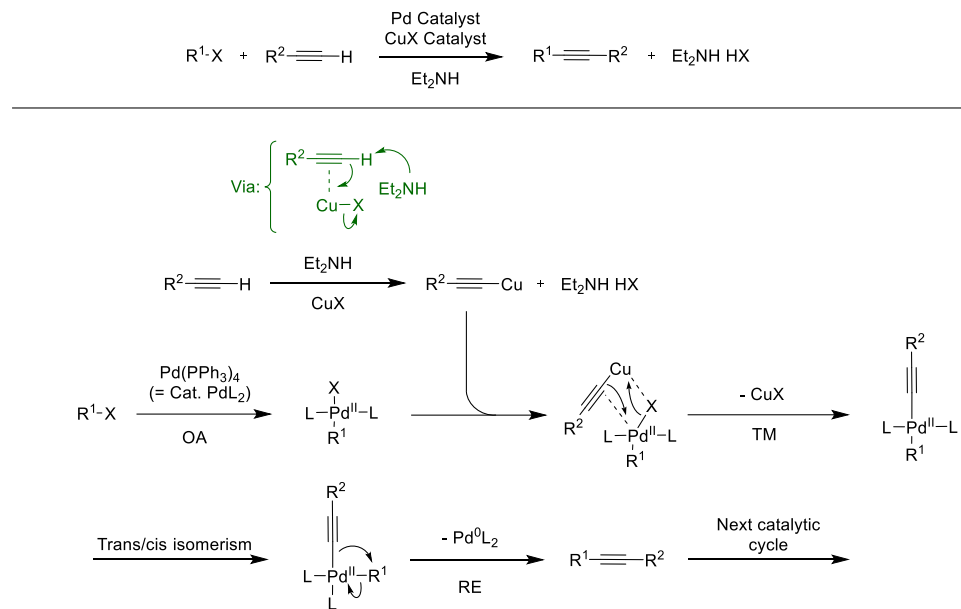


**Figure 21.** Sonogashira cross coupling reaction mechanism.

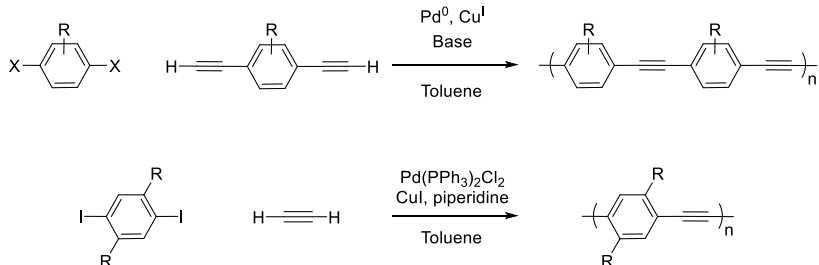


**Figure 22.** Example polymers prepared via a Sonogashira cross coupling reaction.<sup>89,90</sup>

#### 1.4.5 Stille

Stille cross-coupling reactions form C-C bonds between organotin reagents and organohalides or pseudohalides in the presence of a Pd catalyst<sup>54</sup> and are arguably the most popular choice for incorporating five-membered heteroaromatics (e.g., thiophene) into the polymer backbone.<sup>89,91</sup> Stille couplings are stable and usually mild reactions which allow for great functional group tolerance. Furthermore, organotin reagents can be bought or prepared easily via numerous methods and are relatively stable in the presence of oxygen or moist.<sup>91</sup> Therefore, despite the toxicity of organotin reagents, Stille reactions remain one of the most versatile and superior organometallic ways to construct C-C bonds.<sup>91</sup>

The general mechanism for Stille reactions is shown in **figure 23**.<sup>91</sup> The active catalyst is “Pd(0)”. Therefore, if Pd(II) catalysts are used in Stille reactions, they first undergo transmetalation with the organotin reagent to form Pd(0) as a coordinatively unsaturated 14-electron species.<sup>91</sup> Nucleophilic Pd(0) then undergoes an oxidative addition into the electrophilic C-X bond, forming

a stable 16-electron Pd(II) complex ( $R^1PdL_2X$ ), which rapidly undergoes *cis*-to-*trans* isomerism to generate the thermodynamically stable trans configuration.<sup>91,92</sup> The nucleophilic organotin reagent ( $R^2SnR_3$ ) and the electron-withdrawn Pd(II) complex then undergo a slow transmetalation step to form  $XSnR_3$  and  $R^1PdL_2R^2$ . Next, trans-to-cis isomerism takes place, which allows concerted reductive elimination and thereby affords the cross-coupled product ( $R^1-R^2$ ).<sup>91</sup> Furthermore, the active Pd(0) catalyst is regenerated and hence can re-enter the catalytic cycle to eventually form a conjugated polymer. A representative example demonstrating the use of Stille polycondensation in conjugated polymer synthesis is shown in **figure 24**.<sup>93</sup>

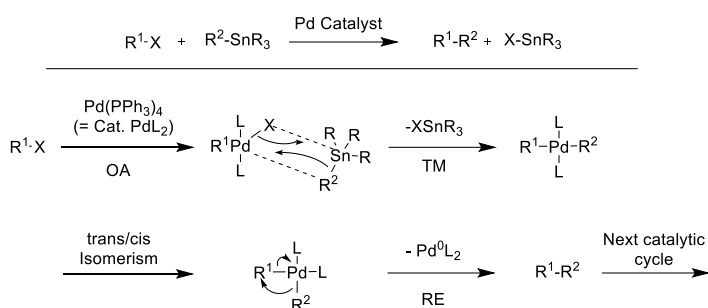


**Figure 23.** Stille cross coupling reaction mechanism.

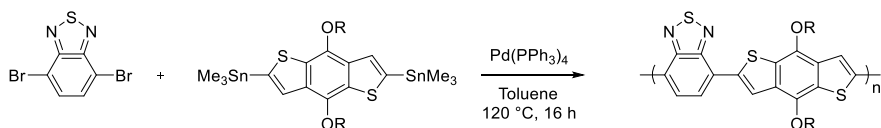


**Figure 24.** Example polymers prepared via a Stille cross coupling reaction.<sup>93</sup>

#### 1.4.6 Suzuki-Miyaura

Another extremely popular cross coupling is the Suzuki-Miyaura reaction between boronic acids/esters and (pseudo)organohalides in the presence of base and a Pd catalyst.<sup>89,94</sup> Suzuki couplings are most widely used in the preparation of benzene or benzene-like containing polymers, with the boronic acid or ester groups typically attached to the benzene unit. Suzuki couplings are compatible with many functional groups and have a lower toxicity compared to Stille. Furthermore, organoborons have a high thermal and chemical stability, are mostly inert to oxygen and moisture and can typically be prepared easily from readily available precursors.<sup>89</sup> Furthermore, they can be purified more easily via crystallization or silica column chromatography. Owing to all these advantages, Suzuki polycondensation reactions have become one of the most popular tactics to prepare conjugated polymers.<sup>89</sup>

The catalytic mechanism for Suzuki reactions is like Stille polycondensations, with the major exception that organoboron species first must be activated with base, to form the boronate, before they can participate in the transmetalation step. The proposed mechanism is illustrated in **figure 25**.<sup>89</sup> As before, the mechanism starts with an oxidative addition of Pd(0) into the electrophilic C-X bond, followed by rapid *cis*-to-*trans* isomerism. A base (like sodium ethoxide, NaOEt) then

exchanges with one of the ligands of the 16-electron Pd(II) complex, thereby activating the palladium. Furthermore, base also interacts with the boronic acid or ester to form an activated boronate. The activated Pd complex and boronate then undergo transmetalation to form a boronate salt and  $R^1PdL_2R^2$ , which isomerizes to the *cis* configuration to allow reductive elimination. This affords the cross-coupled product and regenerates the active catalyst. The examples in **figure 26** demonstrate few typical conjugated polymers prepared via Suzuki polycondensation.<sup>95</sup>

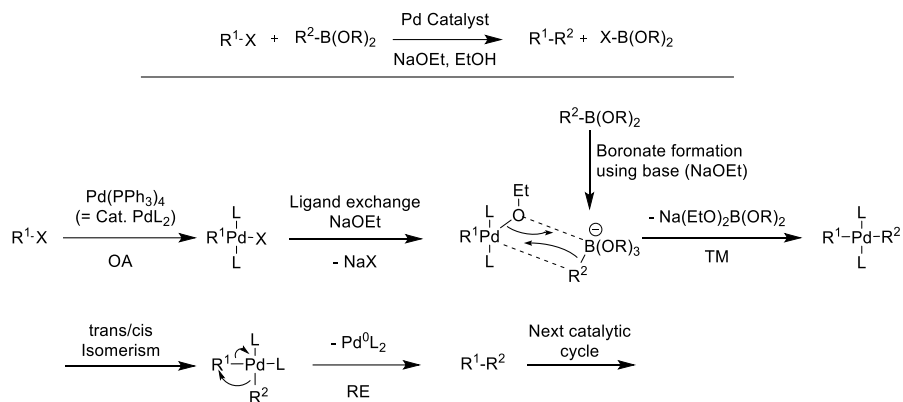


**Figure 25.** Suzuki-Miyaura cross coupling reaction mechanism.

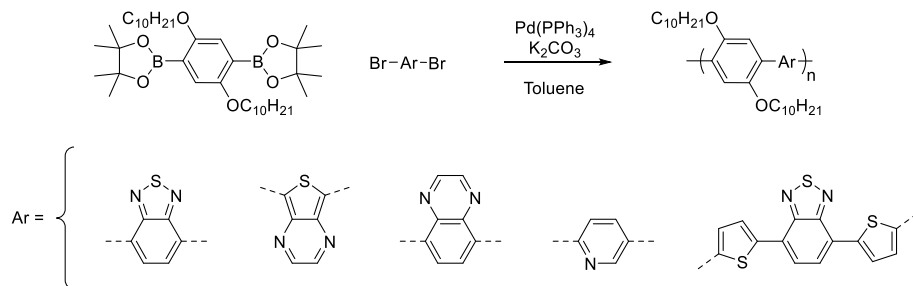


**Figure 26.** Example polymers prepared via a Suzuki-Miyaura cross coupling reaction.<sup>95</sup>

## 1.5 Absorption and Emission of Electromagnetic Radiation

Besides charge transport (via  $\pi$ -conjugation), the ability to harness or emit light is essential for conjugated polymers in organic electronics.

The *absorption* of radiation by materials obeys the Beer-Lambert law,<sup>96</sup> which states that the amount of energy absorbed (absorbance,  $A$ ) by a material is directly proportional to the wavelength-dependent molar absorptivity (or extinction coefficient,  $\varepsilon$ ) and the concentration ( $c$ ) of that sample at a given a path length ( $l$ ) (**Equation 1**). The extinction coefficient is a measure for how strongly a material absorbs light at a particular wavelength. When  $\varepsilon = 0$ , this means the sample is transparent and hence light passes straight through without energy being absorbed. In contrast, when  $\varepsilon > 0$ , the sample absorbs energy. Therefore, the larger the value of  $\varepsilon$  (at a certain concentration), the better the material is at harvesting solar energy.

$$A = \varepsilon(\lambda) c l \quad (Equation 1)$$

The probability of absorption or emission of electromagnetic radiation in an electronic transition is given by the *oscillator strength*. Experimentally, the oscillator strength ( $f$ ) is proportional to the integral of the extinction coefficient, which corresponds to the area under the extinction coefficient ( $\varepsilon$ ) versus wavenumber ( $\nu$ ) curve, as given by **equation 2**.<sup>97</sup> The oscillator strength can also be calculated using time-dependent density functional theory (TD-DFT).

$$f = \frac{2303 mc}{\pi N_A e^2 n} \int \varepsilon(\nu) d\nu \quad (Equation 2)$$

where  $m$  is the mass of an electron,  $c$  is the speed of light,  $N_A$  is Avogadro's number,  $e$  is the electron charge and  $n$  is the refractive index of the medium.

In general, as the planarity and effective conjugation length of the system increases, so do the oscillator strength and extinction coefficient<sup>98</sup> and thus the likelihood of photoexcitation and amount of light absorbed by a molecule increases as well.

*Luminescence* is the emission of light from a substance which is caused by anything but a rise in temperature.<sup>99</sup> Molecules can emit photons of light via radiative relaxation by decaying from an electronically excited state into the ground state. The method of excitation leading to emission can be caused by a photon (photoluminescence), a chemical reaction (chemiluminescence), an electron (electroluminescence) or mechanical action (mechanoluminescence).<sup>99</sup> For conjugated materials or polymers, the two most interesting types of luminescence are probably photoluminescence (PL) and electroluminescence (EL).

The concept of photoluminescence has been recognized for a long time, with reports dating back to 1845 when sir John William Hershel discovered photoluminescence in quinine.<sup>100</sup> The structure of quinine and two other, well-known photoluminescent molecules is illustrated in **figure 27**.

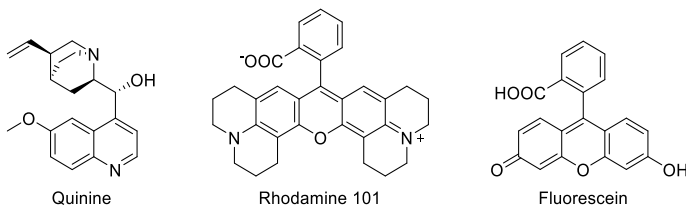


**Figure 27.** Chemical structures of quinine, rhodamine, and fluorescein.

The processes leading to emission as well as most other processes that can occur in conjugated materials are summarized in the Jablonski diagram (**Figure 28**) and summarized in **table 1**. Typically, after promotion of a molecule to an electronically excited state ( $S_1$  or  $S_2$ ), the molecule first relaxes to the lowest vibrational ( $v'_0$ ) level within the excited state  $S_1$ , through heat loss from intermolecular collisions,<sup>99</sup> and before any appreciable emission may occur (Kasha's rule).<sup>101</sup> This

process is extremely quick ( $\sim 10^{-11} - 10^{-14}$  s). The lifetime of the excited state  $S_1$  in its lowest vibrational state is longer ( $\sim 10^{-7} - 10^{-9}$  s).<sup>99</sup> Here, the excited molecule can lose energy to its surroundings via non-radiative decay mechanisms, such as vibrations and rotations. However, if the non-radiative decay mechanism is sufficiently slow, the molecule can lose its excess energy through emission of light (radiative decay), called *fluorescence*.<sup>101</sup>

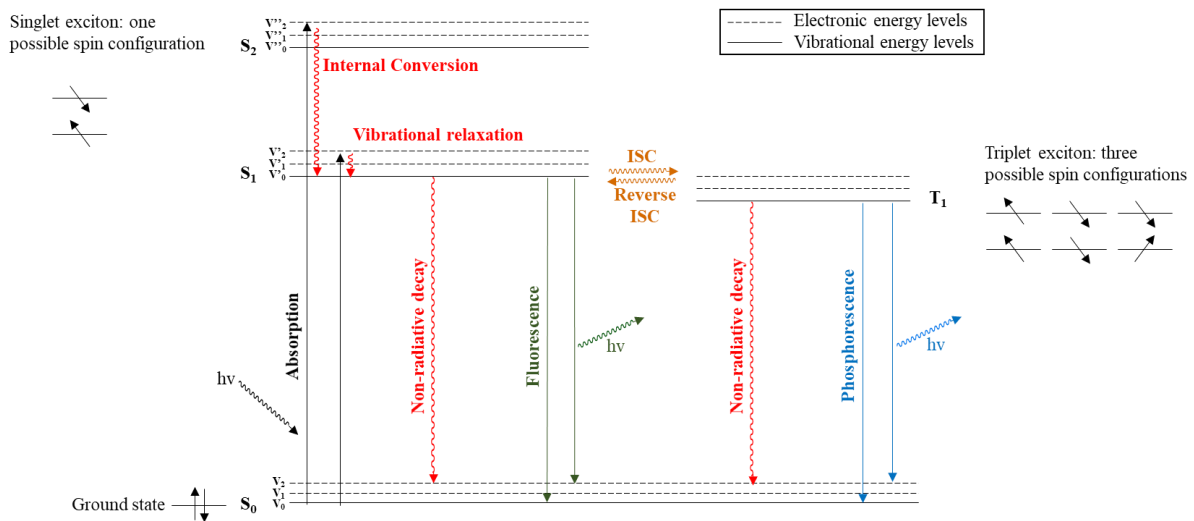


**Figure 28.** Simplified Jablonski diagram.

**Table 1.** Radiative and non-radiative processes and their respective rate of occurrence.

Process	Rate ( $s^{-1}$ )
Absorption	$10^{15}$
Internal conversion and vibrational relaxation	$10^{11} - 10^{14}$
Non-radiative decay	$10^7 - 10^9$
Fluorescence	$10^7 - 10^9$
Intersystem crossing	$0.1 - 10^{13}$ (Variable)
Phosphorescence	$10^3 - 10^6$ (Variable)

Alternatively, the energy may be transferred via intersystem crossing (ISC) to a triplet excited state ( $T_1$ ).<sup>99</sup> In this state, the spin of the two electrons are the same and hence radiative decay to the ground state would have to involve a spin flip. This is a spin-forbidden transition in the absence of spin-orbit coupling, but can take place in the presence of spin-orbit coupling (e.g., through incorporation of heavy atoms, such as iridium).<sup>99</sup> Triplet states are relatively long-lived ( $\sim 10^{-3} - 10^{-6}$  s) and are typically lower in energy than the corresponding singlet state. When the triplet excited state decays into the ground state ( $S_0$ ) through the slow emission of electromagnetic radiation, the process is called *phosphorescence*.<sup>99</sup>

The energy of an emitted photon is smaller (higher in wavelength) compared to the absorbed photon considering that the excited state loses energy before emission occurs. This energetic red-

shift is commonly termed as the “Stokes shift”.<sup>99</sup> **Figure 29** shows the absorption and emission profiles of two hypothetical organic dyes as well as their corresponding potential well diagrams. As observed, the absorption and emission profiles are mirror-images of each other, displaying a small Stokes shift. However, in real life the absorption and emission spectra do not always look this ideal. Instead, inter and intramolecular ground or excited state interactions and energy transfer mechanisms can occur and thereby dramatically affect the spectral features or optoelectronic properties of the material.

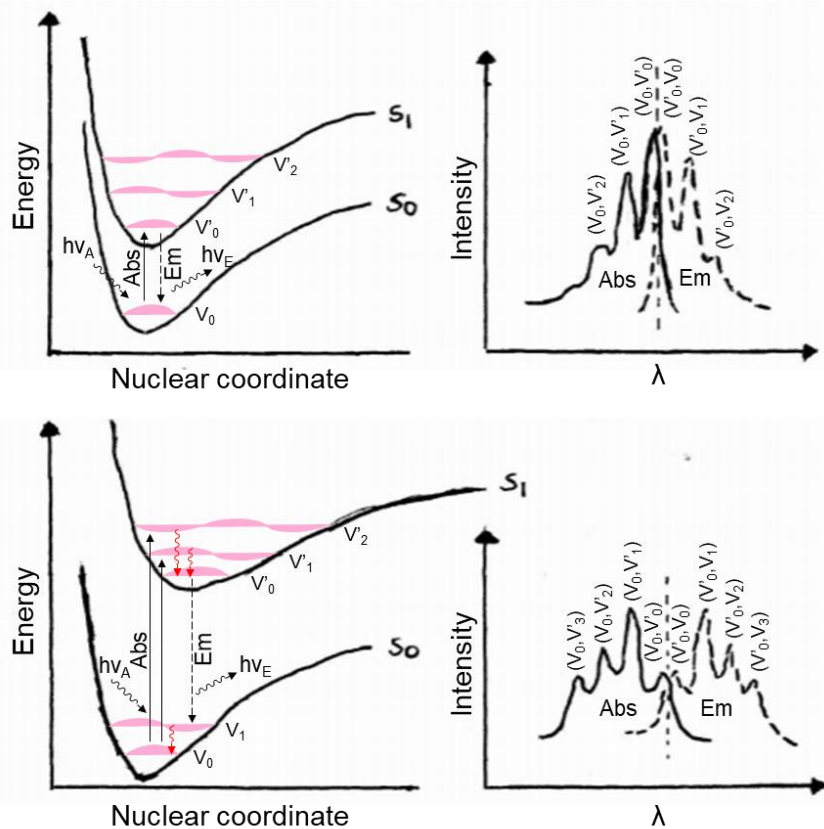


**Figure 29.** Potential energy diagrams with their respective, ideal absorption/emission spectra. Straight (black) and wavy (red) lines correspond to radiative or non-radiative processes, respectively. The vibrational wavefunctions are indicated in pink. a) Fluorophore with similar ground and excited state geometries and b) fluorophore with displaced excited state and ground state geometries.

### 1.5.1 Inter and Intramolecular Interactions

*Aggregates* are complex structures that are formed from the interaction of ground state chromophores. Their formation can heavily influence the photophysics of the material.<sup>102,103</sup> In polymers, aggregates can either form intermolecularly through Coulombic interactions between adjacent polymer chains (H-aggregates) or intramolecularly within a single polymer strand via through-bond interactions (J-aggregates).<sup>102,103</sup> The photophysics of common polymeric films is therefore determined by a competition between H- and J-aggregates.

In H-aggregates, the interpolymer chromophores are arranged in a face-to-face fashion (i.e., the chromophores have perpendicular stacking compared to the molecular plane) (**Figure 30**). This

in turn results in a hypsochromic shift (blue-shift) of the absorption spectrum compared to its isolated monomer and photoluminescence quenching.<sup>102,103</sup> In contrast, J-aggregates form when the chromophores stack in a displaced, head-to-tail manner (i.e., the stacking occurs in a parallel fashion compared to the molecular plane) (**Figure 30**). This leads to a bathochromic shift (red-shift) of the absorption profile and does not result in photoluminescence quenching.<sup>102,103</sup>

Conjugated polymers are two-dimensional systems that allow excitons to transport either in the  $\pi\text{-}\pi$  stacking direction (intermolecular H-aggregates) or along the conjugated backbone (intramolecular J-aggregates).<sup>103</sup> The blue/red shift in the absorption spectrum is therefore highly dependent on the alignment of the transition dipoles between the aggregated chromophores as well as their through-space coupling. More specifically, in H-aggregates the electronic transition between the  $S_0$  ground state and the lowest vibrational energy level ( $v'_0$ ) of the excited state ( $S_1$ ) (i.e., the 0-0 transition) is symmetry-forbidden and therefore the 0-1 transition intensifies compared to the 0-0 transition.<sup>104</sup> Conversely, in J-aggregates the 0-0 transition is symmetry allowed and hence the 0-0 peak intensifies compared to the 0-1 side band.<sup>104</sup> Having structural control over inter and intrapolymer interactions is therefore extremely important.

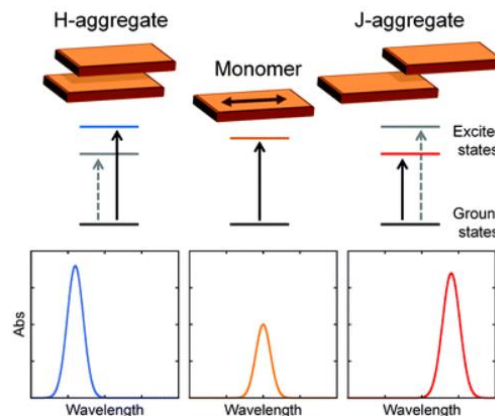


**Figure 30.** Representations of H- and J-aggregates in a dimer of a conjugated material, and their corresponding blue or red-shifted UV-Vis spectrum. Full or dashed arrows depict allowed (strong) and forbidden (weak) transitions, respectively. The double arrow indicates the monomer's transition dipole. Copyright © 2014 American Chemical Society.<sup>104</sup>

Alternatively, interactions can also occur with excited state species, in the case of excimers and exciplexes. *Excimers* are dimeric species that are formed through the interaction of an excited singlet state molecule ( $M^*$ ) with an unexcited one ( $M$ ). The dimer species ( $MM^*$ ) is only stable in the electronically excited state.<sup>99</sup> Similarly, an excited state molecule ( $M^*$ ) can also interact with an ground state molecule of a different nature ( $Q$ ) to form an *exciplex* ( $MQ^*$ ).<sup>99</sup> In the presence of excimers the emission spectrum typically becomes much broader, more featureless and red-shifted compared to normal fluorescence. An excellent, representative example that demonstrates this phenomenon is pyrene (Figure 31).<sup>99,105</sup>

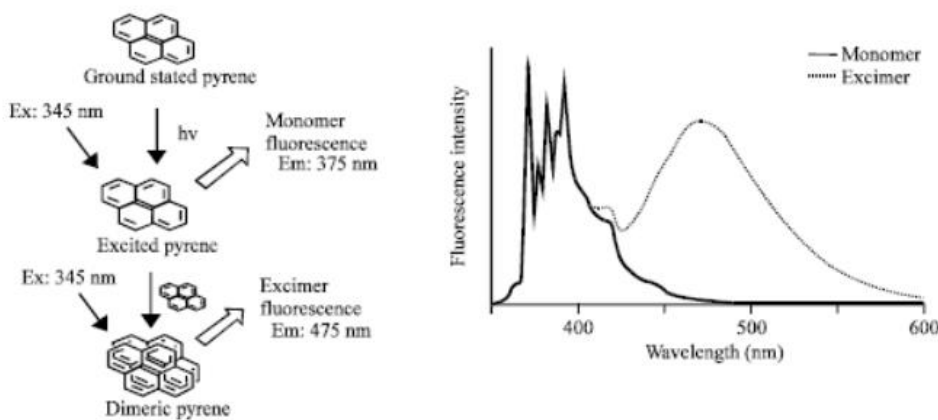


**Figure 31.** Fluorescence spectrum of pyrene as a monomer and excimeric species. Ex stands for excitation. Em stands for emission. Copyright © 2013 Science Alert.<sup>105</sup>

### 1.5.2 Energy Transfer Mechanisms

The energy of excited molecules can also be transferred to different molecules. For example, the excited donor molecule ( $D^*$ ) transfers its energy to the ground state acceptor molecule (A) and thereby bringing the donor molecule to its ground state and exciting the acceptor ( $D + A^*$ ). As a result, the photoluminescence of the donor is quenched.<sup>99</sup> The two possible energy transfer mechanisms are *Förster* and *Dexter transfer*. Where Förster transfer only occurs between species separated over longer distances (i.e., they have to exceed their van der Waals radii), Dexter transport takes place over short distance as it requires direct overlap between the wavefunctions of the donor and acceptor molecule.<sup>99</sup> Schematic representations of both processes for singlet-singlet transfer are shown in **figure 32**.

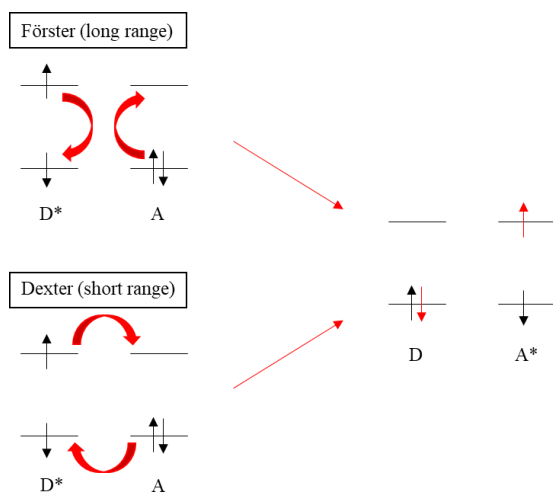


**Figure 32.** Schematic representation of Förster (long range) and Dexter (short range) energy transfer mechanisms.

### 1.5.3 Quantum efficiency

As discussed previously, photoluminescence in conjugated materials arises from the radiative decay of singlet excitons, whereas non-radiative processes (e.g., energy transfer, excimer/exciplex formation and charge separation) can lead to a compromised emission.<sup>106</sup> The

efficiency at which emission occurs from an excited state is called the photoluminescence quantum yield (PLQY,  $\phi_{PL}$ ). Given that the emissive state is formed without the loss of energy during excitation, the PLQY can be simply defined as the ratio between photons emitted ( $N_E$ ) and photons absorbed ( $N_A$ ). Furthermore, it is also related to rate constants as  $\phi_{PL}$  is equal to the ratio between the radiative decay ( $k_r$ ) over the sum of the radiative ( $k_r$ ) and non-radiative decay ( $k_{nr}$ ) (**Equation 3**). The excited lifetime is defined according to **equation 4**.

$$\Phi_{PL} = \frac{N_E}{N_A} = \frac{k_r}{k_r + k_{NR}} \quad (\text{Equation 3})$$

$$\tau = \frac{1}{k_r + k_{NR}} \quad (\text{Equation 4})$$

For PL, the initially excited state (Franck-Condon state) is singlet in nature due to the Pauli exclusion and spin selection principles.<sup>101</sup> Therefore, according to the Jablonski diagram, it is possible to obtain  $\phi_{PL}$  values of 100% via fluorescence or phosphorescence (after ISC).

For EL this is not the case. Instead, the EL process relies on the Coulombic attraction (or charge recombination) of negatively charged electrons ( $e^-$ ) and positively charged holes ( $h^+$ ), which consequently form excitons in the emission layer of an OLED.<sup>107</sup> This means that the hole and electron involved in the excited state were initially not bound together. Therefore, since each hole or electron can have an “up” or “down” spin, their recombination leads to statistical distribution of four possible spin combinations.<sup>107</sup> According to quantum mechanics, this translates to 25% of excitons being singlet and 75% being triplet in nature. For traditional fluorophores, the maximal obtainable internal quantum efficiency (IQE, the EL equivalent of  $\phi_{PL}$ ) is therefore 25%. The other 75% of the emission is lost immediately to non-emissive triplet states as a high exchange energy leads to improbable reverse intersystem crossing.<sup>107</sup>

## 1.6 Device Fundamentals: OPVs and OLEDs

### 1.6.1 Organic Light-Emitting Diodes (OLEDs)

An organic light-emitting diode (OLED) is a device that makes use of an organic, electroluminescent material to emit light in response to electrical current.<sup>108,109</sup> A typical diode is built by depositing electrodes and functional layers on a glass (or other transparent) substrate. One of the simplest OLED device structures is demonstrated in **figure 33**. As observed, the OLED is comprised of a transparent anode, an organic emissive layer, and a reflecting metal cathode. A similar device structure was used for the well-known publication of Holmes and coworkers in 1990.<sup>110</sup>

The electrons (from the cathode) and holes (from the anode) are injected into the emissive, semiconducting layer, where they form an exciton (i.e., a Coulombically bound electron-hole pair) (**Figure 34**). The exciton can then undergo radiative decay to emit light from the emissive

layer, with the photon's energy being equivalent to the bandgap of PPV, which is  $\sim 2.5$  eV or 496 nm. The anode and cathode are chosen to match with the HOMO and LUMO of the electroluminescent layer, respectively. Furthermore, one of the electrodes must be transparent to allow the generated photons to pass through, which in this case is the cathode indium tin oxide (ITO). The design and fine-tuning of different materials can generate blue, green or red emitters; all of which are necessary in color displays.

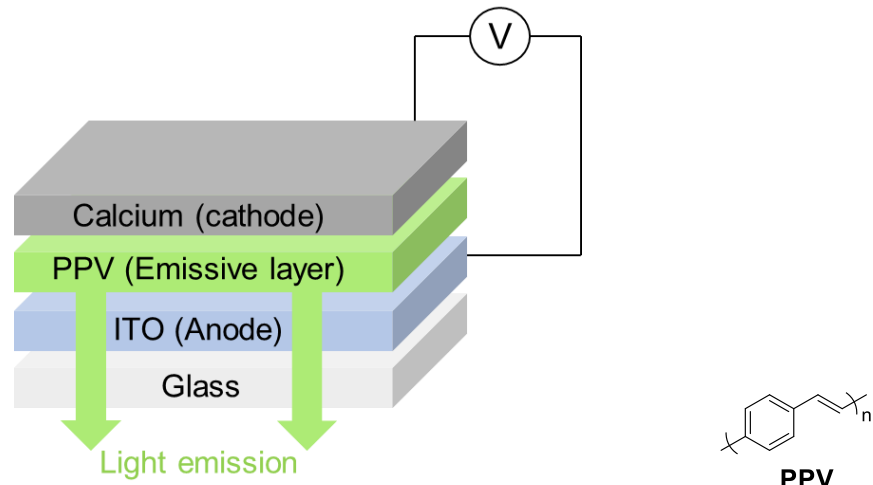


**Figure 33.** (left) Schematic representation of one the simplest OLED device structures, with V standing for an externally applied voltage. (right) Structure of PPV.

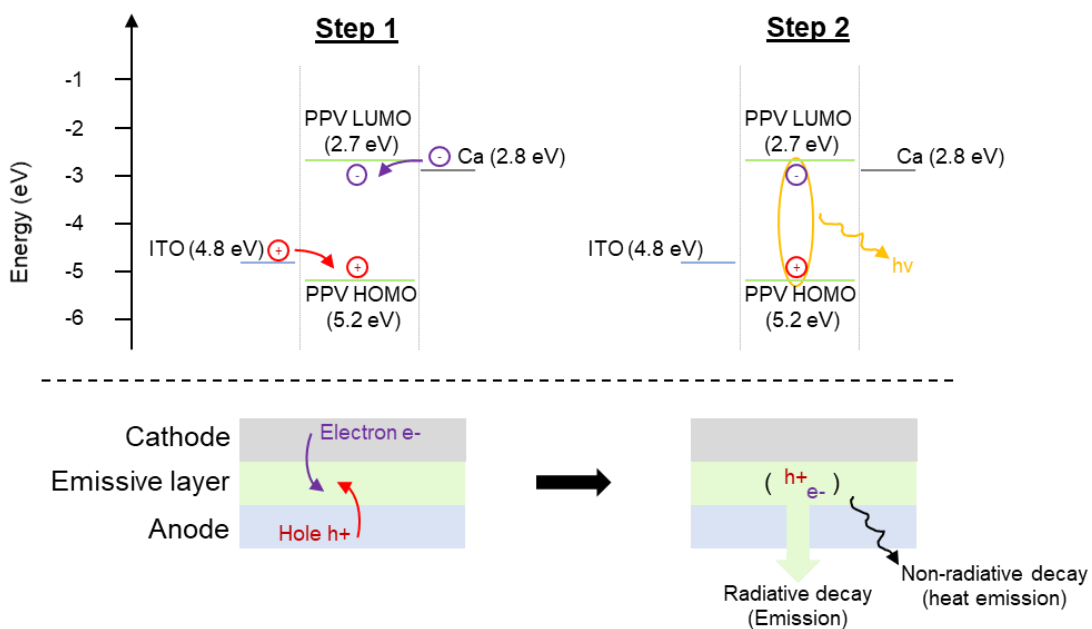


**Figure 34.** Energy diagram and device structure showing the formation of excitons and light generation in OLEDs.

Even though the previous sections show the basics behind OLEDs, the structure of more recent OLED devices is more complex, typically containing additional layers. The two common layers

included to facilitate the entire process and are called the electron/hole transport layer (ETL/HTL) and the electron/hole injection layer (EIL/HIL). A representative example of this was reported by Holmes and coworkers in 1994 (**Figure 35**).<sup>111</sup> Here, PEDOT:PSS was added as a hole injection layer (HIL) on top of the ITO anode to smoothen the ITO surface. This consequently reduces the chance of getting electrical shorts, which in turn prolongs the operation lifetime of the device.<sup>112</sup> The layer also matches the HOMO energy level of active layer more closely (**Figure 36**), and is transparent and compatible with the subsequent organic layers.<sup>113</sup>

The second addition is the CN-PPV layer, which has extra solubilizing groups compared to PPV and thereby makes it more processable and easier to obtain thin, well-defined films. The electron-withdrawing cyano groups lower both the HOMO and LUMO energy level, although the LUMO is more affected (as explained in section **1.3.2**). This results in a narrower bandgap and hence redshifted electroluminescence. Furthermore, the injection of electrons from the cathode into the active CN-PPV layer is facilitated (due to the difference in eV). The PPV layer allows holes to be transported toward the interface with the emissive layer, where they can meet with electrons to form excitons and generate light. By simply changing the device architecture from a single CN-PPV layer to a PPV/CN-PPV structure, the internal quantum efficiency of the device increased significantly from 0.15% to 4%.<sup>111</sup>

This example therefore demonstrates the importance of device structure, and how small changes can sometimes have a dramatic impact. Understanding the role of each layer is therefore needed to generate more efficient devices. However, the work presented in this thesis is mostly concerned with the actual semiconducting materials, rather than optimizing the device itself.

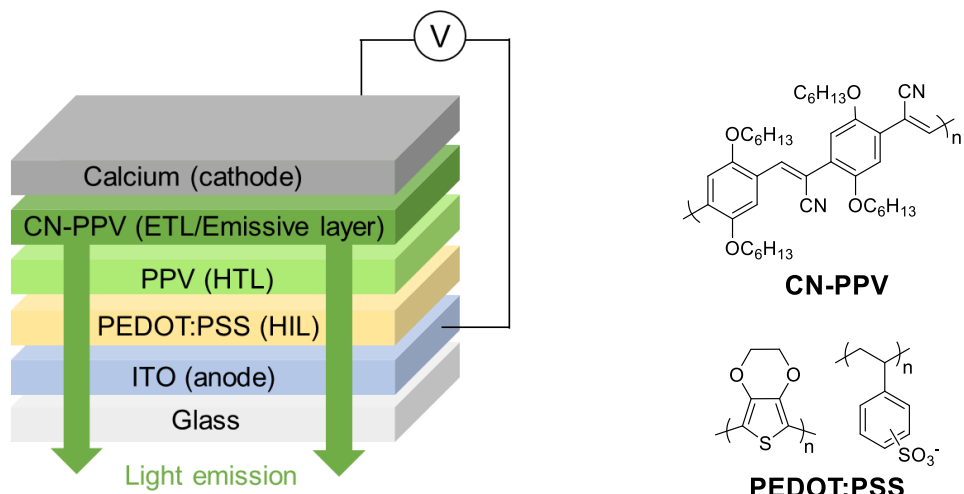


**Figure 35.** (left) Example device structure of a multilayer OLED.

(right) Chemical structure of CN-PPV and PEDOT:PSS.

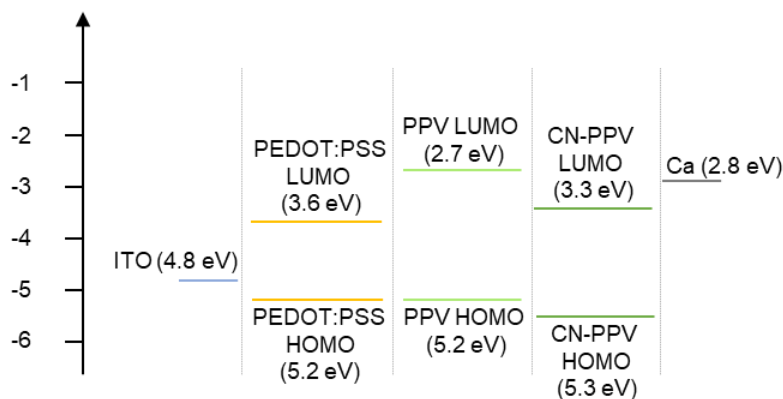


**Figure 36.** Energy level diagram of a multilayer OLED.

The overall structure of an OPV device is quite similar to an OLED (**Figure 37**). The Holmes group published a nice example to demonstrate this further.<sup>114</sup> Here, a blend of CN-PPV and MEH-PPV is sandwiched between the anode and cathode. However, instead of injecting charges into the active layer, the semiconductor makes use of sunlight to generate free charges and electricity. More detail on how this works, will be provided in the following section.

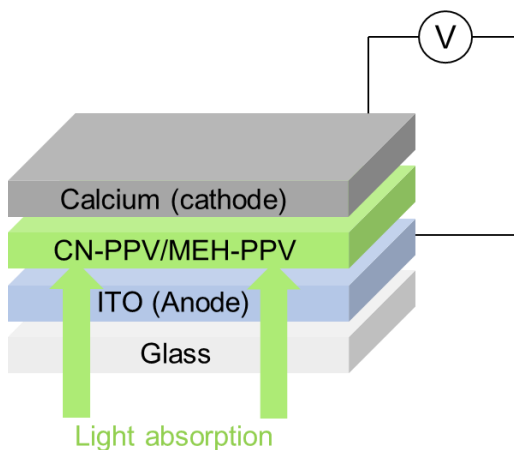


**Figure 37.** Device structure of a basic OPV with the CN-PPV/MEH-PPV blend being the absorbing layer.

### 1.6.2 Organic Photovoltaics (OPVs)

Organic photovoltaics (OPVs) are made of carbon-based materials that can absorb electromagnetic radiation (from sunlight) and convert it into electricity. The process of turning light into electricity can be summarized in a few key steps (**Figure 38**).<sup>115</sup> First, the photoactive material absorbs a photon and gets excited, generating an electron-hole pair or exciton. Next, the exciton diffuses to the donor-acceptor interface, where it can form a charge transfer (CT) state and dissociate to form free charges. Finally, the transport of the free charges to the respective electrodes generates electrical power. To accomplish charge separation, OPVs rely on an active layer that is comprised of an electron-rich donor (hole transporting) and electron-poor acceptor

(electron-transporting) material.<sup>116</sup> These materials are needed to pull the electrostatically bound electron and hole apart and generate free charges.<sup>115,117</sup>

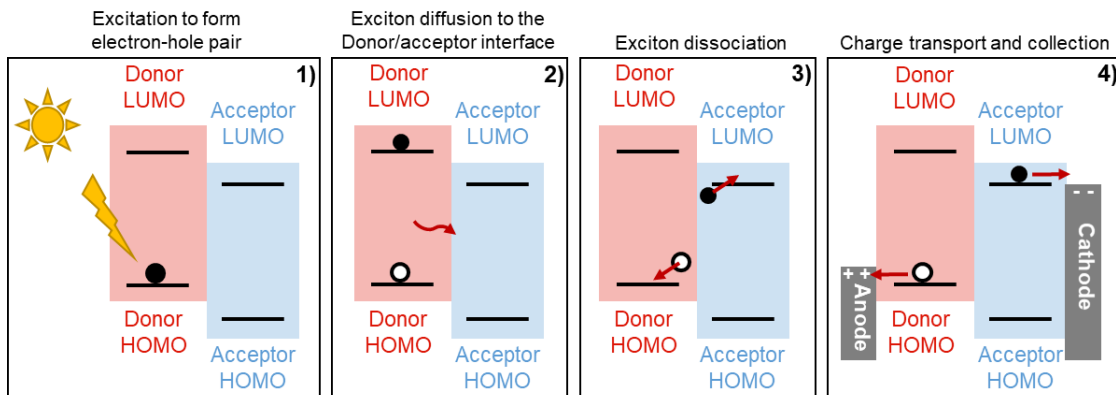


**Figure 38.** Process of converting sunlight into electrical power using a bulk heterojunction.

Upon blending both materials together, they form an interpenetrating network, thereby maximizing the interfacial area for charge dissociation. In most state-of-the-art systems, the donor material is typically a narrow bandgap donor-acceptor polymer, which gets blended with either a fullerene or non-fullerene acceptor.<sup>195</sup>

The efficiency with which a solar cell converts sunlight into usable electricity, is referred to as the power conversion efficiency (PCE). Even though, organic materials have so far been less efficient compared to inorganic solar cells, such as gallium arsenide (~38%) or commercially available silicon modules (~24%),<sup>118</sup> extensive research means they are rapidly improving with current PCE values already approaching 20%.<sup>119</sup>

The power conversion efficiency (PCE) is calculated by **equation 5**;<sup>116</sup>

$$\text{PCE} = \frac{J_{SC} V_{OC} FF}{P_{in}} \quad (\text{Equation 5})$$

where  $P_{in}$  is the power density of incident electromagnetic radiation,  $J_{SC}$  stands for short-circuit density,  $V_{OC}$  is the open-circuit voltage, and FF is the fill factor defined as  $P_{max}/(J_{SC}V_{OC})$ , with  $P_{max}$  being the maximum power density.  $J_{SC}$  is limited by three major processes; the rate at which the donor and acceptor components absorb photons, the efficiency of electron-hole separation, and the efficiency with which the resulting free charges are transported to and collected by the electrodes. The open-circuit voltage is limited by the charge transfer state energy ( $E_{CT}$ ) of the donor-acceptor interface, as defined by **equation 6**.<sup>116</sup>

$$E_{CT} = IE_{(D)} - EA_{(A)} - E_{b(CT)} \quad (\text{Equation 6})$$

Where  $IE_{(D)}$  is the ionisation energy of the donor,  $EA_{(A)}$  is the electron affinity of the acceptor, and  $E_{b(CT)}$  stands for the binding energy of the exciton in the CT state (i.e., the Coulombic

attraction between the  $D^+$  and  $A^-$  components). The  $V_{OC}$  reduces by (non)radiative recombination processes. Therefore, there must be a compromise between the  $J_{SC}$ , which maximizes with increasing absorption of visible and near-infrared radiation, and the  $V_{OC}$ , which maximizes by increasing the difference between  $IE_{(D)} - EA_{(A)}$ .<sup>116</sup> For a single-junction solar cell absorbing photons with only  $E > E_{op}$  (not  $E < E_{op}$ ), the optimum energy of the (relaxed) exciton relative to the ground state ( $E_{op}$ ) is ~1.1-1.4 eV with a PCE of ~34% in the Shockley–Queisser limit. This limit is the maximum theoretical efficiency for single-junction OPVs to generate power, assuming the only loss mechanism in a solar cell is radiative recombination. This theory assumes that no driving force is required for charge separation (i.e., the chosen materials follow  $E_{op} = IE_{(D)} - EA_{(A)}$ ) and no voltage losses arise from non-radiative recombination.<sup>116</sup> However, in practice, this is not the case, leading to additional energy losses ( $E_{loss}$ ) (**Equation 7**);

$$E_{loss} = E_{op} - eV_{OC} \quad (Equation\ 7)$$

where  $e$  is the elementary charge.

While research in the past decade has primarily focused on creating diverse donor materials, the design of novel acceptors remained relatively underexplored.<sup>116</sup> The use of acceptor materials was therefore mostly limited to fullerene acceptors (FAs), such as [6,6]-phenyl-C<sub>61</sub>-butyric acid methyl ester (PC<sub>61</sub>BM) and [6,6]-phenyl-C<sub>71</sub>-butyric acid methyl ester (PC<sub>71</sub>BM). The positive characteristics of FAs include their three-dimensional nature, delocalized LUMOs which create good charge transport pathways, and their ability to mix well with donors to form interpenetrating networks and to stimulate charge separation and transport. However, FAs also have various negative attributes, such as their limited structure tunability, weak absorption of visible and near-infrared light, thermal and photochemical instability, and tedious purification procedures.<sup>116</sup>

Therefore, the development of non-fullerene acceptors (NFAs) has become increasingly popular. As opposed to their FA counterparts, NFAs can be tuned and synthesized relatively easy, and they possess greater thermal and photochemical stability, and improved device lifetimes. Furthermore, they can absorb larger proportions of incident light (in both visible and NIR region) and thereby complement the donor's absorption.<sup>116</sup>

## 1.7 Polymer Definition, Molecular Weights and Polydispersity

*Polymers*, derived from the Greek “poly” (many) and “meros” (parts), are large molecules that are comprised of repeating subunits or monomers along the chain. During the polymerization process, the polymer chains typically reach different lengths, thereby resulting in a distribution of chain lengths or molecular weights. The two most common ways to define molecular weight are via the number average molecular weight ( $M_n$ ) and weight average molecular weight ( $M_w$ ).

The number average molecular weight ( $M_n$ ) is calculated by dividing the total weight (or sum) of all the polymer chains in the sample by the number of chains present in the sample.  $M_n$  is defined according to **equation 8**, where  $N_i$  stands for the number of molecules with weight  $M_i$ .

$$M_n = \frac{\sum_{i=1}^{\infty} N_i M_i}{\sum_{i=1}^{\infty} N_i} \quad (\text{Equation 8})$$

The weight average molecular weight ( $M_w$ ), on the other hand, does not only depend on the number of molecules present in the sample, but also considers that larger chains contribute more to the molecular weight than smaller ones. Therefore,  $M_w$  is defined according to the weight fraction ( $W_i$ ) of each polymer chain (**Equation 9**).

$$M_w = \frac{\sum_{i=1}^{\infty} W_i M_i}{\sum_{i=1}^{\infty} W_i} = \frac{\sum_{i=1}^{\infty} N_i M_i^2}{\sum_{i=1}^{\infty} N_i M_i} \quad (\text{Equation 9})$$

The polydispersity (PDI) index is a measure for how “disperse” your sample is and can be defined as the ratio between the weight average molecular weight and number average molecular weight (**Equation 10**). In other words, the smaller the PDI value becomes (with 1.0 being the smallest), the less all the polymer chains of that sample differ in length.

$$PDI = \frac{M_w}{M_n} \quad (\text{Equation 10})$$

In polymer chemistry, the molecular weights and PDI are typically determined using gel permeation chromatography/size exclusion chromatography (GPC/SEC). In GPC/SEC the sample is passed through a stationary phase (porous gel) to separate the polymer chains according to size. Longer polymer chains pass through the column quickly as they are too big to occupy the pores of the stationary phase. Smaller chains, on the other hand, take more time to elute as they get retained in the pores of the gel. Over time it is therefore possible to obtain a distribution of the different chain lengths in the sample and hence determine the  $M_n$ ,  $M_w$  and PDI.

## 1.8 Introduction to Macrocyclic Encapsulated Conjugated Polymers

Due to their planar nature, conjugated polymers have a high tendency to undergo intra or intermolecular interactions, which as explained previously can dramatically influence the light-harvesting and emitting properties of the polymer (via energy transfer mechanisms, aggregates or excimer/exciplex formation). Non-radiative processes are even more prominent in red-emitting conjugated polymers due to their inherent narrow optical bandgaps, as described by the energy gap law.<sup>120-122</sup> Furthermore, with increasing concentrations (e.g., from solution to solid-state), there is a higher tendency to form aggregates.<sup>106,123</sup> As a result, it remains very challenging to prepare conjugated polymers that are highly emissive in the red region of the electromagnetic spectrum. To further advance organic electronics, it is therefore extremely important to gain synthetic control over the intra and intermolecular interactions in polymers.

To overcome some of the issues associated with planar materials, interpolymer interactions can be suppressed via either noncovalent or covalent encapsulation. In this way, polymers are surrounded with a protective macrocycle, which isolates the polymeric chains from one another and prevents cross-talk.<sup>124</sup> As a result, various desirable properties can be obtained, including increased luminescence and environmental stability.<sup>124–127</sup> Furthermore, macrocyclic encapsulation can restrict charge or exciton transport to only one dimension (i.e., along the polymer backbone), as opposed to the two-dimensional charge transport in regular, naked polymers. This means intermolecular hopping can essentially be “turned off” and hence, for the first time, it is possible to study intramolecular charge transport.

Encapsulated conjugated polymers are commonly referred to as “insulated molecular wires (IMWs)”. This is in analogy with electrical power cords as the conductive polymer strand (or copper wire) is enclosed by a non-conductive macrocycle (or insulator).<sup>124</sup> However, the terminology “insulated molecular wire” can be interpreted incorrectly as a molecular wire or polymer that is “insulated” or non-conductive, and therefore we will refer to them as “encapsulated conjugated polymers”. The following section will discuss various (non)covalently encapsulated conjugated polymers.

### 1.8.1 Noncovalent Encapsulation Strategies

One method to prepare encapsulated conjugated polymers is by sheathing the desired material through a macrocycle using noncovalent interactions. This results in the formation of a pseudopolyrotaxane or polyrotaxane (**Figure 39**). Rotaxanes are complex structures in which a “guest” material is enclosed by a macrocyclic “host” and then capped with bulky termini.<sup>124</sup> When both the guest and the macrocyclic host are repeated, the polymer is called a “polyrotaxane”. Alternatively, when the encapsulated polymer chain is not contained by bulky termini, the polymer is referred to as “pseudopolyrotaxane”.<sup>124</sup> This section will highlight some, existing rotaxane-based materials and discuss why they are interesting for organic electronics.

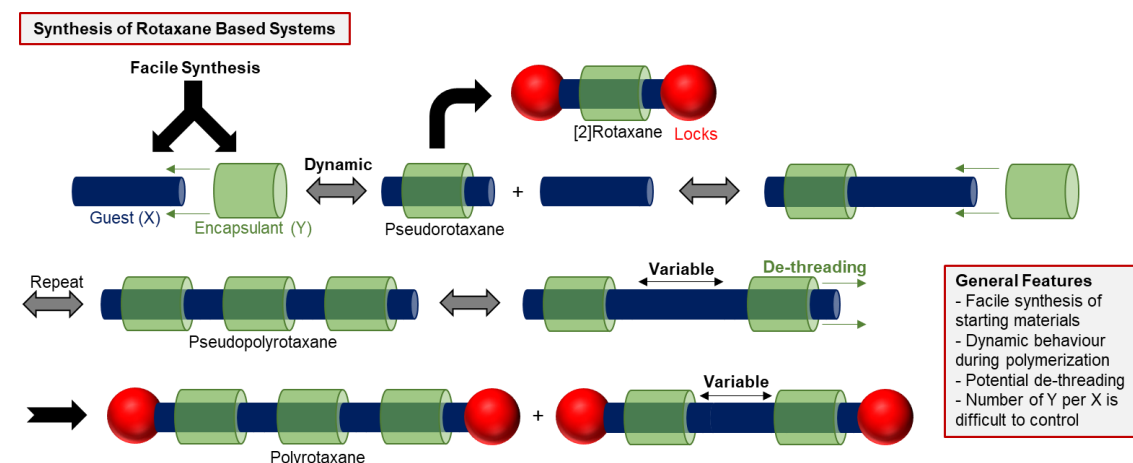


**Figure 39.** Illustration of different types of rotaxane-based, encapsulated materials.

### 1.8.1.1 Cyclodextrin-Based Systems

Cyclodextrins (CDs) are oligosaccharides which organize into a “molecular tube”.<sup>124</sup> They are ideal for generating inclusion complexes<sup>128</sup> or encapsulated conjugated materials due to their unique shape, which enables hydrophobic, hydrogen bonding or covalent bonding interactions to occur.

In 1999, Lagrost and co-workers formed a pseudopolyrotaxane (**I-1**) by an electropolymerization of 2,2'-bithiophene in the presence of hydroxylpropyl- $\beta$ -cyclodextrin (HP- $\beta$ -CD) and aqueous media.<sup>129</sup> The reaction therefore makes use of hydrophobic interactions to organize the hydrogen-bonded complex into a “head-to-head” channel. The resulting pseudopolyrotaxane contained one 2,2'-bithiophene unit per CD cavity and another 2,2'-bithiophene unit between 2,3-rims of two adjacent CDs (**Figure 40, left**).<sup>130</sup> According to Hapiot and co-workers, the reaction follows a “cation radical polymerization” mechanism, where each cyclodextrin mechanically interlocks onto the previously formed polythiophene chain.<sup>131</sup> Yet, due to the dynamic nature of the reaction, the polymer backbone remained largely unprotected, indicating that the density of encapsulation is difficult to control using this method.

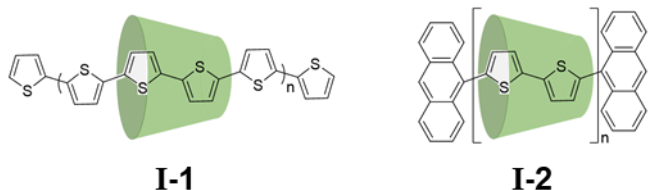


**Figure 40.** Graphic illustration of the cyclodextrin-based pseudopolyrotaxane<sup>130</sup> (left) and polyrotaxane<sup>132</sup> (right).

Therefore, Boogard *et al.* came up with an alternative method to optimize coverage of the polymer backbone.<sup>132</sup> Instead of mechanically interlocking the cyclodextrin unit around the growing polymer, they decided to pre-sheath the 5,5-dibromobithiophene monomer with a CD unit and then polymerize it using Yamamoto conditions (**Figure 40, right**).<sup>132</sup> Anthracene units were used to end-cap the polymer (**I-2**) and avoid de-threading of the CD rings.<sup>132</sup> As a result, a higher coverage was obtained, reaching up to 0.6  $\beta$ -CDs per bithiophene unit (versus 0.03-0.23).

Anderson and co-workers reported the synthesis of a few stilbene/biphenyl conjugated systems (**I-3** and **I-4**) through the use of Suzuki cross coupling reactions (**Figure 41**).<sup>133,134</sup> As observed, the structures contain a stilbene unit surrounded by an  $\alpha$ -CD. Moreover, the planar rotaxane termini allow for potential  $\pi$ - $\pi$  stacking with neighbouring chains, which in turn generates 1D strands that can potentially offer pathways of long-range charge transport.<sup>124</sup>

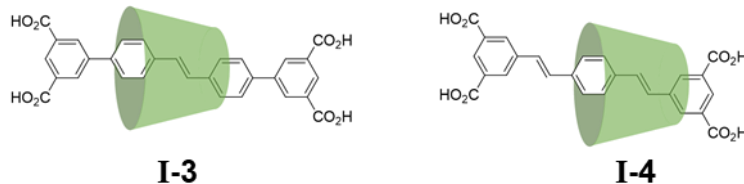


**Figure 41.** Graphic representation of stilbene/biphenyl based rotaxanes prepared by the Anderson group.<sup>133,134</sup>

Later, Anderson and co-workers also developed various polyrotaxanes by threading poly(para-phenylene), poly(4,4'-diphenylene vinylene) and polyfluorene through  $\alpha$  or  $\beta$  CDs (**Figure 42**).<sup>135</sup> Their encapsulated polymers (**I-5 to I-7**) displayed a decrease in intermolecular interactions and thus better photoluminescence efficiencies. Furthermore, the semiconducting properties were preserved leading to working single-layer LED devices.

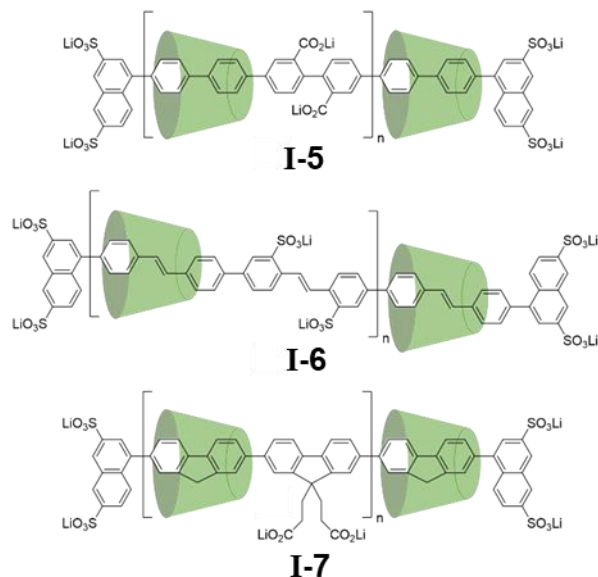


**Figure 42.** Poly(para-phenylene), poly(4,4'-diphenylene vinylene) and polyfluorene based rotaxanes by the Anderson group.<sup>135</sup>

Terao and coworkers followed a different approach.<sup>136</sup> More specifically, they developed a conjugated segment with a pendent CD unit, which undergoes intramolecular self-inclusion to form a rotaxane (**Figure 43**). After functionalizing the unit, the encapsulated rotaxane unit could be polymerized into **I-8**, which possessed a high encapsulation density, rigidity, and PL efficiency. Later, they also investigated charge transport along the  $\pi$ -conjugated chain of **I-9** and **I-10** (**Figure 44**). Here, they discovered that the introduction of an extra phenyl ring into the conjugated backbone led to a 100-fold increase in hole mobility ( $\mu_0$ ), going from  $0.0045$  to  $0.5\text{ cm}^2\text{ V}^{-1}\text{ s}^{-1}$ .<sup>137</sup> Lastly, they investigated the effects of linear (**I-11**) and kinked “zigzag” conjugated backbones (**I-12**).<sup>138</sup> Their results indicate that a combination of macrocyclic encapsulation and a kinked conjugated backbone affords a more regular localization and orbital alignment of the  $\pi$ -orbitals. Consequently, they obtained a record one-dimensional, intramolecular hole mobility of  $\mu_0 = 8.5\text{ cm}^2\text{ V}^{-1}\text{ s}^{-1}$  along the polymer backbone.

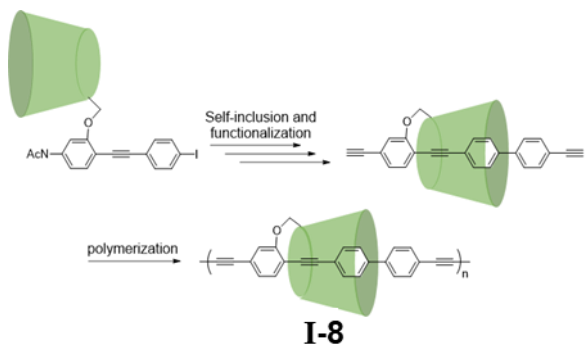


**Figure 43.** Synthesis of polyrotaxane (**I-8**) by Terao and co-workers.<sup>136</sup>

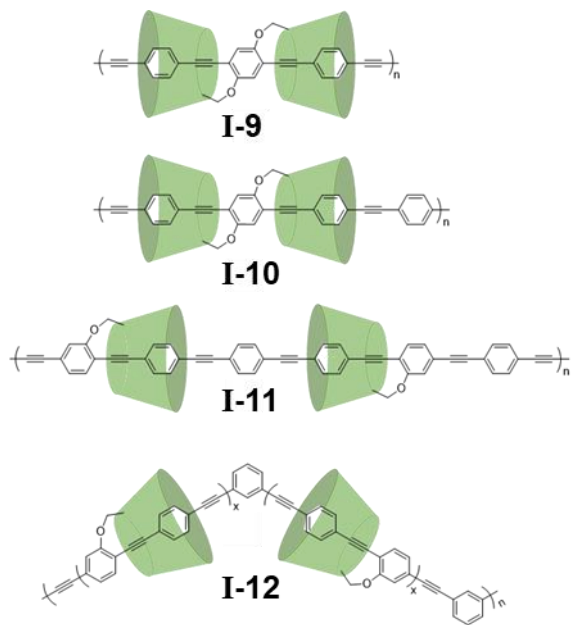


**Figure 44.** Polyrotaxane series (**I-9** to **I-12**) by Terao and co-workers.<sup>137,138</sup>

### 1.8.1.2 Cyclobis(*para*-quat-*p*-phenylene) (**CBPQT**<sup>4+</sup>) systems

In 2009, Ikeda and co-workers designed a new polyrotaxane (**I-13**)<sup>139</sup> with Stoddart's blue box<sup>140</sup> (**CBPQT**<sup>4+</sup>, **Figure 45**). The synthesis relies on electronic donor-acceptor interactions to complex a sexithiophene unit inside **CBPQT**<sup>4+</sup>, followed by electropolymerization. This resulted in the formation of the first thiophene-only polyrotaxane (**I-13**). Moreover, they discovered that the electrochromic properties of **I-13** were superior compared to the naked analogue.<sup>141</sup> As expected, the suppression of intermolecular interactions led to brighter colours and greater contrasts. The polyrotaxane also had a greater charge transport than the naked equivalent, despite the interference of electronic hopping by the tetra-cationic cyclophane. The authors postulate that the faster charge transport originates from the increased ionic nature of the polyrotaxane and hence the rapid compensation of the counterions from the solvent to the polymer backbone. The quick electrochemical response and colour advantages therefore make this polyrotaxane a more ideal material for electrochromic devices.<sup>141</sup>

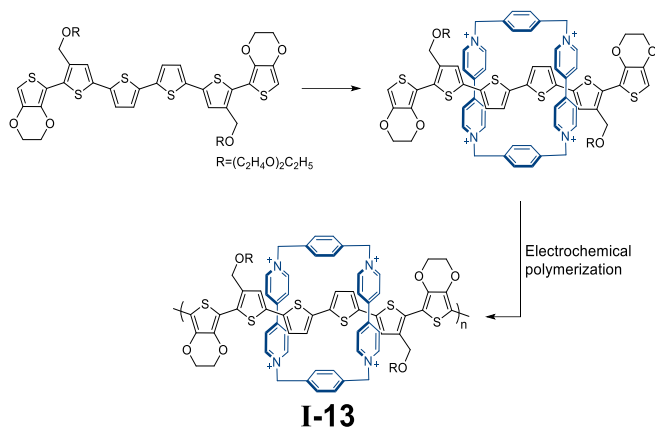


**Figure 45.** CBPQT<sup>4+</sup> based polythiophene rotaxane (**I-13**) developed by Ikeda and coworkers.<sup>139</sup>

### 1.8.1.3 Hydrophobic Cyclophane Systems

Encapsulated conjugated materials can also be prepared via hydrophobic interactions. This strategy can be preferable as most conjugated molecules are inherently hydrophobic and hence do not require extra pre-functionalization.<sup>124</sup> However, it does require the design of water soluble complexes and overcoming the less predictable nature of molecular recognition.

A representative macrocycle that can be used for hydrophobic complexation, was reported by Diederich and coworkers.<sup>142,143</sup> Their cyclophane (**I-14**, **Figure 46**) has water-solubilizing ammonium chloride groups on the outside, but maintains a hydrophobic character inside the cavity. The four benzene rings of the molecule form rigid walls that can surround a host molecule. Upon exposure to aqueous environments, the hydrophobic host and the cyclophane therefore form an inclusion complex.<sup>124</sup>

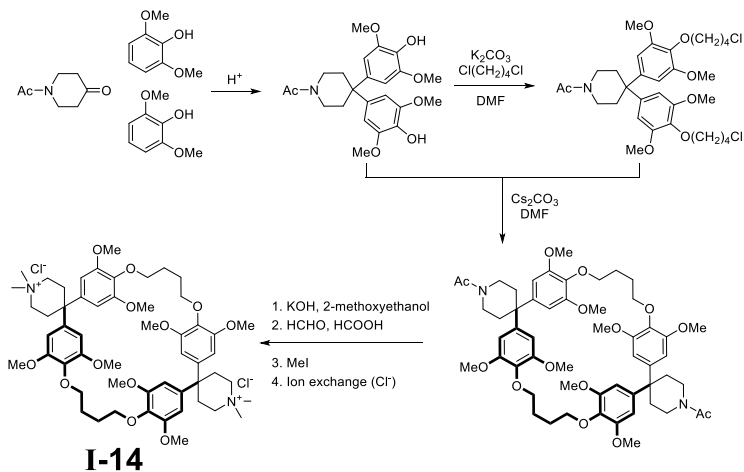


**Figure 46.** Synthesis of a Diederich's water-soluble cyclophane **I-14**.<sup>142,143</sup>

Later, the Anderson group used Diederich's cyclophane to prepare rotaxanes with π-conjugated cores (**I-15**, **Figure 47**).<sup>144</sup> However, due to aggregate/precipitate formation, it was not possible to construct longer poly(phenyl-enebutadiynylene) polyrotaxanes.<sup>124</sup> Therefore, further research endeavours should go to making longer, soluble encapsulated conjugated polymers.

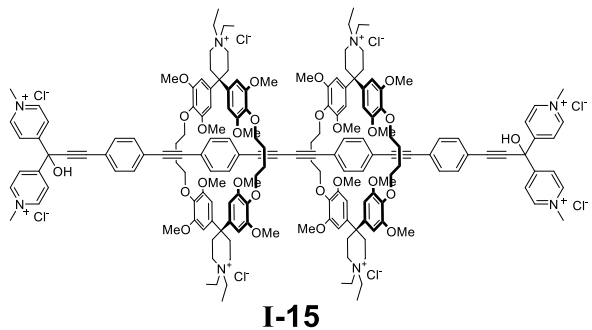


**Figure 47.** Polyrotaxane based on Diederich's cyclophane, prepared by the Anderson group.<sup>144</sup>

#### 1.8.1.4 Metal-Directed Encapsulation

Alternatively, macrocyclic encapsulation can also be achieved using metal-directed coordination (i.e., the metal centre template the macrocycle around the polymer backbone).<sup>145</sup> In 1996, Swager's group prepared one of the first conductive polymetallorotaxanes using electrochemical methods (**I-16**, **Figure 48**).<sup>146</sup> Their supramolecular structure was capable of reversibly binding Copper (I) or Zinc (II) ions (going between **I-16** and **I-17**) while exhibiting local redox conductor behaviour. This demonstrates its potential use as a chemoresistive sensor.<sup>146,147</sup>

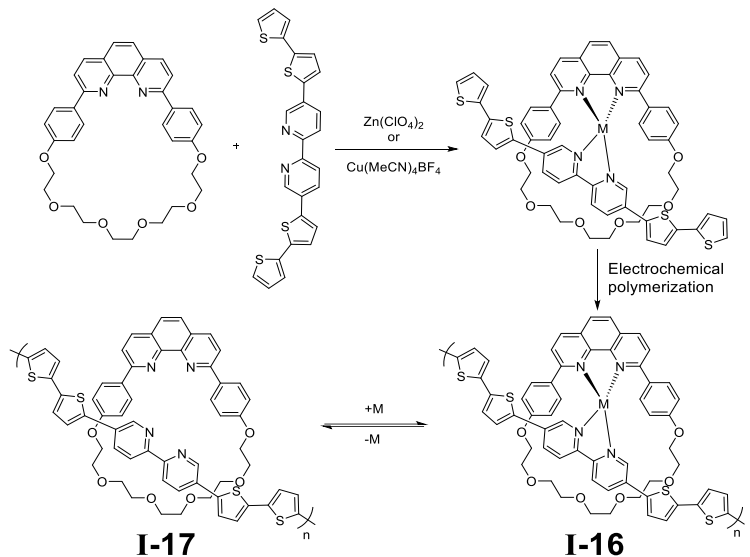


**Figure 48.** Electrochemical synthesis of **I-16** and **I-17** by Swager and coworkers.<sup>146</sup>

More recently, the Goldup group developed a novel and facile synthesis of polyrotaxanes through metal templating.<sup>148</sup> Here, copper was used efficiently to template macrocyclic rings around a semi-conjugated triazole-phenyl system (**I-18**, **Figure 49**), while maintaining control over the encapsulation density.

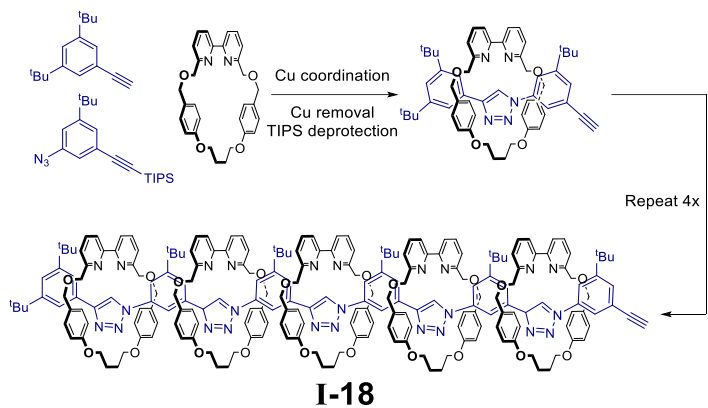


**Figure 49.** Overall synthesis of **I-18** by the Goldup group.<sup>148</sup>

Another interesting example of metal-directed encapsulation was demonstrated by the Anderson group, in 2016.<sup>149</sup> They prepared polyyne rotaxanes (**I-19**, **Figure 50**) with a conjugated chain of up to 24 continuous sp-hybridized carbons, which were end-capped by bulky “supertrityl (Tr\*)” termini. Moreover, **I-19** remained stable at temperatures over 220 °C. Therefore, this article proves that metal-coordinating macrocycles are extremely useful to generate interesting polyyne rotaxanes, but also to protect or improve their stability. Recently, they also developed a method to construct polyyne rotaxanes (**Figure 50, bottom**) through the use of photolabile masked alkyne equivalents (MAEs).<sup>150</sup> After forming the rotaxane, the stable “masked” units can be transformed into their respective alkyne with chemical, light or heat treatments. Further research endeavours relying on MAEs could potentially give access to encapsulated carbon allotropes.

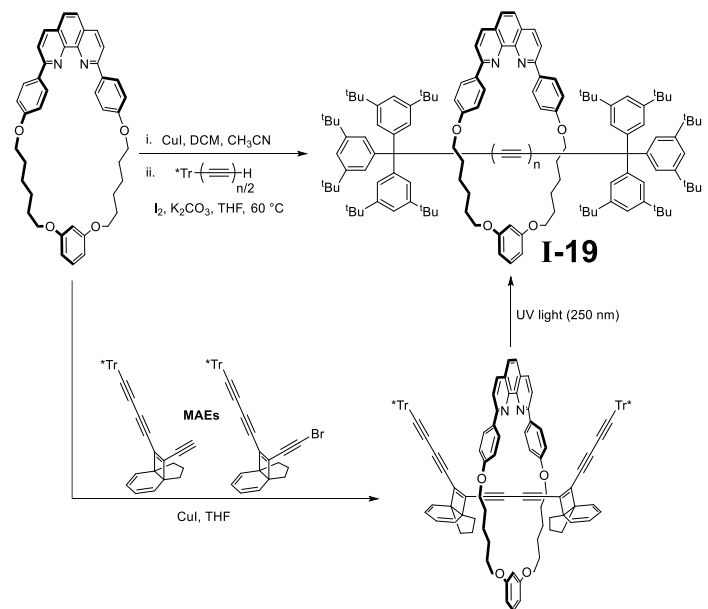


**Figure 50.** Two strategies used to construct polyyne rotaxanes by the Anderson group.<sup>149,150</sup>

In summary, (pseudo)polyrotaxanes have mostly been prepared through the use of cyclodextrin and/or cyclophane units.<sup>124</sup> However, the process is powered by noncovalent interactions and often requires aqueous media. Therefore, to induce water-solubility, a charged polymer backbone is often required, which in turn can dramatically influence the optoelectronic properties of the polymer. Furthermore, it sometimes leads to ineffective encapsulation, leaving the polymer backbone more exposed.<sup>124</sup> Alternatively, the use of metals, to template macrocycles around conjugated backbones, is much more precise and reliable. However, additional synthetic steps might be needed to incorporate binding sites into both the polymer and macrocycle.<sup>124</sup> Methods that can access neutral and densely encapsulated conjugated polymers are therefore of high interest.

### 1.8.2 Covalent Encapsulation Strategies

Another interesting method is to design polymers which are surrounded by their own macrocyclic side chains. This section will disclose some of the  $\pi$ -conjugated polymers that are protected from only one side (i.e., half encapsulated) or from both sides (i.e., fully encapsulated). The synthesis of covalently encapsulated conjugated polymers typically requires pre-functionalization of the chromophore, followed by a one or multistep encapsulation (**Figure 51**).

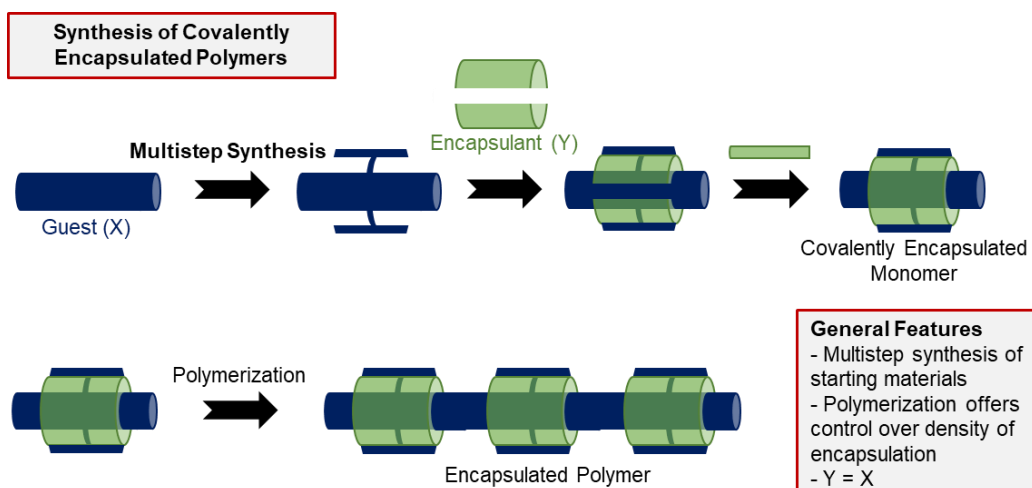


**Figure 51.** Illustration of the synthesis of covalently encapsulated conjugated polymers.

#### 1.8.2.1 Half Encapsulated Conjugated Polymers

The concept of “half encapsulation” started in the 90s, where alkyl straps was initially used to improve the solubility or stability of the polymer. Schlüter and coworkers pioneered this concept by preparing an unsaturated, half encapsulated ladder polymer (**I-20**, **Figure 52**).<sup>151</sup> The introduction of the flexible alkyl straps was essential, as it gave the polymer a higher solubility and hence allowed the formation of longer polymer chains (instead of early chain termination).

Similarly, Scherf and coworkers prepared a poly(para-phenylene) ladder polymer (**I-21**, **Figure 52**) with  $M_n = 12\text{--}13 \text{ kDa}$ .<sup>152</sup> However, here the alkylene loop was installed to make the polymer chiral. The resulting PPV polymer was highly fluorescent with good chiroptical activities, which

is ideal for generating circularly polarized light (CPL). The overall synthesis of **I-21** is demonstrated in **figure 53**.

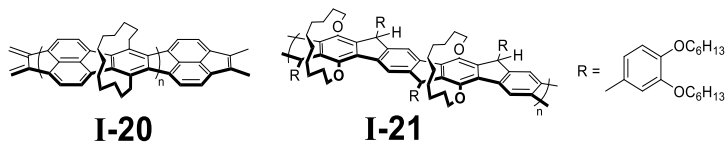


**Figure 52.** Chemical structures of **I-20** and **I-21**.

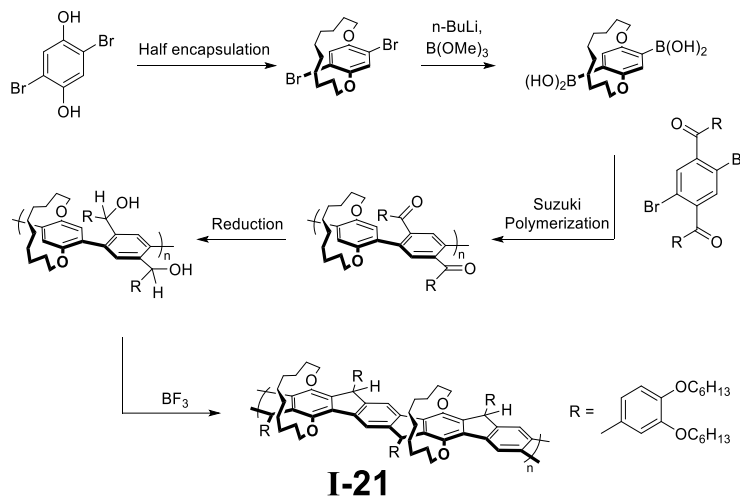


**Figure 53.** Overall synthesis of half encapsulated ladder polymer **I-21** by Scherf and coworkers.<sup>152</sup>

Swager and coworkers prepared an electron-deficient analogue of PPV by introducing pyridyls in the conjugated backbone (**I-22**, **Figure 54**).<sup>153</sup> In comparison with the non-encapsulated reference polymer, their poly(pyridylvinylenephenylene) polymer exhibited reduced interchain interactions, increased solution and film photoluminescence and improved electroluminescent quantum efficiencies in LED devices.

Likewise, Chiavarone and coworkers suppressed the solid-state packing in PPV polymers via half encapsulation (**I-23**).<sup>154</sup> The introduction of the alkyl straps led to a reduction in non-radiative quenching mechanisms and hence afforded materials with high radiative efficiency, or in this case superfluorescence (or cooperative emission).

In 2009, Smith and coworkers prepared a half encapsulated PPV polymer.<sup>155</sup> However, instead of encapsulating alkyl straps, they used an m-terphenyl unit to create a 3D cyclophane-like structure (**I-24**). In other words, the oxacyclophane unit not only reduces the interchain interactions, but also generates pockets that enable the detection or sensing of molecular analytes. Moreover, the material can be used as fluorescent sensor as the emission quenches 100-fold when the pockets are occupied.

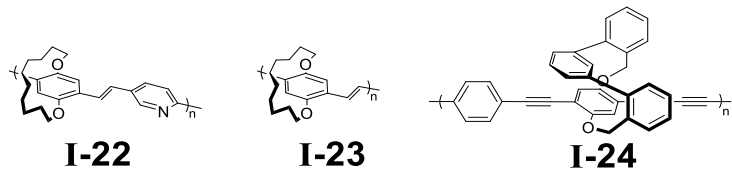


**Figure 54.** Chemical structures of half encapsulated conjugated polymers **I-22**, **I-23** and **I-24**.<sup>153–155</sup>

More recently, McCulloch and coworkers reported a conjugated polymer (**I-25**, **Figure 55**) for optical sensing.<sup>156</sup> Their polymer consists of pegylated benzo[1,2-b:4,5-b']dithiophene (BDT) and bithiophene units. By modifying the length of the encapsulating polyethylene glycol (PEG) chain, different ions (such as Na<sup>+</sup> and K<sup>+</sup>) could be detected. Therefore, this type of polymer could be of interest for health or environmental monitoring.

In 2018, Hawker and coworkers compared an alkyl encapsulated BDT polymer (**I-26**) with the naked dialkylated counterpart.<sup>157</sup> The study shows that half encapsulation accounts for different packing effects, a decrease in aggregation via π-π stacking and enhanced photoluminescence. The difference in properties between the half encapsulated and naked polymer, were a direct result of the change in interchain interactions. Therefore, to engineer high performance materials, it is essential to gain better control over interchain interactions.

Lastly, Gavvalapalli and coworkers prepared an adamantly-strapped phenylacetylene polymer (**I-27**) that does not require pendant alkyl chains for solubility.<sup>158</sup> Instead, the bulky strap provides sufficient solubility, while creating the opportunity to use the remaining phenyl sites for lateral polymerizations or to construct ladder polymers or nanoribbons.

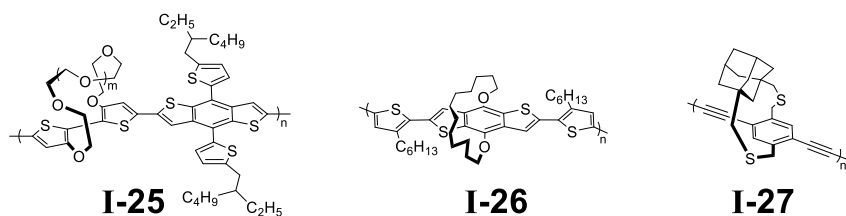


**Figure 55.** Chemical structures of half encapsulated conjugated polymers **I-25**, **I-26** and **I-27**.<sup>156–158</sup>

### 1.8.2.2 Fully Encapsulated Conjugated Polymers

Osuku and co-workers pioneered the concept of full encapsulation.<sup>159</sup> In 2006, they prepared meso-meso linked porphyrin arrays (**I-28**) and triply linked conjugated porphyrin tapes (**I-29**), which were fully protected with alkylene chains (**Figure 56**). The introduction of alkyl straps led to higher chemical stabilities and solubilities, which is typically difficult to achieve for such extended π-systems.<sup>159</sup>

Later, Takeuchi and co-workers published an orthogonally strapped porphyrin monomer with four terminal bithiophene units (**I-30**).<sup>160</sup> The thiophene units were used as electrochemical handles to

generate conjugated polymer networks. The 3D network displayed efficient energy transfer from the oligothiophenes to the porphyrin, indicating its suitability for light-harvesting applications.

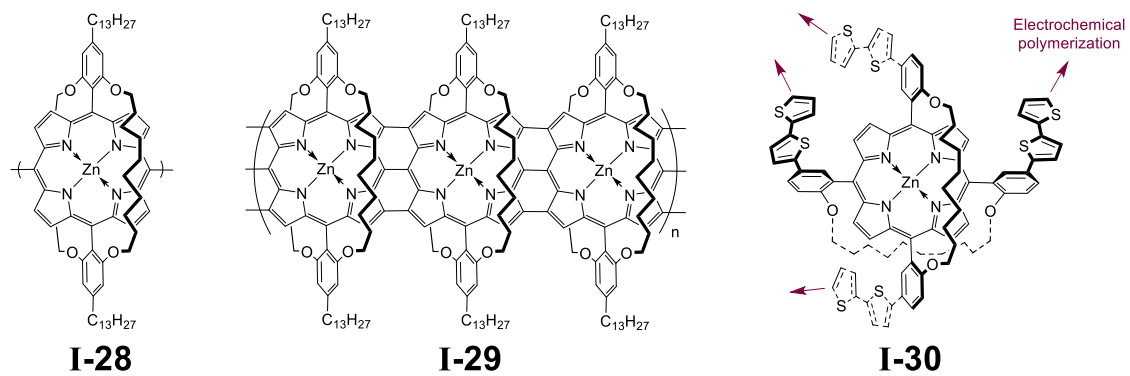


**Figure 56.** Chemical structures of fully encapsulated conjugated polymers **I-28**, **I-29** and **I-30**.<sup>159,160</sup>

In 2007, Höger prepared a fluorescent phenylacetylene polymer, which was encapsulated through  $\pi$ -conjugated macrocycles (**I-31**, **Figure 57**).<sup>161</sup> The conjugated ring not only decreases intermolecular interactions, but also induces structural rigidity and allows the transfer of absorbed photon energy onto the conjugated polymer backbone. This means high exciton densities can be generated on the backbone of the conjugated polymer, thereby allowing excitons to interact, which leads to fluorescence. The phenomenon therefore occurs within single polymer chains which is of interest in energy efficient applications.

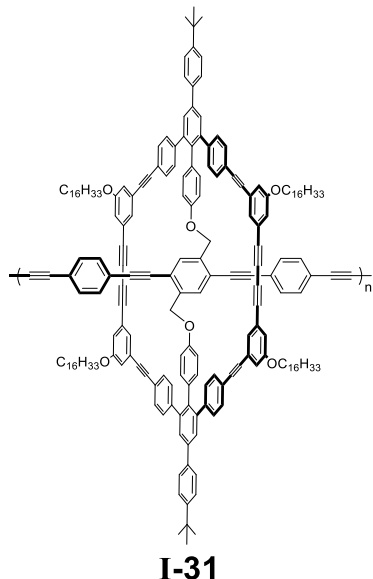


**Figure 57.** Chemical structure of polymer **I-31**.<sup>161</sup>

In 2010, Sugiyasu and coworkers reported a series of encapsulated bithiophene containing polymers (**I-32** to **I-34**, **Figure 58**).<sup>125</sup> As observed, the encapsulating straps tie up adjacent thiophene units, thereby protecting the  $\pi$ -conjugated backbone from interpolymer interactions, but also restricting rotational motion between thiophene units. As a result, the polymers have an improved backbone co-planarity and effective conjugation length (ECL).

Later, they also compared the photophysical properties of the fully encapsulated polythiophene (**I-33**) with the more exposed **I-32** and **P3HT**.<sup>162</sup> They found that with increasing protection (or encapsulation), higher solution and film PLQYs could be obtained as well as a red shift due to enhanced planarization. The results also indicate that interchain interactions have a tremendous impact on stimulated emission, which suggests encapsulated polymers hold great promise in light emitting devices. The electrochemical experiments done on the EDOT analogue (**I-34**) indicate that  $\pi$ - $\pi$  interactions can strongly influence the generation and stability of charge carriers on the polymers.<sup>163</sup>

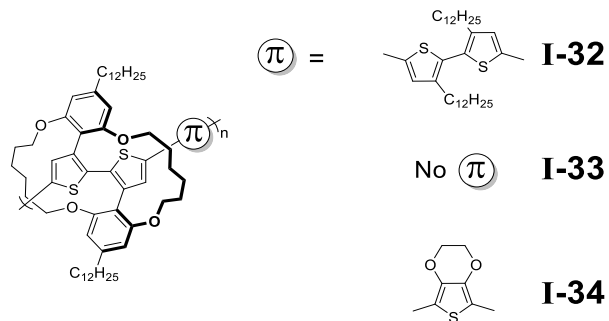


**Figure 58.** Chemical structures of encapsulated conjugated polymers **I-32**, **I-33** and **I-34**.<sup>125,162,163</sup>

Following a similar procedure, Pan et al. also prepared various encapsulated phenyl polymers (**I-35** to **I-38**, **Figure 59**) in 2013.<sup>126</sup> The series of polymers were thermoformable, miscible and could be fine-tuned to emit in the entire visible spectrum. However, more importantly, they managed to prepare one of the only solid, state red-emitting polymers, reaching an impressive  $\Phi_F$  of up to 13%.<sup>106</sup> This is very remarkable as solid-state quenching is commonly observed in red-emitting conjugated polymers.

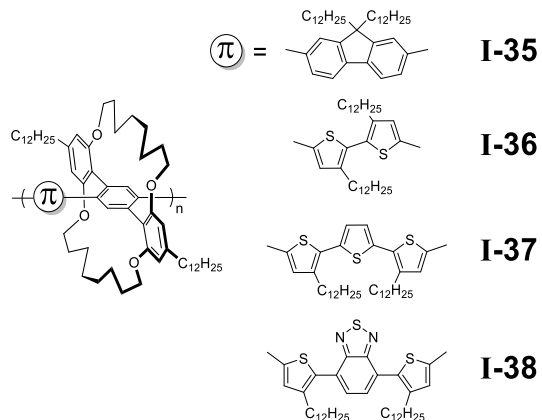


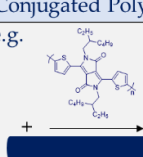
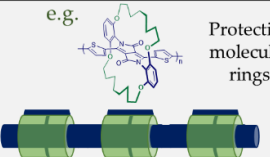
**Figure 59.** Chemical structures of fully encapsulated conjugated polymers **I-35**, **I-36**, **I-37** and **I-38**.<sup>125,162,163</sup>

## 1.9 Dissertation Scope and Objectives

In this dissertation, we propose an ambitious research strategy to construct novel organic semiconductors based on the concept of covalent encapsulation. More specifically, we will introduce protective molecular rings around (planar) conjugated backbones and thereby suppress

or control interactions between individual polymer chains. In this way, we hope to preserve the polymer's highly conductive backbone and excellent optoelectronic device performance, but also gain other attractive properties, such as improved photoluminescence.

Furthermore, we hope to improve our fundamental understanding about interpolymer interactions and eventually overcome some of the limitations of organic polymers in electronic/energy applications. The schematic illustration of the concept is demonstrated in the **figure 60**.

Conjugated Polymer	Problem	Proposed Solution
e.g.  Charge travels along polymer backbone Increased planarity = higher mobility	Increased planarity leads to close packing of polymers  Undesirable interpolymer interactions	e.g. 

**Figure 60.** The general idea behind encapsulated conjugated materials, demonstrated with a DPP example.

**Chapter II** focuses on the synthesis and properties of a series of encapsulated conjugated polymers based on diketopyrrolopyrrole (DPP). The polymers each have a different density of encapsulation (i.e., some polymer backbones are more protected than others) and we study how this affects their solution and solid-state absorption and photoluminescence, and/or their quenching behaviour. This chapter therefore explores if molecular encapsulation can potentially be used to optimize the optoelectronic properties of DPP-based conjugated polymers.

**Chapter III** deals with encapsulated naphthalene diimide (NDI) based conjugated polymers. NDIs are a class of chromophores that have consistently held the top spot in terms of performance in organic transistors, but also perform extremely well as non-fullerene acceptor (NFA) in organic solar cells. However, it is still quite poorly understood why this building block is so superior. More specifically, it has not yet been established whether their excellent performance stems from intra or interpolymer interactions. To investigate and answer this fundamental question, we therefore designed a new series of polymers based on NDI, in which we compare the reference NDI polymer with both a bulky and encapsulated equivalent. The polymers should therefore have a different degree of aggregation (and intermolecular interactions), which we hope to study with grazing incidence wide-angle X-ray scattering (GIWAXS) and correlate to their device performance.

**Chapter IV** discusses the synthesis of a series of perylene diimide (PDI) molecules. The series is comprised of a literature PDI molecule, a bulky in-between molecule, and an encapsulated PDI one. Here, the aim is to compare all three molecules and investigate how structural influences (like molecular encapsulation) affect the photophysical properties of the PDI chromophore. It is hoped that molecular encapsulation can suppress intermolecular interactions and thereby afford a

bright solid-state emitter based on PDI. PDI molecules are typically very bright in solution. However, due to their large and planar core, they tend to stack with each other, thereby undergoing intermolecular interactions which lead to photoluminescence quenching in the solid state. Therefore, constructing bright solid-state emitters based on PDI, remains extremely challenging.

In **Chapter V**, we no longer use the concept of encapsulation to prevent intermolecular interactions, but instead use the straps to precisely engineer through-space molecular architectures, thereby controlling the distances or geometries between certain building blocks. This is of great interest in organic electronics (e.g., organic photovoltaics). The donor-acceptor interface, where charge separation and recombination occurs, is arguably the most important part of organic bulk heterojunctions (organic photovoltaics; OPVs).<sup>164</sup> Consequently, the relative orientation between the interfacial donor and acceptor components can dramatically influence solar efficiency.<sup>165</sup> Therefore, by knowing the exact configuration and studying how the properties differentiate between different orientations, it should be possible to improve our understanding and help towards the development of more efficient OPV materials. This chapter proposes a unique and novel model system which can potentially be used to investigate this further.

# Chapter II

## Molecularly Encapsulated DPP-Based Conjugated Polymers

### Introduction

Since its discovery in the early 1970s, diketopyrrolopyrrole (DPP) was historically regarded as a colourant, primarily functioning as a high-grade pigment in inks, paints, automotive finishes or the coloration of plastics.<sup>166,167</sup> However, in recent years organic pigments and dyes have become increasingly important in the (opto)electronics industry, with widespread use in OPVs<sup>168–170</sup>, OLEDs<sup>171</sup>, OFETs<sup>169,172</sup>, chemosensing<sup>173,174</sup> and lasing applications.<sup>175</sup>

Diketopyrrolopyrrole (DPP) is one of the most popular chromophores used in polymer synthesis as it has various desirable properties including excellent light-harvesting, ambipolar charge transport, facile synthesis and structural modification, good solution-processability and chemical stability.<sup>106,170</sup> Furthermore, DPP's electron-deficient structure allows it to be coupled with electron-donating molecules to form narrow bandgap polymers.<sup>106</sup> However, as discussed previously planar chromophores typically have a high propensity to aggregate through  $\pi$ - $\pi$  stacking, which can dramatically influence the light harvesting and emitting properties of the material or polymer, especially in the (more concentrated) solid state.<sup>106</sup> Developing DPP-based polymers with high photoluminescence in the solid state therefore remains extremely challenging.

### Previous Work

In our recent work, we prepared a series of novel, red-emitting DPP-based conjugated polymers that are covalently encapsulated through their own macrocyclic side chains.<sup>106</sup> Our findings demonstrated that molecular encapsulation can not only lead to suppressed intermolecular interactions, but also afford polymers with lower energetic disorder, less conformational defects, and enhanced backbone co-linearity. Furthermore, the suppression of inter and intramolecular interactions led to a remarkable (3 to 4-fold) increase in solution and solid-state PLQYs compared to the naked counterparts, and thereby allowed DPP polymers to be used, for the first time, as an emissive solid-state material. Nevertheless, the difference in PLQY between solution and solid state is still relatively large and therefore it is vital their ratio ( $\Phi_R$ ) is improved further.

### Project Objectives

In this chapter/study,<sup>176</sup> the aim was to prepare and characterize a novel series of encapsulated DPP polymers, and see how their change in encapsulation density influences their solution-to-solid-state photoluminescence and/or quenching behavior. Therefore, this chapter explores how molecular encapsulation can potentially be used to further optimize the optoelectronic properties of DPP-based conjugated polymers.

## Synthetic Design

The synthesis of traditional DPP-based conjugated polymers (**Figure 61**) relies on three simple steps, namely: 1) preparation of the DPP core through reaction of diethyl succinate with a (hetero)aromatic nitrile under basic conditions (mechanism in **figure 62**) alkylation of the amide nitrogen to achieve greater solubility, and 3) polymerization of the DPP unit with another (hetero)aromatic comonomer.<sup>177,178</sup> The main components of DPP polymers are; the DPP core (black), aromatic substituents (red),  $\pi$ -conjugated segments (purple) and alkyl side chains (blue); all of which can be tuned to achieve desirable properties.<sup>170</sup>

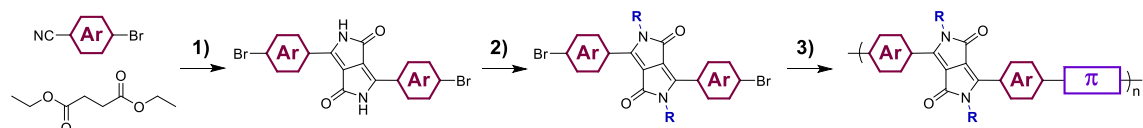


**Figure 61.** Generic synthesis of traditional DPP-based polymers. The four main components are the DPP core (black), aromatic substituents (Ar, red),  $\pi$ -conjugated segments ( $\pi$ , purple) and alkyl side chains (R, blue).

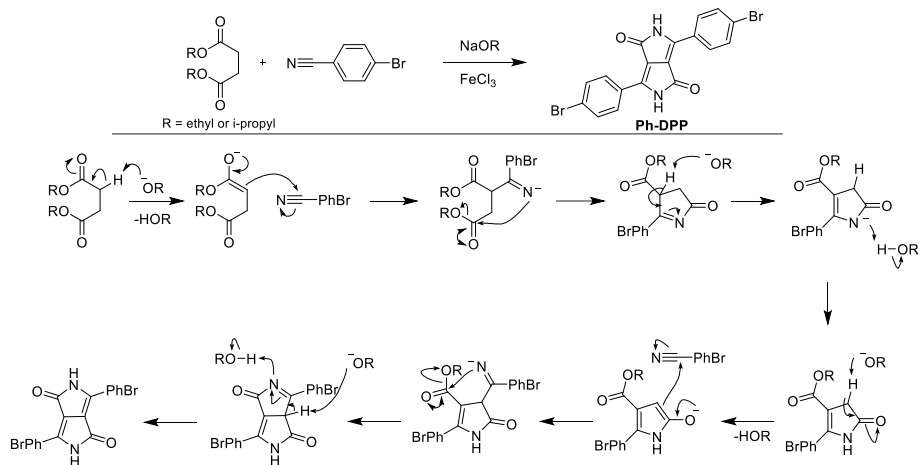


**Figure 62.** Reaction mechanism for the construction of the Ph-DPP core.

Therefore, to construct the encapsulated conjugated polymers based on DPP, without influencing the backbone conjugation, the amide nitrogen positions are the only viable option to install more functionality. More specifically, we envisioned the use of an aromatic building block that can be transformed into an encapsulating macrocycle, while maintaining the required solubility for polymerizations or polymers (**Figure 63**).

Prior to our work, the main strategy to install aromatic units directly onto the imide nitrogens of DPP was via nucleophilic aromatic substitution ( $S_NAr$ ) with electron-withdrawn aryl fluorides.<sup>179–181</sup> However, given the electron-rich nature of our aromatic building block, this option was unsuitable for this project. Alternatively, we found a few articles, in which diketofurofuran (**DFF**) (i.e., the oxygen equivalent of DPP) was reacted with very simple anilines to afford diarylated DPP molecules.<sup>178,182,183</sup> This strategy was identified as a good starting point for this project.

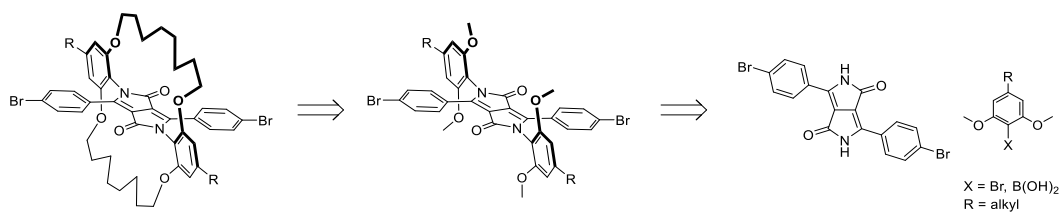


**Figure 63.** Initial predicted retrosynthetic pathway to make the encapsulated DPP monomer (**II-4**).

The final retrosynthetic and forward pathway towards the encapsulated DPP monomer (**II-4**) is shown in **figure 64**. As observed, the series of encapsulated DPP polymers was prepared following few overall steps. First, both DFF and a 2,6-dimethoxyaniline unit had to be prepared and reacted with each other. After obtaining the diarylated DPP (**II-1**) a demethylation was performed to give **II-2**, followed by a subsequent encapsulation with alkylene straps to afford the encapsulated DPP monomer (**II-4**).

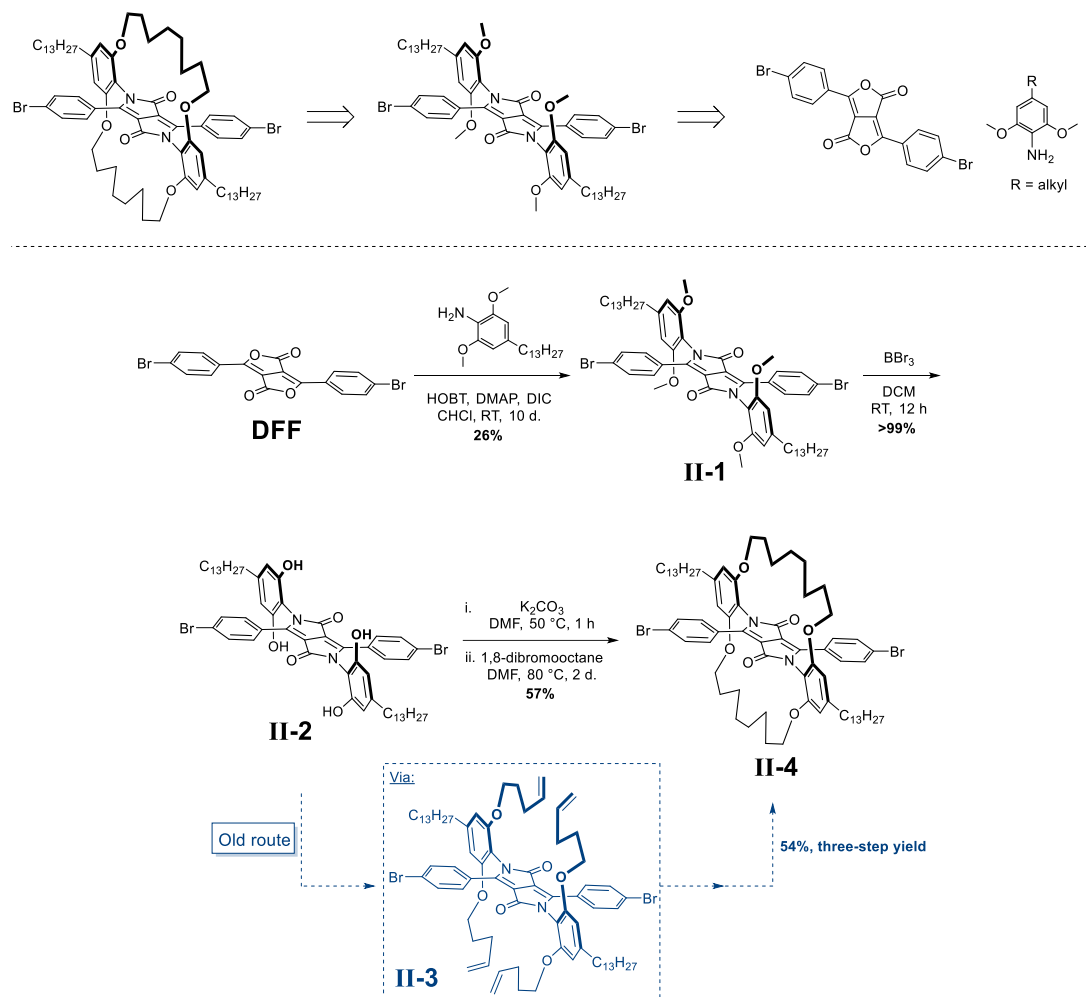


**Figure 64.** Final retrosynthesis (top) and forward synthesis (bottom) of the encapsulated DPP monomer starting from DFF via our improved (black) and old (blue) method.

Although, our previously reported method (via **II-3**, in blue)<sup>106</sup> also gave access to the target monomer in respectable yields, the synthesis was quite lengthy and more costly. However, more

importantly, we discovered that the use of Pd/C during the hydrogenation step can be quite problematic as Pd/C does not tolerate aryl halides well. As a result, the reaction often affords dehalogenated side products, which complicates isolation of the monomer (from side products) and hence lead to an early chain termination during the polymerization process.

Instead, we discovered a more direct route, which replaces the final three steps (alkylation, Grubbs metathesis and olefin hydrogenation) by a one-step alkylation with 1,8-dibromo-octane and affords the monomer in a better overall yield (3% increase). Moreover, the olefin hydrogenation step is removed, thereby eliminating problematic, dehalogenated side products. The structure of the encapsulated monomer was proven by X-ray crystallography, which confirmed successful encapsulation around the DPP core (**Figure 65**).<sup>106</sup>

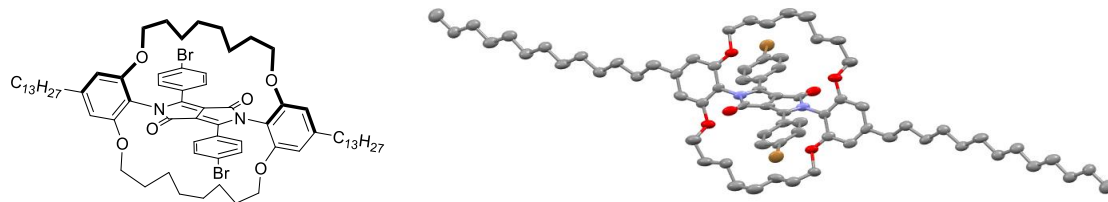


**Figure 65.** Chemical (left) and X-ray structure (right) of the encapsulated DPP monomer.

The synthesis of the novel encapsulated DPP polymers is shown in **figure 66**. First, **E-DPP** was synthesized in excellent yield (92%) using a nickel-catalyzed Yamamoto reaction. **E-DPP** is only made of encapsulated diphenyl DPP units. This places the encapsulating rings relatively close by, being distanced two backbone phenyl rings apart. Next, the thieno[3,2-b]thiophene (TT) containing **E-DPP-TT** was prepared, which increases the distance between encapsulating rings further (or reduces the encapsulation density). **E-DPP-TT** was synthesized in a near-quantitative yield of 97% using a Stille polycondensation reaction. Lastly, the density of encapsulation was also increased compared to **E-DPP**, by using an (orthogonally) encapsulated 9,10-diphenylanthracene comonomer. **E-DPP-ANT** was obtained in 57% yield through a Suzuki polycondensation. The lower yield of **E-DPP-ANT** can be attributed to its higher solubility, which leads to a greater removal of lower molecular weight chains during Soxhlet purifications. The polymers were prepared in good number average molecular weights ( $M_n$ ) above 30 kDa. The GPC data is summarized in **table 2**.

**Table 2.** Physical properties of the encapsulated DPP polymers prepared in study two.  
<sup>a</sup>Determined by GPC (CB) against PS standards.

Polymer	Yield (%)	$M_n$ (kDa) <sup>a</sup>	$M_w$ (kDa) <sup>a</sup>	PDI <sup>a</sup>
E-DPP	92	~80.6	~370.8	4.6
E-DPP-TT	97	~33.4	~113.6	3.4
E-DPP-ANT	57	~55.4	~130.5	2.4

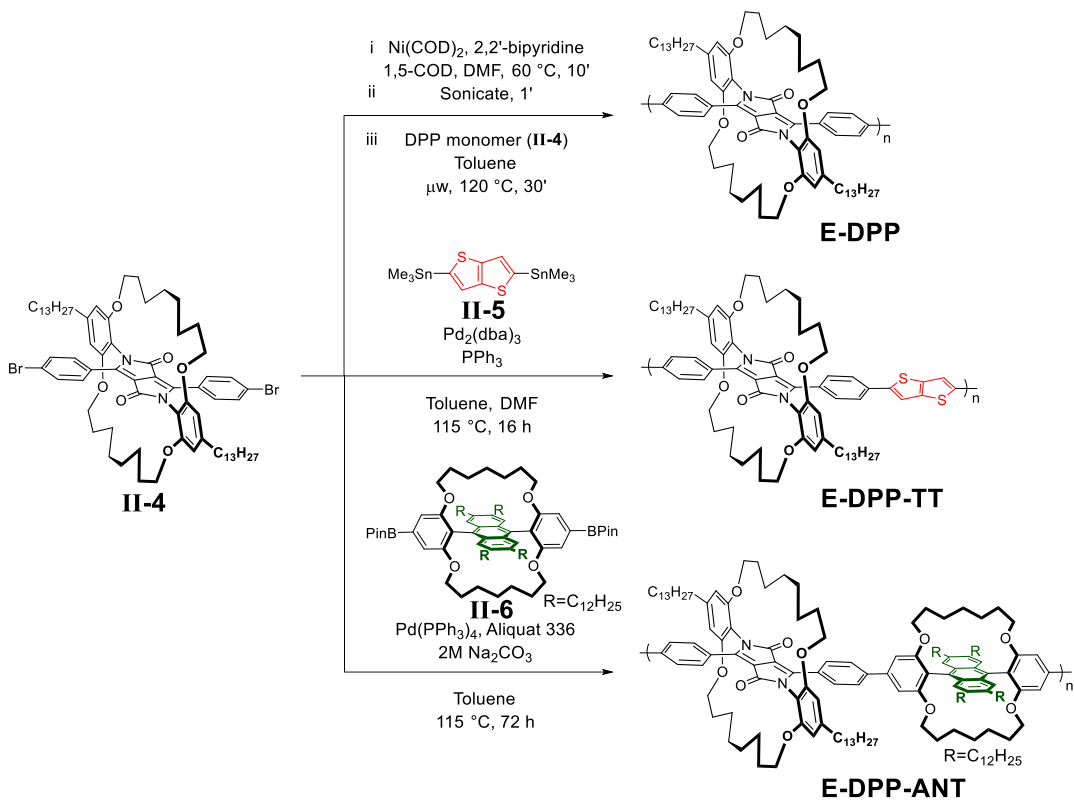


**Figure 66.** Synthesis of the encapsulated DPP polymers.

### Optical and (Photo)Physical Properties

The solution and film absorption and emission spectra of the novel encapsulated DPP polymers are demonstrated in **figure 67**, whereas the photophysical data is detailed in **table 3**.

For **E-DPP**, the solution absorption spectrum is relatively featureless, having a  $\lambda_{\text{max}}$  at  $\sim 560$  nm. The PL spectrum is sharper and more resolved with a  $\lambda_{\text{max}}$  at  $\sim 609$  nm and a second peak at  $\sim 670$  nm, which corresponds to the 0-1 transition. In thin film, **E-DPP** is a red emitter with a PL  $\lambda_{\text{max}}$  at  $\sim 629$  nm and CIExy coordinates of 0.69 and 0.31, respectively. The film absorption profile displays a bit more vibronic fine structure compared to solution, whereas the PL spectrum maintains a similar vibronic structure compared to solution, but with an increase in the intensity of the 0-1 transition.

Overall, the spectral observations for **E-DPP-TT** are like **E-DPP**. However, the absorption and emission profiles are more red-shifted than **E-DPP**, as **E-DPP-TT** is a more planar polymer. The solution absorption  $\lambda_{\text{max}}$  and PL  $\lambda_{\text{max}}$  are at  $\sim 576$  nm and  $\sim 617$  nm, respectively. This further redshifts in thin film to an absorption  $\lambda_{\text{max}}$  of  $\sim 602$  nm and PL  $\lambda_{\text{max}}$  of  $\sim 636$  nm. According to the DFT optimized geometries (**Figure 68**), **E-DPP-TT** has dihedral angles of approximately  $20^\circ$  between the DPP phenyl and TT unit, while **E-DPP** is more twisted with a  $35^\circ$  angle between the diphenyl DPP units.

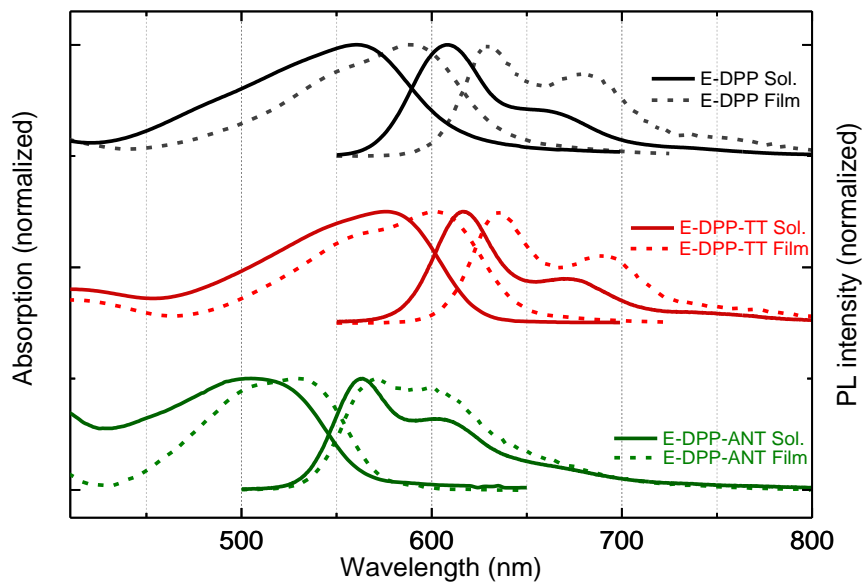


**Figure 67.** Absorption and photoluminescence profiles of **E-DPP** (black), **E-DPP-TT** (red) and **E-DPP-ANT** (green) in chloroform solution (solid line) and thin film (dashed line).

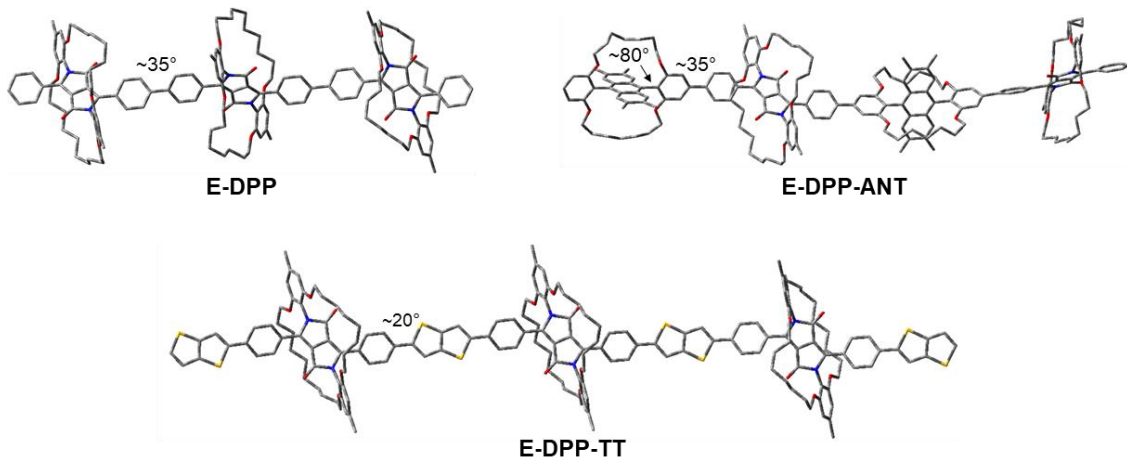


**Figure 68.** Geometry optimized (B3LYP/6-31g\*) oligomers of **E-DPP**, **E-DPP-TT** and **E-DPP-ANT**.

The absorption and emission profiles of **E-DPP-ANT** are considerably blue-shifted compared to **E-DPP** and **E-DPP-TT**. In thin film, **E-DPP-ANT** is an orange emitter ( $\text{CIE}_{xy} = 0.54, 0.46$ ) with a PL  $\lambda_{\text{max}}$  of  $\sim 570$  nm. The blue-shift is attributed to the twisty nature of the polymer backbone. Besides the dihedral angles of  $\sim 35^\circ$  between the DPP and ANT monomers, the encapsulated 9,10-diphenylanthracene has large internal dihedrals of  $\sim 80^\circ$  between the phenyls and anthracene. In other words, electronic communication along the  $\pi$ -conjugated backbone is poorer and consequently widens the bandgap. The blue-shift due to incorporation of anthracenes is also supported by previous literature.<sup>178,184</sup> The limited electronic communication, increased encapsulation density and greater steric shielding (from the anthracene dodecyl chains) encountered in **E-DPP-ANT**, provide a reason for the minimal red-shift in PL of only 7 nm when going from solution ( $\sim 563$  nm) to solid-state ( $\sim 570$  nm).

In summary, the absorption and photoluminescence profiles of all polymers provide good evidence that the optical properties in solution are well retained in the solid state, which is attributed to the suppression of intermolecular interactions and hence a result of encapsulation. This is particularly evident from the more finely resolved thin film PL spectra as conventional (naked) polymers exhibit more broadening (and reduced fine structures), which is reminiscent of aggregation.

The photoluminescence quantum yields ( $\Phi_F$ ) of the three DPP polymers are high in solution (> 50%) and retained remarkably well in thin film (up to 41%) for polymers that emit above 560 nm. The **E-DPP-TT** polymer, featuring the non-encapsulated aromatic TT spacer, has the highest solution photoluminescence ( $\Phi_F = 71\%$ ) of the series, but the lowest thin film  $\Phi_F$  of 19%. The thin film to solution PLQY ratio ( $\Phi_R$ ) is therefore 0.27, which is very comparable to the values obtained in our previous polymer series.<sup>106</sup> In contrast, **E-DPP** has a lower initial solution  $\Phi_F$  of 51%, which is retained much better in the solid state with a  $\Phi_F$  of 32%. This translates to an impressive  $\Phi_R$  of 0.62 and thereby reduced aggregation-caused quenching. The reduction in ACQ is likely due to the increased density of encapsulation of **E-DPP** compared to **E-DPP-TT**. The introduction of the orthogonally encapsulated anthracene spacer in **E-DPP-ANT** increases the density of encapsulation even further. This results in an even higher thin film  $\Phi_F$  of 41% and hence lower ACQ, having a  $\Phi_R$  of 0.72. Therefore, with increasing levels of encapsulation, ACQ is suppressed more effectively within this series.

**Table 3.** Optical properties of the orange/red-emitting conjugated DPP-based polymers.

Polymer	State	$\lambda_{\text{abs max}}$	$\lambda_{\text{em max}}$	$\Phi_F$ (%)	$\Phi_R$
<b>E-DPP</b>	Solution	560	609	51±5	0.62
	Film	589	629	32±4	
<b>E-DPP-TT</b>	Solution	576	617	71±7	0.27
	Film	602	636	19±2	
<b>E-DPP-ANT</b>	Solution	505	563	57±6	0.72
	Film	529	570	41±4	

Yet, even though our results indicate that increased encapsulation is effective for suppressing ACQ, our series also reveals that the more densely encapsulated polymers; **E-DPP** and **E-DPP-ANT** display a lower intrinsic solution  $\Phi_F$  of 51% and 57%, respectively (versus 71% for **E-DPP-TT**). This suggests that besides eliminating intermolecular PL quenching pathways, encapsulation possibly also introduces new intramolecular routes for non-radiative decays (e.g., extra vibrations). Nevertheless, to the best of our knowledge the thin film  $\Phi_F$  and  $\Phi_R$  values reported

here are unprecedented for conjugated polymers emitting above 560 nm.<sup>176</sup> Lastly, we note that this covalent design strategy is superior to noncovalent approaches as even rotaxane polymers, which are so densely encapsulated that they do not quench in solution in the presence of methyl viologen, still aggregate considerably in the solid state ( $\Phi_R < 0.5$ ).<sup>185</sup>

## Conclusions

In this chapter, we disclosed a novel series of encapsulated conjugated polymers based on DPP and investigated how systematic variations in their density of encapsulation influenced the polymer's PLQYs and solution-to-solid-state quenching effects (or ACQ). The photophysical information supports that molecular encapsulation is very effective at suppressing inter and intramolecular interactions and retaining the solution spectral profiles in the solid-state. Furthermore, the novel polymers display the highest solid-state fluorescence quantum yields (up to 41%) ever reported in this region of the electromagnetic spectrum, with unprecedently suppressed ACQ.<sup>176</sup> Overall, the trend suggests that even though the more densely encapsulated DPP polymers have a lower intrinsic solution PLQY, their solid-state PLQY is much better retained and higher than less encapsulated ones and hence ACQ is more suppressed. Therefore, we hope to further develop bright solid-state polymeric emitters, which can give access to next-generation technologies (e.g., OLETs or electrically pumped organic lasers).

## Final Notes

Our past study proved that encapsulated conjugated polymers could outcompete their naked counterparts, whereas this chapter demonstrates that the photoluminescence quantum yields can be improved significantly with increased density of encapsulation. However, to compete with the current state-of-the-art materials, their device performance must be improved further.

The polymers presented in this chapter are comprised of phenyl DPP (Ph-DPP) units and therefore have a relatively twisted backbone. In literature, there is very little evidence Ph-DPP based conjugated polymers which possess good optoelectronic performance. The performance of more planar conjugated systems, such as thiophene DPP (Th-DPP), on the other hand, are much better.<sup>186</sup> This is because smaller dihedral angles lead to increased backbone planarity, narrower optical bandgaps (near-IR region) and often an increase in charge mobility.<sup>186</sup> In the following chapter the encapsulation concept will therefore be applied to a more planar conjugated system.

# Chapter III

## Molecularly Encapsulated NDI Polymers

### Background Information

To date, many of the most successful organic semiconductors have been based on imide-functionalized molecules because of the following reasons. First, the imide group is strongly electron-withdrawing, thereby enabling fine-tuning of the frontier molecular orbitals (FMOs) and bandgap, which is one of the major concerns for the development of optoelectronic materials.<sup>187</sup> Second, as the synthesis of conjugated polymers typically follows traditional cross coupling reactions with electron-rich organometallics (e.g., organotin, or boronic acids/esters), the presence of imides gives rise to molecules with electron-deficient halides, thereby facilitating both oxidative addition and transmetallation.<sup>91</sup> This consequently increases the chance of forming high molecular weight polymers, which in turn typically results in improved device performances.<sup>91</sup> Third, the alkyl chain on the imide nitrogen can be tuned to obtain a good balance between solubility and solid-state packing effects, which can enhance the charge transport properties.<sup>188</sup> Lastly, the carbonyl groups of the imide can be used to increase the backbone coplanarity through conformational locking or hydrogen-bonding interactions with the co-monomer.<sup>187</sup> Careful tuning of imide-functionalized materials can therefore result in narrow bandgap semiconductors that have a great effective conjugation length (ECL) and improved charge mobility.<sup>187</sup>

### Rylene Diimides & Derivatives

Rylene diimides are a class of hydrocarbon molecules that contain oligo(*peri*-naphthalene) units, linked together at position 1 and 8 of each adjacent naphthalene, and have two six-membered dicarboxylic imide rings attached onto the terminal naphthalene units (**Figure 69**).<sup>189</sup> Rylene diimides and other closely related molecules (like in **figure 70**) have become increasingly popular in organic electronics due to their attractive properties (e.g., good charge transport, high electron affinity, and thermal and (photo)chemical stability). Moreover, their chemistry is relatively established and the molecules provide various functionalization opportunities at both the rylene skeleton and the imide nitrogens.<sup>189–191</sup> The two simplest rylene diimides; 1,4,5,8-Naphthalenetetracarboxylic acid diimide (NDI) and Perylene-3,4,9,10-tetracarboxylic acid diimide (PDI) are among the most studied molecules in organic electronics.<sup>190</sup>

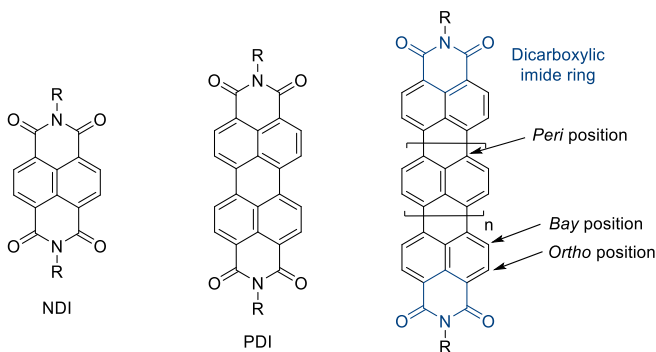


**Figure 69:** The general structure of rylene diimides, with NDI and PDI being the simplest ones.

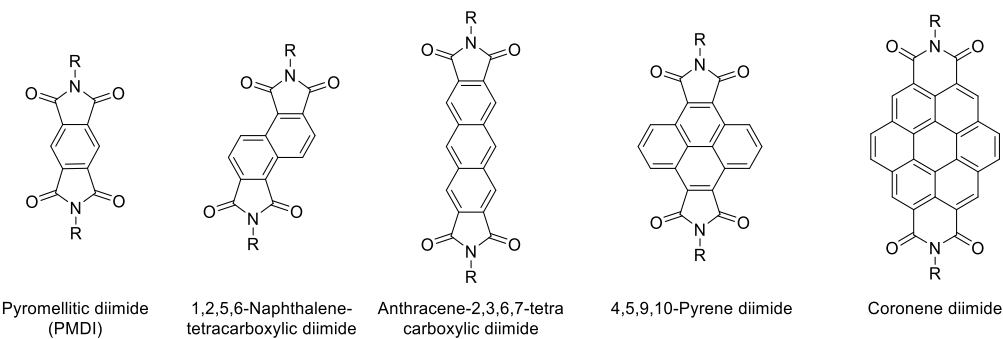


**Figure 70.** Molecules closely related to rylene diimide family.

### Naphthalene Diimides (NDIs)

Naphthalene diimides are structural analogues of perylene diimides and likewise possess good thermal, (photo)chemical and oxidative stability, high electron affinities and mobilities, and excellent device performance.<sup>187</sup> However, the NDI core seems to have preference over PDI as they are more soluble and easier to obtain in a regioisomerically pure form after bromination. Moreover, upon polymerization, the backbone of NDI polymers is typically more planar, which is in contrast to PDI compounds as the bay position is sterically hindered, thereby imparting a twist.<sup>187</sup> As a result, extensive research has been done on NDI polymers, resulting in some of the most successful organic electronic devices.<sup>187</sup>

### Introduction

Among the countless, reported NDI-based conjugated polymers, P(NDI-2OD-T2) (or N2200, active ink)<sup>192,193</sup> and P(NDI-2OD-T) (or PCE8)<sup>194,195</sup> are among the most studied and best performing ones (**Figure 71**). This is particularly remarkable as, in contrast to most, p-type organic semiconductors (i.e., positive type or hole transporting materials), the development of efficient n-type semiconductor polymers (i.e., negative type or electron transporting materials) has remained extremely scarce.<sup>192,196</sup>

One of the first studies highlighting the importance of n-type semiconductors in organic electronics was reported by Facchetti and coworkers.<sup>192</sup> Here, they showed that N2200 possessed remarkable n-channel field-effect mobilities of up to ~0.85 cm<sup>2</sup> V<sup>-1</sup> s<sup>-1</sup> under ambient conditions.

Furthermore, the polymer was highly soluble, allowing it to be processed using various techniques (e.g., spin-coating, gravure, or inkjet printing). Interestingly, N2200 remains to outperform almost any other n-type polymer in organic electronics. A lot of research efforts have therefore been devoted to gain a deeper understanding as to why this is the case.

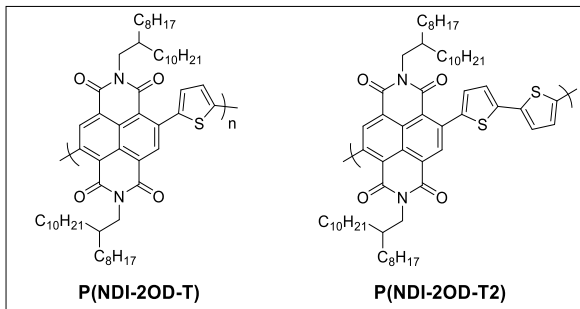


**Figure 71.** Chemical structure of P(NDI-2OD-T), also known as PCE8 and P(NDI-2OD-T2), also known as N2200.

A study by Caironi and coworkers provides important insights into the unusually high electron mobility of N2200 (despite its unique face-on molecular orientation and low degree of crystallinity).<sup>197</sup> Their study suggests that N2200 films adopt an exceptionally low degree of energetic disorder, meaning that the charge carriers experience a very uniform energy landscape and thereby transport efficiently.

In 2012, Neher and coworkers provided further insights into the optical properties and microstructure of N2200.<sup>198</sup> Their UV-Vis measurements are shown in **figure 72**, below. As observed, the absorption of N2200 displays a high-energy peak originating from the  $\pi-\pi^*$  transition, and a low-energy peak attributed to intrachain charge transfer (CT) between the donor (bithiophene) and acceptor (NDI) units. The absorption spectrum undergoes a redshift going from chloronaphthalene (CN) to toluene, reaching to the red-to-NIR region for chlorobenzene (CB) and toluene. The toluene solution thereby most closely resembles the film absorption spectrum. The CN spectrum, on the other hand, is much more blue-shifted with a band centered around 620 nm.

Similar features are also observed for the photoluminescence spectra as the peak moves from 720 nm (with a long tail reaching 1000 nm) for CN, to a more defined, narrow peak at 860 nm (with a side shoulder around 950 nm) for the toluene solution. Again, the toluene solution PL spectral features are most similar to the film. Interestingly, even though the difference in shifts seems to correlate well with the polarity of the solvents (i.e., solvatochromism), they provide evidence that this is not the case. Instead, the differences are primarily attributed to aggregation of the polymer chain. Therefore, the authors claim that the CN spectra of the N2200 polymer originates from isolated chains, whereas the spectral profiles in the toluene solution (and other solutions) is caused by an increase in aggregated species.<sup>198</sup>

**Figure 73** demonstrates the absorption spectrum of N2200 in different concentrations and solvents. As seen, there are no significant concentration-dependent differences, which indicates that the observed aggregation is attributed to intramolecular aggregation (e.g., coiling of the chains) or agglomerates (**Figure 74, left**). In most solvents, the polymer therefore finds itself in a pre-aggregated state whether dilute or concentrated.

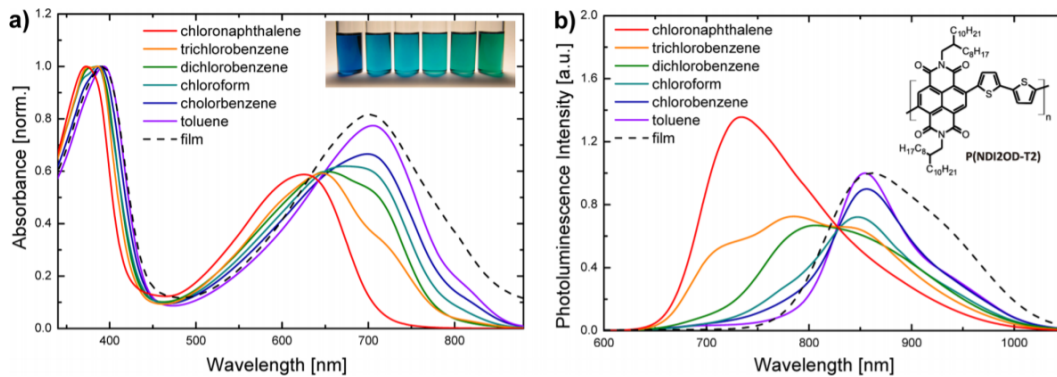


**Figure 72.** a) Absorption and b) photoluminescence spectra of N2200 in various solvents (1 g/L). The PL spectra were recorded using an excitation wavelength of 560 nm. © 2012 American Chemical Society.<sup>198</sup>

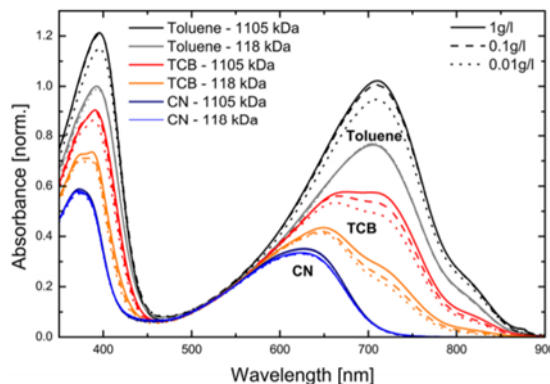


**Figure 73.** Absorption spectra of N2200 in toluene (black/grey), trichlorobenzene (TCB) (red/orange) and chloronaphthalene (CN) (blue/purple) at different concentrations. © 2012 American Chemical Society.<sup>198</sup>

In the same study, they also performed DFT calculations on N2200 oligomers. Here, they showed that in stacks of N2200, the NDI units are close in proximity, thereby suggesting there is a favourable structure for interchain electron transport.<sup>198</sup> Moreover, the conformation of the oligomer alters inside the stack compared to isolated chains, showing an 11° out-of-plane tilt for the NDI units and a reduction in the dihedral thiophene twist (going from 44° to 34°) (**Figure 74, right**). These results suggest that the change in conformation upon stacking accounts for the observed red-shifting in film (or solutions with increased aggregation). This study therefore shows the importance of microstructure on the photophysical properties of N2200.

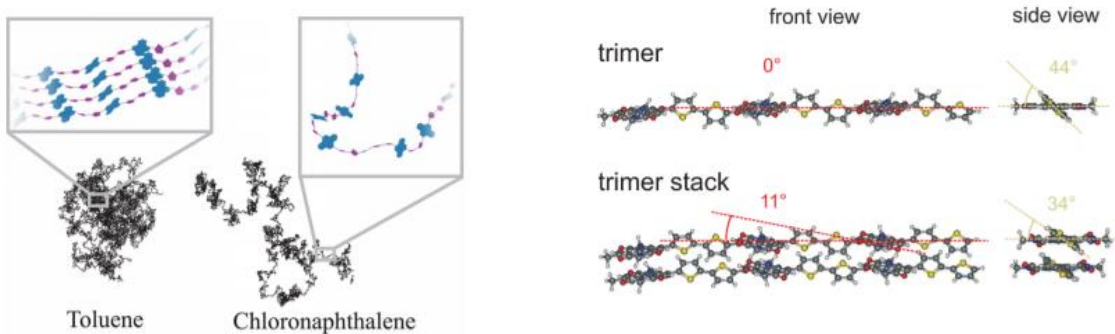


**Figure 74.** (Left) Schematic representation of the stacking of N2200 in solution. (right) Geometry optimized trimers for N2200 as an isolated chain and in a stack. © 2012 American Chemical Society.<sup>198</sup>

Where N2200 has most commonly been used in organic transistors, its smaller brother PCE8 or P(NDI-2OD-T) is a bit more known as a non-fullerene acceptor in organic photovoltaics. A recent example demonstrating the excellent performance of PCE8 in OPVs, was reported by Wang and coworkers.<sup>195</sup> Here, they realized an all-polymer solar cell, reaching an PCE of up to 8.0% when blended with PBDTS-TPD (**Figure 75**). Moreover, the device was more efficient than the fullerene (PC<sub>71</sub>BM) equivalent, thereby showcasing the importance of non-fullerene acceptors.

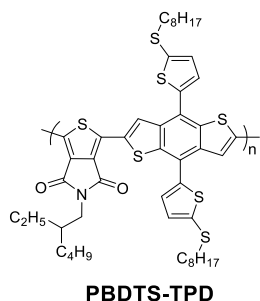


**Figure 75.** Chemical structure of PBDTS-TPD.

However, as explained, NDI-based polymers are generally quite large and planar, and have a great propensity to self-aggregate through  $\pi$ - $\pi$  stacking in both solution and thin film.<sup>199</sup> This can result in a decrease in miscibility with donor polymers and hence greatly influences their OPV performance. Therefore, gaining greater synthetic control over the intermolecular interactions and aggregation behavior of these materials is very important, but challenging.

Besides energy level matching between the donor and acceptor materials, the morphology and orientation of the donor-acceptor interface strongly influences the overall performance.<sup>200</sup> While crystal behavior of organic semiconductors is strongly associated with the exciton or charge transport properties, (post)processing techniques can strongly influence the microstructural behavior of the film. Understanding how polymers arrange in space or pack, their crystallinity, orientation, and how these factors influence their device performance, is therefore of key importance.

In the past, several strategies have been introduced to control the morphology of materials, including solvent or additive optimization, thermal or solvent vapor annealing, and different coating techniques; most of which rely on kinetically trapping the finely phase-separated morphology through rapid evaporation of the solvent.<sup>199</sup> This means they are more prone to batch variations, and thereby result in reproducibility and scalability issues, which is a concern to industry. Therefore, materials must possess robust film morphologies, which are unaffected by different coating methods and have good air and mechanical stability, as well as high PCE values.

However, in this thesis we are more interested in controlling the morphology or packing of NDI-based conjugated polymers through modifications of the chemical structure itself. A few representative examples are discussed in this section. In 2015, Kim and coworkers reported a series of P(NDI-T) polymers, with different alkyl chains attached to the imide nitrogen, and investigated how these simple structural changes affected the polymer's packing behavior and device performance.<sup>201</sup> The respective polymers (**Figure 76**) were blended with **PTB7-Th** for testing in OPV devices.

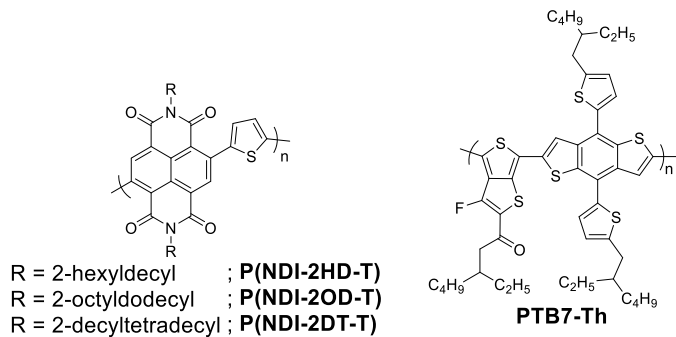


**Figure 76.** NDI polymer structures with different length alkyl chains (left) and the donor polymer (**PTB7-Th**) used to make blends and prepare OPVs devices.<sup>201</sup>

The NDI polymers were prepared using standard Stille polymerization conditions and afforded polymers with similar molecular weights and polydispersities (M<sub>n</sub> = 34-48 kDa, PDI = 1.8-2.1). It can therefore be reasonably assumed that any noticeable differences between them, are a direct result of the difference in chain length (rather than a higher/lower molecular weight). Furthermore, their UV-Vis spectral profiles in solution (400-650 nm) and as pristine film (400-750 nm) lay directly on top of each other and are thus nearly identical.<sup>201</sup> However, when looking at their packing (analyzed by grazing incidence wide-angle X-ray scattering (GIWAXS) data) and device performance, small differences can be observed (a summary of the most important data, is provided in **table 4**).

As seen, the lamellar spacing rises with increasing chain length. The distance goes from 22.5 to 23.8 and 25.1 Å for **P(NDI-2HD-T)**, **P(NDI-2OD-T)**, and **P(NDI-2DT-T)**, respectively. A similar trend is observed for the π-stacking distances. By decreasing the chain length, shorter π-

stacking distances are obtained (going from 4.33 Å for **P(NDI-2DT-T)** to 4.22 Å for **P(NDI-2HD-T)**). The shorter  $\pi$ -stacking distance can lead to an increased electron mobility due to increased orbital overlap and interestingly affords OPVs with better device performance in this article.<sup>201</sup> The PCE values of each PTB7-Th/NDI polymer blend, are summarized in **table 4**.

**Table 4.** Summary of the GIWAXS and OPV device data reported by Kim and coworkers.<sup>201</sup>

Polymer	Lamellar spacing (Å)	$\pi$ -stacking spacing (Å)	OPV PCE values in blend (%)
<b>P(NDI-2HD-T)</b>	22.5	4.22	5.96
<b>P(NDI-2OD-T)</b>	23.8	4.27	5.05
<b>P(NDI-2DT-T)</b>	25.1	4.33	3.25

Later, the Kim group also investigated what happens with NDI-based polymers when the branching point of the alkyl chains is positioned further away (or closer by) (**Figure 77**).<sup>202</sup> They found that by moving the branching point further away, NDI polymer chains display enhanced intermolecular interactions, as expected from a reduction in steric hindrance. In their series, the electron mobility in organic transistors (OFETs) therefore increased from 0.034 cm<sup>2</sup> V<sup>-1</sup> s<sup>-1</sup> in **P(NDI1-T)** to 0.22 cm<sup>2</sup> V<sup>-1</sup> s<sup>-1</sup> in **P(NDI4-T)**. A similar trend was observed when testing the **P(NDIm-T)/PBDTTTPD** blends for OPVs. Here the PCE increases from 6.1% to 6.5 and 7.1% for **P(NDI1-T)**, **P(NDI2-T)** and **P(NDI3-T)**, respectively. However, there is slight drop again (from 7.1% to 6.8%) for **P(NDI4-T)**, which has the furthest branch. The authors attribute the better performance of **P(NDI3-T)** to its enhanced intermolecular interaction, which they refer to as “pre-aggregation”, as evidenced by the side shoulder between 600-700nm in the solution UV-Vis absorption spectrum.<sup>202</sup> To summarize, the articles by Kim and coworkers demonstrate that the alkyl side chains can be modified or fine-tuned to enhance the properties of a polymer, although the exact properties cannot always be precisely predicted.

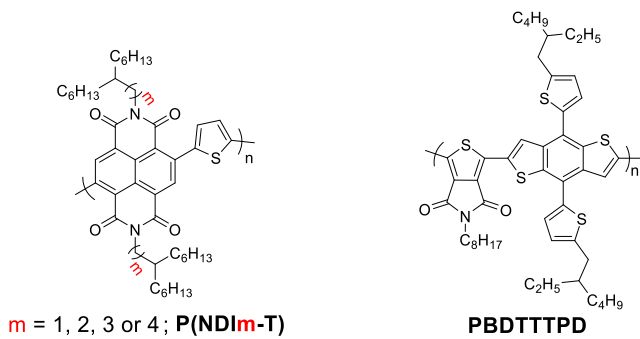


**Figure 77.** NDI polymer structures with different branching points (left) and the donor polymer (**PBDTTTPD**) used to make blends and prepare OPVs devices.<sup>202</sup>

More recently, a different approach to modulate the distance between neighbouring NDI polymer chains was reported by Bao and coworkers.<sup>199</sup> More specifically, they modified **P(NDI-2OD-TT)**

(or **N2200**) by introducing a bulky 2,6-diisopropylbenzene ring on some of the NDI units. By doing so, they gradually increased the bulk of the polymer (going from  $x = 0$  to  $x = 1$ ) (**Figure 78**). Their results indicate that by replacing exactly half of the polymer backbone with bulky NDI units ( $x = 0.5$ ), an optimum PCE of 8.5% could be obtained; a 60% increase in performance compared to the reference **N2200** polymer. The addition of some bulk therefore minimizes self-aggregation of the NDI polymer, ensuring it interacts or mixes better with the donor polymer.

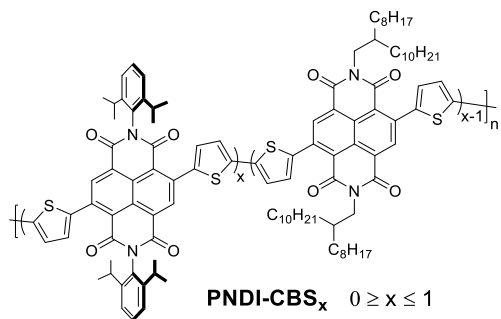


**Figure 78.** N2200-modified polymer (**PNDI-CBS<sub>x</sub>**), investigated by the Bao group.<sup>199</sup>

The above examples highlight the importance of having structural control over the intermolecular interactions in conjugated polymers. However, as noted the current chemistry to control intermolecular interactions in NDI polymers is rather limited, with strategies heavily relying on modifications of the alkyl side chains or a very limited number of phenyl substituents.

Herein, we propose an alternative strategy to molecularly engineer/alter the aggregation behaviour and packing of NDI-based polymers, based on molecular encapsulation. More specifically, we propose the design of three NDI polymers; **P(NDI-2OD-T)** as the reference polymer, a bulky **P(NDI-DMP-T)** polymer and an encapsulated **P(E-NDI-T)** polymer for comparison (**Figure 79**). The polymers should therefore have a different degree of packing, which we hope to study with grazing incidence wide-angle X-ray scattering (GIWAXS).

GIWAXS is a popular technique that has been used to study the film morphology of the active layer in organic solar cells. It provides more detail to the molecular packing, orientations and crystallinity of the sample and can therefore give essential information for understanding the results.

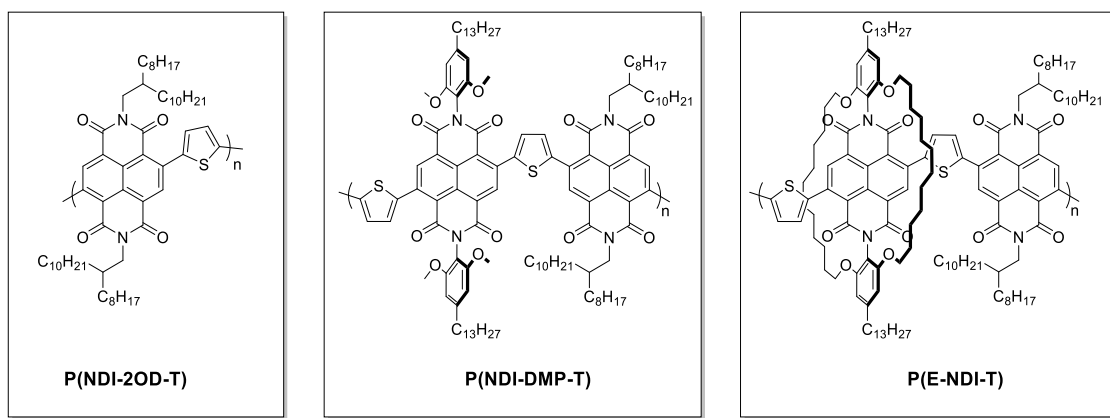


**Figure 79.** Chemical structures of the three NDI polymers prepared in this project.

## Project Objectives

The aim of this chapter was to design a new series of conjugated polymers based on NDI and investigate how structural changes affect the polymer's morphology, packing, and photophysical properties. More specifically, we will conduct a comparative investigation between a known, literature NDI polymer, and a novel bulky and encapsulated equivalent. By doing so, we hope to gain a deeper understanding on the structure-property relationships in conjugated NDI polymers.

## Synthetic Design

The conventional synthesis of NDI-based conjugated polymers proceeds through three steps, namely: bromination of the NDI core, imidization and polymerization. To construct an encapsulated NDI polymer, we therefore envisioned an analogous route (**Figure 80**).

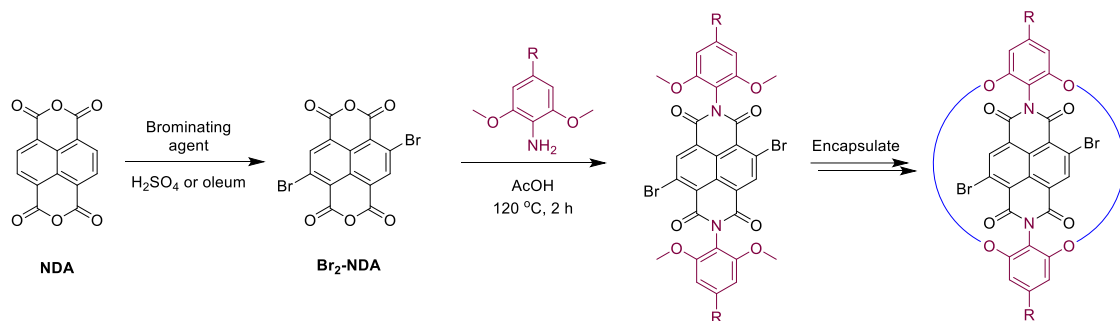


**Figure 80.** Overall, initial synthetic strategy to make the encapsulated NDI-based monomer.

The first step towards encapsulated NDI materials was the bromination of 1,4,5,8-Naphthalenetetracarboxylic dianhydride (**NDA**). The bromination of **NDA** has been reported by various research groups<sup>203–208</sup> and was not expected to impose any problems. However, it was found that the bromination of **NDA** can be quite tricky, often giving rise to a mixture of isomers with large batch-to-batch variations. Furthermore, most papers did not discuss the initial bromination step and for those that did, proper characterization of **Br<sub>2</sub>-NDA** was often missing. Therefore, to find the most reliable method to brominate **NDA**, it was decided to test the reported

three major strategies and compare the characterization of their resulting product with that of commercial **Br<sub>2</sub>-NDA**. The three tested strategies are shown in **figure 81**.

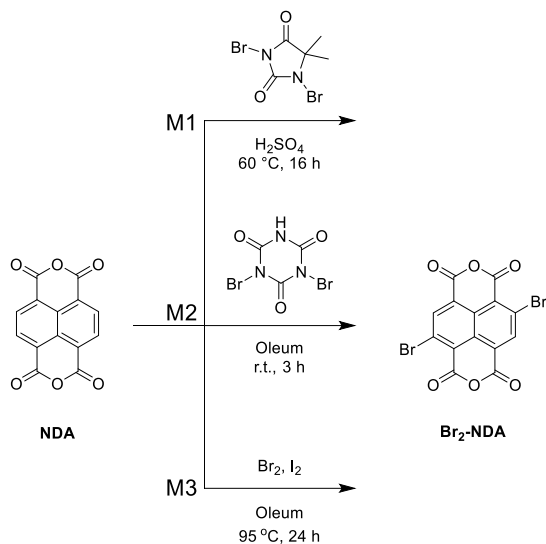


**Figure 81.** Three of the major synthetic strategies used for the 2,6-bromination of **NDA**. The brominating agents for method 1 (M1), method 2 (M2) and method 3 (M3) are 1,3-dibromo-5,5-dimethylhydantoin (DBH), dibromoiso-cyanuric acid (DBI) and molecular bromine ( $\text{Br}_2$ ), respectively.

Based on the  $^1\text{H}$  NMR results (**Figure 82**), it was found that the product obtained via method 1 (M1) most closely matched the spectra of the commercial product. Furthermore, M1 was the most cost-effective as the brominating agent “1,3-dibromo-5,5-dimethylhydantoin”<sup>203,204</sup> is much cheaper than both dibromoiso-cyanuric acid (M2)<sup>205,206</sup> and bromine (M3).<sup>207,208</sup> Following method 1, the product was obtained as a mixture of isomers in 44% yield, with **Br<sub>2</sub>-NDA** being the most predominant isomer. Unfortunately, the undesired isomers could not be separated at this stage.

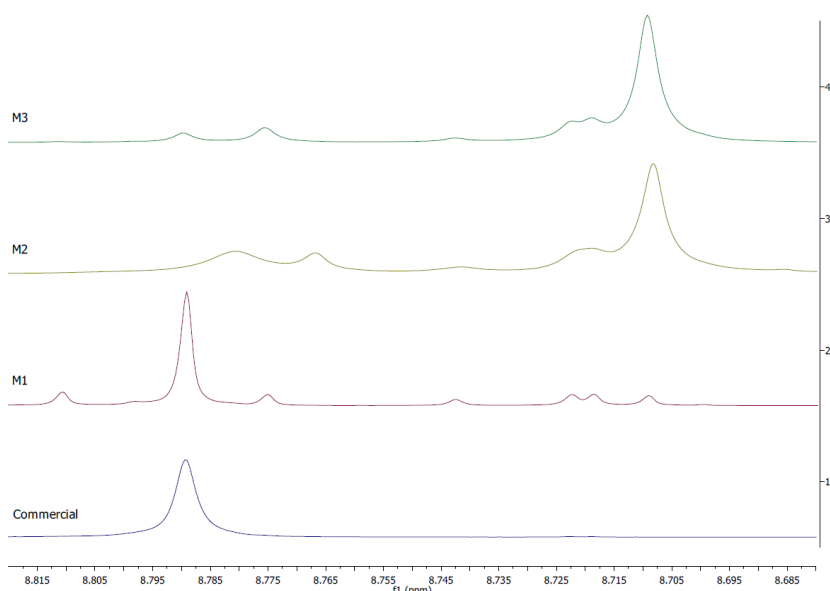


**Figure 82:** Comparison of the  $^1\text{H}$  NMR fragments of commercial and synthesized (method 1-3) **Br<sub>2</sub>-NDA**.

Next, the crude **Br<sub>2</sub>-NDA** was reacted with 2,6-dimethoxy-4-tridecylaniline in acetic acid in attempt to make the corresponding NDI molecule. However, instead of forming the anticipated diimide, a nucleophilic aromatic substitution ( $S_{\text{N}}\text{Ar}$ ) reaction occurred (**Figure 83**). This was unexpected as acidic conditions (like acetic acid) are known to activate the imide carbonyl groups and hence lower the risk of  $S_{\text{N}}\text{Ar}$ . Although, it is not fully understood why this is the case, we are convinced that this phenomenon is specific to the aniline in question. Based on literature, it is unlikely that our 2,6-dimethoxyaniline prefers  $S_{\text{N}}\text{Ar}$  over imidization because of steric reasons, as more bulky anilines such as 2,6-diisopropylaniline<sup>209</sup> and 2,4,6-trimethylaniline<sup>210</sup> have been used successfully before. Therefore, unless the oxygen lone pairs (of the methoxy groups) make 2,6-dimethoxy-4-tridecylaniline bulkier than 2,6-diisopropylaniline, steric encumbrance is not going to be the underlying reason. Instead, we suggest that the electronics of our aniline somehow disfavour nucleophilic attack at the carbonyl(s) due to possible hydrogen-bonding of the carbonyl oxygens with the aniline NH<sub>2</sub> hydrogens or maybe inductive withdrawal of electron-density via the methoxy groups on the aniline core.

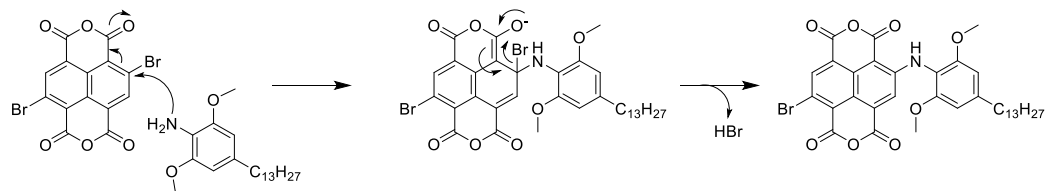


**Figure 83.** Proposed  $S_{\text{N}}\text{Ar}$  mechanism between 2,6-dimethoxy-4-tridecylaniline and **Br<sub>2</sub>-NDA**. The mechanism only demonstrates what happens with one equivalent of aniline. With two or more equivalents, either the second bromine is displaced in the same fashion or the aniline attacks onto the carbonyls through an imidization/condensation reaction.

To overcome the  $S_{\text{N}}\text{Ar}$  problem, an alternative pathway was followed (**Figure 84**). First, electron-deficient **Br<sub>2</sub>-NDA** underwent a Stille cross coupling with 2 equivalents of 2-(tributylstannylyl)thiophene in the presence of Pd(PPh<sub>3</sub>)<sub>4</sub>Cl<sub>2</sub> to afford **Th<sub>2</sub>-NDA** in 39% yield. The relatively low yield can be attributed to the presence of unwanted isomers in the starting material. When starting with commercially available **Br<sub>2</sub>-NDA** instead, an excellent yield of 93% was obtained. The cross coupling reaction works extremely well considering that electron-rich Pd<sup>0</sup> can easily insert into the super electron-deficient NDA C-X bond (via oxidative addition).<sup>91</sup> Moreover, electron-rich organometallics, such as organotinns, facilitate the transmetallation step.<sup>91</sup> As a result, the reaction proceeds very quickly (typically up to 3-4 h only) and with excellent yields.

Next, 2,6-dimethoxy-4-tridecylaniline was reacted with **Th<sub>2</sub>-NDA** in acetic acid to give **Th<sub>2</sub>-NDI** in 34% yield. The yield is comparable to the NDI molecules obtained in literature<sup>209,210</sup> and is in line with our previous research, where a yield of 26% was achieved for coupling diketofurofuranone (DFF) with 2,6-dimethoxy-4-tridecylaniline.<sup>106</sup>

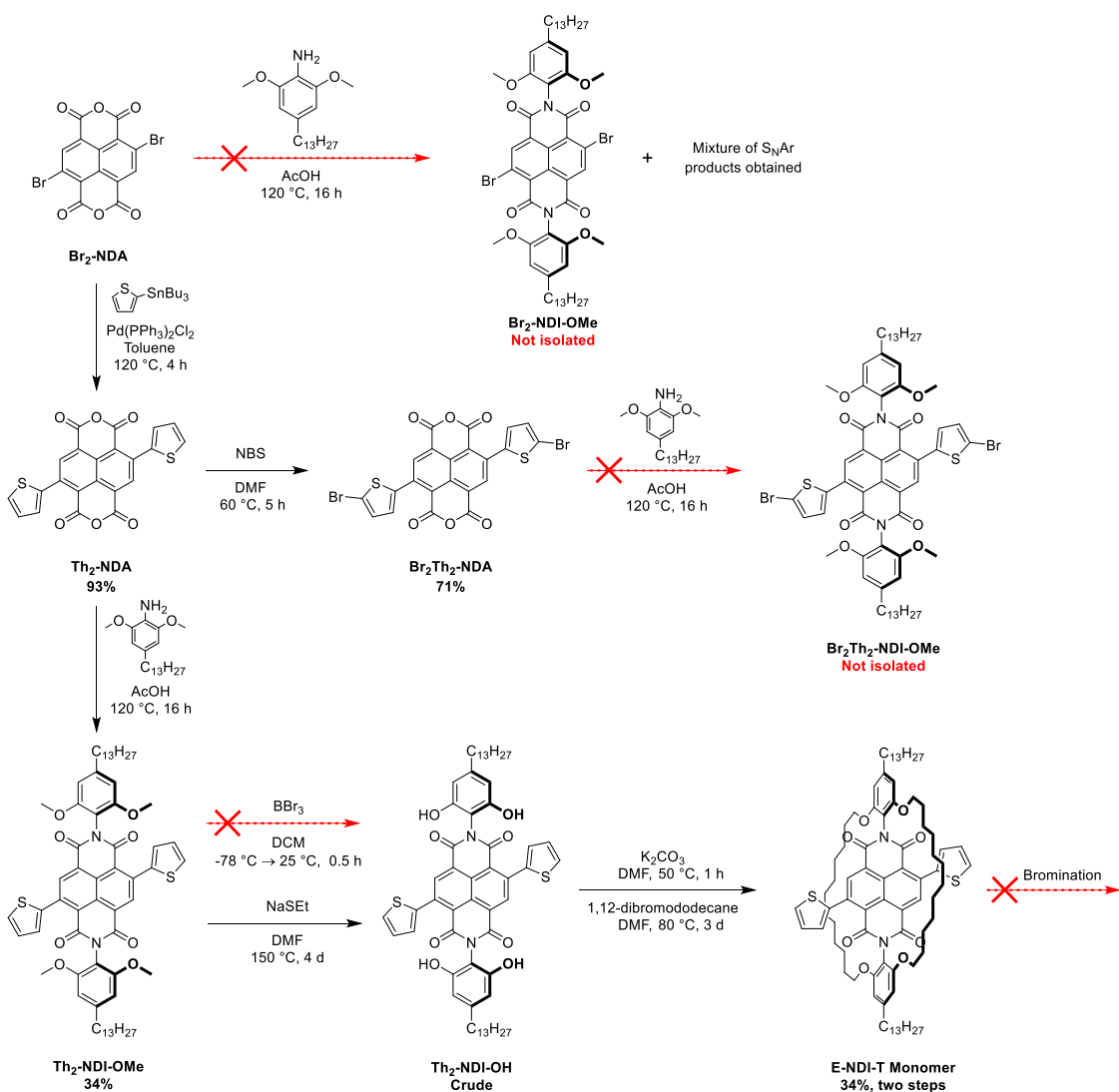


**Figure 84.** Synthetic strategy used to prepare the encapsulated NDI monomer (**E-NDI-T**).

It was then attempted to demethylate the four methoxy groups using BBr<sub>3</sub>. However, it was found that the conditions were too harsh as the starting material started to decompose in less than half an hour at -78 °C. Instead, the use of excess sodium ethane thiolate (NaSEt) in DMF gave the desired tetra-ol crude product (**Th<sub>2</sub>-NDI-OH**), which was subsequently subjected to encapsulation using 1,12-dibromododecane in dilute and basic conditions. The encapsulated product (**E-NDI-T**) was obtained in two step yield of 34% yield (**Figure 84**).

The <sup>1</sup>H NMR spectrum and assignment of **E-NDI-T** are shown in **figure 85** and **86**. The most de-shielded proton (#1) can be found on the NDI core (Ring A), which translates to a singlet of one proton. The next three signals (#2-4) are all doublet of doublets which integrate to two protons each and correspond to the protons on the thiophene ring (Ring B). Next, there is another, slightly more shielded singlet (#5), which is characteristic for protons on the aniline ring (Ring C) and integrates to four. The methoxy groups (#6, O-CH<sub>2</sub>-) give rise to a triplet which integrates to eight protons. The next, slightly more shielded triplet (#7) integrates to four protons and corresponds

to the benzylic methyl groups ( $\text{Ar}-\text{CH}_2-$ ). Lastly, the protons in the alkyl chains also closely match with the expectations.

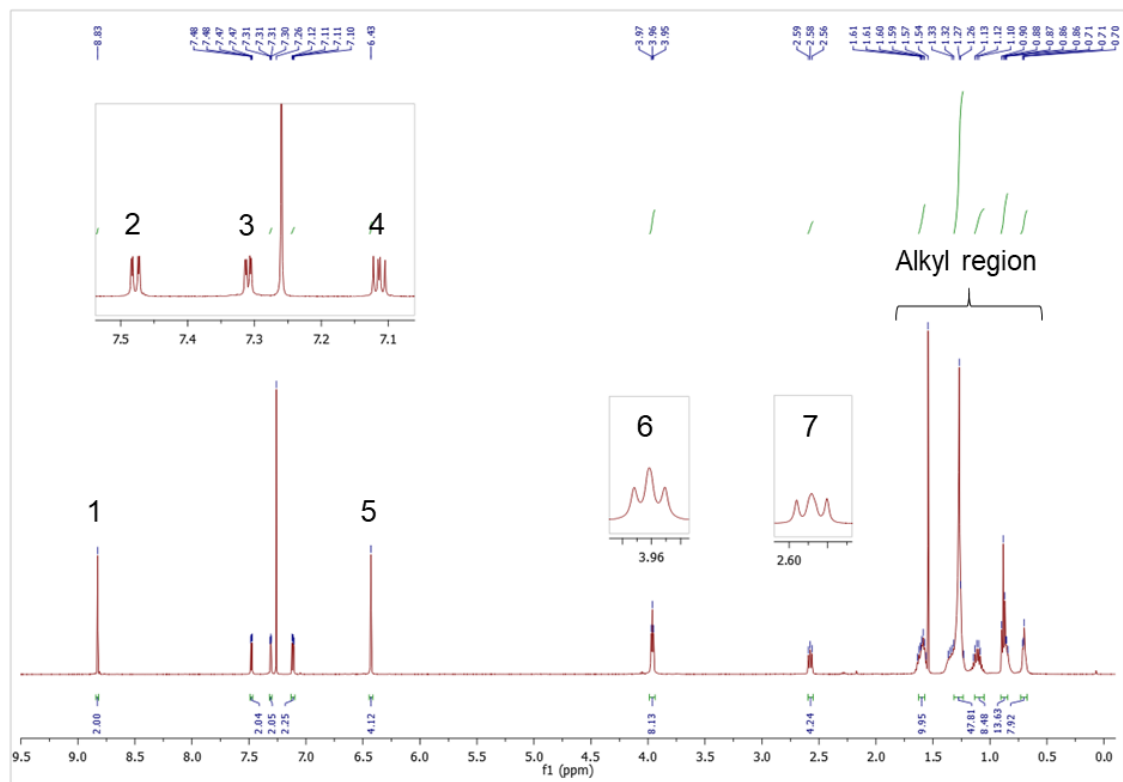


**Figure 85.**  $^1\text{H}$  NMR spectrum of **E-NDI-T**.

The identity of **E-NDI-T** was further confirmed through HRMS and X-ray crystallography. The single crystal was grown inside an NMR tube via liquid diffusion with chloroform and methanol (1:3). As observed, the crystal structure confirms that the straps shield the NDI core (**Figure 87**).

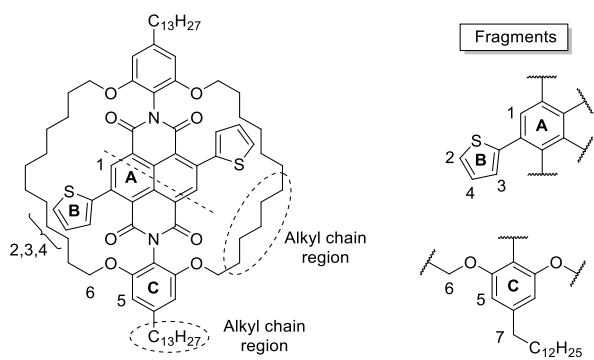


**Figure 86.**  $^1\text{H}$  NMR assignment of **E-NDI-T**.

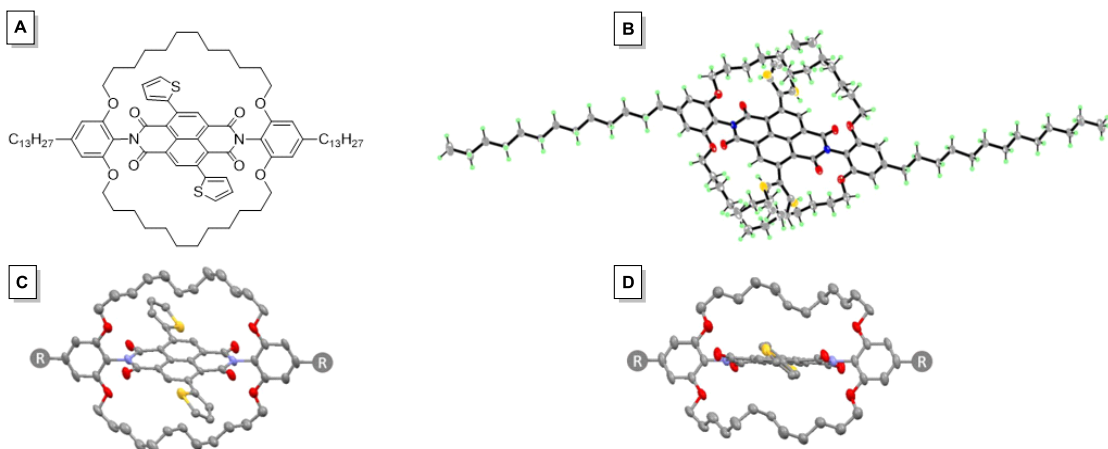


**Figure 87.** Chemical structure (A) and different X-ray structure views (B-D) of the encapsulated NDI monomer. In C and D, the structural disorder of the thiophene rings is removed, whereas the alkyl chains (R) are omitted.

Initial attempts to brominate the thiophene units of **E-NDI-T** with NBS failed as the electron-rich aryls (of the aniline unit) were more reactive and hence brominated instead. The formation of the phenyl brominated E-NDI-T molecule was confirmed by  $^1\text{H}$  NMR, as observed from **figure A 8** in the appendix. Alternative lithiation-bromination attempts with tetrabromomethane were also tried and looked promising. However, separation of the resulting, different brominated isomers was unsuccessful via silica column chromatography or recrystallization attempts. Therefore, instead of preparing a dibrominated monomer and constructing the polymer with a conventional Stille cross coupling reaction, we decided to use the encapsulated building block as it is and make a polymer through direct arylation polymerization (DAP).

The conjugated polymers (**Figure 88**) were prepared through a direct arylation polymerization procedure, using N,N'-bis(2-octyldodecyl)-2,6-dibromo-1,4,5,8-naphthalene diimide (**Br<sub>2</sub>-NDI-2OD**) as the co-monomer. As observed, the polymer series is comprised of the reference polymer **P(NDI-2OD-T)**, an in-between, bulky dimethoxyphenyl polymer **P(NDI-DMP-T)**, and lastly the encapsulated **P(E-NDI-T)** polymer. All polymers were obtained in reasonable number average molecular weights ( $M_n$ ) of approximately 15 kDa (**Table 5**) and display good solubilities in various solvents.

**Table 5.** Physical properties of the conjugated NDI polymers.

Polymer	$M_n$ (kDa)	$M_w$ (kDa)	PDI
P(NDI-2OD-T)	16.1	42.2	2.62
P(NDI-DMP-T)	16.3	29.5	1.81
P(E-NDI-T)	14.6	38.4	2.46

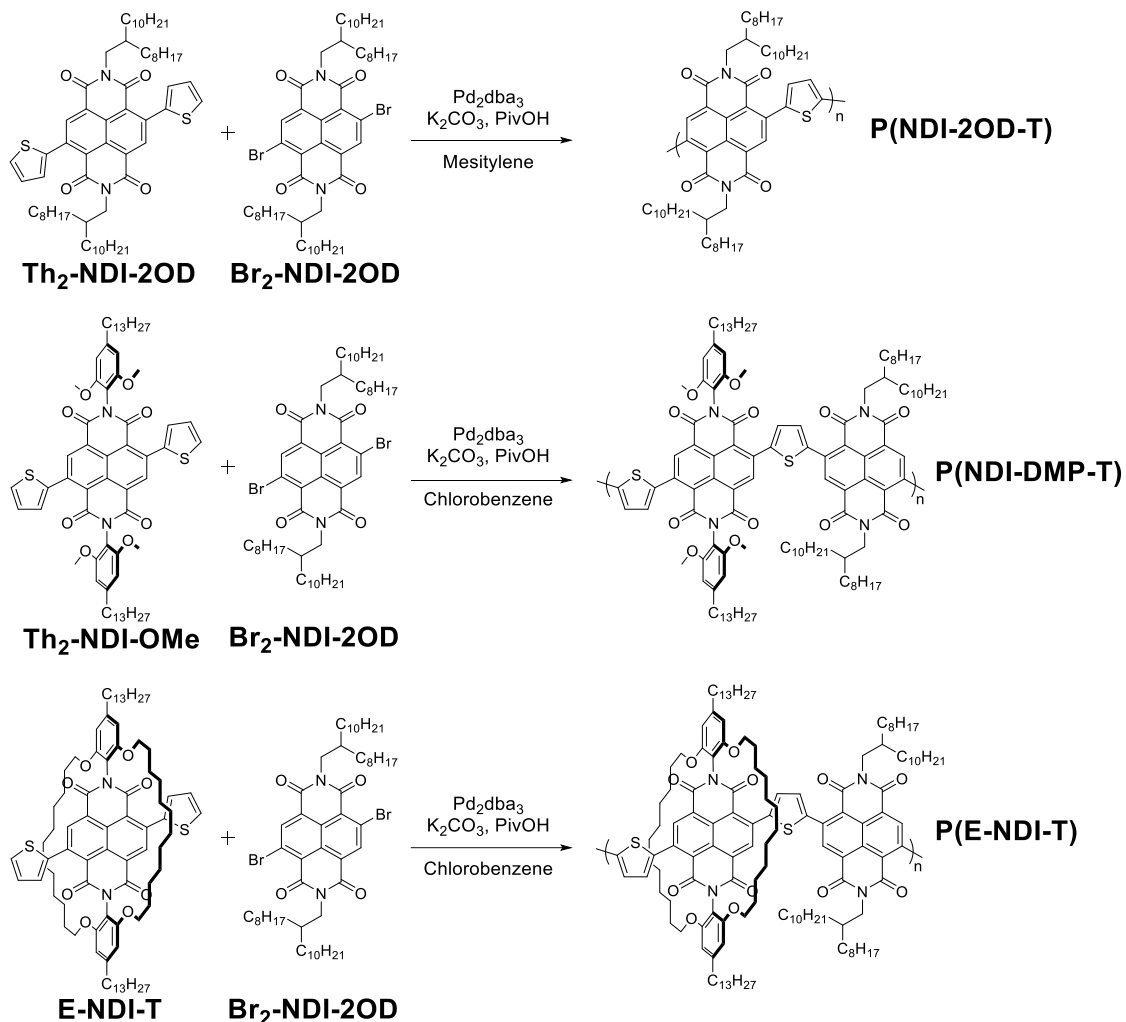


**Figure 88.** Synthesis of the novel NDI polymers; **P(NDI-2OD-T)**, **P(NDI-DMP-T)** and **P(E-NDI-T)**.

## Results & Discussion

### Photophysical Results

The solution and thin film absorption and emission spectra of the three NDI polymers are shown in **figure 89** and summarized in **table 6**. As observed, the spectral profiles of the solution absorption spectra are relatively featureless and nearly identical for all polymers, having a  $\lambda_{\max}$  at 545, 549 and 546 nm for **P(NDI-2OD-T)**, **P(NDI-DMP-T)** and **P(E-NDI-T)**, respectively. The thin film absorption spectra, on the other hand, show a much clearer difference between the different polymers. For **P(NDI-2OD-T)**,  $\lambda_{\max}$  is significantly red-shifted (by 51 nm) to 596 nm when going from solution to solid-state. In contrast, **P(NDI-DMP-T)** and **P(E-NDI-T)** display only minor redshifts of 3 and 1 nm, respectively. In other words, with increased shielding of the polymer backbone, the formation of aggregates is more suppressed, thereby retaining the absorption profile better when going from solution to thin film. This trend is consistent with our previous studies on encapsulated conjugated materials.

Similarly, the photoluminescence of the three polymers is nearly identical in solution, with a  $\lambda_{\text{max}}$  at  $\sim$ 636 nm. This suggests, that in solution, the emission originates from isolated (non-aggregated) chains. In thin film, on the other hand, the spectra are again more red-shifted depending on how exposed the polymer chains are. For **P(NDI-2OD-T)**, the  $\lambda_{\text{max}}$  red-shifts from 636 nm to 725 nm when going from solution to solid state. This can be attributed to interchromophore interactions. For **P(NDI-DMP-T)**, this effect is much more reduced and hence the thin film photoluminescence spectra are only red-shifted by 31 nm (From  $\lambda_{\text{max}} = 639$  nm to 670 nm) compared to solution. Even though, the absorption results already suggested  $\pi$ - $\pi$  interactions are significantly suppressed, the PL spectra seem to indicate there is still some degree of aggregation. Lastly, for **P(E-NDI-T)**, the photoluminescence spectrum remains nearly identical when going from solution to the solid-state, as the  $\lambda_{\text{max}}$  is only red-shifted by 5 nm (from 535 nm to 540 nm). Therefore, both the absorption and PL data of **P(E-NDI-T)** seem to suggest little to no evidence of aggregate formation.

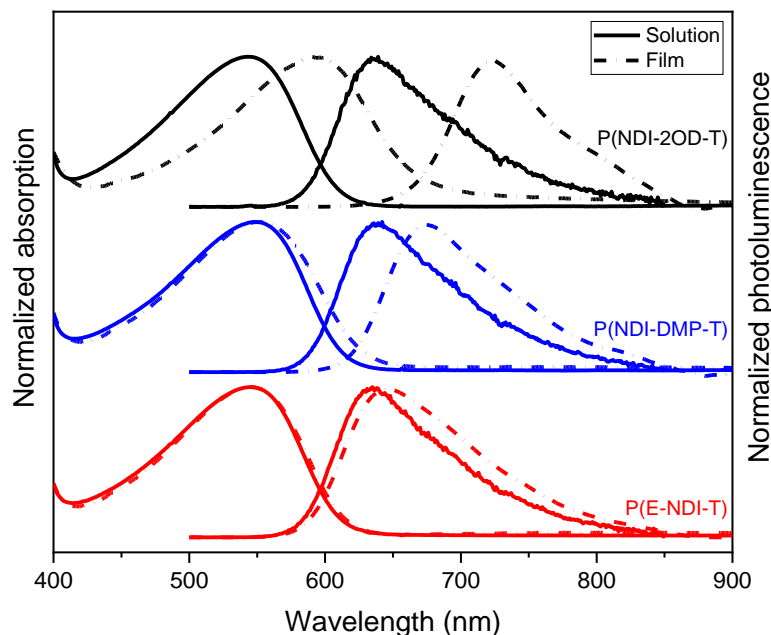


**Figure 89.** Normalized absorption and photoluminescence spectra of P(NDI-2OD-T) (black), P(NDI-DMP-T) (blue) and P(E-NDI-T) (red) in a 0.01 g/L chloroform solution (solid line) and  $\sim$ 100 nm thin film (dashed line).

To further investigate the effects of the interchromophore interactions, we also measured the photoluminescence quantum yields (PLQYs) of the three different polymers in both solution and solid-state. The results are summarized in **table 6**. As observed, the solution PLQYs of all polymers are relatively low, with 3.6%, 4.1% and 3.2% for **P(NDI-2OD-T)**, **P(NDI-DMP-T)** and **P(E-NDI-T)**, respectively. However, surprisingly, the thin film PLQYs for both **P(NDI-2OD-T)** and **P(NDI-DMP-T)** enhanced quite a lot, reaching 9.2% and 6.1%, respectively. **P(E-NDI-T)**, on the other hand, only demonstrates a modest increase from 3.2 to 3.7%. The increase in PLQY for both **P(NDI-2OD-T)** and **P(NDI-DMP-T)** can be attributed to aggregation-induced emission (AIE) through twisted intramolecular charge transfer (TICT) processes in the solid state. In

contrast, **P(E-NDI-T)** efficiently suppresses intermolecular interactions and hence retains its PLQY at higher concentrations (i.e., thin film).

**Table 6.** Summary of the photophysical properties of **P(NDI-2OD-T)**, **P(NDI-DMP-T)** and **P(E-NDI-T)**.

Sample	$\lambda_{\text{max,abs}}$ (nm)	$\lambda_{\text{max,em}}$ (nm)	$\varphi$ (%) <sup>a</sup>	PL lifetimes (ns) <sup>b</sup>			Average PL lifetime (ns)	$k_r^c$	$k_{\text{nr}}^c$
P(NDI-2OD-T) in CHCl <sub>3</sub>	545	636	3.6±0.3	$\tau_1 = 0.31$ (97.0%)		$\tau_3 = 4.26$ (3.0%)	$\tau_{\text{AVG}} = 0.429$	0.84	22.47
P(NDI-DMP-T) in CHCl <sub>3</sub>	549	639	4.1±0.1	$\tau_1 = 0.29$ (78.2%)	$\tau_2 = 0.61$ (19.6%)	$\tau_3 = 5.60$ (2.2%)	$\tau_{\text{AVG}} = 0.470$	0.87	20.40
P(E-NDI-T) in CHCl <sub>3</sub>	546	635	3.2±0.2	$\tau_1 = 0.27$ (72.2%)	$\tau_2 = 0.57$ (25.4%)	$\tau_3 = 4.36$ (2.4%)	$\tau_{\text{AVG}} = 0.444$	0.72	21.80
P(NDI-2OD-T) film	596	725	9.2±0.3	$\tau_1 = 0.89$ (92.1%)		$\tau_3 = 4.26$ (7.9%)	$\tau_{\text{AVG}} = 1.156$	0.80	7.86
P(NDI-DMP-T) film	552	670	6.1±0.3	$\tau_1 = 0.23$ (35.5%)	$\tau_2 = 0.61$ (61.0%)	$\tau_3 = 5.60$ (3.5%)	$\tau_{\text{AVG}} = 0.65$	0.94	14.45
P(E-NDI-T) film	547	640	3.7±0.2	$\tau_1 = 0.20$ (63.1%)	$\tau_2 = 0.57$ (34.0%)	$\tau_3 = 4.36$ (2.9%)	$\tau_{\text{AVG}} = 0.446$	0.83	21.59

<sup>a</sup> Excitation at 520 nm, <sup>b</sup> Fluorescence lifetimes measured at 375 nm, and percentage weights are reported between parentheses. <sup>c</sup> Rate constants for radiative ( $k_r$ , 10<sup>8</sup> s<sup>-1</sup>) and non-radiative decay ( $k_{\text{nr}}$ , 10<sup>8</sup> s<sup>-1</sup>) were calculated from the  $\varphi$  and  $\tau$  values according to the formulae  $k_r = \varphi/\tau$  and  $k_{\text{nr}} = (1 - \varphi)/\tau$ , where  $\tau$  corresponds to the weighted average of the lifetimes.

These results/trends are further corroborated by the PL lifetimes (**Table 6**). For all polymers, the weighted-average PL lifetimes ( $\tau_{\text{AVG}}$ ) are lower in solution than in thin film, which translates to higher PLQYs in thin film. For **P(NDI-2OD-T)**, both solution and film follow a bi-exponential decay, in which the fast-decaying component ( $\tau_1$ ) dominates exciton deactivation. As seen, the PL lifetime increases from  $\tau_1 = 0.31$  ns (or  $\tau_{\text{AVG}} = 0.43$  ns) in solution to 0.89 ns (or  $\tau_{\text{AVG}} = 1.18$  ns) in film. Therefore, we suggest that the increased face-to-face  $\pi$ - $\pi$  stacking interactions cause a strong aggregation-induced emission, which is supported by the PLQY values (3.6 % in solution vs. 9.2% in film). For **P(NDI-DMP-T)**, a similar trend is observed. However, the difference is much smaller due to partial suppression of interchromophore interactions. The average lifetimes for **P(NDI-DMP-T)** are 0.47 ns in solution and 0.65 ns in thin film, which again closely matches with the difference in PLQYs (4.1% in solution vs. 6.1% in thin film). In contrast, **P(E-NDI-T)** remains relatively unaffected due to suppression of intermolecular interactions. This translates to a  $\tau_{\text{AVG}}$  of 0.44 ns in solution and 0.45 ns in thin film, which compares to the difference in PLQYs (3.2% in solution versus 3.7% in thin film).

## GIWAXS data

GIWAXS was performed on all three polymers to validate the observations from the optical spectroscopy. **Figure 90** shows the scattering data, and the radial integrals and **table 7** contains the extracted d-spacings of the novel materials.

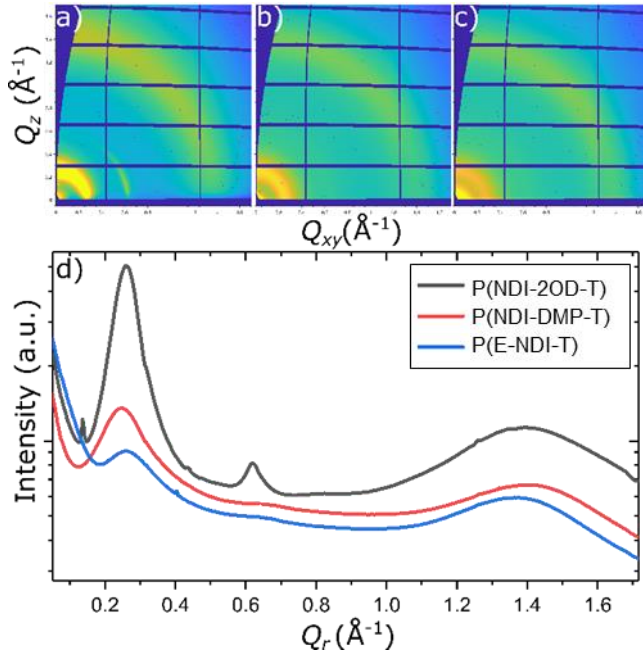


**Figure 90.** GIWAXS scattering data of a) **P(NDI-2OD-T)**, b) **P(NDI-DMP-T)**, and c) **P(E-NDI-T)**, and their respective radial integrals d).

**Table 7.** Summary of the extracted d-spacings in **P(NDI-2OD-T)**, **P(NDI-DMP-T)** and **P(E-NDI-T)**.

	Angstroms <sup>-1</sup>			Angstrom		
	100	200	010	100	200	010
<b>P(NDI-2OD-T)</b>	0.26	0.62	1.39	24.169	10.121	4.51
<b>P(NDI-DMP-T)</b>	0.25	NA	1.37	25.316	NA	4.59
<b>P(E-NDI-T)</b>	0.26	NA	1.33	24.169	NA	4.72

The parent polymer **P(NDI-2OD-T)** shows the typical 100 lamellar packing with a distance of 25 Å as has been reported previously, along with some preference for face-on orientation relative to the substrate as seen by the 200 peak at 0.6 Q. Looking at the two novel derivatives it can be seen that the polymers pack in, in general, in a similar manner. However, on addition of the alkylphenyl group (like in **P(NDI-DMP-T)**), the amount of long-range order is reduced, whereas full encapsulation (like in **P(E-NDI-T)**) reduces the crystallinity even further. Looking at the 010 peaks, it can clearly be seen that on going from the parent polymer **P(NDI-2OD-T)** to the non-encapsulated **P(NDI-DMP-T)** and finally **P(E-NDI-T)** the pi-stacking distance increases as

would be expected by adding the encapsulating rings. Therefore, with the combined photophysical and crystallographic characterization we can report with confidence that in the solid state, the electronic coupling between adjacent polymer chains is reduced upon molecular encapsulation.

Conventional conjugated polymers typically undergo substantial photoluminescence quenching when going from solution to the solid state. The combined morphological and photophysical results therefore show the surprising result that i) the extremely well-known polymer **P(NDI-2OD-T)** undergoes strong aggregation induced emission and ii) this phenomenon originates in some form or another from the interchain packing. It has previously been shown that molecular encapsulation allows a polymer to maintain, to some extent, its properties in solution in the solid state.<sup>106,176</sup> In this work, we find the same concept applies as both the absorption and emission shapes, yields and lifetimes are almost identical. However, in contrast to almost all other reported conjugated polymers, the emissivity of the non-encapsulated derivative increases further in the solid state, resulting in a relatively high emission PLQY for this wavelength region. The phenomenon of AIE is well known and has been reported in numerous conjugated polymer systems, including ones containing naphthalene diimide units. Crucially however, in almost every example of conjugated polymer AIE, specific groups (such as vinylenes or TPEs), that are well known to induce AIE-like properties, are introduced for this reason.<sup>211-216</sup> There are almost no examples of a ‘regular’ conjugated polymer undergoing AIE. Moreover, it is remarkable that it has not been previously observed in these specific systems, which have been extensively studied. In fact, we can find only one other example of AIE in a conventional (i.e., without vinylene groups) conjugated polymer, where emissive efficiency was enhanced through the formation of close contacts between adjacent polymer chains.<sup>217</sup>

To determine the origin of the observed AIE in this system, it is useful to consider all the possible mechanisms through which it could be occurring. NDI-based small molecules have previously been shown to undergo enhanced emission in the solid state predominantly through J-aggregation.<sup>218-222</sup> However, the pi-stacking distance as measured by GIWAXS for **P(NDI-2OD-T)** is ~ 4.5 Å, which is considerably higher than those reported for small molecule NDIs displaying J-aggregates. Furthermore, the red-shifted emission of NDI-T based polymers has been demonstrated to originate from the crystallization induced planarization of the conjugated backbone rather than J-aggregates.<sup>198</sup> Here, we observe a stepwise reduction in AIE when going from **P(NDI-2OD-T)** to **P(NDI-DMP-T)** and **P(E-NDI-T)** films, which correlates extremely well with the increased 010 distances interlayer separation.

In conclusion, the crystallization of the pi-conjugated faces of the polymer results not only in a planarization, but also in the suppression of non-radiative decay pathways, and thereby a substantially increased photoluminescence efficiency. We believe that this is the first observation

of this effect in a non-vinylene containing conjugated polymer and suggest that it could provide a novel design strategy for obtaining good emissive efficiency in narrow bandgap conjugated polymers. This obstacle has recently been identified as a major hurdle that must be overcome to increase the efficiency of OPV devices.<sup>223</sup> Finally, we note that **P(NDI-2OD-T)** and related polymers are the most successful conjugated polymers used in all-polymer solar cells and this previously unreported AIE may provide a clue as to why they have performed so well.

## Conclusions

This chapter reports the synthesis of molecularly encapsulated, conjugated naphthalene diimide based conjugated polymers and compares it to a bulky and naked equivalent. The encapsulated polymer surprisingly has a lower photoluminescence quantum yield compared to the naked reference polymer, which contrasts with the current conventional ‘wisdom’. Instead, our results reveal a previously unobserved aggregation induced emission phenomena in one of the most well studied conjugated polymers [**P(NDI-2OD-T)**]. Structural characterization confirmed that this AIE was due to the crystallization of the pi-conjugated faces of the polymer chains. Therefore, we believe that having control over the crystallization of conjugated polymers may be key to enhance their emissive properties and device performance.

# Chapter IV

## Molecularly Encapsulated PDI Molecules

### Introduction

Intermolecular interactions play a key role in defining the properties of conjugated materials and how they perform in organic electronics. Therefore, it is essential to gain better synthetic control over the solution and solid-state properties of these materials.

PDI s are relatively large and planar chromophores that have a strong propensity to aggregate through  $\pi$ - $\pi$  stacking, which can greatly diminish their photoluminescence at higher concentrations<sup>224–226</sup> and hence limit their use in various applications. Therefore, it is of utmost importance to gain a deeper understanding of the structure-property relationships in PDI chromophores and how to control their aggregation behavior and photophysical properties in both solution and film.

The three main strategies to suppress aggregation in PDI dyes are based on functionalizations on i) the bay positions, ii) the imide positions and iii) the ortho positions (**Figure 91**). For option i), sterically demanding units can be introduced via a simple nucleophilic aromatic substitution ( $S_NAr$ ) onto the halogenated PDI core.<sup>227,228</sup> However, even though introducing bulky groups at the bay positions reduces  $\pi$ - $\pi$  stacking, it often bends the PDI core<sup>229,230</sup>, which can undesirably influence the photophysical properties of the dye.<sup>231</sup>

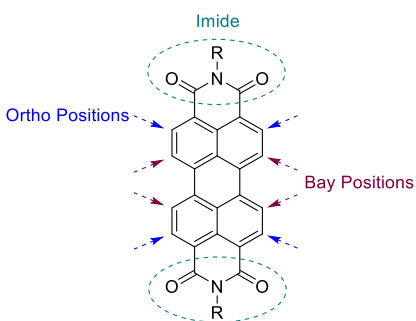


**Figure 91.** General structure of perylene diimides (PDIs).

The second option to protect both faces of the PDI chromophore from intermolecular interactions, without disrupting its planarity, is the use of bulky substituents on the imide positions.<sup>232</sup> This strategy was reported recently by Wong and coworkers.<sup>224</sup> Their synthesis includes various PDI derivatives, which have different degrees of bulk on the imide positions, ranging from simple phenyl moieties to more congested 3,5-di-*tert*-butylphenyl and trityl groups.<sup>224</sup> While their X-ray crystal data confirm that increasing the bulk of the substituents leads to more spatially shielded dyes, the UV-vis data still suggest that these materials undergo significant aggregation.<sup>224</sup>

Therefore, introducing congested groups at the imide positions of PDIs does not guarantee the absence of aggregate formation, nor does it offer control over their photophysical properties.

Alternatively, we propose to encapsulate the PDI core with alkylene straps, as has been demonstrated in other conjugated materials.<sup>106,124–127,144,160,162,163,233</sup> This design tactic makes use of recently discovered ortho functionalization (i.e., the 2, 5, 8, 11 positions) of PDIs<sup>234,235</sup> to install 1,3-dimethoxybenzene groups, followed by further functionalization to fully encapsulate the PDI core with alkylene straps.

## Project Objectives

In this chapter, the aim was to prepare an encapsulated PDI molecule and investigate how molecular encapsulation influences the photophysical properties of the PDI molecule. Furthermore, it is hoped that through molecular encapsulation and thus the suppression of intermolecular interactions, a photoluminescent PDI-based solid-state emitter could be obtained.

## Synthetic Design & Characterization

The double encapsulated perylene diimide molecule (**PDI-Encap**) was prepared according to the steps outlined in **figure 92**. First, Perylene-3,4,9,10-tetracarboxylic dianhydride (**PDA**) was converted in the corresponding **PDI** molecule upon treatment with 2-octyldodecylamine. After silica column chromatography, **PDI** was obtained in an excellent yield of 93%. Using a previous procedure<sup>235</sup>, **PDI** was then subjected to an ortho-directed, iridium-catalyzed borylation to afford **PDI-BPin** in a respectable 51% yield. The proposed reaction mechanism for the direct borylation can be seen in **figure 93**. The Iridium catalyst coordinates to one of the carbonyl oxygens to form **complex IV-1** and cleaves the *ortho* C-H bond through a concerted metalation deprotonation (CMD) mechanism.<sup>234</sup> **Complex IV-2** then undergoes a transmetalation with  $B_2Pin_2$ , yielding **complex IV-3** and side product  $HBPin$ . Finally, reductive elimination leads to C-B bond formation (**IV-4**) and regeneration of the active catalyst.<sup>234</sup> The cycle repeats itself for the remaining three *ortho* positions to generate the tetraborylated product (**PDI-BPin**). A further Suzuki-Miyaura cross coupling reaction with 2-bromo-1,3-dimethoxy-benzene, using  $Pd_2dba_3$  and SPhos, generated the **PDI-OMe** in a good yield (79%). SPhos was chosen as the preferred ligand in this catalytic system due to its known efficient coupling of sterically encumbered substrates.<sup>236</sup> Following a demethylation with  $BBr_3$ , crude **PDI-OH** was reacted with 1,8-dibromoocetane, in dilute and basic conditions, to yield 4% of the double encapsulated perylene diimide (**PDI-Encap**) as the only isolable product after chromatographic purification. Although this yield sounds very low, it is not unreasonable considering that eight  $S_N2$  reactions are taking place at once, and intermolecular or polymeric can potentially be generated in the process.

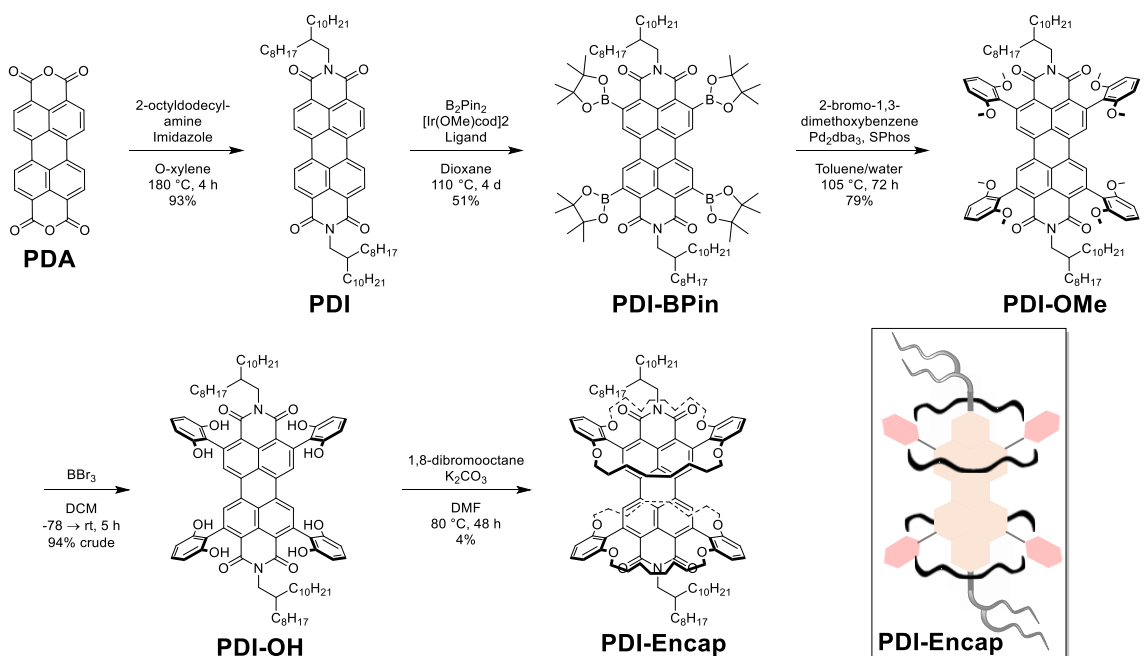


**Figure 92.** Synthesis of the double encapsulated perylene diimide (**PDI-Encap**).

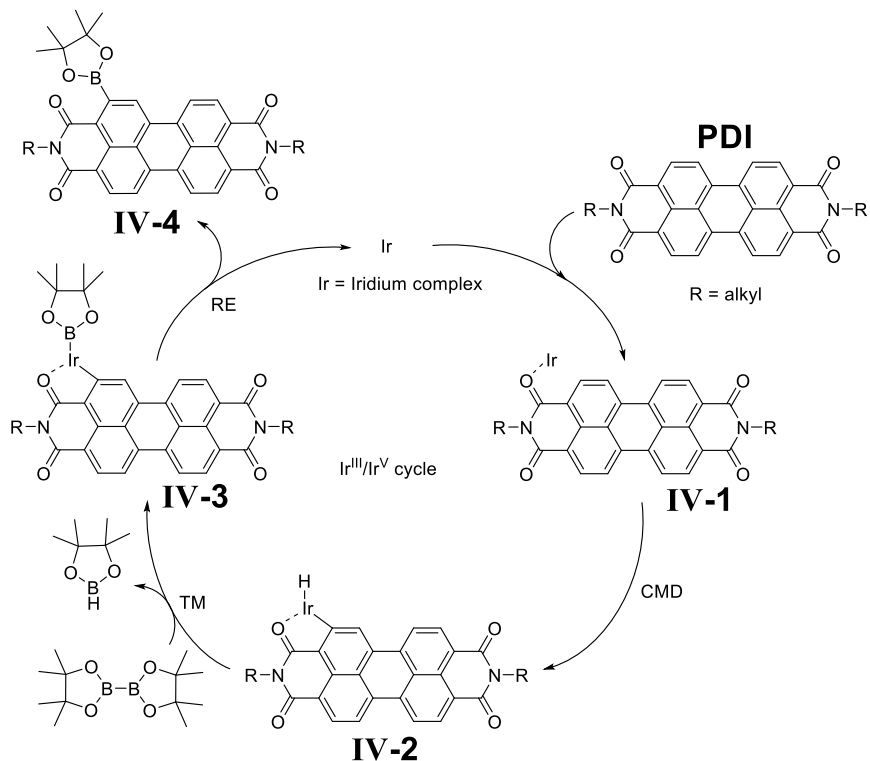


**Figure 93.** Proposed mechanism for the ortho borylation of PDI. Ir denotes the iridium catalyst/complex.

Both **PDI-OMe** and **PDI-Encap** were fully characterized using a combination of NMR spectroscopy, X-ray crystallography, HRMS and/or elemental analysis. The  $^1\text{H}$  NMR fragment (**Figure 94**) of **PDI-OMe** shows three aromatic proton environments. The singlet at  $\sim 8.3$  ppm is the most de-shielded peak (denoted “a”) and corresponds to the aromatic C-H protons of the electron-deficient PDI core, thereby integrating to four protons. Position b is assigned to the the

triplet at ~7.4 ppm; or the *para* position of the dimethoxybenzene ring. As expected, this integrates to four protons. Position c is ascribed to the doublet at ~6.8 ppm and corresponds to the eight protons from the *meta* position of the dimethoxybenzene ring. All aromatic signals therefore closely match the expectations. The first peak in the alkyl chain region is much more shielded (at below 4 ppm) and corresponds to a doublet, which integrates to four protons. This signal belongs to the N-alkyl CH<sub>2</sub>. The last signal in this NMR fragment, is a singlet at below 3.8 ppm. This is ascribed to the four methoxy groups and therefore integrates to 24 protons. The remaining peaks corresponding to the alkyl chain region (see appendix), were omitted for clarity, but also integrate correctly and follow the expected multiplicities.

In comparison, the <sup>1</sup>H NMR spectrum of **PDI-Encap** seems to retain all the aromatic signals and the N-alkyl chain CH<sub>2</sub> (positions a, b, c, and d) observed for **PDI-OMe** (**Figure 94**). However, the peak corresponding to the methoxy groups for **PDI-OMe** is now split into two different chemical environments due to anisotropy. The two anisotropic O-CH<sub>2</sub> protons (position e) are a first indication that the alkylene straps are indeed encapsulating the PDI core. Further proof was provided by 2D NMR experiments. The <sup>1</sup>H-<sup>13</sup>C HSQC spectrum indicates that the two anisotropic protons (e) are bound to the same carbon atom (see appendix), which suggests they undergo slow conformational/chemical exchange. This is also confirmed by <sup>1</sup>H-<sup>1</sup>H ROESY NMR (**Figure 94, bottom left**) and arises from the conformational restriction of the encapsulating alkylene straps. Furthermore, the protons on the alkylene straps are very shielded (< 0.9 ppm, see appendix), which indicates that these protons are proximal to the π-system of the PDI chromophore, as expected upon encapsulation.

The X-ray crystal structure of **PDI-Encap** unambiguously proved that the alkylene straps engage in horizontal encapsulation, rather than vertical looping or cross encapsulation (**Figure 96**). Interestingly, the side products could not be isolated. However, their formation cannot be precluded due to the low yield of **PDI-Encap**. **PDI-Encap** crystallizes in the triclinic  $P\bar{1}$  space group with one half of a **PDI-Encap** molecule and one CHCl<sub>3</sub> molecule in the asymmetric unit. The **PDI-Encap** molecules stack along the crystallographic *a* axis in an offset manner with 9.9 Å centroid-to-centroid separation distances between adjacent PDI cores. As seen, neighboring **PDI-Encap** molecules are aligned in a parallel fashion (**Figure 97**). Therefore, the packing of **PDI-Encap** appears to be driven by the crystallization of the encapsulating straps, rather than π-π interactions. This is in stark contrast to traditional PDI dyes as they typically undergo π-stacking in the crystalline state.<sup>237,238</sup> As a result of the horizontally aligned alkylene straps and the bulky peripheral aryl groups, intermolecular π-π interactions are absent in the crystal structure of **PDI-Encap**.

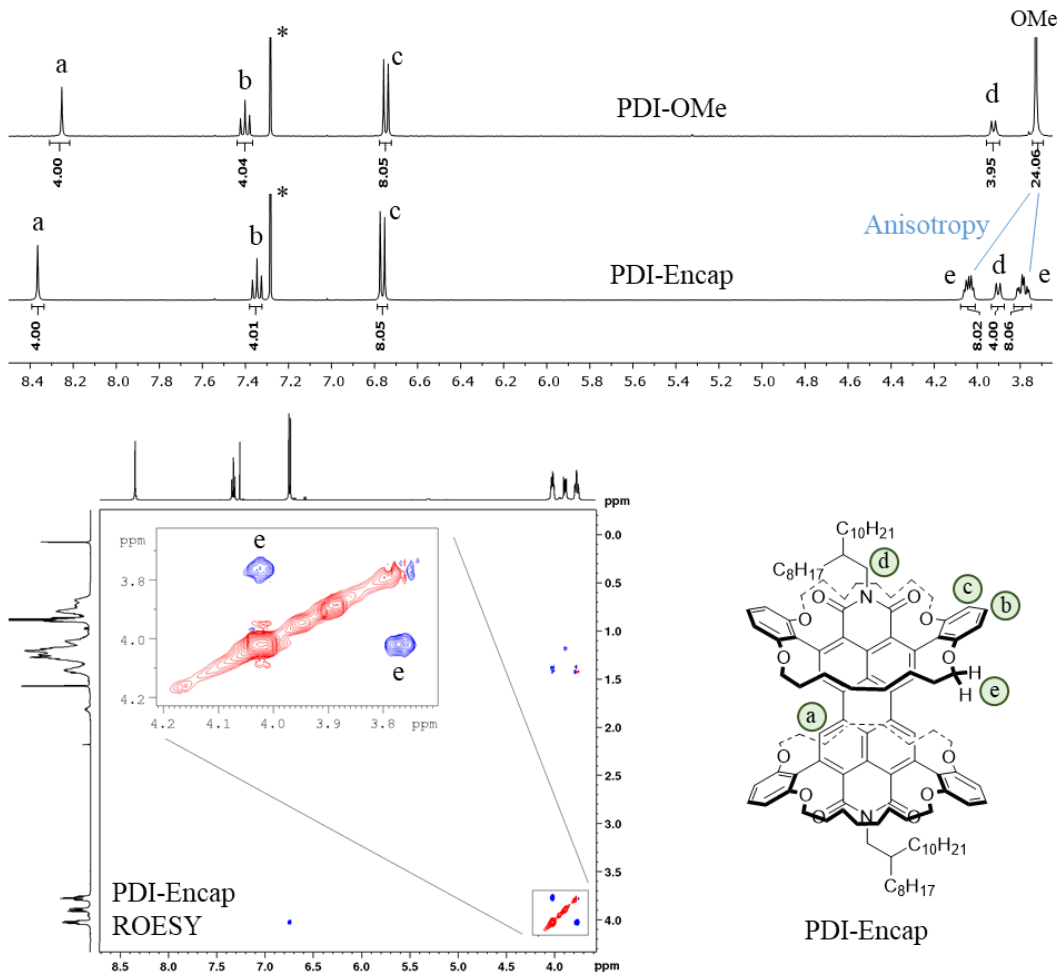


**Figure 94.** Fragment of the  $^1\text{H}$  NMR spectra of PDI-OMe and PDI-Encap (top).  $^1\text{H}$ - $^1\text{H}$  ROESY spectrum of PDI-Encap (bottom left). Structural assignment of PDI-Encap (bottom right). The shifts are reported in ppm and referenced against residual  $\text{CHCl}_3$  in  $\text{CDCl}_3$ .

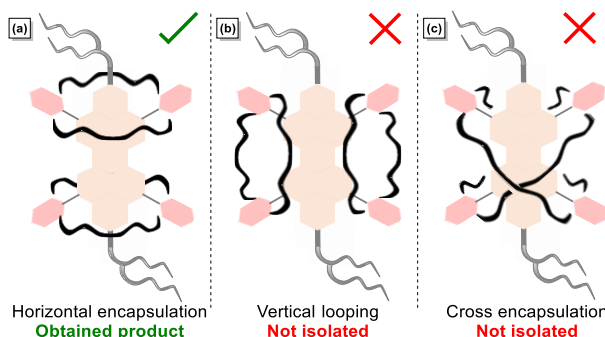


**Figure 95.** Cartoon of the potential encapsulation products (excluding intermolecular products). (a) Observed horizontal encapsulation; (b) Non-isolated vertical looping; (c) Non-isolated cross encapsulation.

PDI-OMe, on the other hand, crystallizes in the monoclinic  $P2_1/c$  space group with one **PDI-OMe** and two  $\text{CHCl}_3$  molecules in the asymmetric unit. The **PDI-OMe** molecules stack along the (011) Miller plane (**Figure 97**) with 10.2 Å centroid-to-centroid separation distances. The planes of neighboring PDI-cores close an angle of 58°. The molecular stacks are stabilized by C–H···π and C–H···O interactions in the absence of π–π interactions, as caused by steric hindrance of the peripheral aryl groups.

The contrast in packing between **PDI-Encap** and **PDI-OMe** therefore suggests that the interdigitation and parallel alignment in **PDI-Encap** is promoted by the spacing and alignment of the encapsulating alkylene groups. Molecular encapsulation might, therefore, provide an approach to control the arrangement of fluorophores in the solid state as well as suppress  $\pi-\pi$  stacking, for which it is most commonly used.<sup>106,125–127,160,162,163,233</sup>

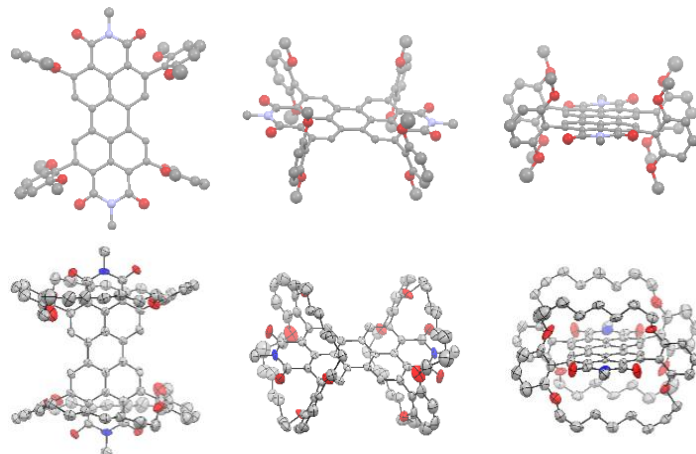


**Figure 96.** X-ray structures of the meso compounds of **PDI-OMe** (top) and **PDI-Encap** (bottom) viewed from three different perspectives. The branched 2-octyldodecyl chains, hydrogen atoms and solvent molecules are omitted for clarity.

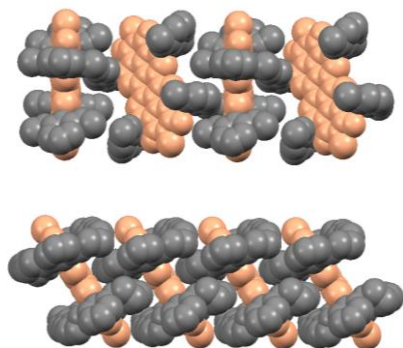


**Figure 97.** X-ray crystal structures of molecular stacks of **PDI-OMe**, viewed along the (100) Miller plane (top), and **PDI-Encap**, viewed along the (01 $\bar{1}$ ) Miller plane (bottom). The branched 2-octyldodecyl chains, all hydrogen atoms and solvent molecules are omitted for clarity. Color scheme: PDI cores – orange, peripheral aryl and encapsulating alkylene groups – grey.

## Results & Discussion

### Photophysical Results

The solution and film absorption spectra of **PDI**, **PDI-OMe** and **PDI-Encap** are shown in figure 98. The spectral profiles of the solution absorption spectra are near-identical for the three dyes, consisting of four well-resolved vibronic bands at a  $\lambda_{\text{max}}$  of ~430, ~460, ~485 and ~530 nm, which correspond to the 0-3', 0-2', 0-1' and 0-0' transitions, respectively. For **PDI**, the thin film absorption spectrum is red shifted compared to solution and displays reduced vibronic fine structure. The spectrum is broader, which is indicative of aggregation in the solid-state; a phenomenon that is typical for most perylene diimides.<sup>237,238</sup> In contrast, the spin-coated thin films

of **PDI-OMe** and **PDI-Encap** retain mostly the same absorption profile as in solution, suggesting unimolecular behavior and a suppression in the formation of aggregates. The sharper absorption onset for the thin film of **PDI-Encap** compared to **PDI-OMe** suggests that it is more rigid and less prone to conformational disorder in the solid state.<sup>106,239,240</sup>

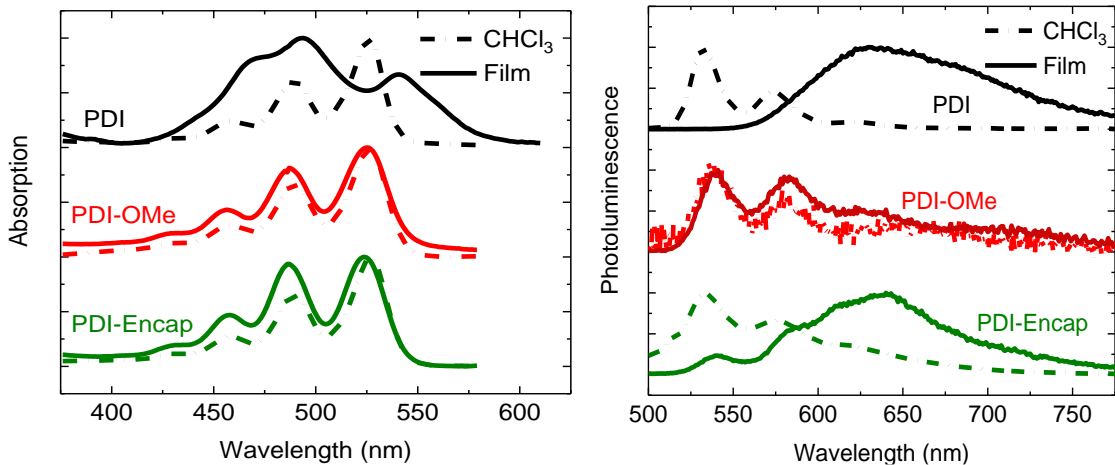


**Figure 98.** UV-Vis absorption (left) and photoluminescence (right) spectra of **PDI** (black), **PDI-OMe** (red) and **PDI-Encap** (green) in both solution and thin film.

The absorption and photoluminescence (PL) spectra of the three dyes in solution (**Figure 98**) display the typical mirror image, that is established for rigid luminophores that emit from  $\pi-\pi^*$  states.<sup>241</sup> However, the PL spectra for **PDI-OMe** and **PDI-Encap** are broader compared to **PDI**, having more poorly resolved vibronic fine structures and shallower onsets. This suggests, that in the excited state, there is a degree of intramolecular charge transfer (ICT) character between the electron-rich peripheral aryl rings and electron-deficient PDI cores. This statement is further supported by the density functional theory (DFT) calculations discussed below, as well as by time-resolved PL data (**Table 8**).

In solution, **PDI** shows a monoexponential decay with a lifetime ( $\tau$ ) of  $\sim 4$  ns, ascribed to fluorescence from a  $\pi-\pi^*$  state. In contrast, **PDI-OMe** and **PDI-Encap** display biexponential decays, consisting of a fast-decaying component (i.e., on a sub-ns timescale) and a longer-lived state ( $\tau = 3.4$  and  $2.3$  ns for **PDI-OMe** and **PDI-Encap**, respectively). These data indicate that multiple states/processes contribute to the PL decay of **PDI-OMe** and **PDI-Encap**. The presence of a fast, non-radiative decay component for **PDI-OMe** and **PDI-Encap** is responsible for their low solution PLQYs (< 1%) compared to that of **PDI** (67%). Furthermore, since the measurements were taken on dilute solutions, it is expected that that PL quenching (for **PDI-OMe** and **PDI-Encap**) stems from the fast formation of ICT states with reduced luminescence efficiency. This is further supported by DFT calculations (*vide infra*).

**Table 8.** Solution and thin film PLQY and transient PL lifetimes for **PDI**, **PDI-OMe** and **PDI-Encap**.

Compound	CHCl <sub>3</sub> solution		Thin film	
	PLQY	Transient PL lifetimes	PLQY	Transient PL lifetimes
<b>PDI</b>	24% ( $\lambda_{\text{exc}} = 445 \text{ nm}$ ) 67% ( $\lambda_{\text{exc}} = 520 \text{ nm}$ )	$\tau = 4.02 \text{ ns}$	22% ( $\lambda_{\text{exc}} = 445 \text{ nm}$ ) 20% ( $\lambda_{\text{exc}} = 520 \text{ nm}$ )	$\tau_1 = 1.60 \text{ ns}$ $\tau_2 = 5.06 \text{ ns}$
<b>PDI-OMe</b>	< 1% ( $\lambda_{\text{exc}} = 445 \text{ nm}, 520 \text{ nm}$ )	$\tau_1 = 0.01 \text{ ns}$ $\tau_2 = 3.37 \text{ ns}$	< 1% ( $\lambda_{\text{exc}} = 445 \text{ nm}, 520 \text{ nm}$ )	$\tau_1 = 0.03 \text{ ns}$ $\tau_2 = 0.54 \text{ ns}$ $\tau_3 = 3.13 \text{ ns}$
<b>PDI-Encap</b>	< 1% ( $\lambda_{\text{exc}} = 445 \text{ nm}, 520 \text{ nm}$ )	$\tau_1 = 0.04 \text{ ns}$ $\tau_2 = 2.33 \text{ ns}$	< 1% ( $\lambda_{\text{exc}} = 445 \text{ nm}, 520 \text{ nm}$ )	$\tau_1 = 0.04 \text{ ns}$ $\tau_2 = 0.41 \text{ ns}$ $\tau_3 = 2.90 \text{ ns}$

The spectral profiles of the film PL spectra are very different for all dyes (**Figure 98, right**). For **PDI**, the PL spectrum is clearly broadened around 550-800 nm, leading to less features than in solution. The PLQY remains relatively high at ~20%, which can be attributed to emission from intermolecular species. However, the biexponential PL decay ( $\tau_1 = 1.6 \text{ ns}$ ,  $\tau_2 = 5 \text{ ns}$ ) (**Table 8**) suggests that the nature of such emissive aggregates is heterogeneous and might be partially excimeric. Indeed, formation of excimers is supported by the literature on similarly stacked perylene bisimides.<sup>242-245</sup> Here, excimers can favor fast (sub-ns) charge separation/radical formation,<sup>246</sup> which is ultimately responsible for the unusually fast (~5 ns) excimer emission observed from PDI films.

**PDI-OMe** and **PDI-Encap** display low thin film PLQYs (< 1%) in-line with their low intrinsic solution PLQYs. Their weak film PL spectra therefore complicate unambiguous assignment of their spectral features. Nevertheless, it can be observed that the PL spectrum of **PDI-OMe** spectrum displays vibrational fine-structure and suppressed aggregate/excimer emission. This is attributed to the crystal packing observed for **PDI-OMe** (**Figure 97**), which prevents intermolecular interactions both in the ground state and the excited state. In contrast, the PL spectrum of **PDI-Encap** displays some fine structure but also a significantly broadened band at longer wavelengths. Therefore, as the film UV-Vis data and crystallographic analysis suggest that aggregation is greatly suppressed in **PDI-Encap**, the featured, yet broadened spectrum can likely be attributed to an admixture of  $\pi-\pi^*$  and ICT emission. This is also in agreement with the DFT data below.

### Theoretical DFT Calculations

The surprising photophysical properties of **PDI-OMe** and **PDI-Encap** were further investigated using DFT/time-dependent DFT (TD-DFT) calculations based on B3LYP/6-31G\*.<sup>247</sup> The gas phase optimized geometries of both dyes show that the highest occupied molecular orbital (HOMO) and lowest unoccupied molecular orbital (LUMO) are each delocalized across the core

of the PDI chromophore, while the first eight lower lying occupied molecular orbitals (HOMO-1 – HOMO-8) are all localized on the electron-rich peripheral benzene groups (**Figure 99**).

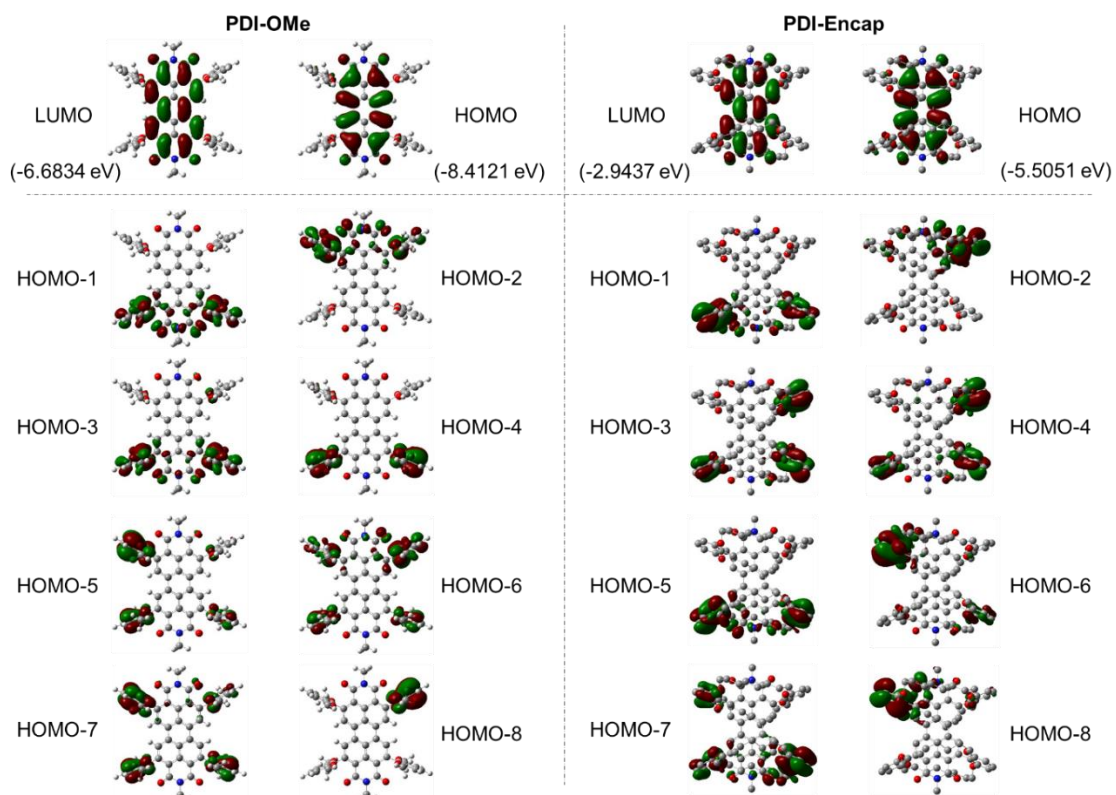


**Figure 99.** HOMO and LUMO distributions of **PDI-OMe** (left) and **PDI-Encap** (right), calculated using B3LYP/6-31G\*.

TD-DFT (**Table 9**) shows that the transitions to the 5 lowest singlet states of **PDI-Encap** can all be predominantly assigned to charge transfer from the peripheral aryl rings to the PDI core (HOMO-1-5 → LUMO), with no significant local excitation (HOMO→LUMO) of the PDI chromophore. This greatly contrasts with the data calculated for some highly emissive literature PDI derivatives.<sup>234</sup> For both **PDI** and an electron-withdrawn 2,5,8,11-benzonitrile substituted PDI (**PDI-PhCN**), the  $S_0 \rightarrow S_1$  transition is predominantly assigned to local excitation of the PDI chromophore (HOMO→LUMO) (**Table 10 & 11**). Therefore, we propose that fluorescence from the luminophoric PDI core of **PDI-Encap** and **PDI-OMe** is quenched by intramolecular charge transfer (ICT) between the electron-rich peripheral aryl groups and the PDI core.

To improve our understanding of the thin film PL results we also performed TD-DFT calculations on the crystal structure geometries. Here, we assume that the gas phase and crystal structures are more representative of the solution and thin film, respectively. For the gas phase optimized geometry of **PDI-Encap**, the lowest energy transition displaying a strong oscillator strength (*ca.* 0.42) is the local HOMO → LUMO  $\pi\text{-}\pi^*$  transition ( $S_0 \rightarrow S_6$ , **Table 9**). The same is predicted for **PDI-OMe** ( $S_0 \rightarrow S_3$ , **Table 12**). The data correlate well with the solution PL spectra, which display well-resolved vibronic fine structures (**Figure 98**).

**Table 9.** TD-DFT calculation for **PDI-Encap** in the gas phase.

No.	Transition	Energy (cm <sup>-1</sup> )	Wavelength (nm)	Osc. Strength	Orbital contributions	Dominant contribution
<b>1</b>	S <sub>0</sub> → T <sub>1</sub>	10622	941	0	HOMO → LUMO (95%)	$\pi \rightarrow \pi^*$
<b>2</b>	S <sub>0</sub> → T <sub>2</sub>	17286	579	0	H-2 → LUMO (80%), H-1 → LUMO (12%)	ICT
<b>3</b>	S <sub>0</sub> → T <sub>3</sub>	17382	575	0	H-5 → LUMO (16%), H-2 → LUMO (15%), H-1 → LUMO (62%)	ICT
<b>4</b>	S <sub>0</sub> → S <sub>1</sub>	17643	567	0.0003	H-2 → LUMO (82%), H-1 → LUMO (13%)	ICT
<b>5</b>	S <sub>0</sub> → S <sub>2</sub>	17723	564	0.0031	H-5 → LUMO (10%), H-2 → LUMO (15%), H-1 → LUMO (71%)	ICT
<b>6</b>	S <sub>0</sub> → T <sub>4</sub>	18219	549	0	H-4 → LUMO (34%), H-3 → LUMO (52%)	ICT
<b>7</b>	S <sub>0</sub> → S <sub>3</sub>	18270	547	0.0513	H-4 → LUMO (40%), H-3 → LUMO (35%), HOMO → LUMO (18%)	ICT
<b>8</b>	S <sub>0</sub> → S <sub>4</sub>	18588	538	0.0272	H-4 → LUMO (32%), H-3 → LUMO (58%)	ICT
<b>9</b>	S <sub>0</sub> → T <sub>5</sub>	18594	538	0	H-4 → LUMO (58%), H-3 → LUMO (39%)	
<b>10</b>	S <sub>0</sub> → T <sub>6</sub>	18893	529	0	H-5 → LUMO (77%), H-1 → LUMO (19%)	
<b>11</b>	S <sub>0</sub> → S <sub>5</sub>	19038	525	0.0259	H-5 → LUMO (79%)	ICT
<b>12</b>	S <sub>0</sub> → S <sub>6</sub>	19361	516	0.415	H-7 → LUMO (14%), H-4 → LUMO (17%), HOMO → LUMO (58%)	$\pi \rightarrow \pi^*$

**Table 10.** TD-DFT calculation for **PDI** in the gas phase.

No.	Transition	Energy (cm <sup>-1</sup> )	Wavelength (nm)	Osc. Strength	Orbital contributions	Dominant contribution
<b>1</b>	S <sub>0</sub> → T <sub>1</sub>	10037	996	0	HOMO → LUMO (99%)	$\pi \rightarrow \pi^*$
<b>2</b>	S <sub>0</sub> → S <sub>1</sub>	19719	507	0.6684	HOMO → LUMO (100%)	$\pi \rightarrow \pi^*$

**Table 11.** TD-DFT calculation for **PDI-PhCN** in the gas phase.

No.	Transition	Energy (cm <sup>-1</sup> )	Wavelength (nm)	Osc. Strength	Orbital contributions	Dominant contribution
<b>1</b>	S <sub>0</sub> → T <sub>1</sub>	10425	959	0	HOMO → LUMO (98%)	$\pi \rightarrow \pi^*$
<b>2</b>	S <sub>0</sub> → T <sub>2</sub>	18983	527	0	H-1 → LUMO (91%)	ICT
<b>3</b>	S <sub>0</sub> → T <sub>3</sub>	19208	521	0	H-2 → LUMO (91%)	ICT
<b>4</b>	S <sub>0</sub> → S <sub>1</sub>	19461	514	0.6791	HOMO → LUMO (100%)	$\pi \rightarrow \pi^*$

The contrast is greater between the TD-DFT data obtained for the crystal structure geometries of **PDI-Encap** and **PDI-OMe**. For **PDI-OMe**, the gas phase and crystal structure geometries are very similar (**Table 12 & 13**), meaning the lowest energy transition with a strong oscillator strength (*ca.* 0.34, S<sub>0</sub> → S<sub>4</sub>, **Table 13**) is  $\pi-\pi^*$  in nature. Therefore, the spectral features of the PL

for **PDI-OMe** are very similar in solution and film (**Figure 98**). This is in contrast with **PDI-Encap**. While the lowest energy  $\pi-\pi^*$  transition ( $S_0 \rightarrow S_5$ , **Table 14**) retains the gas phase oscillator strength (*ca.* 0.48) and approximate energy in the crystal structure geometry of **PDI-Encap**, an ICT transition ( $S_0 \rightarrow S_3$ , **Table 14**) at lower energy with a high oscillator strength (*ca.* 0.19) is also predicted. The additional ICT character therefore likely translates to the broad, low energy PL band that is observed for the thin film of **PDI-Encap**.

**Table 12.** TD-DFT calculation for **PDI-OMe** in the gas phase.

No.	Transition	Energy (cm <sup>-1</sup> )	Wavelength (nm)	Osc. Strength	Orbital contributions	Dominant contribution
<b>1</b>	$S_0 \rightarrow T_1$	10549	948	0	HOMO → LUMO (97%)	$\pi \rightarrow \pi^*$
<b>2</b>	$S_0 \rightarrow T_2$	17697	565	0	H-1 → LUMO (94%)	ICT
<b>3</b>	$S_0 \rightarrow T_3$	17778	562	0	H-2 → LUMO (94%)	ICT
<b>4</b>	$S_0 \rightarrow S_1$	18497	541	0.0001	H-1 → LUMO (98%)	ICT
<b>5</b>	$S_0 \rightarrow S_2$	18566	539	0.0516	H-2 → LUMO (97%)	ICT
<b>6</b>	$S_0 \rightarrow T_4$	18827	531	0	H-8 → LUMO (34%), H-3 → LUMO (50%)	ICT
<b>7</b>	$S_0 \rightarrow S_3$	19201	521	0.4284	H-4 → LUMO (14%), HOMO → LUMO (84%)	$\pi \rightarrow \pi^*$

**Table 13.** TD-DFT calculation for **PDI-OMe** in crystal form.

No.	Transition	Energy (cm <sup>-1</sup> )	Wavelength (nm)	Osc. Strength	Orbital contributions	Dominant contribution
<b>1</b>	$S_0 \rightarrow T_1$	10235	977	0	HOMO → LUMO (96%)	$\pi \rightarrow \pi^*$
<b>2</b>	$S_0 \rightarrow T_2$	17093	585	0	H-2 → LUMO (26%), H-1 → LUMO (63%)	
<b>3</b>	$S_0 \rightarrow S_1$	17583	569	0.0077	H-2 → LUMO (12%), H-1 → LUMO (76%)	ICT
<b>4</b>	$S_0 \rightarrow T_3$	18550	539	0	H-6 → LUMO (11%), H-3 → LUMO (23%), H-2 → LUMO (41%), H-1 → LUMO (17%)	ICT
<b>5</b>	$S_0 \rightarrow T_4$	18568	539	0	H-7 → LUMO (15%), H-3 → LUMO (45%), H-2 → LUMO (19%), H-1 → LUMO (12%)	ICT
<b>6</b>	$S_0 \rightarrow S_2$	18764	533	0.0802	H-2 → LUMO (71%), HOMO → LUMO (15%)	ICT
<b>7</b>	$S_0 \rightarrow S_3$	18974	527	0.0008	H-3 → LUMO (85%)	ICT
<b>8</b>	$S_0 \rightarrow S_4$	19259	519	0.3373	H-4 → LUMO (28%), H-1 → LUMO (11%), HOMO → LUMO (47%)	$\pi \rightarrow \pi^*$

**Table 14.** TD-DFT calculation for **PDI-Encap** in crystal form.

No.	Transition	Energy (cm <sup>-1</sup> )	Wavelength (nm)	Osc. Strength	Orbital contributions	Dominant contribution
<b>1</b>	S <sub>0</sub> → T <sub>1</sub>	9863	1014	0	H-2 → LUMO (25%), HOMO → LUMO (73%)	ICT
<b>2</b>	S <sub>0</sub> → T <sub>2</sub>	16317	613	0	H-1 → LUMO (97%)	ICT
<b>3</b>	S <sub>0</sub> → T <sub>3</sub>	16376	611	0	H-2 → LUMO (72%), HOMO → LUMO (25%)	ICT
<b>4</b>	S <sub>0</sub> → S <sub>1</sub>	16425	609	0.0014	H-1 → LUMO (85%)	ICT
<b>5</b>	S <sub>0</sub> → S <sub>2</sub>	16428	609	0.0085	H-2 → LUMO (51%), H-1 → LUMO (13%), HOMO → LUMO (34%)	ICT
<b>6</b>	S <sub>0</sub> → T <sub>4</sub>	17976	556	0	H-3 → LUMO (85%)	ICT
<b>7</b>	S <sub>0</sub> → T <sub>5</sub>	18289	547	0	H-6 → LUMO (10%), H-4 → LUMO (85%)	ICT
<b>8</b>	S <sub>0</sub> → S <sub>3</sub>	18574	538	0.1876	H-4 → LUMO (52%), H-2 → LUMO (20%), HOMO → LUMO (23%)	ICT
<b>9</b>	S <sub>0</sub> → S <sub>4</sub>	18579	538	0.0045	H-3 → LUMO (92%)	ICT
<b>10</b>	S <sub>0</sub> → S <sub>5</sub>	19064	525	0.4794	H-4 → LUMO (37%), H-2 → LUMO (18%), HOMO → LUMO (35%)	π → π* & ICT

To further differentiate between **PDI-OMe** and **PDI-Encap**, the low frequency vibration modes (< 20 cm<sup>-1</sup>) of both molecules (**Figure 100 & 101**) were analyzed. While **PDI-OMe** has 6 different low frequency vibration modes which are mainly attributed to the peripheral aryl rings, **PDI-Encap** only has 3 modes, which are caused by vibrations in the alkylene straps. Therefore, the data suggest that there is a higher rate of non-radiative decay for **PDI-OMe** than for **PDI-Encap**, which agrees with what can be reasonably inferred from the fluorescence lifetime data. In other words, the encapsulating straps are preferred over bulk.

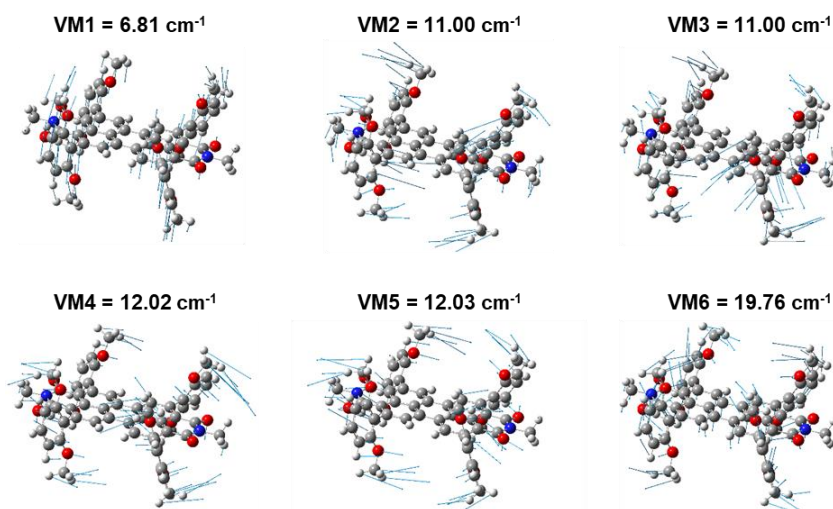


**Figure 100.** Low frequency vibration modes (VMs) of **PDI-OMe** in the optimized gas phase.

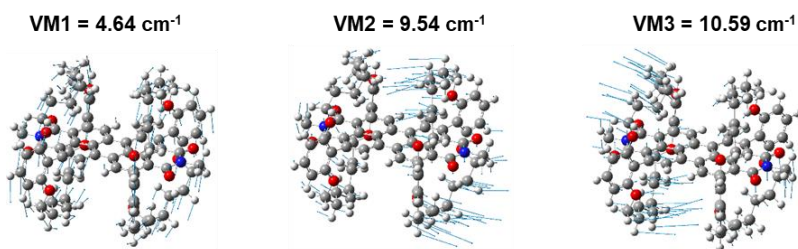


**Figure 101.** Low frequency vibration modes (VMs) of **PDI-Encap** in the optimized gas phase.

## Conclusions

Our strategy is successful at preparing novel encapsulated PDI dyes and suppressing intermolecular  $\pi$ - $\pi$  interactions in both solution and the solid-state. Furthermore, as opposed to bulk strategies, we discovered that covalent encapsulation provides additional benefits as it can be used to rigidify molecular architectures and potentially direct solid-state packing or 3D crystal growth. However, we should also note that the encapsulation strategy used electron-rich peripheral aryls, which introduced charge transfer character and thereby led to photoluminescence quenching. Therefore, this work highlights both the power of encapsulation as a synthetic tool for chromophore control but also their potential non-innocence with regards to underlying photophysical properties.

# Chapter V

## Through-Space Polymers: Part 1

### Introduction

In the previous chapters, we have seen that conjugated polymer strands or molecules can be spatially separated using encapsulating alkylene straps. However, the exact distance between different polymer chains remains very difficult to control. Therefore, in this chapter we would like to further extend the use of this encapsulation strategy to control the distance or orientation between two building blocks, which can be of great interest in the field of organic photovoltaics.

The donor-acceptor interface (photoactive layer, **figure 102**) is the most important part of organic bulk heterojunctions (organic photovoltaics; OPVs) as it dictates the efficiencies of charge generation and recombination.<sup>164,248</sup> Consequently, parameters such as the distance and relative orientation of the interfacial donor and acceptor components can dramatically influence the performance of optoelectronic devices (e.g., OLEDs, photodetectors and OPVs).<sup>165</sup> However, in typical donor-acceptor polymer blends there is very limited structural control over the interface as their preparation (nanoscale blending) leads to numerous, random donor-acceptor configurations. The exact configuration is therefore exceedingly difficult to deconvolute, which in turn limits our understanding and makes the design of highly efficient OPVs extremely challenging.<sup>164</sup> To further advance organic photovoltaics, it is therefore extremely important to gain a deeper understanding on the nature of the donor-acceptor interface and how to precisely control or manipulate it.

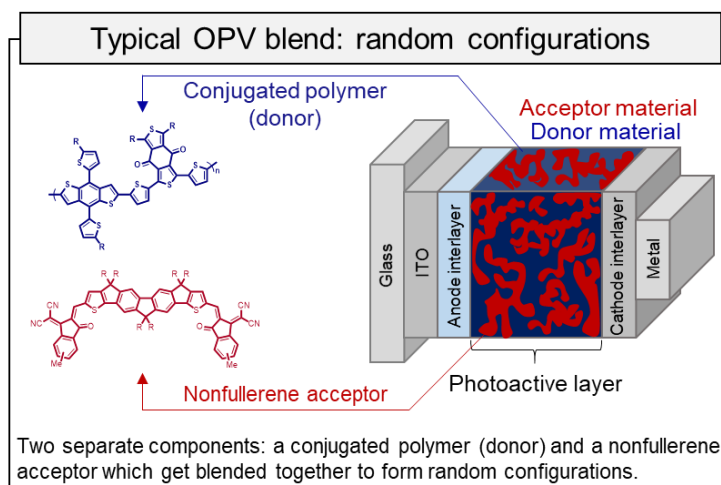


**Figure 102.** General OPV device structure with typical, representative materials in the photoactive layer.

However, despite significant efforts, it remains extremely challenging to develop materials with fixed geometries or obtain different geometries between the same materials. Past studies have

therefore often had to compromise and compare one “pure” orientation with a mixed orientation. In fact, until recent (~2017) there has not been a single report in which two truly isolated and different orientations (e.g., face-on versus edge-on) in one material system could be obtained and studied.<sup>248</sup> Consequently, very little is known about the origin of nonradiative recombination in OPVs, its relation to different geometries or orientations and how to overcome or suppress it.

One of the first studies that showed control over the molecular orientations in OPV materials was reported by Nguyen and coworkers.<sup>248</sup> Here, they fabricated “well-defined interfaces of known molecular orientation” and studied their resulting OPV device performance (**Figure 103**). First, polymer (**p-SIDT(FBTTh<sub>2</sub>)<sub>2</sub>**) was casted from a chlorobenzene solution to form predominantly the face-on conformation (the ratio was 99.5:0.5 for face-on to edge-on), as evidenced by GIWAXS experiments. When the polymer was casted from chlorobenzene with 4 % (v/v), on the other hand, the polymer took on the edge-on conformation (94:6 edge-on to face-on). Both polymer conformations were compared through OPV devices.

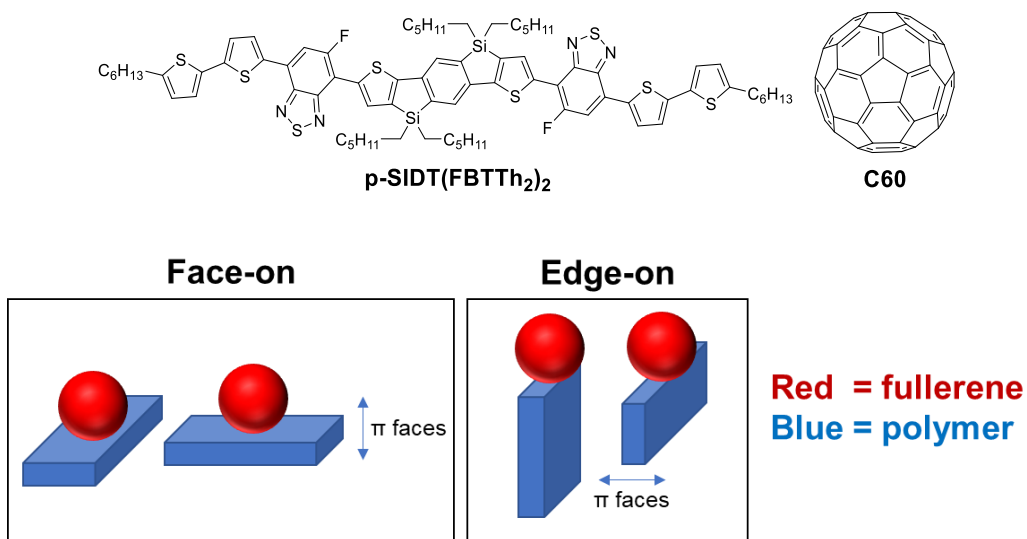


**Figure 103.** Structure of polymer **p-SIDT(FBTTh<sub>2</sub>)<sub>2</sub>** designed by Nguyen and coworkers (top).<sup>248</sup> Cartoon representation of the face-on and edge-on orientations (bottom).

Their results show that devices with the face-on orientation led to higher radiative efficiencies and open circuit voltages ( $V_{OCs}$ ), which is attributed to the formation of a higher charge transfer (CT) state energy and less nonradiative recombination. In contrast, devices with the edge-on conformation afforded a more efficient charge generation and thereby higher internal quantum efficiencies (IQEs). This is turn is caused by the lower activation energy for charge generation as well as the reduced electronic coupling between ground state (GS) and charge transfer (CT) states.<sup>248</sup> The results therefore indicate that the differences in morphology or orientation can indeed dramatically impact their OPV device performance. However, a clear preference of one orientation over the other could not be provided at this point. Instead, the authors propose improvements for both type of orientations to achieve high-performance OPVs. For the face-on

orientation, which has good radiative efficiencies, geminate recombination should be reduced by limiting the electronic coupling, whereas for the edge-on orientation, the charge generation is efficient, but more research needs to be done to improve the radiative efficiencies. This study therefore not only shows the importance of orientations in optoelectronic devices, but also highlights its great complexity and demand for novel synthetic design strategies.

Another very interesting, but different study was reported by McGehee and coworkers.<sup>165</sup> Here, they investigated what happens if you change the relative orientation between a fullerene acceptor and a donor-acceptor polymer (i.e., whether the fullerene sits on top of the donor or acceptor part of the polymer backbone) (**Figure 104**). The fullerene unit was forced onto the two respective locations by incorporating more bulk (branched vs linear alkyl chains) on either the acceptor or donor unit, as evidenced by NMR spectroscopy. Interestingly, upon testing both orientations in OPV devices, it was found that the (A-A) system which lets the fullerene dock on the polymer acceptor unit, greatly outperformed the other (A-D) system, reaching PCE's of 6-8% (vs only 1.7%). Therefore, this work suggests that to achieve high-performance OPVs, it is important to control or obtain the preferred intermolecular orientation at the interface. However, due to the dynamic, intermolecular nature of this system, it remains difficult to gain full control over where the fullerene resides. Furthermore, the importance of various molecular or structural factors on charge separation are not fully established, which complicates the design of efficient OPV materials.<sup>165</sup>

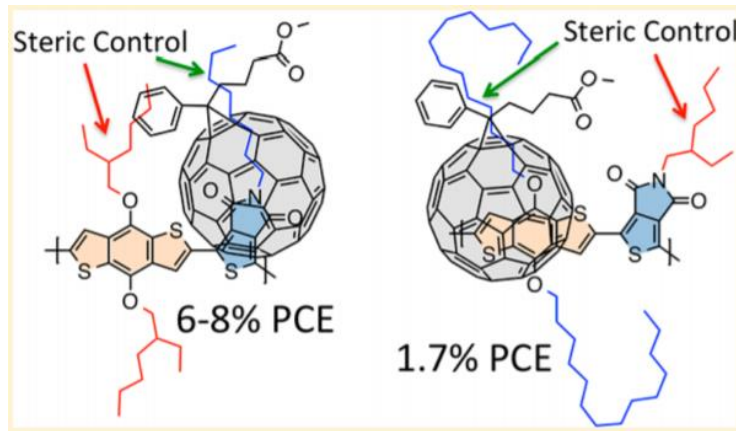


**Figure 104.** Fullerene/polymer system reported by McGehee and coworkers.<sup>165</sup>  
Copyright © 2014 American Chemical Society.

The following section will outline a few methods that have been used to study CT states. In 2017, Friend, Rao and co-workers showcased a novel technique used to study the local energetic landscape and electronic dynamics at and near the interface.<sup>249</sup> The authors make use of an ultrafast pump-push-probe technique that measures the electro-absorption signal caused by electron-hole pairs generated across the interface of p- and n-type materials, thereby allowing them to map the local energetic landscape of charges moving away from the interface.

In regular time-resolved optical pump-probe spectroscopic methods the sample first gets excited by a laser pulse to form excitons/charges and then interrogated by a probe pulse to measure the change in absorption (or transmission) generated by the pump pulse.<sup>249</sup> Excited states generated by the pump pulse correspond to a lower ground-state population, thereby leading to a ground-state bleach (GSB) in absorption. All excited states have a photo-induced absorption (PIA) feature, whereas initial excitations can also contribute through stimulated emission (SE). The regular pump-probe (PP) method therefore provides useful information on the specific site or chromophore being probed, and not on neighbouring areas (**Figure 105 c**). Furthermore, as the gathered information is based only on whichever site/chromophore the excitation is located on, these methods do not allow any interface specificity. The authors therefore demonstrate a way of obtaining more information based on the latter two points, using a novel pump-push-probe (PPP) technique.<sup>249</sup>

Here, they postulate that as excitons dissociate at the interface of p- and n-type materials (or the p-n junction), the electron-hole pairs can act as a local dipole and therefore influence surrounding molecules by creating an external electric field (i.e., the Stark effect). This effect consequently changes the absorption spectra of the neighbouring molecules, typically resulting in an absorption redshift (due to a decreased optical absorption gap). The difference between the absorption spectra (with and without electric field) is referred to as electroabsorption (EA) (**Figure 105 b**),<sup>250</sup> and can be tracked as a function of time at the interface. When the exciton separates across the interface, the electric field will change and thus become time-dependent, thereby leading to a time-dependent Stark shift and EA signal.<sup>249</sup> This means that the separation of the electron-hole pair can be tracked on femtosecond timescales by monitoring the dynamic EA signals.<sup>251</sup> Furthermore, it provides insights into the energetic landscape that the charges experience as they migrate.

The main difference is therefore the addition of a third “push” to generate cleaner EA signatures on more localized areas. In the PPP experiment, a pump pulse excites the material to form excitons across the donor-acceptor interface. This is followed by a time-delayed push pulse, which excites hole polarons and briefly delocalizes them. The holes then relax or jump onto neighbouring polymer chains. Therefore, the push pulse makes the hole move further away, which consequently alters the local potential (or electric field distribution) of the electron-hole pair (**Figure 105 d**).<sup>249</sup> The difference in EA signals between the regular pump-probe (PP) method, and the novel pump-push-probe (PPP) technique (so with and without push) therefore provides the missing/additional information (**Figure 105 e**). In fact, the subtracted EA signal reports only on the few molecules that are affected by the change in electric field caused by the movement of the charges and therefore provides spatial resolution.

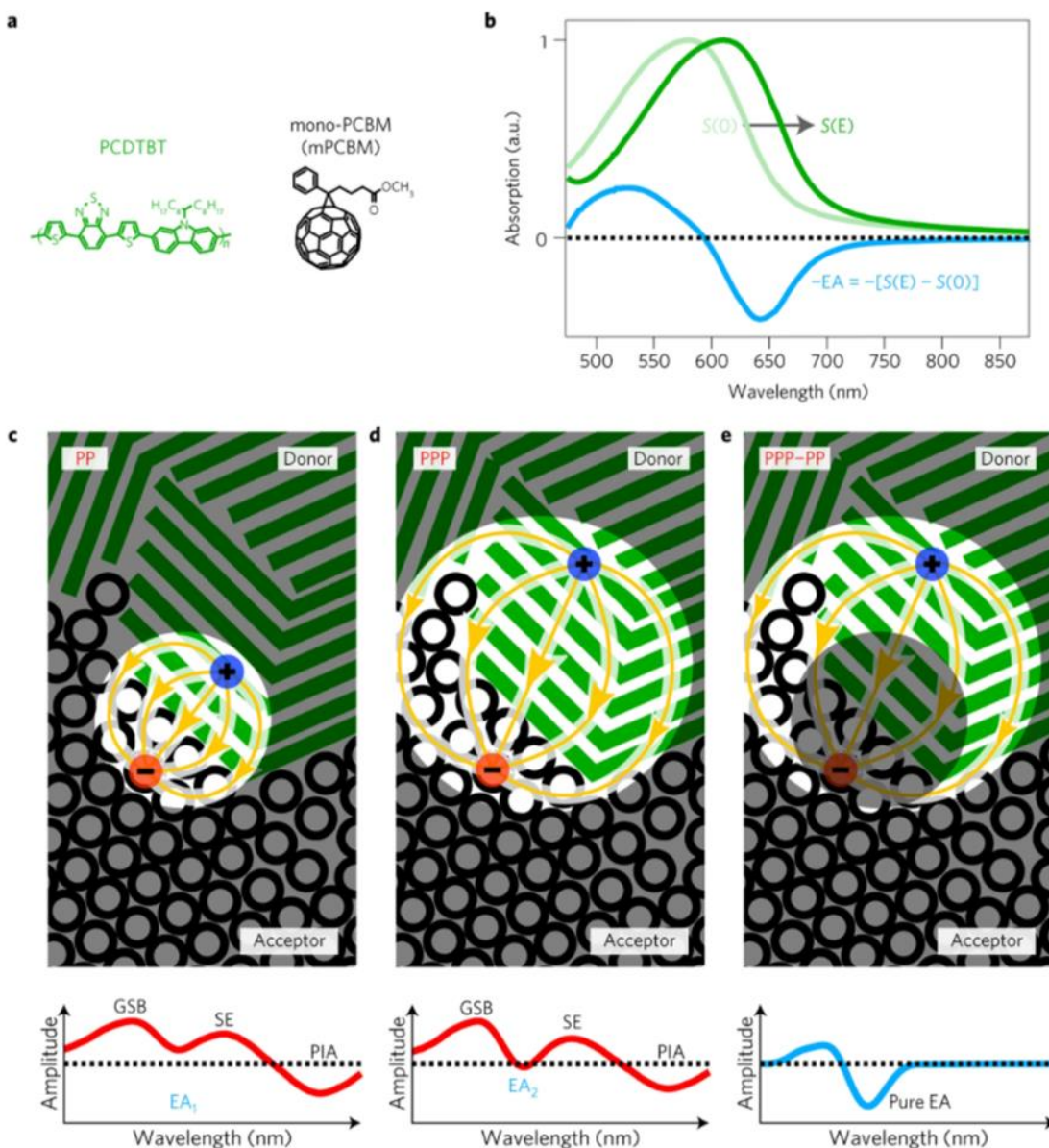


**Figure 105.** The origin of electroabsorption (EA) signals in PP and PPP measurements.<sup>249</sup> a) Chemical structure of PCDTBT and mPCBM. b) Spectral representation of the electroabsorption signal, as indicated by the difference in the ground-state  $S(0)$  absorption and the shifted absorption in the presence of an electric field  $S(E)$ . The electroabsorption signal is flipped in sign for an easier/more clear demonstration. c) States probed by the PP technique (top) and a qualitative spectrum (bottom) indicating the different components. While the ground-state bleach (GSB), stimulated emission (SE) and photo-induced absorption (PIA) all relate to the site occupied by the electron and hole, the electroabsorption feature is specific to the molecules that are influenced by the electric field (in the bright circle). d) States probed by the PPP technique, indicating the increased distance between the electron-hole pair as a result of the push pump. The spectral profile (at bottom) shows an increase in the EA signal (denoted  $EA_2$ ) compared to the prior situation. e) The difference/subtraction of the two techniques (PPP-PP) indicated by the brightened area, from which a clean EA signal, near the interface, can be retrieved. © 2017 Macmillan Publishers Limited, part of Springer Nature.

Their technique was used to study the differences between a 4:1 and 1:4 blend of PCDTBT and mPCBM (Structures in **Figure 105 a)**). The 1:4 blend is known to give the best OPV performance, with charge collection quantum yields approaching 100%,<sup>252</sup> whereas the 4:1 blend efficiently generates excitons, but has an inefficient long-range charge separation. Their study revealed that in the unoptimized 4:1 blend, charges are formed at the lowest energy sites, but that further migration away from the interface is energetically unfavourable (or uphill), which leads to low

external quantum efficiencies (EQEs) and high recombination of the electron-hole pair.<sup>249</sup> In contrast, the optimized 1:4 blend has favourable interfacial energetics, meaning that the hole polarons rapidly migrate from higher energy interfacial sites to more stable, ordered sites and should therefore help overcome the Coulombic interaction of the electron-hole pair. Understanding the energetic landscape at and around the interface is therefore key to explain the difference in performance between the two different blends. This novel PPP technique is therefore extremely useful, and as opposed to conventional optical, photoelectron or X-ray techniques, it is not restricted to CT states at/near the surface of the sample but can also provide (for the first time) information on CT states that are “buried” inside the bulk material.

A study by Baldo et al. demonstrates the use of imaging techniques to study the dynamics of CT states in a donor-acceptor blend of m-MTDATA and 3TPYMB (**Figure 106**).<sup>253</sup> The blend heterostructure was amorphous with highly fluorescent, localized, and long-lived CT states (~μs), and therefore allowed them to study the CT state dynamics. Furthermore, the blend has an external quantum yield of photocurrent generation of 34% and an internal quantum efficiency (IQE) of 40%,<sup>254</sup> and therefore served as a representative example to investigate the underlying mechanisms that drive charge dissociation.<sup>253</sup> Here, they made use of an optical microscope, connected to a scanning detector, to monitor CT state diffusion in time and space. The diffusion of the CT states is characterized by spatially imaging the transient photoluminescence. The resulting data was compiled to generate a 3D image containing the position (x-axis), time (y-axis) and intensity (z-axis) of the CT state. By doing so, the authors discovered that the CT states in the m-MTDATA:3TPYMB blend move over distances of 5-10 nm before settling into lower energy CT states. Furthermore, they showed that there was a variation in the spacing between the electron and hole during transport, as described by an inchworm-like stretching motion. The combination of imaging techniques and simulations can therefore provide additional understanding on the dynamics of CT states and help identify the optimum trade-off between diffusion and trapping. It would therefore be very insightful to apply this method to materials with different geometries.

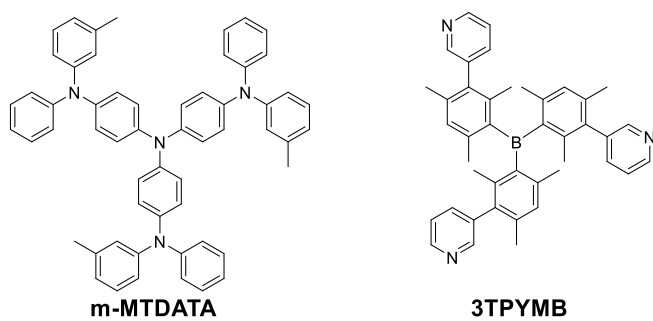


**Figure 106.** Structure of the materials used in Baldo's study.<sup>253</sup>

Lastly, due to the complexity of the interface, researchers have also had to resort to calculating/estimating the interface using DFT computations.<sup>255,256</sup> Although, modelling can be

very insightful to explain certain results, such computations remain an educated guess of what the interfacial structure looks like in real life. Therefore, we strongly believe there is a great demand for novel synthetic tools to engineer precise structures.

## Project Objectives

In this chapter, we want to demonstrate that through synthetic control (i.e., by using covalent straps) the molecular orientation of the donor and acceptor components can be precisely engineered, thereby providing a clear picture of the exact interfacial structure. It is therefore hoped that this model system can be used to study how subtle changes in the structure or orientation can influence the optoelectronic properties and overall device performance. Furthermore, it can potentially be used to investigate how certain distances between the donor and acceptor interface or rigidifications of the straps alter their performance. Having great control over the donor-acceptor interface should therefore provide lots of fundamental understanding, which can help pave the way towards next-generation photovoltaic materials or devices.

The model system proposed in this section is based on a perylene diimide (PDI) acceptor and a benzodithiophene (BDT) polymer. PDI non-fullerene acceptors (NFAs) and BDT conjugated polymers are both commonly used as OPV materials and were therefore selected for this research. A few representative examples of PDI based NFAs<sup>257–259</sup> and BDT based polymers<sup>260–262</sup> are shown in **figure 107**.

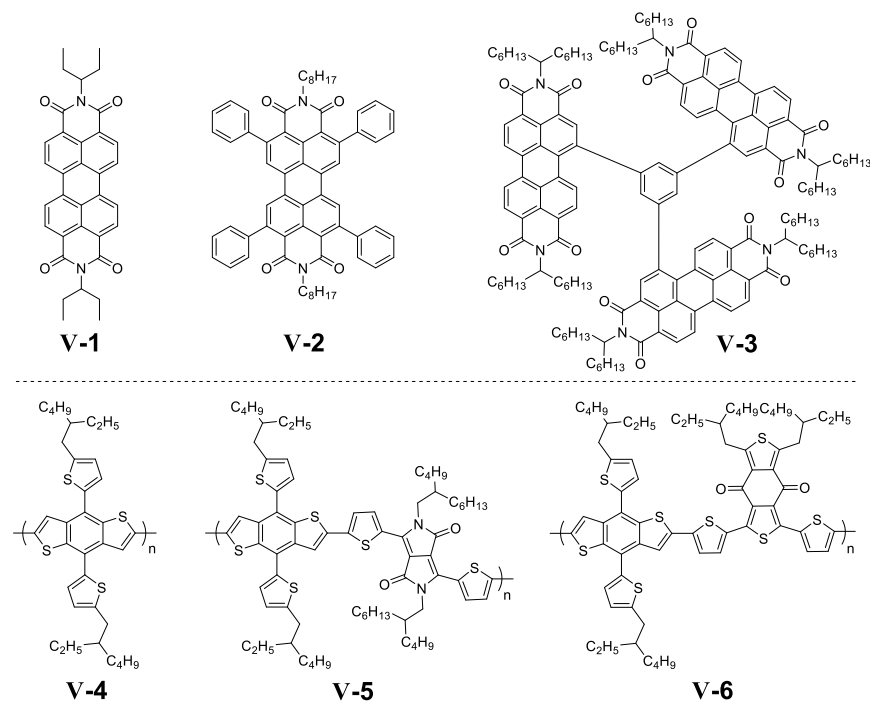


**Figure 107.** Previous examples of PDI NFAs (**V1-3**) and BDT donor polymers (**V4-6**) used in OPVs.<sup>257–262</sup>

## Synthetic Design & Characterization

In the past, scientists have shown that small molecules can be strapped together in a face-to-face fashion, as shown in **figure 108**.<sup>263–265</sup> It should therefore be noted that these studies were an inspiration to the work presented in this chapter.

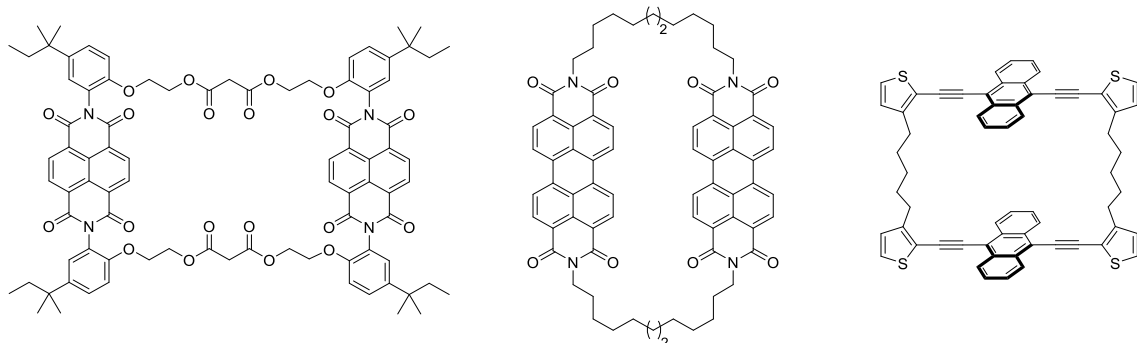


**Figure 108.** Examples of different through-space systems developed in the past.<sup>263–265</sup>

This chapter focusses on the synthetic design of a novel through-space polymer system that can potentially be used to study the donor-acceptor interface in more detail. The first through-space target polymer is seen in **figure 109**. As observed, **TS-P1** is composed of two main components: a perylene diimide (PDI) non-fullerene acceptor (in orange) and a benzodithiophene (BDT) donor polymer (in blue).

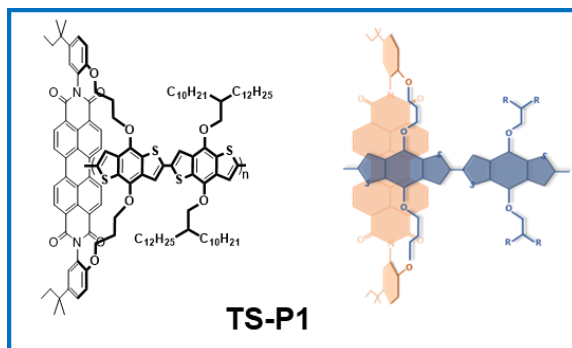


**Figure 109.** Chemical structure and cartoon representation of the through space polymer **TS-P1**.

The synthesis of the through space monomer (**TS-M1**) is shown in **figure 110**. First, **BDT-Q** is reacted with a THP protected propyl bromide chain under basic conditions to form **BDT-THP** in a near quantitative yield (98%). The THP protecting group was selected so it could withstand treatment with base. Next, it was lithiated using n-BuLi and quenched with CBr<sub>4</sub> to form corresponding brominated product; **Br<sub>2</sub>-BDT-THP** in 39%. The THP group was then removed using acidic (PPTS) conditions and transformed into a tosyl leaving group with *p*-toluenesulfonyl chloride and triethylamine. **Br<sub>2</sub>-BDT-OH** and **Br<sub>2</sub>-BDT-OTs** were obtained in 59% and 67% yield, respectively. Meanwhile, **PDI-Diol** was prepared from **PDA** and 2-amino-4-tert-amylphenol using an imidazole melt, after which it was treated with **Br<sub>2</sub>-BDT-OTs** in dilute,

basic conditions to afford **TS-M1** in 56% yield. The dilute conditions were used to minimize potential polymeric side products arising from concentration-dependent, incorrect stoichiometries.

Successful formation of the through space monomers was confirmed using NMR spectroscopy and mass spectrometry. It was also attempted to grow single crystals for X-ray crystallography using the solvent layering technique; however, this was unsuccessful. The proton assignment and corresponding NMR for **TS-M1** are shown in **figure 111 & 112**. As observed, the most deshielded protons (a – d) belong to the *ortho* and *bay* positions of the PDI core. However, interestingly the  $^1\text{H}$  NMR spectrum shows four different environments, indicating there are two different environments for both the *ortho* and *bay* protons. In regular, symmetrical *N,N*-dialkylated PDI molecules you would only see two environments of four protons each (one *ortho* and one *bay* environment). The extra environments in **TS-M1** are therefore likely attributed to through space H –  $\pi$  interactions between the PDI and BDT cores. The next three signals (e – g) belong to the aniline component, each corresponding to two protons, as expected. The singlet at ~6.5 ppm (h) has two protons and corresponds to the only aromatic proton on the BDT segment. Next, there are two -OCH<sub>2</sub>- signals (i, j and k,m) which are both split due to anisotropy arising from the through-space arrangement of the molecule. This is further corroborated by a HSQC experiment, which clearly shows that in both cases the anisotropic protons are attached to the same carbon. The remaining methylene group between the methoxies are assigned to signal n and integrate to four protons. The final three signals (o – q) belong to the alkyl chain on the aniline, and their multiplicities and integrations are also in line with the expectations.

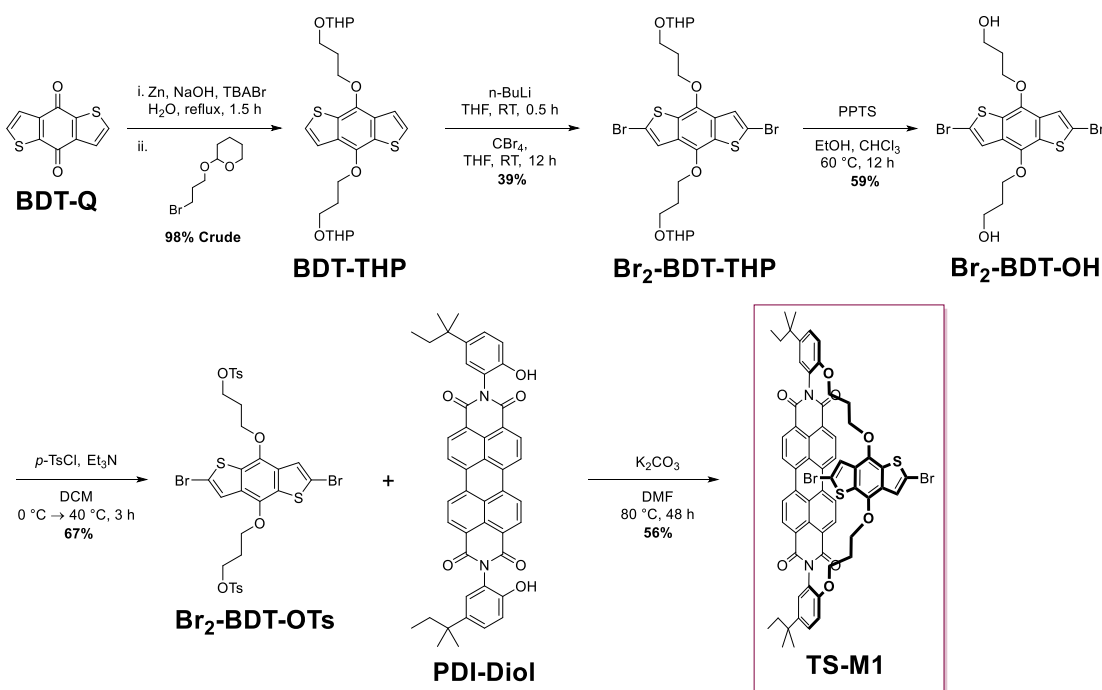


**Figure 110.** Synthesis of through space monomers **TS-M1**.

The through space (**TS-P1**) and reference (**Ref-P1**) polymer (**Figure 113**) were prepared following a traditional Stille cross coupling reaction for DPP or BDT comonomers. All polymers were obtained in respectable number average molecular weights ( $M_n$ ) of above 14 kDa (**Table 15**) and display good solubilities in common organic solvents. The relatively large difference in molecular weights between the reference and through space polymer is likely attributed to the additional steric hindrance caused by the through-space PDI unit.

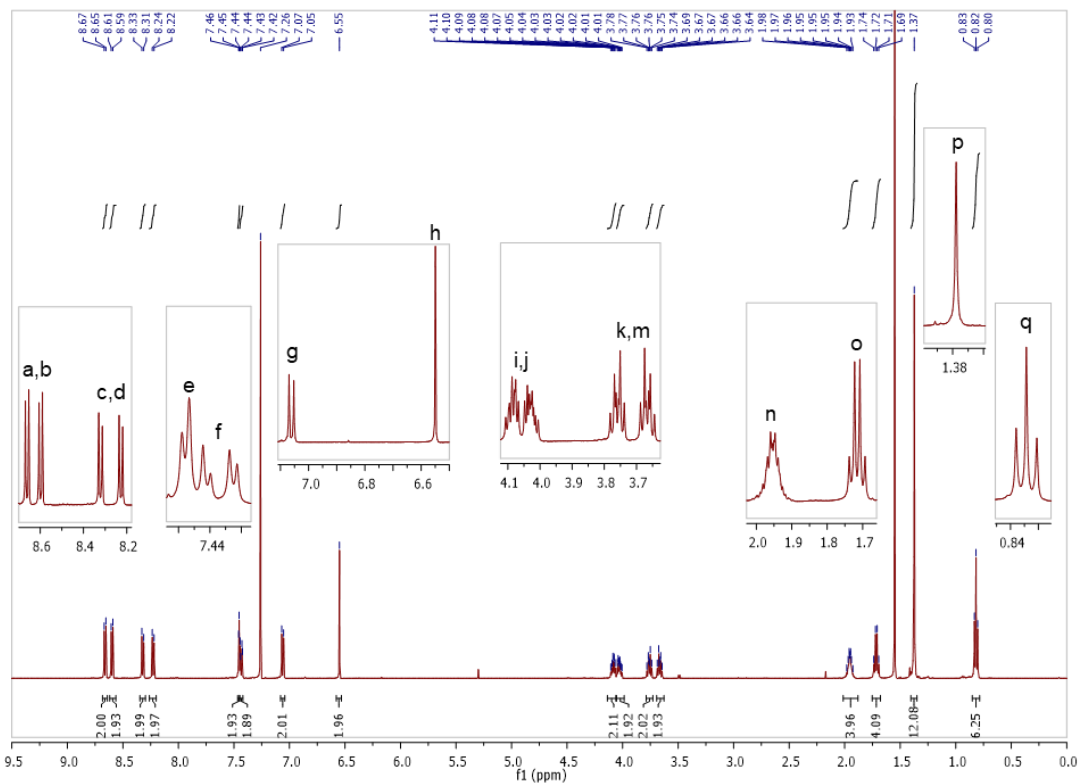


**Figure 111.**  $^1\text{H}$  NMR spectrum of TS-M1.

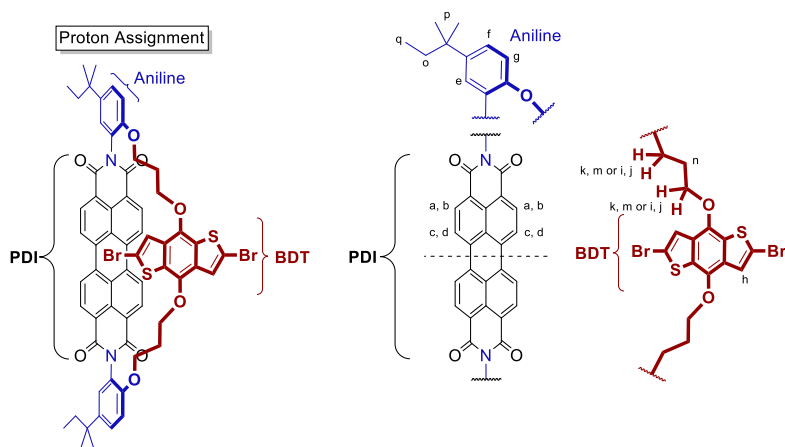


**Figure 112.**  $^1\text{H}$  NMR assignment of TS-M1.

**Table 15.** Physical properties of **Ref-P1** and **TS-P1**.

Polymer	Yield (%)	M <sub>n</sub> (kDa)	M <sub>w</sub> (kDa)	PDI
<b>Ref-P1</b>	89	63.1	232.5	3.68
<b>TS-P1</b>	91	14.8	48.8	3.30

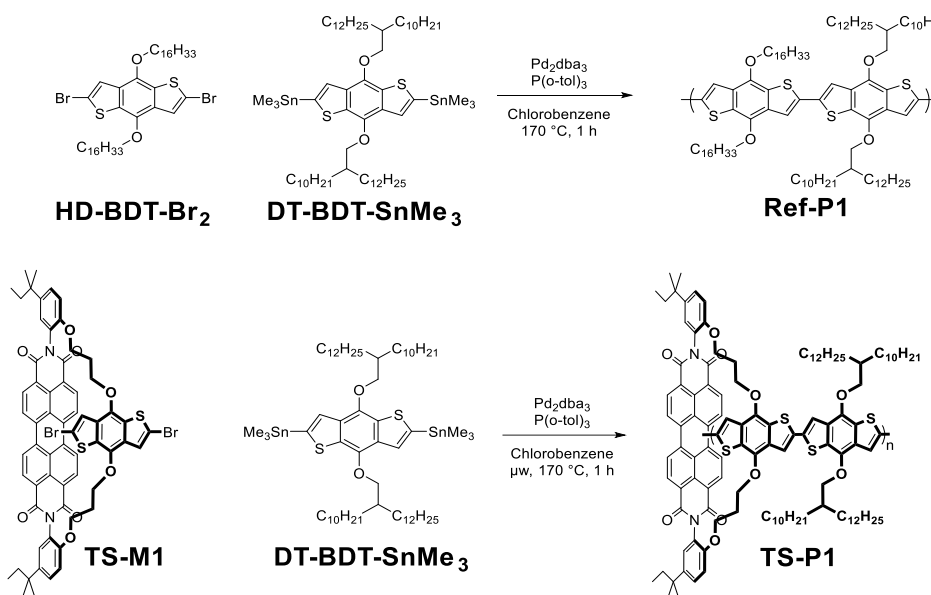


**Figure 113.** Synthesis of reference polymer **Ref-P1** and through space polymer **TS-P1**.

## Results & Discussion

### Photophysical Results

The solution and thin film absorption and emission spectra of the through space and reference polymer are shown in **figure 114** and summarized in **table 16**. Starting with **Ref-P1**, the solution absorption and emission profiles display a characteristic mirror image that is established for rigid luminophores that emit from  $\pi-\pi^*$  states. The three vibronic bands, in the solution absorption spectrum, are resolved clearly at  $\sim 460$ ,  $\sim 480$ , and  $\sim 525$  nm ( $\lambda_{\text{max}}$ ), corresponding to the 0-2', 0-1', and 0-0' transitions, respectively. The vibronic bands in the solution emission are at  $\sim 520$  ( $\lambda_{\text{max}}$ ),  $\sim 560$ , and  $\sim 615$  nm. In film, the absorption spectrum looks very similar compared to solution and is only red shifted by  $\sim 15$  nm. Although the profile looks slightly broadened, the features remain very pronounced. The film emission is more red shifted than in solution. However, the shift looks exaggerated due to the change in the relative intensities of the 0'-0 and 0'-1 transitions compared to solution.

**Table 16.** Summary of the photophysical data of Ref-P1 and TS-P1. \*Signal too weak to detect.

Sample	$\lambda_{\text{max,abs}}$ (nm)	$\lambda_{\text{max,em}}$ (nm)
Ref-P1 in CHCl <sub>3</sub>	525	520
Ref-P1 Film	540	650
TS-P1 in CHCl <sub>3</sub>	500	510
TS-P1 Film	540	/*

Overall, **TS-P1** has a strong resemblance with **Ref-P1** in both solution and thin film spectra. The solution absorption of **TS-P1** is slightly blue-shifted, with a  $\lambda_{\text{max}}$  at ~500 nm. Furthermore, there is a slight shoulder at 530 nm, which was not there in the spectrum of **Ref-P1** and is most likely attributed to the presence of the PDI component (as it absorbs in that region). The solution emission profiles of **TS-P1** and **Ref-P1** look very similar. The film absorption profiles also closely match each other, with no major visible differences. Lastly, the film emission spectrum of **TS-P1** could not be obtained with our spectrometer given its relatively low film photoluminescence. It should however be noted that the photoluminescence generated by **TS-P1** decreased over a 100-fold (compared to **Ref-P1**) under the same settings (also demonstrated in **picture 1**).

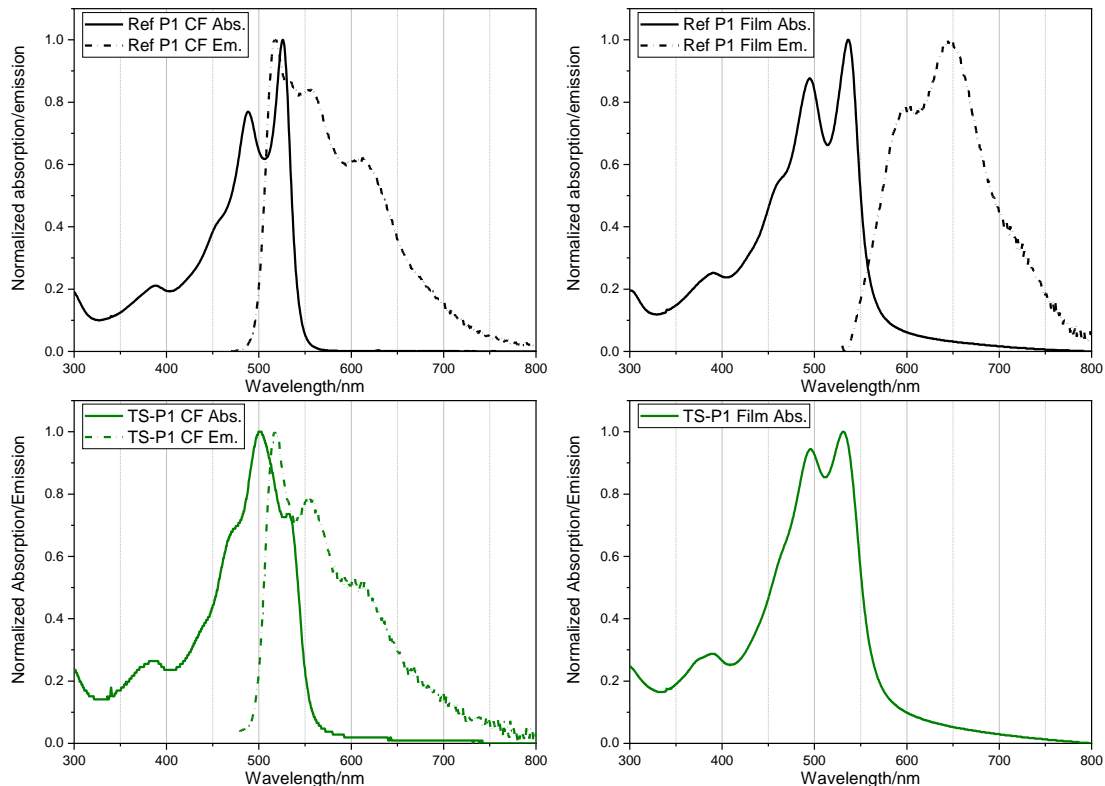


**Figure 114.** UV-Vis absorption and emission spectra for **Ref-P1** (in black) and **TS-P1** (in green).



**Picture 1.** A dilute solution of **Ref-P1** (left) and **TS-P1** (right) under UV light.

### Computational Results

Next, the HOMO and LUMO level and distributions were calculated via DFT using the B3LYP/6-31G\* dataset (**Figure 115**). As observed, the HOMO is localized over the BDT polymers, whereas the LUMO is localized over the PDI core. The through-space model polymer should therefore behave like a “true” charge transfer state.

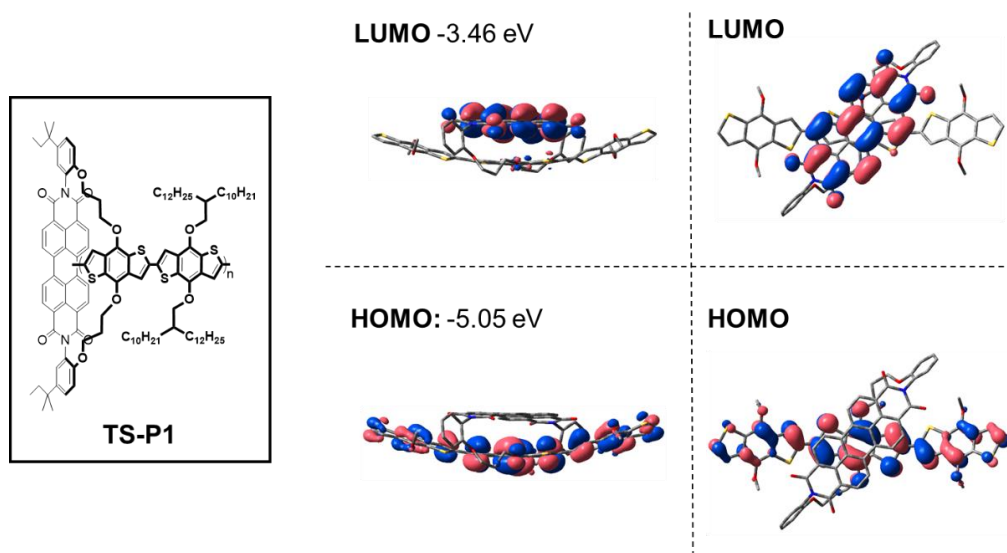


**Figure 115.** HOMO and LUMO levels and orbital distributions of **TS-P1** calculated using B3LYP/6-31G\*.

**Table 17.** TD-DFT data of **TS-P1** calculated using B3LYP/6-31G\*.

No.	Transition	Energy (cm <sup>-1</sup> )	Wavelength (nm)	Osc. Strength	Orbital contributions
<b>1</b>	S <sub>0</sub> → T <sub>1</sub>	8414	1188	0	HOMO → LUMO (95%)
<b>2</b>	S <sub>0</sub> → S <sub>1</sub>	8962	1115	0.008	HOMO → LUMO (98%)
<b>3</b>	S <sub>0</sub> → T <sub>2</sub>	10173	983	0	H-4 → LUMO (96%),
<b>4</b>	S <sub>0</sub> → T <sub>3</sub>	11751	851	0	H-2 → LUMO (65%), H-1 → LUMO (32%)
<b>5</b>	S <sub>0</sub> → S <sub>2</sub>	11997	834	0.0039	H-2 → LUMO (27%), H-1 → LUMO (72%)
<b>6</b>	S <sub>0</sub> → T <sub>4</sub>	12256	816	0	H-2 → LUMO (33%), H-1 → LUMO (66%)
<b>7</b>	S <sub>0</sub> → S <sub>3</sub>	12310	812	0.0059	HOMO → L+1 (81%)
<b>8</b>	S <sub>0</sub> → T <sub>5</sub>	14121	708	0	H-3 → LUMO (94%)
<b>9</b>	S <sub>0</sub> → T <sub>6</sub>	15712	636	0	H-3 → LUMO (97%)
<b>10</b>	S <sub>0</sub> → S <sub>4</sub>	16021	624	0.0063	H-2 → LUMO (65%), H-1 → LUMO (32%)

## Through-Space Polymers: Part 2

In the previous section, we confirmed that a through-space model system could be obtained. Here, the focus is to extend this further by changing the BDT polymer into a potentially more useful, narrow bandgap polymer. The two through space target polymers of this study are shown in **figure 116**. As seen, **TS-P2** and **TS-P3** have a donor-acceptor BDT-DPP polymer backbone. The difference between **TS-P2** and **TS-P3** lies in which part of the polymer (either the BDT or DPP unit) resides on top of the PDI acceptor. The aim is therefore to investigate how different relative orientations between both components influence the interface and optoelectronic properties of these materials.

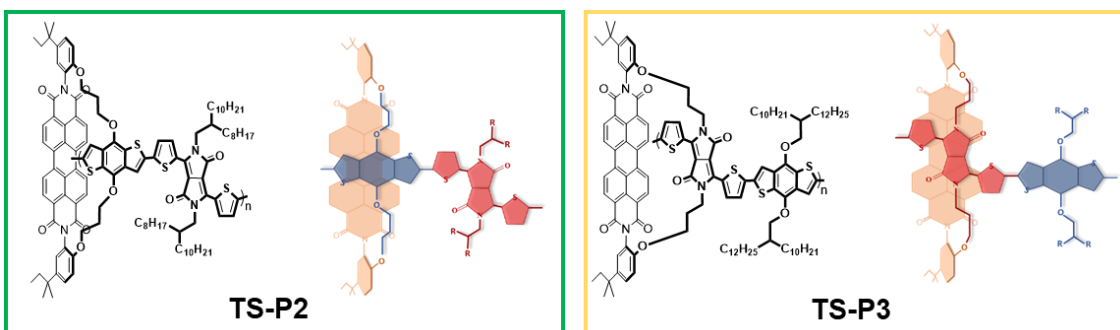


**Figure 116.** Chemical structures and cartoon representation of the through space polymers **TS-P2** and **TS-P3**.

### Synthetic Design & Characterization

First, **TS-M2** was prepared through a Miyaura stannylation of **TS-M1** with hexamethylditin, affording the product in 66% yield (**Figure 117**). Unfortunately, however, the product could only be obtained in 90% purity and was therefore used in the polymerization without further purification.

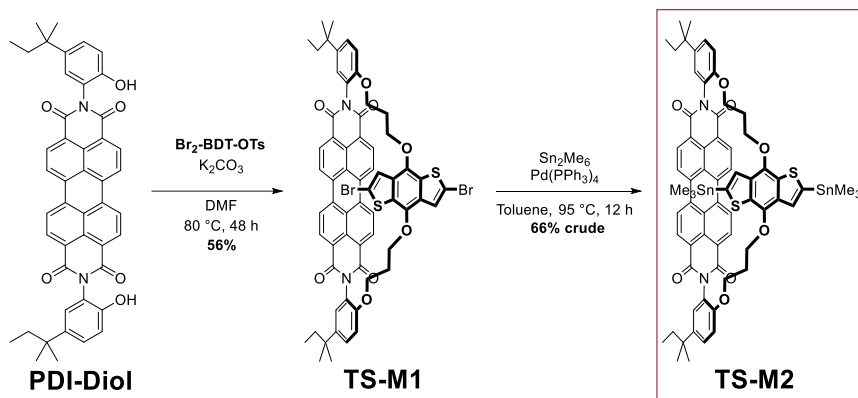


**Figure 117.** Synthesis of **TS-M2**.

**TS-M3** was prepared following a similar synthetic route to **TS-M1** (**Figure 118**). **DPP** was first alkylated to **DPP-THP** and deprotected to **DPP-OH** (in a 29% two-step yield), followed by a tosylation to generate **DPP-OTs** (in 43%). After forming the through space unit, **TS-PDI-DPP**

(in 36%), it was brominated with NBS in an ice-salt bath to afford the desired through space monomer (**TS-M3**) in a yield of 40%. Due to structural similarities, **TS-M2** and **TS-M3** follow a similar <sup>1</sup>H NMR assignment to **TS-M1** and hence will not be discussed further.

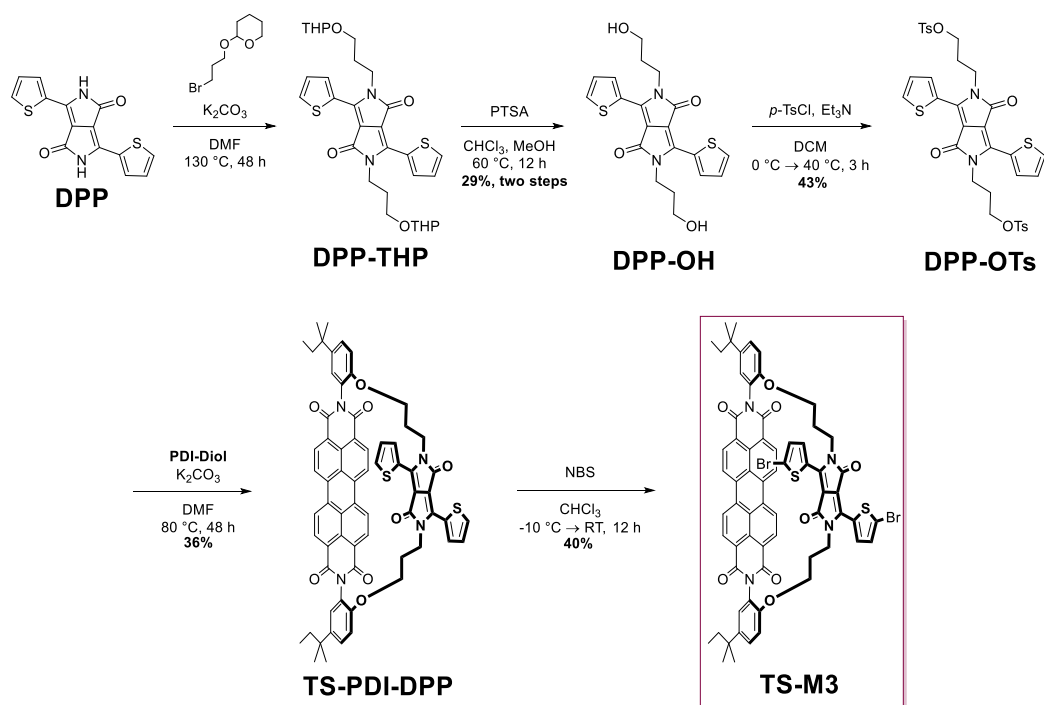


**Figure 118.** Synthesis of **TS-M3**.

The synthesis of **Ref-P2**, **TS-P2** and **TS-P3** are detailed in **figure 119**. All polymers were obtained in molecular weights over 10 kDa and possess good solubilities in common organic solvents. The physical data is summarized in **table 18**.

**Table 18.** Physical properties of **Ref-P2**, **TS-P2** and **TS-P3**. \*Due to the relatively high molecular weights of **TS-P3**, it might be less comparable with the other polymers.

Polymer	Yield (%)	M <sub>n</sub> (kDa)	M <sub>w</sub> (kDa)	PDI
<b>Ref-P2</b>	88%	58.2	220.3	3.78
<b>TS-P2</b>	64%	11.2	31.7	2.83
<b>TS-P3</b>	88%	99.0*	2746.0*	27.75*

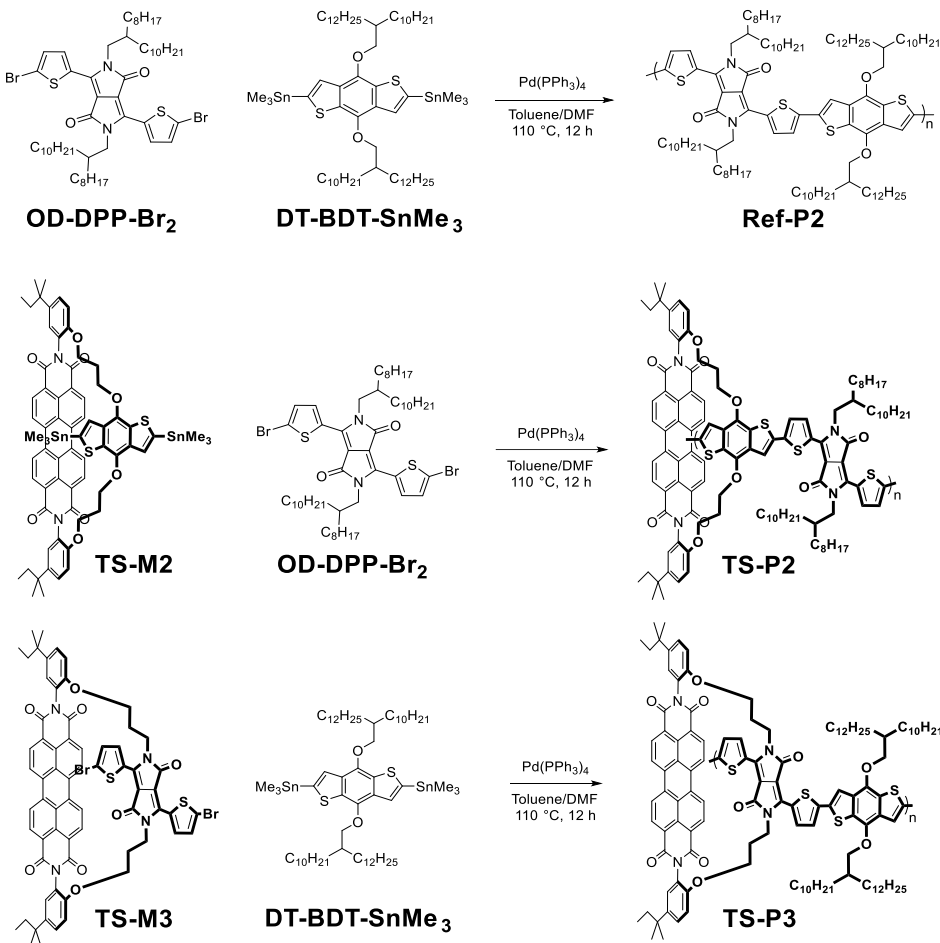


**Figure 119.** Synthesis of **Ref-P2**, **TS-P2** and **TS-P3**.

## Results & Discussion

### Photophysical Results

In **figure 120**, the solution and film absorption spectra of **Ref-P2**, **TS-P2** and **TS-P3** are shown. As observed, the absorption profiles for **Ref-P2** are very similar in both solution and film, with a vibronic band at  $\sim 750$  nm and  $\sim 675$  nm corresponding to the  $0-0'$  and  $0-1'$  transition, respectively. The only small difference is that the film spectrum is slightly broader, having a less steep high-wavelength onset. When looking at the UV-Vis profiles of **TS-P2**, we can see that the spectrum has two major parts; the part where the PDI molecule absorbs (peaks at  $\sim 500$  nm and  $\sim 540$  nm) and the part where BDT-DPP polymer absorbs (between  $\sim 600$ - $850$  nm). The presence of the PDI peaks therefore clearly confirms the structural differences between **TS-P2** and **Ref-P2**. The absorption profiles of **TS-P2** in solution and film are mostly similar, except for a change in the relative intensity of the different transitions. However, as observed, the region between  $600$ - $900$  nm looks very different compared to both **Ref-P2** and **TS-P3**, which we attribute to the presence of aggregated species. The solution spectrum of **TS-P2** has an absorption  $\lambda_{\text{max}}$  at  $\sim 690$  nm and a side shoulder at  $\sim 760$  nm. The intensity of the  $0-0'$  transition reduces slightly from solution to film. Lastly, **TS-P3** has an absorption  $\lambda_{\text{max}}$  at  $\sim 725$  nm in both solution and film. The absorption

profiles in both solution and film look nearly identical, with a slightly less steep onset and a more intense 0-1' transition in thin film. The photoluminescence could not be recorded on our spectrometer. However, the materials are currently being investigated in collaboration with the research groups of Jenny Nelson and Richard Friend.

**Table 19.** Summary of the photophysical properties of **Ref-P2**, **TS-P2** and **TS-P3**.

\*Emission could not be detected by our spectrometer.

Sample	$\lambda_{\text{max,abs}} \text{ (nm)}$	$\lambda_{\text{max,em}} \text{ (nm)}$
<b>Ref-P2 in CHCl<sub>3</sub></b>	750	/*
<b>Ref-P2 Film</b>	750	/*
<b>TS-P2 in CHCl<sub>3</sub></b>	690 + 760	/*
<b>TS-P2 Film</b>	675 + 745	/*
<b>TS-P3 in CHCl<sub>3</sub></b>	730	/*
<b>TS-P3 Film</b>	730	/*

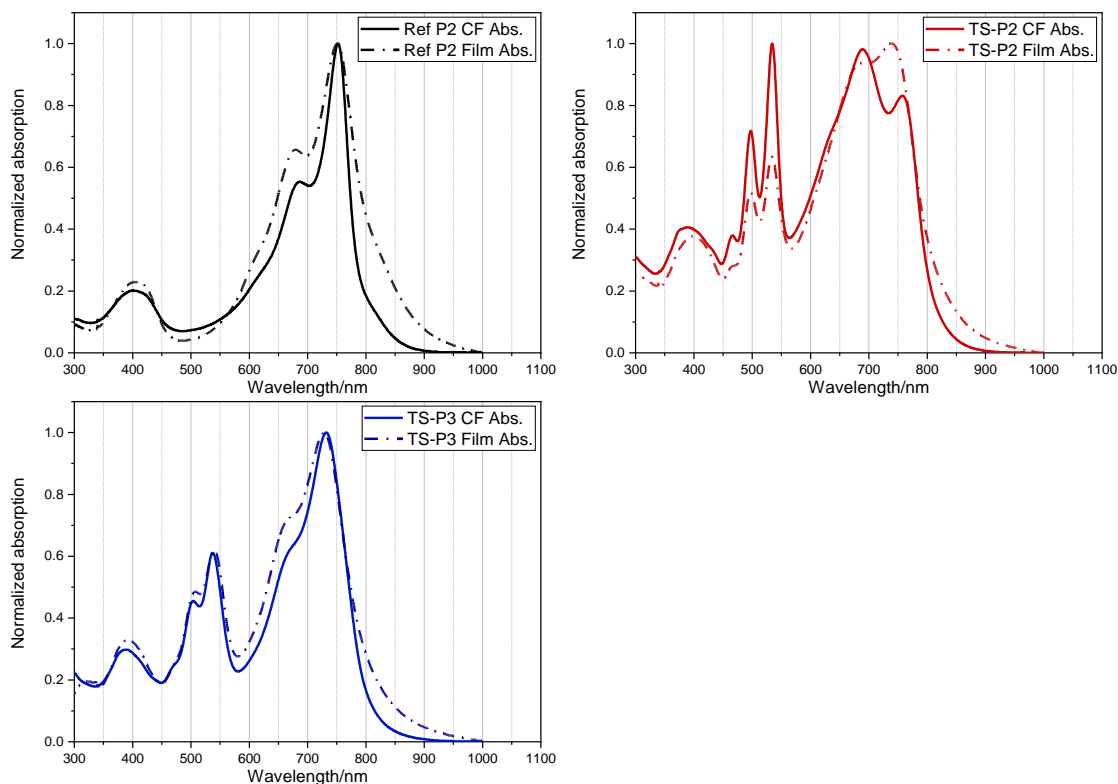


**Figure 120.** UV-Vis absorption and emission spectra of **Ref-P2** (black), **TS-P2** (red) and **TS-P3** (blue).

## Computational Results

Next, the HOMO and LUMO level and distributions were calculated via DFT using the B3LYP/6-31G\* dataset (**Figure 121 & 122**). As before, the HOMO is localized over the polymer backbone, whereas the LUMO is localized over the PDI core.

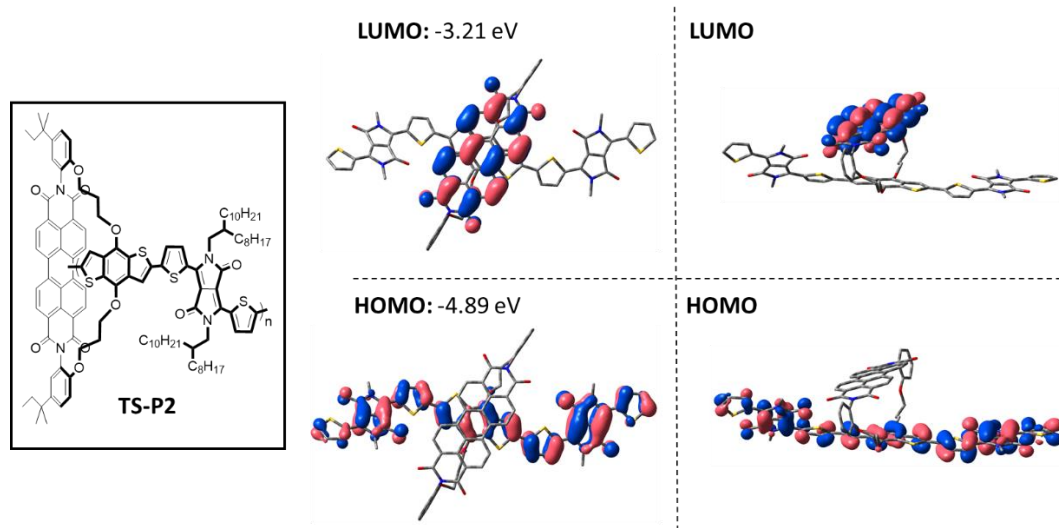


**Figure 121.** HOMO and LUMO levels and orbital distributions of **TS-P2** calculated using B3LYP/6-31G\*.

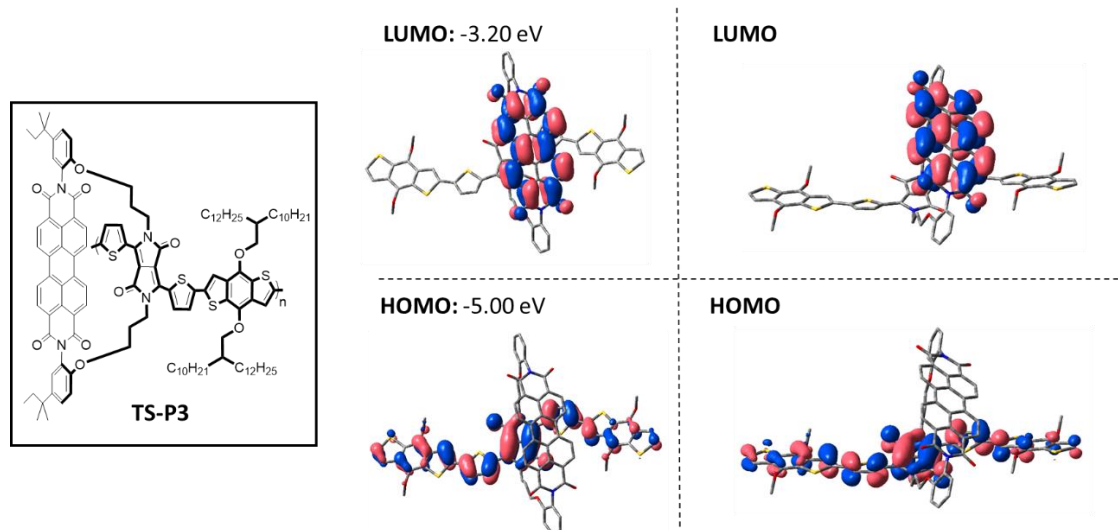


**Figure 122.** HOMO and LUMO levels and orbital distributions of **TS-P3** calculated using B3LYP/6-31G\*.

The TD-DFT data of **TS-P2** and **TS-P3** are summarized in **table 20 and 21**, respectively. As observed, the computations predict a CT-state energy at 907 nm for **TS-P2** versus 860 nm for **TS-P3**, each having a different oscillator strength. The CT states are therefore clearly different, which we hope to investigate further in the future. Besides CT-state energy absorption, the polymer backbone itself is predicted to absorb around 655 nm for **TS-P2** and 641 nm for **TS-P3**, which means that according to DFT, there should only be a small difference in the polymer absorption. However, the UV-Vis data presented before indicates a more significant difference. A speculative

explanation as to why **TS-P3**'s absorption is much more red-shifted compared to **TS-P3** (despite having practically the same polymer backbone), might be to do with a through-space interaction between the electron-deficient PDI core and the electron-rich BDT core (**Figure 123**). This interaction can potentially reduce the strength of the BDT donor and thus blue shift the absorption of the polymer.

**Table 20.** TD-DFT data of **TS-P2** calculated using B3LYP/6-31G\*.

No.	Transition	Energy (cm <sup>-1</sup> )	Wavelength (nm)	Osc. Strength	Orbital contributions
<b>1</b>	S <sub>0</sub> → T <sub>1</sub>	7441	1344	0	H-1 → L+2 (27%), HOMO → L+1 (57%), HOMO → L+2 (11%)
<b>2</b>	S <sub>0</sub> → T <sub>2</sub>	7811	1280	0	H-1 → L+1 (46%), H-1 → L+2 (14%), HOMO → L+2 (34%)
<b>3</b>	S <sub>0</sub> → T <sub>3</sub>	10036	996	0	H-3 → LUMO (99%)
<b>4</b>	S <sub>0</sub> → S <sub>1</sub>	11020	907	0.0005	HOMO → LUMO (95%)
<b>5</b>	S <sub>0</sub> → T <sub>4</sub>	11020	907	0	HOMO → LUMO (95%)
<b>6</b>	S <sub>0</sub> → T <sub>5</sub>	12596	794	0	H-1 → LUMO (95%)
<b>7</b>	S <sub>0</sub> → S <sub>2</sub>	12597	794	0.0001	H-1 → LUMO (95%)
<b>8</b>	S <sub>0</sub> → T <sub>6</sub>	13823	723	0	H-2 → L+1 (37%), H-1 → L+2 (12%), HOMO → L+1 (17%), HOMO → L+3 (18%)
<b>9</b>	S <sub>0</sub> → T <sub>7</sub>	15075	663	0	H-2 → LUMO (98%)
<b>10</b>	S <sub>0</sub> → S <sub>3</sub>	15078	663	0.0009	H-2 → LUMO (98%)
<b>11</b>	S <sub>0</sub> → S <sub>4</sub>	15266	655	1.3892	HOMO → L+1 (98%)

**Table 21.** TD-DFT data of **TS-P3** calculated using B3LYP/6-31G\*.

No.	Transition	Energy (cm <sup>-1</sup> )	Wavelength (nm)	Osc. Strength	Orbital contributions
<b>1</b>	S <sub>0</sub> → T <sub>1</sub>	7437.23839	1344.58511	0	HOMO → L+1 (93%)
<b>2</b>	S <sub>0</sub> → T <sub>2</sub>	9929.491575	1007.10091	0	H-3 → LUMO (98%)
<b>3</b>	S <sub>0</sub> → S <sub>1</sub>	11625.67554	860.1650688	0.0002	HOMO → LUMO (99%)
<b>4</b>	S <sub>0</sub> → T <sub>3</sub>	11626.48209	860.1053972	0	HOMO → LUMO (99%)
<b>5</b>	S <sub>0</sub> → T <sub>4</sub>	14221.97425	703.1372598	0	H-1 → L+1 (50%), HOMO → L+2 (29%)
<b>6</b>	S <sub>0</sub> → T <sub>5</sub>	15440.67799	647.6399551	0	H-2 → L+1 (47%), H-1 → LUMO (11%), H-1 → L+2 (11%)
<b>7</b>	S <sub>0</sub> → S <sub>2</sub>	15530.20553	643.9064815	0.884	H-1 → LUMO (18%), HOMO → L+1 (74%)
<b>8</b>	S <sub>0</sub> → S <sub>3</sub>	15593.11678	641.3086071	0.3174	H-2 → LUMO (17%), H-1 → LUMO (57%), HOMO → L+1 (25%)

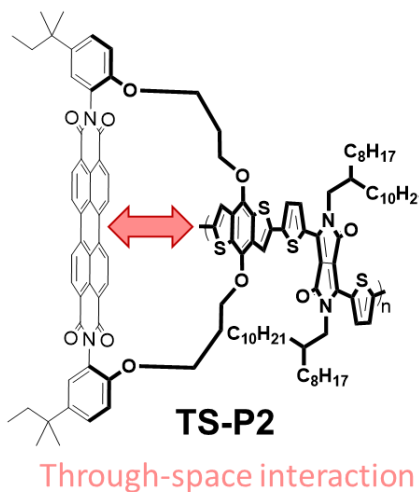


**Figure 123.** The speculative, proposed through-space interaction in **TS-P2**, which might be responsible for reducing the strength of the BDT donor and thereby blue-shifting the polymer's absorption.

## Conclusions

In the first part of this chapter, we have demonstrated that through-space polymeric model system could be prepared. The calculated LUMO and HOMO distributions are clearly separated over the electron-deficient PDI non-fullerene acceptor and the BDT polymer backbone. The through-space model polymer should therefore behave like a “true” charge transfer state. Furthermore, the inherent charge transfer character of the through space polymer should be able to provide us with the opportunity to study, for the first time, both molecular (dilute) charge transfer states and bulk (or more concentrated) ones.

The second part of this chapter shows that this concept can also be extended to include other, and maybe more representative, narrow bandgap polymers. The developed materials demonstrate it is possible to synthetically control the position of the NFA acceptor with respect to the conjugated polymer backbone and can therefore potentially reveal if there is an optimum relative position/orientation. According to our preliminary results this should indeed be the case as TS-P2 and TS-P3 behaved differently, having a different absorption and CT state energy. It is therefore hoped that this model system can be used to study how subtle changes in the structure or orientation can influence the optoelectronic properties and overall device performance. Furthermore, we propose that it can be used to investigate how certain distances between the donor and acceptor interface or rigidifications of the straps alter their performance.

However, there are also some drawbacks that need to be considered. First, the use of suitable materials, serving as either the non-fullerene acceptor or the polymer backbone, is more restricted compared to the conventional two-part system. For example, our current system (discussed in this chapter) is based on neither the best NFA, nor the record-holding polymer backbone. Even though we can imagine a wide range of different backbone polymers to be incorporated into the through-

space system, strapping it onto its most preferred NFA counterparts might not always be possible. The efficiency of these systems, in terms of both fundamental OPV processes and device performance, is therefore yet to be established. Finally, it is also important to realize that these molecular architectures are synthetically much more demanding than conventional systems and might therefore be too cost-inefficient to be used in industrial applications.

To conclude, even though there are still some complex hurdles to be overcome, we strongly believe the through-space design model is an important development in this field, which is expected to provide a lot of essential and fundamental understanding.

## Thesis Summary

In this thesis, we have introduced the concept of molecular encapsulation as a synthetic tool to modify intermolecular interactions between conjugated materials. Furthermore, the concept was applied to construct encapsulated versions of various well-known materials in the optoelectronic field. This thesis thereby focusses on how molecular encapsulation influences the (photo)physical properties, and/or device performance of conjugated materials and polymers.

The second chapter demonstrates a series of encapsulated, red/orange-emitting DPP-based p-type conjugated polymers. Here, we have shown that as you increase the density of encapsulation, the polymer backbones are more protected from intermolecular interactions, thereby affording higher photoluminescence quantum yields in thin film. However, it was also discovered that the initial solution PLQYs seemed to drop with an increase in the density of the straps (due to the introduction of additional vibration modes). Nevertheless, the ratio between thin film and solution PLQYs of the three, presented polymers remain among the highest ever reported in literature for polymers that emit in this region of the electromagnetic spectrum. In conclusion, this polymer series demonstrates that through control over density of encapsulation it was possible to greatly suppress aggregation-caused quenching (ACQ) in our red-emitting conjugated polymers and generate the most emissive red conjugated polymers in the solid state, to date.

The third chapter focusses on the use of encapsulation to molecularly engineer/alter the aggregation and packing behaviour of (relatively) planar, n-type conjugated polymers based on naphthalene diimide (NDI). The polymer series studied in this chapter includes the naked reference polymer P(NDI-2OD-T), a bulky in-between equivalent P(NDI-DMP-T) and the encapsulated polymer P(E-NDI-T). Through comparison, it was possible to link the photophysical properties of the different NDI polymers to their change in overall structure and morphology. While our study demonstrates that molecular encapsulation remains a powerful technique to suppress intermolecular interactions and retain the solution properties of the polymer in the solid-state, it also revealed that, for the first time, the famous, reference polymer (P(NDI-2OD-T)) undergoes aggregation induced emission; an effect that is suppressed upon encapsulation due to an increasing pi-stacking distance. The naked reference polymers therefore exhibited the highest thin film photoluminescence quantum yield, which we believe to be one of the reasons why its performance has been so superior. In conclusion, this chapter highlights that AIE through pi-stacking may be an attractive, alternative method to enhance the radiative properties of conjugated polymers, in contrast to the current paradigm where it is viewed as a potential source of optical quenching.

In the fourth chapter, we investigated the influence of molecular encapsulation on the photophysical properties of PDI chromophores. As before, we demonstrated that our strategy

proved successful at suppressing intermolecular  $\pi$ - $\pi$  interactions in both solution and the solid-state. However, the ultimate aim to obtain bright, PDI-based solid-state emitters was not achieved as the electron-rich peripheral aryls (use to install the encapsulating straps) introduced charge transfer character into our molecule, thereby leading to photoluminescence quenching. Interestingly however, it was found that the encapsulating straps could potentially be used to rigidify the molecular structure or direct crystal or solid-state packing. In conclusion, this chapter highlights both the power of encapsulation as a synthetic tool for chromophore control but also their potential non-innocence with regards to underlying photophysical properties.

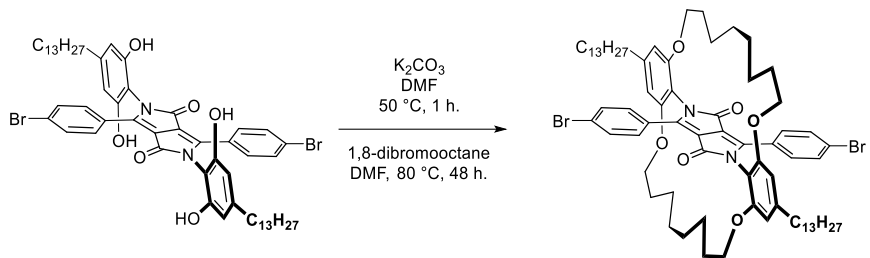
In the final chapter, we proposed that the encapsulation concept can be used as a powerful, synthetic tool to control the distance or orientation between two different building blocks and explained why this can be of great interest to the field of organic photovoltaics. Here, we have first demonstrated the complex synthesis required to make such molecular, through-space architectures. The initial photophysical and computational results, as well as fixed chemical structure suggest that the through-space model polymer should be able to behave like a “true” charge transfer state. Later, we also demonstrated that it is possible to construct potentially more useful narrow bandgap polymers and control where the NFA acceptor is positioned on the polymer backbone (i.e., either on donor unit or acceptor unit). These systems should therefore be able to reveal if there is an optimum relative position/orientation. In fact, the preliminary results indicate that there is a clear difference between the **TS-P2** and **TS-P3** polymers (as evidenced from the calculated CT state energy, and the UV-Vis data). We therefore hope that this model system can be used to study, for the first time, how subtle changes in the structure or D-A orientation can influence the optoelectronic properties, CT state and overall OPV device performance. Furthermore, we propose that it can be used to investigate how certain distances between the donor and acceptor interface or rigidifications of the straps alter their performance. Having great control over the donor-acceptor interface should therefore provide lots of fundamental understanding, which can help pave the way towards next-generation photovoltaic materials or devices.

## **Experimental Section**

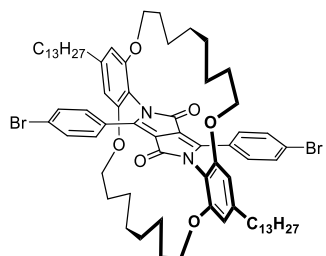
### **General information**

All reactions were performed in dry glassware under argon atmosphere and magnetic stirring, unless stated otherwise. Light-sensitive reactions were covered in foil. Chemicals were purchased from chemical suppliers (Merck, TCI, Fluorochem, Acros Organics, Alfa Aesar, SLS, Fisher Scientific, Apollo Scientific and Manchester Organics) and used as received unless stated otherwise. The reactions were monitored through thin layer chromatography (TLC) using DC Fertigfolien ALUGRAM aluminium sheets coated with silica gel. Column chromatography was carried out using Geduran silica gel 60 (40-63 µm) or Biotage® Isolera™ Four with Biotage® SNAP/ SNAP ultra-cartridges (10 g, 20 g, 50 g or 100 g). <sup>1</sup>H NMR spectra were recorded on a 400 MHz Avance III HD Spectrometer, 400 MHz Neo Prodigy Spectrometer, 400 MHz Smart Probe Spectrometer, 500 MHz DCH Cryoprobe Spectrometer or a 700 MHz TXO Cryoprobe Spectrometer in the stated solvent using residual protic solvent CHCl<sub>3</sub> ( $\delta$  = 7.26 ppm, s) or DMSO-d6 ( $\delta$  = 2.50 ppm, s) as the internal standard. <sup>1</sup>H NMR chemical shifts are reported to the nearest 0.01 ppm and quoted using the following abbreviations: s, singlet; d, doublet; t, triplet; q, quartet; qn, quintet; sxt, sextet; m, multiplet; br, broad; or a combination of these. The coupling constants (J) are measured in Hertz. <sup>13</sup>C NMR spectra were recorded on the 500 MHz DCH Cryoprobe Spectrometer in the stated solvent using the residual protic solvent CHCl<sub>3</sub> ( $\delta$ = 77.16 ppm, t) or DMSO-d6 ( $\delta$  = 39.52 ppm, s) as the internal standard. <sup>13</sup>C NMR chemical shifts are reported to the nearest 0.1 ppm. Mass spectra were obtained using a Waters LCT Premier, Waters Vion IMS Qtof, Finnigan MAT 900XP or Waters MALDI micro-MX spectrometer at the Department of Chemistry, University of Cambridge. The absorption and photoluminescence of all samples was measured using a Shimadzu UV-3600 Plus spectrophotometer, an Edinburgh Instruments FLS980 Spectrometer or a Edinburgh Instruments FS5 Spectrofluorometer, unless stated otherwise. DFF, II-1, II-2, II-6, Br<sub>2</sub>-NDA, Th<sub>2</sub>-NDA, Br<sub>2</sub>-NDI-2OD, Th<sub>2</sub>-NDI-2OD, Br<sub>2</sub>Th<sub>2</sub>-NDI-2OD, PDI, PDI-Bpin, DT-BDT-SnMe<sub>3</sub>, HD-BDT-Br<sub>2</sub>, and OD-DPP-Br<sub>2</sub> were prepared according to literature procedures.<sup>10,106,205,235,266–274</sup>

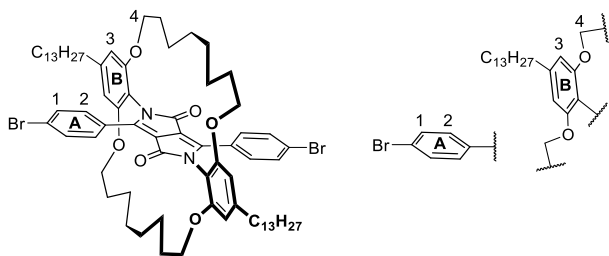
## Experimental Procedures: Chapter II



### Encapsulated Monomer (II-4)<sup>106</sup>

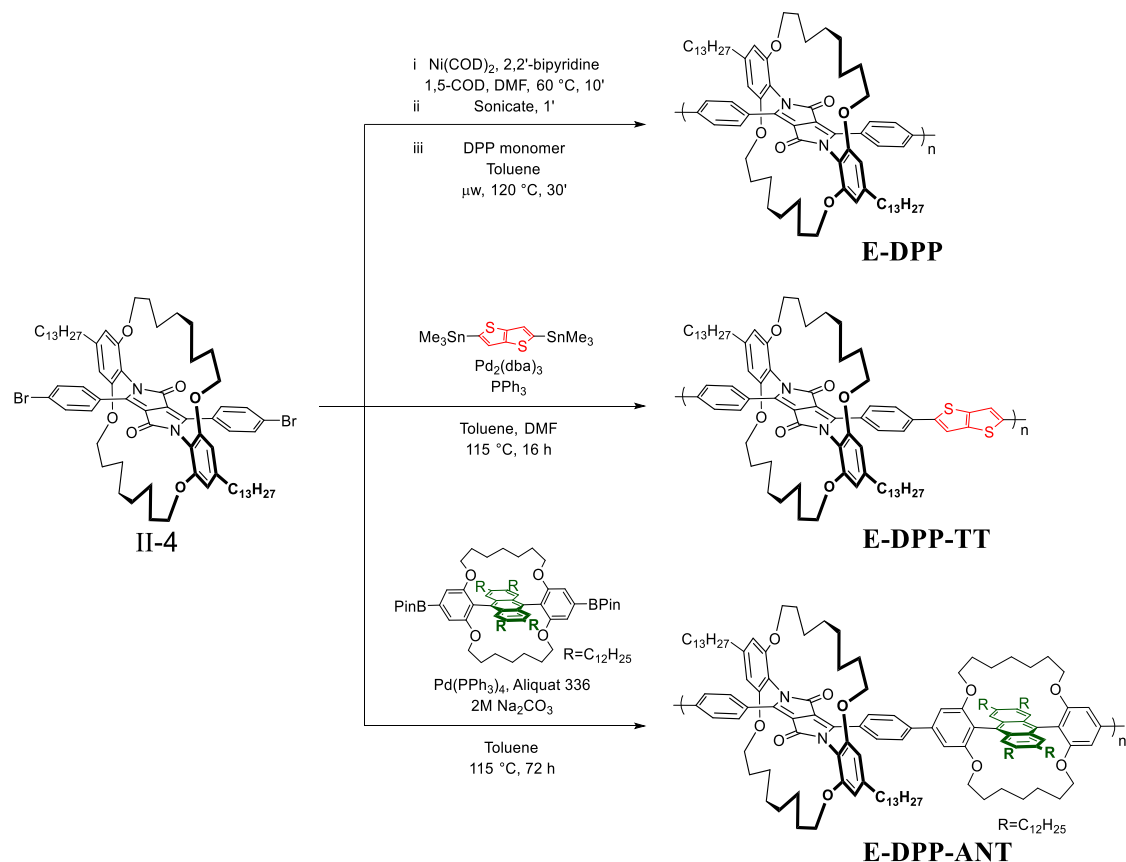


To a 250 mL round-bottomed flask under argon, DPP tetra-ol (515.0 mg, 0.5015 mmol),  $K_2CO_3$  (464.4 mg, 3.3601 mmol) and dry DMF (55 mL) were added, and the mixture was heated to 50 °C for 1 h. To this, a solution of 1,8-dibromo-octane (203  $\mu$ L, 1.1033 mmol) in dry DMF (55 mL) was added dropwise over 1 h. The resulting mixture was heated to 80 °C and left stirring for 2 days. The reaction mixture was concentrated *in vacuo*, re-dissolved in the minimal amount of chloroform and hexane and purified by column chromatography (using 50 to 70% chloroform in hexane). The product fractions were concentrated *in vacuo*, sonicated in methanol, and dried under high vacuum to yield pure monomer (356.9 mg, 0.2861 mmol, 57%).

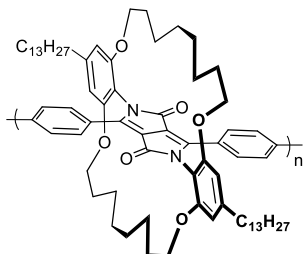


**R<sub>f</sub>** = 0.73 (Chloroform); **Mp:** 198.6–202.6 °C; **<sup>1</sup>H NMR** (400 MHz,  $CDCl_3$ )  $\delta$  7.69 (d, *J* = 8.7 Hz, 4H, #1), 7.39 (d, *J* = 8.7 Hz, 4H, #2), 6.40 (s, 4H, #3), 3.90 (t, *J* = 5.0 Hz, 8H, #4), 2.63 – 2.53 (m, 4H), 1.60 (d, *J* = 13.0 Hz, 12H), 1.27 (s, 36H), 0.88 (t, *J* = 6.8 Hz, 6H); **<sup>13</sup>C NMR{H}** (150 MHz,  $CDCl_3$ )  $\delta$  162.2, 156.3, 147.3, 146.2, 131.5, 130.0, 127.8, 125.2, 112.3, 109.8, 106.4, 69.6, 37.0, 32.1, 31.4, 30.5, 30.1, 29.8, 29.8, 29.8, 29.7, 29.6, 29.5, 29.5, 26.7, 22.8, 14.3; **LRMS** (MALDI-TOF): 1248.1 [M]<sup>+</sup>. Structure supported by **X-ray crystallography** (crystals were grown in an NMR tube by layering methanol on top of a solution of **II-4** in chloroform).

## Encapsulated DPP Polymer Synthesis



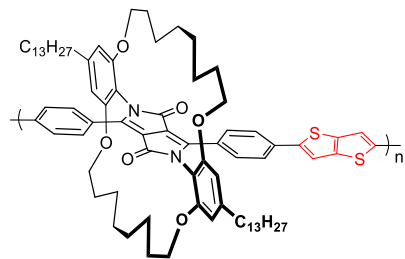
### E-DPP Polymer



In a nitrogen glovebox,  $\text{Ni}(\text{COD})_2$  (66.0 mg, 0.24 mmol), and 2,2'-bipyridine (27.7 mg, 0.24 mmol) were added to a 5 mL oven-dried microwave vial and it was sealed. The vial was flushed with argon for 5 minutes and then a solution of 1,5-cyclooctadiene (30  $\mu\text{L}$ , 0.24 mmol) in degassed DMF (970  $\mu\text{L}$ ) was added. The resulting mixture was briefly sonicated, stirred at 60 °C for 10 minutes and briefly sonicated again to obtain a purple-coloured mixture. Next, a solution of encapsulated DPP monomer (II-4) (120 mg, 0.0962 mmol) in dry, degassed toluene (5 mL) was added and the reaction mixture was heated in a microwave reactor for 30 minutes at 120 °C. The resulting red-coloured gelly polymer was dissolved in the minimal amount of chlorobenzene and precipitated into a pre-stirring mixture of methanol (150 mL) and concentrated HCl (10 mL). The resulting solids/flakes were then filtered into a cellulose soxhlet thimble, which was then

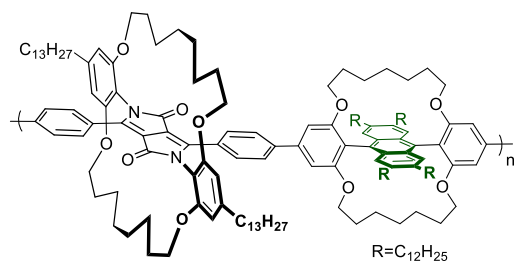
subjected to soxhlet extractions in acetone (100 °C), hexane (100 °C) and chloroform (100 °C). The chloroform fraction was concentrated *in vacuo*, dissolved in the minimal amount of chloroform, and precipitated into a pre-stirring mixture of methanol (150 mL) and concentrated HCl (10 mL). After filtration, the polymer was obtained as red/dark pink solids/flakes (96.7 mg, 92% yield); Mn ~80.6 kDa, Mw ~370.8 kDa, PDI = 4.601. **Anal. Calcd.** for C<sub>72</sub>H<sub>98</sub>N<sub>2</sub>O<sub>6</sub>: C, 79.51; H, 9.08; N, 2.58; O, 8.83. Found: C, 78.89; H, 9.12; N, 2.57 (average of two runs).

### E-DPP-TT Polymer



Encapsulated DPP Monomer (II-4) (140 mg, 0.1122 mmol), 2,5-Bis(trimethylstannyl)-thieno[3,2-b]thiophene (52.3 mg, 0.1122 mmol), Pd<sub>2</sub>(dba)<sub>3</sub> (2.2 mg, 0.0024 mmol) and PPh<sub>3</sub> (2.5 mg, 0.0095 mmol) were placed in a dry 10 mL microwave vial and it was degassed for 45 minutes. Meanwhile, anhydrous toluene and DMF were bubbled with argon (45 min). Next, the degassed anhydrous toluene (2 mL) and DMF (0.2 mL) were added to the monomer/catalyst mixture and it was heated to 115 °C for 16 h. The gloopy red/pink product was re-dissolved in a minimal amount of chlorobenene and precipitated from stirring methanol (~200 mL) by dropwise addition. The resulting solids were filtered into a soxhlet cellulose thimble and subsequently purified by soxhlet extraction in acetone (100 °C), hexane (100 °C) and chloroform (100 °C). The pink/red chloroform fraction was concentrated *in vacuo*, dissolved in the minimal amount of chlorobenzene, precipitated into stirring methanol (as above) and collected by filtration to afford the polymer as a purple flaky solid (134 mg, 97%); Mn ~33.4 kDa, Mw ~113.6 kDa, PDI = 3.405. **Anal. Calcd.** for C<sub>78</sub>H<sub>100</sub>N<sub>2</sub>O<sub>6</sub>S<sub>2</sub>: C, 76.43; H, 8.22; N, 2.29; O, 7.83; S, 5.23. Found: C, 72.73; H, 8.00; N, 2.31 (average of two runs).

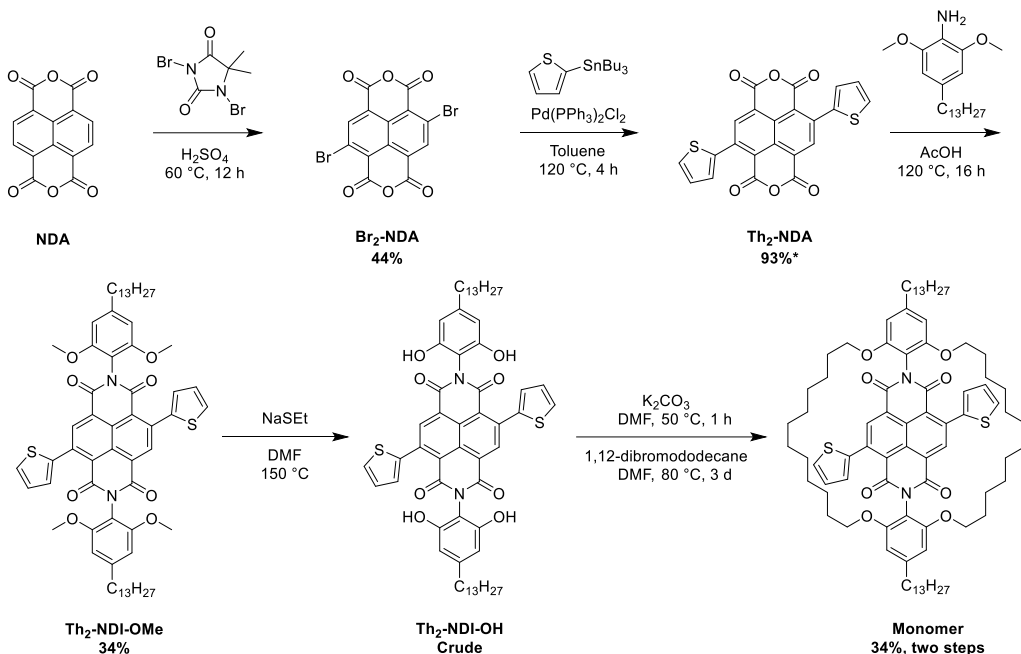
## E-DPP-ANT Polymer



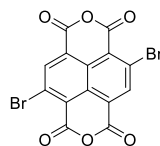
The encapsulated anthracene monomer (II-6) (90.9 mg, 60  $\mu\text{mol}$ ), encapsulated DPP monomer (II-4) (75 mg, 60.0  $\mu\text{mol}$ ) and Pd(PPh<sub>3</sub>)<sub>4</sub> (0.7 mg, 0.6  $\mu\text{mol}$ , 1 mol%). were combined in a 5 mL microwave vial under argon. Degassed toluene (2 mL containing 1 drop of Aliquat 336) and degassed 2 M aqueous Na<sub>2</sub>CO<sub>3</sub> (0.27 mL) were then added sequentially to the reaction vial. The resulting mixture was degassed with argon for 10 minutes and then stirred in a preheated (115 °C) oil bath for 72 h in the absence of light. The resulting, orange-coloured liquid/gel was dissolved in the minimal amount of chlorobenzene and precipitated into a pre-stirring mixture of methanol (150 mL) and concentrated HCl (10 mL). The resulting stringy flakes were then filtered into a cellulose soxhlet thimble, which was then subjected to soxhlet extractions in acetone (100 °C), hexane (100 °C) and chloroform (100 °C). The chloroform fraction was concentrated *in vacuo*, dissolved in the minimal amount of chlorobenzene, and precipitated into a pre-stirring mixture of methanol (150 mL) and concentrated HCl (10 mL). After filtration, the polymer was obtained as an orange-coloured, rubbery polymer (80.5 mg, 57% yield); Mn ~55.4 kDa, Mw ~130.5 kDa, PDI = 2.358. **Anal. Calcd.** for C<sub>160</sub>H<sub>234</sub>N<sub>2</sub>O<sub>10</sub>: C, 81.93; H, 10.06; N, 1.19; O, 6.82. Found: C, 81.86; H, 9.93; N, 1.18 (average of two runs).

## Experimental Procedures: Chapter III

### Encapsulated Monomer synthesis



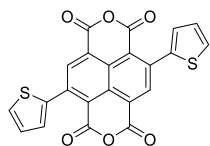
### 2,6-dibromo-1,4,5,8-naphthalenetetracarboxylic acid dianhydride (Br<sub>2</sub>-NDA)<sup>269–271</sup>



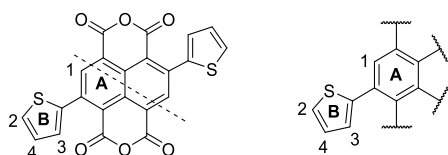
Under Argon, 1,3-dibromo-5,5-dimethylhydantoin (14.94 g, 52.22 mmol) was added portionwise (4 portions over 1 h) to a slurry of 1,4,5,8-Naphthalenetetracarboxylic dianhydride (10.00 g, 37.08 mmol) in sulfuric acid (100 mL) and the reaction was heated to 60 °C for 12 h. The resulting reaction mixture was poured carefully onto ice (500 mg) and H<sub>2</sub>O (500 mL) was added. The mixture was left in icewater for half an hour. Next, the yellow solids were collected by filtration, sonicated in methanol and filtered again to yield a mixture of brominated products. The crude product was placed into a beaker together with hot DMF (~ 4 mL/g). At room temperature, the suspension was filtered, and the yellow solid product was washed with methanol. Lastly, the product was sonicated in methanol and collected again by filtration to yield relatively pure Br<sub>2</sub>-NDA (9.79g, 22.98 mmol, 44%).

**<sup>1</sup>H NMR** (400 MHz, DMSO) δ 8.79 (s, 2H); **HRMS** (ASAP-TOF): Calculated for C<sub>14</sub>H<sub>3</sub>O<sub>6</sub>Br<sub>2</sub><sup>+</sup>: 424.8296. Found m/z 424.8299 [M+H]<sup>+</sup>.

**(2,6-thiophen-2-yl)naphthalene-1,4,5,8-tetracarboxylic Dianhydride (Th<sub>2</sub>-NDA)<sup>272</sup>**

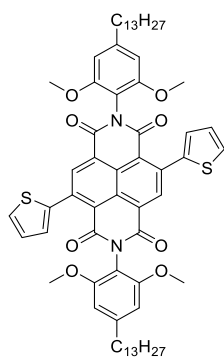


Under N<sub>2</sub>, Br<sub>2</sub>-NDA (880 mg, 2.0662 mmol) and Pd(PPh<sub>3</sub>)<sub>2</sub>Cl<sub>2</sub> (145.2 mg, 0.2069 mmol) were placed into a three-necked round-bottomed flask (equipped with reflux condensor). It was flushed with argon for 10 min. Next, anhydrous toluene (26 mL) and 2-(tributylstannylyl)thiophene (1.76 mL, 5.5414 mmol) were added. The mixture was heated to 120 °C and left stirring for 8 h. The dark red solids were collected by filtration (while warm) and washed with toluene. Next, the solids were boiled and filtered from a minimal amount of methanol and then from chloroform. The desired product was obtained as a red solid (831 mg, 1.9222 mmol, 93%).



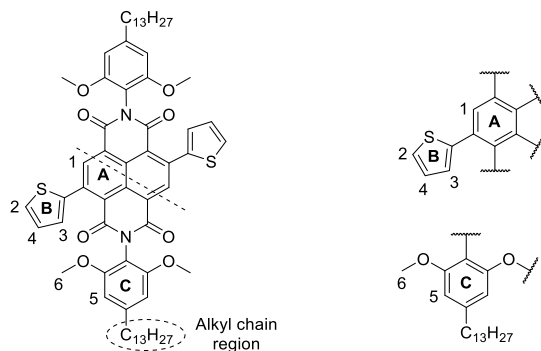
**<sup>1</sup>H NMR** (400 MHz, DMSO) δ 8.50 (s, 2H, #1), 7.91 (dd, *J* = 5.1, 1.2 Hz, 2H, #2), 7.57 (dd, *J* = 3.5, 1.0 Hz, 2H, #3), 7.27 (dd, *J* = 5.0, 3.6 Hz, 2H, #4). **HRMS** (IMS-QTOF): Calculated for C<sub>22</sub>H<sub>8</sub>O<sub>6</sub>S<sub>2</sub><sup>+</sup>: 431.9762. Found *m/z* 431.9761 [M].

**2,7-bis(2,6-dimethoxy-4-tridecylphenyl)-4,9-di(thiophen-2-yl)benzo[lmn][3,8]phenanthroline-1,3,6,8(2H,7H)-tetraone (Th<sub>2</sub>-NDI-OMe)**



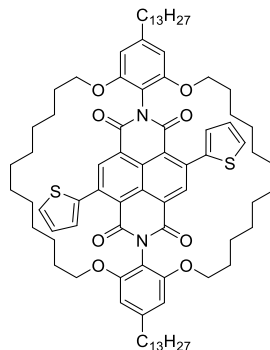
Under argon, 2,6-dimethoxy-4-tridecylaniline (620.7 mg, 1.8500 mmol) and Th<sub>2</sub>-NDA (200 mg, 0.4625 mmol) were dissolved in AcOH (12 mL) and heated to 120 °C. The reaction was left stirring for 3 h. The reaction mixture was added slowly into stirring MeOH (100-150 mL) and left stirring for 10 min. The resulting orange solids were collected by filtration, dissolved in the minimal amount of a 1-to-1 mixture of DCM and hexane and wet-loaded onto a silica column. The crude was purified via column chromatography (biotage) using chloroform/hexane and later chloroform/methanol (stepwise column from 50% CHCl<sub>3</sub> in hexane, to 100% CHCl<sub>3</sub> and finally 2% MeOH in CHCl<sub>3</sub>). The product fractions were concentrated *in vacuo*, sonicated in methanol

and collected by filtration (wash with MeOH) to yield pure, bright orange solid product (167.5 mg, 0.1569 mmol, 34%)



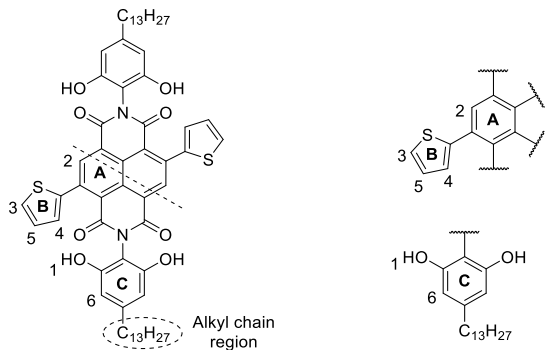
$R_f$  = 0.37 (100%  $\text{CHCl}_3$ );  $^1\text{H NMR}$  (500 MHz,  $\text{CDCl}_3$ )  $\delta$  8.81 (s, 2H, #1), 7.47 (dd,  $J$  = 5.1, 1.2 Hz, 2H, #2), 7.31 (dd,  $J$  = 3.6, 1.2 Hz, 2H, #3), 7.11 (dd,  $J$  = 5.1, 3.6 Hz, 2H, #4), 6.48 (s, 4H, #5), 3.75 (s, 12H, #6), 2.66 – 2.59 (m, 4H), 1.65 (dt,  $J$  = 15.7, 7.7 Hz, 4H), 1.27 (s, 40H), 0.89 (t,  $J$  = 7.0 Hz, 6H).  $^{13}\text{C NMR}\{\text{H}\}$  (126 MHz,  $\text{CDCl}_3$ )  $\delta$  161.79, 161.49, 155.57, 145.89, 140.87, 140.11, 136.69, 128.34, 127.80, 127.31, 126.02, 124.04, 109.75, 104.62, 55.95, 37.04, 31.94, 31.34, 29.71, 29.65, 29.58, 29.38, 22.71, 14.14.  $\text{HRMS}$  (ASAP-TOF): Calculated for  $\text{C}_{64}\text{H}_{79}\text{N}_2\text{O}_8\text{S}_2^+$ : 1067.5278. Found  $m/z$  1067.5228 [ $\text{M}+\text{H}]^+$ .

### Encapsulated Th<sub>2</sub>-NDI Monomer



### Step 1: Synthesis of crude Th<sub>2</sub>-NDI-OH

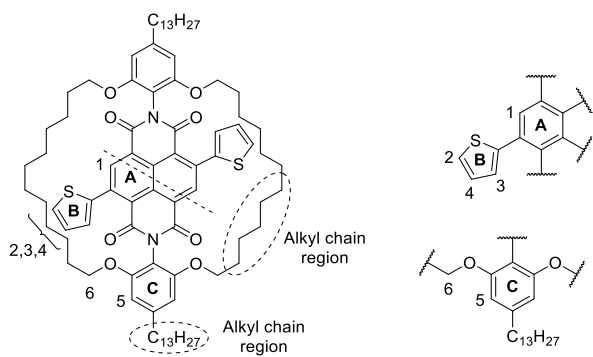
To a 100 mL round-bottomed flask under argon, 2,7-bis(2,6-dimethoxy-4-tridecylphenyl)-4,9-di(thiophen-2-yl)benzo[lmn][3,8]phenanthroline-1,3,6,8(2H,7H)-tetraone (600 mg, 0.5621 mmol), NaSEt (technical ~90%, 1.4185 g, 16.8628 mmol) and anhydrous DMF (36 mL) were added and it was heated to 150 °C for 4 days. The reaction mixture was poured into pre-stirring water (~200 mL) and 1M HCl (~50 mL) and filtered. The solids were dried *in vacuo*. The resulting crude NDI tetra-ol was obtained as a dark red solid (~568.5 mg) and used in the subsequent reaction without further purification.



**<sup>1</sup>H NMR** (400 MHz, DMSO) δ 9.33 (s, 4H, #1), 8.51 (s, 2H, #2), 7.78 (d, *J* = 4.7 Hz, 2H, #3), 7.39 (d, *J* = 2.9 Hz, 2H, #4), 7.20 – 7.13 (m, 2H, #5), 6.23 (s, 4H, #6), 2.44 (s, 4H), 1.55 (s, 4H), 1.25 (s, 40H), 0.85 (d, *J* = 6.8 Hz, 6H). **HRMS** (ASAP-TOF): Calculated for C<sub>60</sub>H<sub>71</sub>N<sub>2</sub>O<sub>8</sub>S<sub>2</sub><sup>+</sup>: 1011.4674. Found *m/z* 1011.4690 [M+H]<sup>+</sup>.

#### Step 2: Encapsulation of crude Th<sub>2</sub>-NDI-OH

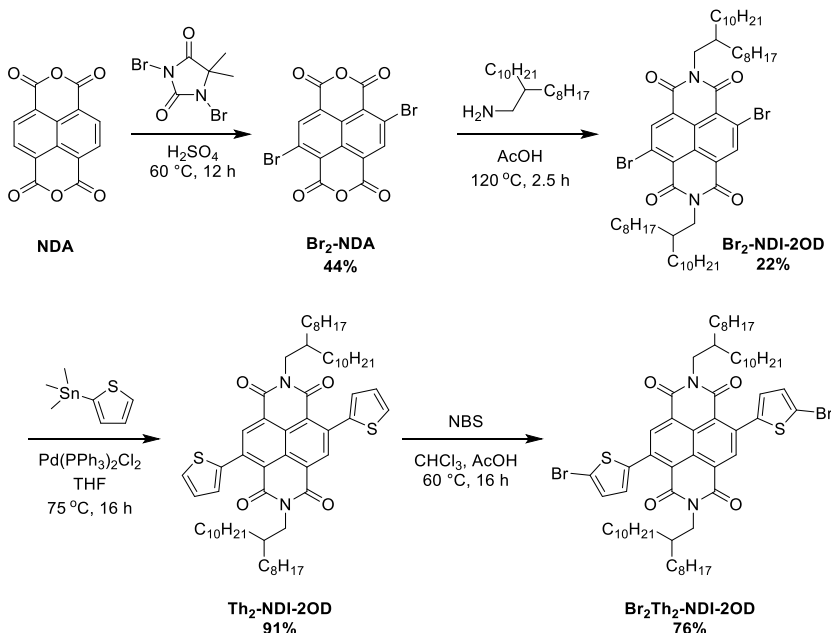
The crude Th<sub>2</sub>-NDI-OH was placed into a 250 mL round-bottomed flask under argon. K<sub>2</sub>CO<sub>3</sub> (413.3 mg, 2.9935 mmol) and anhydrous DMF (75 mL) were added and the reaction mixture was heated to 50 °C for 1 h. Next, a solution 1,12-dibromododecane (322.6 mg, 0.9832 mmol) in anhydrous DMF (75 mL) was added dropwise over 1 h and the mixture was heated to 80 °C for 2 days. The reaction mixture was concentrated in *vacuo*, dissolved in a minimal amount of DCM and hexane and purified by column chromatography (stepwise column; 50% CHCl<sub>3</sub> to 75-80% CHCl<sub>3</sub> and 100% CHCl<sub>3</sub> in hexane). The product fractions were concentrated *in vacuo* to afford red/orange coloured solid product (257.2 mg, 0.1913 mmol, 34% two-step yield).



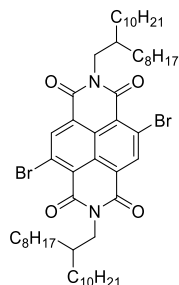
**<sup>1</sup>H NMR** (500 MHz, CDCl<sub>3</sub>) δ 8.83 (s, 2H, #1), 7.48 (dd, *J* = 5.1, 1.2 Hz, 2H, #2), 7.31 (dd, *J* = 3.6, 1.2 Hz, 2H, #3), 7.11 (dd, *J* = 5.1, 3.6 Hz, 2H, #4), 6.43 (s, 4H, #5), 3.96 (t, *J* = 5.3 Hz, 8H, #6), 2.60 – 2.55 (m, 4H), 1.63 – 1.57 (m, 10H), 1.26 (d, *J* = 6.3 Hz, 48H), 1.11 (dd, *J* = 16.0, 7.4 Hz, 8H), 0.90 – 0.85 (m, 14H), 0.73 – 0.67 (m, 6H). **<sup>13</sup>C NMR{H}** (126 MHz, CDCl<sub>3</sub>) δ 161.62, 161.35, 155.31, 145.82, 140.87, 140.36, 136.81, 128.56, 128.28, 127.85, 127.35, 126.08, 123.98, 109.77, 105.12, 69.07, 37.14, 32.09, 31.44, 29.86, 29.85, 29.83, 29.81, 29.79, 29.73, 29.72, 29.53, 28.81, 28.72, 28.01, 27.82, 26.35, 22.86, 14.29. **HRMS** (IMS QTOF): Calculated for C<sub>84</sub>H<sub>114</sub>N<sub>2</sub>O<sub>8</sub>S<sub>2</sub>Na<sup>+</sup>: 1365.7909. Found *m/z* 1365.7896 [M+Na]<sup>+</sup>. Structure confirmed by **X-ray**

**crystallography** (crystals were grown in an NMR tube by layering methanol on top of a solution of **E-NDI-T monomer** in chloroform).

### Reference Monomer Synthesis<sup>10</sup>



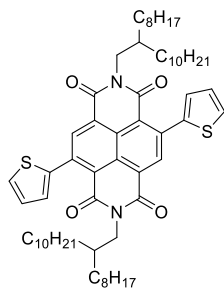
### N,N'-bis(2-octyldodecyl)-2,6-dibromo-1,4,5,8-naphthalene diimide (**Br<sub>2</sub>-NDI-2OD**)<sup>10</sup>



Under Argon to a single-necked 500 mL round-bottomed flask equipped with reflux condenser, **Br<sub>2</sub>-NDA** (4.08 g, 9.5781 mmol) and 2-octyldodecylamine (9.85 g, 33.1013 mmol) were added and it was degassed for 10 min. Next,  $\text{AcOH}$  (200 mL) was added and it was heated to  $120^\circ\text{C}$  until all solids dissolved (~2.5 hours). The reaction mixture was purified using column chromatography (silica, chloroform) and the product fractions were concentrated in vacuo. Lastly, the solids were sonicated in acetone (3x) and collected by filtration to afford the product (2.05 g, 2.0762 mmol, 22%).

**<sup>1</sup>H NMR** (400 MHz,  $\text{CDCl}_3$ )  $\delta$  9.00 (s, 2H), 4.15 (d,  $J = 7.3$  Hz, 4H), 1.99 (s, 2H), 1.41 – 1.17 (m, 64H), 0.89 – 0.83 (m, 12H). **HRMS** (IMS QTOF): Calculated for  $\text{C}_{54}\text{H}_{84}\text{Br}_2\text{N}_2\text{O}_4^+$ : 982.4798. Found  $m/z$  982.4778 [M]<sup>+</sup>.

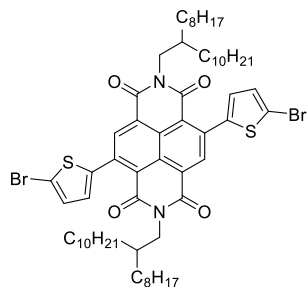
**N,N'-bis(2-octyldodecyl)-2,6-bis(thiophen-2-yl)-1,4,5,8-naphthalene diimide (Th<sub>2</sub>-NDI-2OD)<sup>273</sup>**



Under Argon, to a 25 mL microwave vial, NDI2OD-Br<sub>2</sub> (400 mg, 0.4061 mmol), Pd(PPh<sub>3</sub>)<sub>2</sub>Cl<sub>2</sub> (6.6 mg, 0.0093 mmol) were added and it was degassed for 10 min. Next, 2-(Tributylstannylyl)thiophene (0.31 mL, 0.9783 mmol) and dry THF (9 mL) were added and it was heated at 75 °C for 16 h. The reaction mixture was concentrated *in vacuo*, crystallized from the minimal amount of <sup>i</sup>PrOH and collected by filtration (wash with MeOH). The product was dried under high vacuum and obtained as an orange solid (366 mg, 0.3692 mmol, 91%).

**<sup>1</sup>H NMR** (500 MHz, CDCl<sub>3</sub>) δ 8.76 (s, 2H), 7.56 (dd, *J* = 5.1, 1.2 Hz, 2H), 7.29 (dd, *J* = 3.6, 1.2 Hz, 2H), 7.19 (dd, *J* = 5.1, 3.6 Hz, 2H), 4.06 (d, *J* = 7.4 Hz, 4H), 1.97 – 1.89 (m, 2H), 1.33 – 1.16 (m, 64H), 0.86 (q, *J* = 7.1 Hz, 12H). **<sup>13</sup>C NMR{H}** (126 MHz, CDCl<sub>3</sub>) δ 162.72, 162.52, 140.96, 140.38, 136.79, 128.36, 128.18, 127.61, 127.57, 125.54, 123.54, 45.04, 36.60, 32.06, 32.04, 31.72, 31.70, 30.20, 30.20, 29.81, 29.78, 29.76, 29.70, 29.49, 29.46, 26.53, 22.83, 22.81, 14.26. **HRMS** (IMS QTOF): Calculated for C<sub>62</sub>H<sub>90</sub>N<sub>2</sub>O<sub>4</sub>S<sub>2</sub><sup>+</sup>: 990.6342. Found *m/z* 990.6322 [M]<sup>+</sup>.

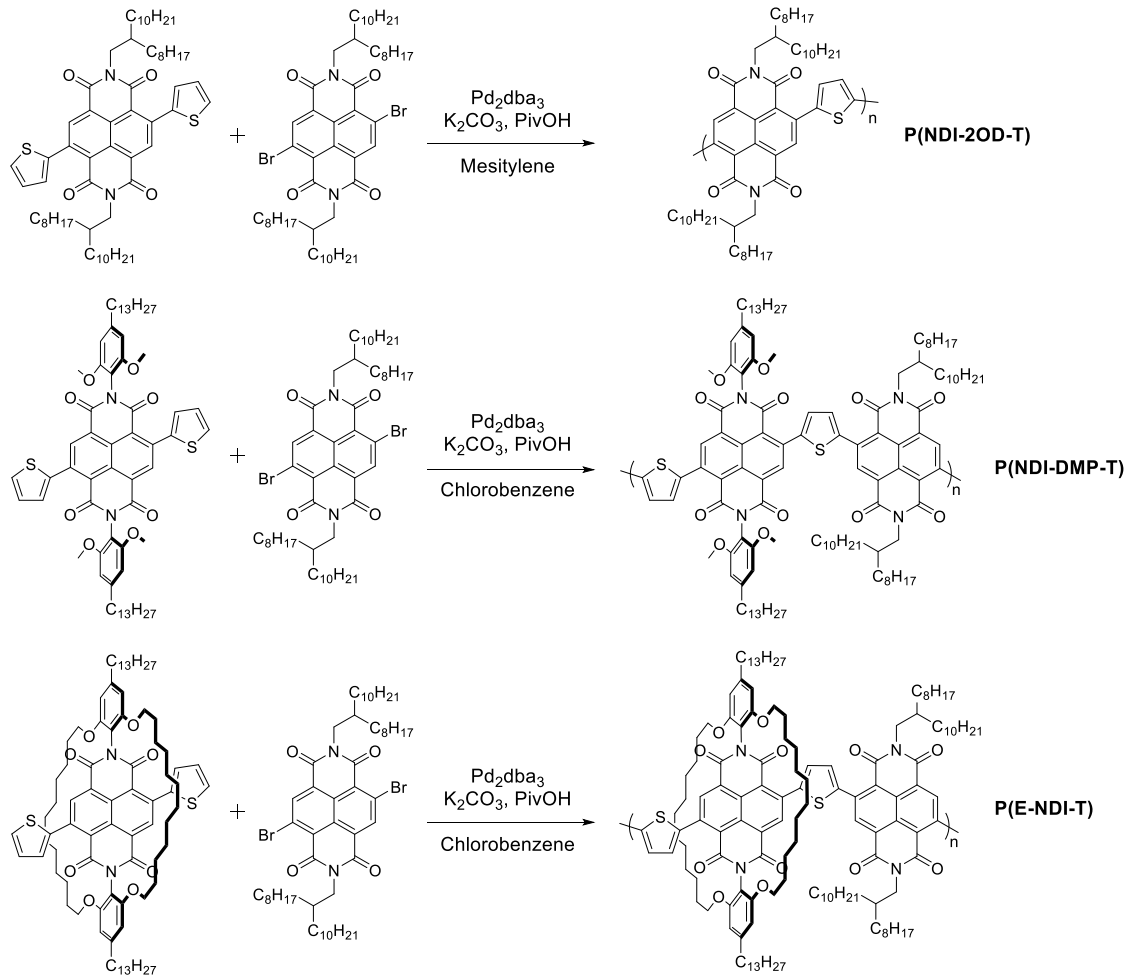
**N,N'-bis(2-octyldodecyl)-2,6-bis(5-bromothiophen-2-yl)-1,4,5,8-naphthalene diimide (Br<sub>2</sub>Th<sub>2</sub>-NDI-2OD)<sup>273</sup>**



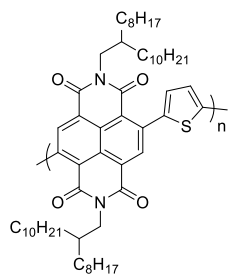
Under Argon, NDI2OD-Th<sub>2</sub> (365 mg, 0.3681 mmol) was dissolved in chloroform (11 mL) and AcOH (11 mL). To this, NBS (163.8 mg, 0.9203 mmol) was added in one portion and it was stirred for 16 h at 60 °C. The orange solution turned dark red. The reaction mixture was concentrated in vacuo, sonicated in MeOH (2x) and collected by filtration. Next, the solids were boiled in ethanol and collected by filtration again. Lastly, the solids were purified by column chromatography (silica, 1:1 DCM/Hexane) to afford the product as pure, dark red/purple solids (321 mg, 0.2793 mmol, 76%).

**<sup>1</sup>H NMR** (400 MHz, CDCl<sub>3</sub>) δ 8.72 (s, 2H), 7.14 (d, *J* = 3.7 Hz, 2H), 7.08 (d, *J* = 3.7 Hz, 2H), 4.07 (d, *J* = 7.2 Hz, 4H), 1.94 (s, 2H), 1.25 (d, *J* = 20.3 Hz, 64H), 0.86 (q, *J* = 6.3 Hz, 12H). **HRMS (IMS QTOF)**: Calculated for C<sub>82</sub>H<sub>115</sub>N<sub>2</sub>O<sub>8</sub>S<sub>2</sub><sup>79</sup>Br<sup>81</sup>Br<sup>+</sup>: 1171.4429 Found *m/z* 1171.4436 [M+Na]<sup>+</sup>.

### Polymer Synthesis



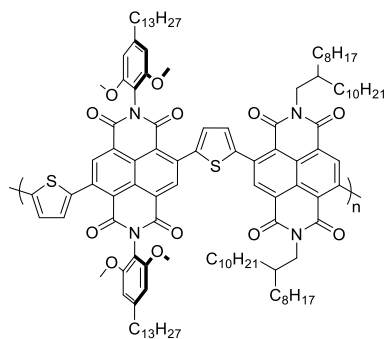
### P(NDI-2OD-T)



To a pre-dried μw vial under argon, Br<sub>2</sub>-NDI (75 mg, 0.0761 mmol), encapsulated Th<sub>2</sub>-NDI (79 mg, 0.0797 mmol, 1.05 eq.), K<sub>2</sub>CO<sub>3</sub> (31.6 mg, 0.2283 mmol), PivOH (7.8 mg, 0.0761 mmol) and Pd<sub>2</sub>dba<sub>3</sub> (0.7 mg, 7.64x10<sup>-4</sup> mmol) were added and it was degassed for 30 minutes. Next, degassed

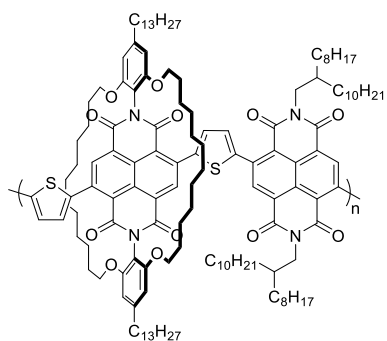
mesitylene (1.3 mL) was added and the mixture was stirred for 5 minutes at room temperature. The mixture was then placed into a pre-heated (120 °C) oil bath and left stirring for 48 h. After cooling to room temperature, the polymer was precipitated into stirring methanol (200 mL), filtered and purified by soxhlet extraction with acetone (100 °C) and chloroform (100 °C). The chloroform fraction was concentrated *in vacuo*, precipitated in stirring methanol (~150 mL) and collected by filtration to afford a purple-coloured polymer (120.8 mg, 0.0665 mmol, 87%); Mn = 16.1 kDa, Mw = 42.2 kDa, PDI = 2.62.

### P(NDI-DMP-T)



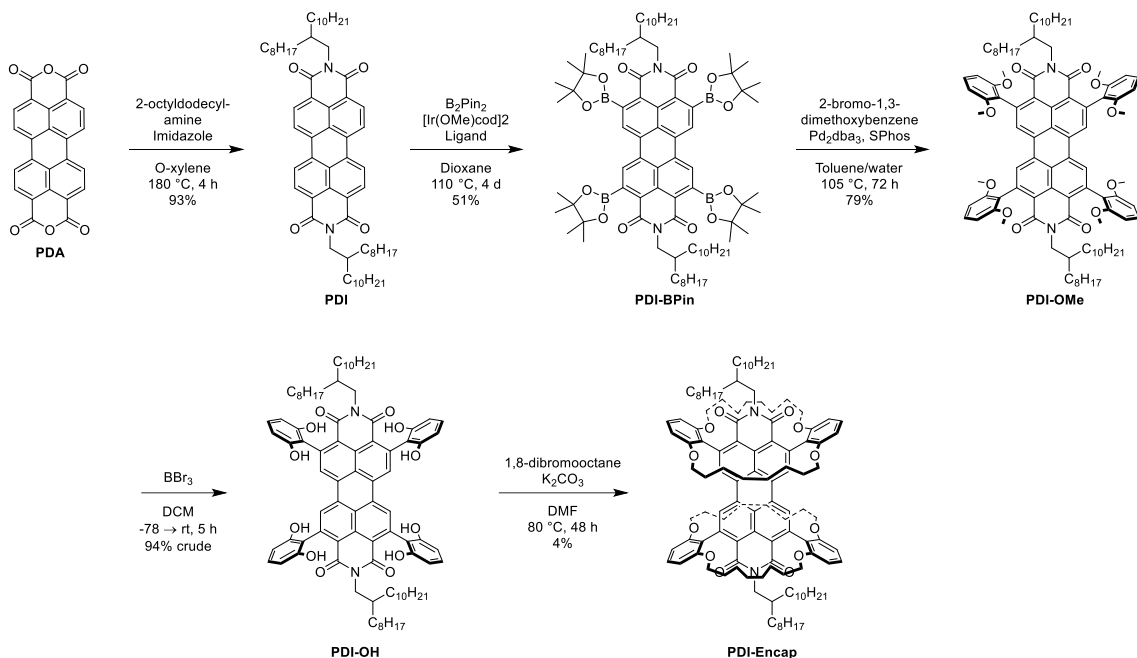
To a pre-dried μw vial under argon, Br<sub>2</sub>-NDI (75 mg, 0.0761 mmol), Th2-NDI-OMe (81.2 mg, 0.0761 mmol), K<sub>2</sub>CO<sub>3</sub> (31.6 mg, 0.2286 mmol), PivOH (7.8 mg, 0.0764 mmol) and anhydrous chlorobenzene (0.2 mL) were added. The mixture was stirred for 10 minutes at room temperature. Next, Pd<sub>2</sub>dba<sub>3</sub> (0.7 mg, 0.7644 μmol) was added and the mixture was placed into a pre-heated (100 °C) oil bath and left stirring for 20 h. After cooling to room temperature, the polymer was dissolved in the minimal amount of chlorobenzene, precipitated into stirring methanol (200 mL), filtered, and purified by soxhlet extraction with acetone (100 °C), hexane (100 °C) and chloroform (100 °C). The chloroform fraction was concentrated *in vacuo*, dissolved in the minimal amount of chlorobenzene, and precipitated into stirring methanol (200 mL) to afford a purple-coloured polymer (48.1 mg, 0.0254 mmol, 33%); Mn = 16.3 kDa, Mw = 29.5 kDa, PDI = 1.81.

### P(E-NDI-T)

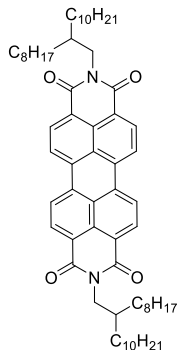


To a pre-dried  $\mu$ w vial under argon, Br<sub>2</sub>-NDI (55 mg, 0.0558 mmol), encapsulated Th<sub>2</sub>-NDI (75 mg, 0.0558 mmol), K<sub>2</sub>CO<sub>3</sub> (23.2 mg, 0.1675 mmol), PivOH (5.7 mg, 0.0558 mmol) and Pd<sub>2</sub>dba<sub>3</sub> (0.5 mg, 5.46x10<sup>-4</sup> mmol) were added and it was degassed for 30 minutes. Next, anhydrous chlorobenzene (0.15 mL) was added, and the mixture was stirred for 5 minutes at room temperature. The mixture was then placed into a pre-heated (100 °C) oil bath and left stirring for 14 h. After cooling to room temperature, the polymer was dissolved in the minimal amount of chlorobenzene, precipitated into stirring methanol (200 mL), filtered, and purified by soxhlet extraction with acetone (100 °C), hexane (100 °C) and chloroform (100 °C). The chloroform fraction was concentrated *in vacuo*, dissolved in the minimal amount of chlorobenzene, and precipitated into stirring methanol (200 mL) to afford a red-purple coloured polymer (79.8 mg, 0.0368 mmol, 66%); Mn = 14.6 kDa, Mw = 38.4 kDa, PDI = 2.46.

## Experimental Procedures: Chapter IV



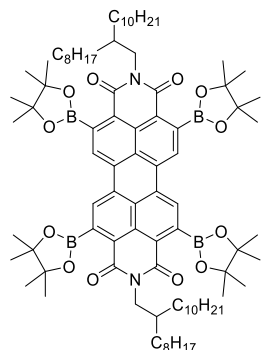
### Synthesis of N,N'-bis(2-octyldodecyl)-perylene-3,4,9,10-bis(dicarboxidamide) (PDI)<sup>205</sup>



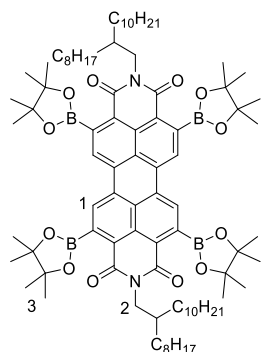
Under argon, a mixture of 3,4,9,10-perylenetetracarboxylic dianhydride (3.00 g, 7.6468 mmol), 2-octyldodecylamine (5.60 g, 18.8190 mmol), o-xylene (13.5 mL), and imidazole (4.12 g, 60.5170 mmol) was stirred at 180 °C for 4 h. Upon cooling to room temperature, MeOH (~100 mL) was added to the reaction mixture and it was sonicated and filtered. The red-coloured, clumpy solids were sonicated in MeOH and filtered three more times to obtain a more fine, red powdered solid. Lastly, the crude product was purified via column chromatography on silica using DCM and hexane (gradual column; 50% → 100% DCM). The product was obtained a red solid (6.80 g, 7.1471 mmol, 93 %).

**<sup>1</sup>H NMR** (400 MHz, CDCl<sub>3</sub>) δ 8.64 (d, *J* = 8.0 Hz, 4H), 8.56 (d, *J* = 8.1 Hz, 4H), 4.14 (d, *J* = 7.2 Hz, 4H), 2.01 (s, 2H), 1.29 (dd, *J* = 55.7, 14.7 Hz, 64H), 0.84 (t, *J* = 6.7 Hz, 12H). **HRMS** (ASAP-TOF): Calculated for C<sub>64</sub>H<sub>91</sub>N<sub>2</sub>O<sub>4</sub><sup>+</sup>: 951.6970. Found *m/z* 951.6979 [M+H]<sup>+</sup>.

**Synthesis of N,N'-bis(2-octyldodecyl)-2,5,8,11-tetrakis(4,4,5,5-tetramethyl-1,3,2-dioxaborolan-2-yl)-perylene-3,4,9,10-tetracarboxylic acid diimide (PDI-BPin)**

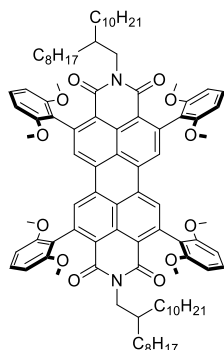


In a glovebox, PDI (5.00 g, 5.2552 mmol), [Ir(OMe)cod]<sub>2</sub> (105.0 mg, 0.1584 mmol), tris(pentafluorophenyl)phosphine (336.3 mg, 0.6319 mmol) and bis(pinacolato)diboron (10.68 g, 42.0517 mmol) were stirred in dry dioxane (125 mL) at 110 °C for 4 days. The solvent was removed under reduced pressure, and the residue was purified by trituration from hot <sup>i</sup>PrOH and a minimal amount of DCM. After cooling to room temperature, the solids were collected by filtration. The product was obtained as a red solid (3.90 g, 2.6774 mmol, 51%).

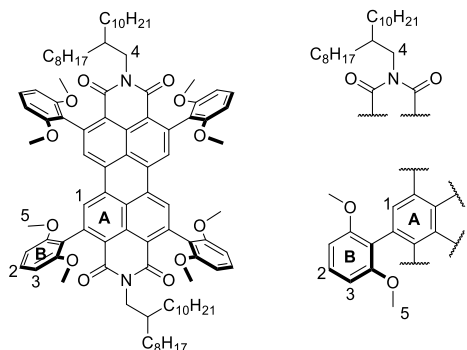


**<sup>1</sup>H NMR** (500 MHz, CDCl<sub>3</sub>) δ 8.53 (s, 4H, #1), 4.06 (d, *J* = 6.8 Hz, 4H, #2), 1.97 (m, 2H), 1.55 (s, 48H, #3), 1.45 – 1.21 (m, 64H), 0.87 (dd, *J* = 7.0, 6.3 Hz, 12H). **<sup>13</sup>C NMR{H}** (125 MHz, CDCl<sub>3</sub>) δ 165.7, 138.7, 133.5, 128.1, 126.9, 126.6, 126.1, 84.7, 44.6, 36.8, 32.12, 32.08, 32.0, 30.2, 29.9, 29.5, 26.4, 25.2, 22.9, 14.3. **HRMS** (ASAP-TOF): Calculated for C<sub>88</sub>H<sub>135</sub>B<sub>4</sub>N<sub>2</sub>O<sub>12</sub><sup>+</sup>: 1456.0394. Found *m/z* 1456.0387 [M+H]<sup>+</sup>. **Anal. Calcd.** for C<sub>88</sub>H<sub>134</sub>B<sub>4</sub>N<sub>2</sub>O<sub>12</sub>: C, 72.63; H, 9.28; N, 1.92. Found: C, 72.55; H, 9.30; N, 2.16 (average of two runs).

**Synthesis of N,N'-Bis(2-octyldodecyl)-2,5,8,11-tetrakis(2-(1,3-dimethoxybenzene))perylene-3,4,9,10-tetracarboxylic acid diimide (PDI-OMe)**

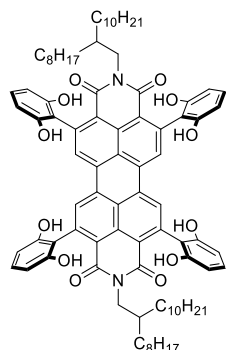


Under argon, PDI-BPin (3.60 g, 2.4737 mmol), Pd<sub>2</sub>dba<sub>3</sub> (453.0 mg, 0.4947 mmol), K<sub>2</sub>CO<sub>3</sub> (3.42 g, 24.7370 mmol), Sphos (434.3 mg, 1.0600 mmol) and 2-bromo-1,3-dimethoxybenzene (18.03 g, 83.0688 mmol) were stirred in toluene (144 mL) and water (36 mL) at 105 °C for 72 h. After cooling to room temperature, water was added, and the reaction mixture was extracted with DCM (2 x). The organic layers were washed with brine, dried over MgSO<sub>4</sub>, and concentrated *in vacuo*. The crude product was purified by column chromatography on silica using DCM. Next, the solids were triturated from hot <sup>i</sup>PrOH and a minimal amount of DCM and collected by filtration. Lastly, the product was sonicated in methanol, collected by filtration, and dried in *vacuo* to afford orange-coloured solids (2.91 g, 1.9455 mmol, 79%).

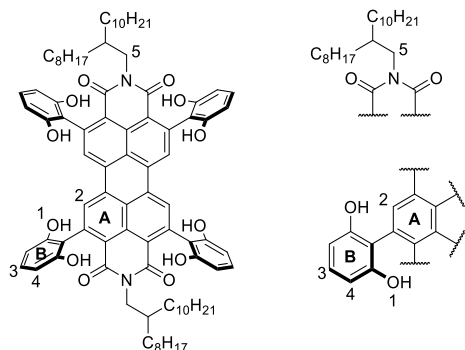


**<sup>1</sup>H NMR** (500 MHz, CDCl<sub>3</sub>) δ 8.23 (s, 4H, #1), 7.38 (t, *J* = 8.4 Hz, 4H, #2), 6.72 (d, *J* = 8.5 Hz, 8H, #3), 3.90 (d, *J* = 7.5 Hz, 4H, #4), 3.70 (s, 24H, #5), 1.88 – 1.77 (m, 2H), 1.26 – 1.13 (m, 64H), 0.85 (td, *J* = 7.0, 5.2 Hz, 12H). **<sup>13</sup>C NMR{H}** (125 MHz, CDCl<sub>3</sub>) δ 163.1, 156.8, 140.4, 133.6, 131.4, 129.1, 128.4, 125.9, 122.0, 120.7, 104.5, 56.1, 44.0, 36.2, 32.06, 32.05, 31.2, 30.4, 29.9, 29.82, 29.80, 29.51, 29.46, 26.5, 22.8, 14.3. **HRMS** (ASAP-TOF): Calculated for C<sub>96</sub>H<sub>123</sub>N<sub>2</sub>O<sub>12</sub><sup>+</sup>: 1495.9056. Found *m/z* 1495.9076 [M+H]<sup>+</sup>. Structure confirmed by **X-ray crystallography** (crystals were grown in an NMR tube by layering methanol on top of a solution of **PDI-OMe** in chloroform).

**Synthesis of N,N'-Bis(2-octyldodecyl)-2,5,8,11-tetrakis(2-resorcinol)perylene-3,4,9,10-tetracarboxylic acid diimide (PDI-OH)**

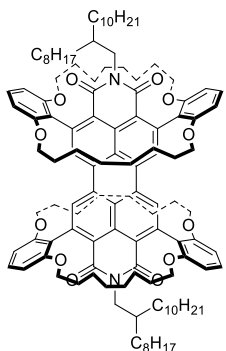


To a 25 mL  $\mu$ w vial under argon, BBr<sub>3</sub> (1M in DCM, 5.34 mL) was added dropwise to a solution of PDI-OMe (400 mg, 0.2674 mmol) in anhydrous DCM (4.8 mL) at -78 °C. The reaction was then left to warm to room temperature and stirred for 5 h. The reaction mixture was slowly poored into a pre-stirring saturated NaHCO<sub>3</sub> solution (~200 mL) and it was extracted with DCM (2x). The organic phase was washed with brine, dried over MgSO<sub>4</sub> and concentrated and dried *in vacuo* to afford the product as a red solid (347 mg, 0.2505 mmol, 94% crude). The crude was used in the subsequent step without further purification.

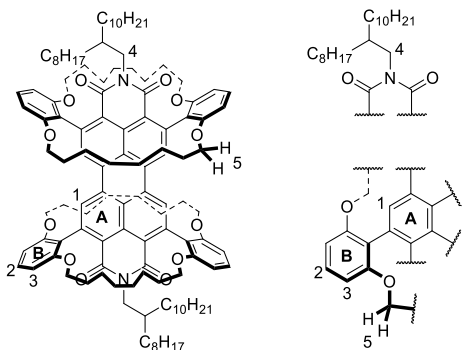


**<sup>1</sup>H NMR** (400 MHz, DMSO)  $\delta$  9.03 (s, 8H, #1), 8.34 (s, 4H, #2), 6.97 (t,  $J$  = 8.1 Hz, 4H, #3), 6.41 (d,  $J$  = 8.2 Hz, 8H, #4), 3.76 (d,  $J$  = 6.4 Hz, 4H, #5), 1.76 (m, 2H), 1.19 (dd,  $J$  = 29.2, 7.7 Hz, 6H), 0.81 (dd,  $J$  = 7.0, 6.0 Hz, 12H). **<sup>13</sup>C NMR{H}** (125 MHz, DMSO)  $\delta$  162.1, 154.5, 141.2, 131.9, 130.3, 128.4, 127.9, 124.3, 121.7, 117.6, 106.7, 31.34, 31.30, 30.7, 30.6, 29.40, 29.35, 29.1, 29.04, 29.02, 28.96, 28.7, 28.63, 25.57, 25.5, 22.09, 22.09, 14.0, 13.9. **HRMS** (MALDI-TOF): Calculated for C<sub>88</sub>H<sub>107</sub>N<sub>2</sub>O<sub>12</sub><sup>+</sup>: 1383.7819. Found *m/z* 1384.0034 [M+H]<sup>+</sup>.

### Synthesis of Double Encapsulated PDI (PDI-Encap)



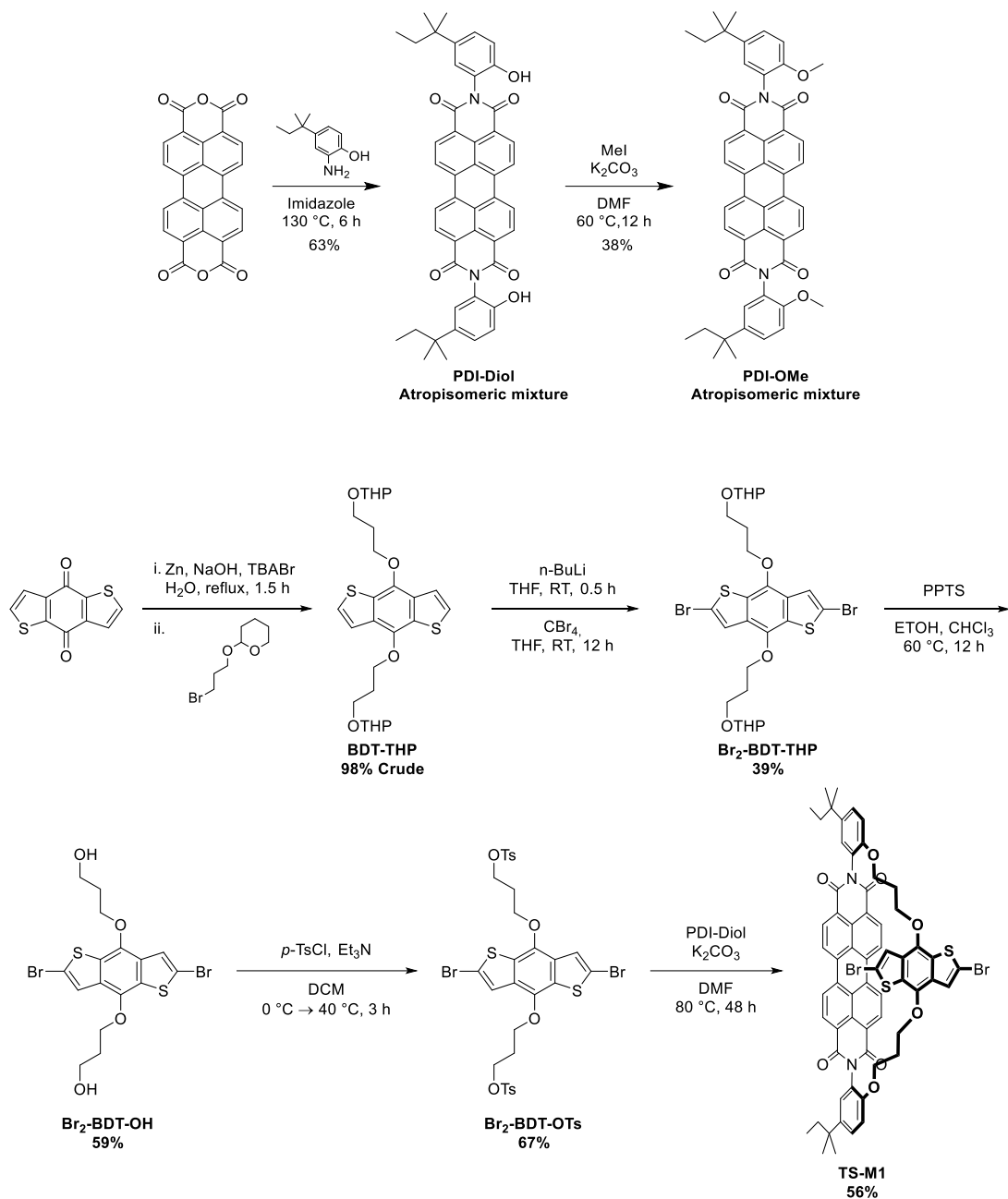
Under argon, PDI-OH (850 mg, 0.6142 mmol) and K<sub>2</sub>CO<sub>3</sub> (1.6964 g, 12.2741 mmol) were stirred in dry DMF (170 mL) and heated to 50 °C for 1 h. Next, a solution of 1,8-dibromo-octane (0.51 mL, 2.7692 mmol) in dry DMF (170 mL) was added dropwise and the reaction mixture was heated to 80 °C for 48 h. The crude reaction mixture was concentrated in vacuo, absorbed onto silica, and purified by silica column chromatography using DCM and hexane (30% DCM → 50 % DCM in hexane). The product was obtained as an orange solid (43 mg, 0.0236 mmol, 4%).



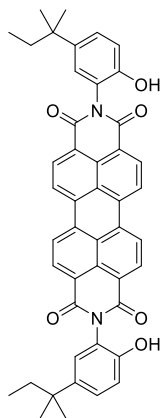
**<sup>1</sup>H NMR** (500 MHz, CDCl<sub>3</sub>) δ 8.34 (s, 4H, #1), 7.32 (t, *J* = 8.3 Hz, 4H, #2), 6.74 (d, *J* = 8.3 Hz, 8H, #3), 4.05 – 3.98 (m, 8H, #5), 3.88 (d, *J* = 7.3 Hz, 4H, #4), 3.76 (td, *J* = 9.1, 3.0 Hz, 8H, #5), 1.80 (dt, *J* = 12.4, 6.1 Hz, 2H), 1.40 (ddd, *J* = 9.4, 8.5, 5.3 Hz, 12H), 1.23 (tdd, *J* = 19.0, 15.0, 6.7 Hz, 56H), 1.13 – 1.04 (m, 12H), 0.87 (td, *J* = 7.0, 4.0 Hz, 12H), 0.82 – 0.62 (m, 32H). **<sup>13</sup>C NMR{H}** (125 MHz, CDCl<sub>3</sub>) δ 162.9, 156.6, 141.7, 133.2, 130.9, 129.0, 128.5, 125.5, 124.4, 121.6, 108.2, 70.7, 44.1, 36.2, 32.09, 32.08, 30.9, 30.7, 30.4, 30.2, 29.89, 29.85, 29.8, 29.54, 29.52, 27.8, 26.2, 22.8, 14.3. **HRMS** (ASAP-TOF): Calculated for C<sub>120</sub>H<sub>163</sub>N<sub>2</sub>O<sub>12</sub><sup>+</sup>: 1824.2201. Found *m/z* 1824.2170 [M+H]<sup>+</sup>. **Anal. Calcd.** for C<sub>120</sub>H<sub>162</sub>N<sub>2</sub>O<sub>12</sub>: C, 78.99; H, 8.95; N, 1.54. Found: C, 78.83; H, 9.02; N, 1.72 (average of two runs). Structure confirmed by **X-ray crystallography** (crystals were grown in an NMR tube by layering methanol on top of a solution of **PDI-Encap** in chloroform).

## Experimental Procedures: Chapter V

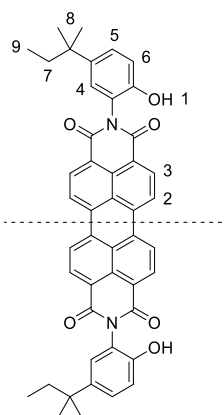
### Synthesis of Through-Space Monomer 1 (TS-M1)



**2,9-bis(2-hydroxy-5-(tert-pentyl)phenyl)perylene-3,4,9,10-tetracarboxylic diimide (PDI-Diol)**



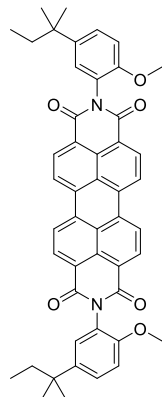
Perylene-3,4,9,10-tetracarboxylic dianhydride (3.00 g, 7.6468 mmol), 2-amino-4-tert-amylphenol (3.43 g, 19.1170 mmol) and imidazole (25 g) were placed in a flask under argon and heated to 130 °C for 6 h. Next, ethanol (20-30 mL) was added, and it was heated to 90 °C for 12 h. The reaction mixture was poured into 1M HCl solution. The solids were collected by filtration and washed with 1M HCl (3x). The solids were then dissolved (mostly) in ethyl acetate, dried over MgSO<sub>4</sub> and concentrated in vacuo. Next, the residue was sonicated in MeOH, filtered, and washed with Et<sub>2</sub>O to afford the product as an atropisomeric mixture and as a fine dark red powder (3.43 g, 4.7984 mmol, 63%). The product was used in the next step without further purification.



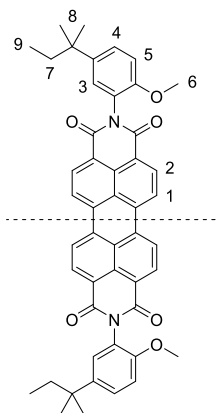
**<sup>1</sup>H NMR** (400 MHz, DMSO) δ 9.45 (s, 2H', #1), 9.34 (s, 2H, #1), 8.84 (s, 4H', #2), 8.65 (s, 4H, #2), 8.52 (d, *J* = 7.9 Hz, 4H', #3), 8.43 (d, *J* = 7.5 Hz, 4H, #3), 7.33 (s, 2H', #4), 7.28 (d, 2H', #5), 7.24 (d, 2H, #5), 7.22 (s, 2H, #4), 6.95 (d, *J* = 8.7 Hz, 2H', #6), 6.91 (d, *J* = 8.4 Hz, 2H, #6), 1.66 – 1.52 (m, 4H'+4H, #7), 1.25 (s, 12H', #8), 1.21 (s, 12H, #8), 0.70 (m, *J* = 7.0 Hz, 6H'+6H, #9). Minor atropisomer'. **<sup>13</sup>C NMR{H}** (100 MHz, DMF) δ 163.98, 163.82, 152.65, 152.37, 141.51, 141.28, 135.28, 134.95, 131.71, 131.44, 130.27, 129.76, 129.56, 129.02, 128.12, 127.98, 127.96, 127.07, 126.61, 124.82, 124.76, 124.48, 123.75, 123.54, 117.15, 116.74, 38.20, 38.18, 37.88, 37.82, 29.25, 29.16, 9.97, 9.89. **HRMS** (ASAP-TOF): Calculated for C<sub>46</sub>H<sub>39</sub>N<sub>2</sub>O<sub>6</sub><sup>+</sup>:

715.2808. Found  $m/z$ : 715.2817 [M+H]<sup>+</sup>. Structure confirmed by **X-ray crystallography** (crystals were grown in an NMR tube by slow evaporation from a DMF solution).

**2,9-bis(2-methoxy-5-(tert-pentyl)phenyl)perylene-3,4,9,10-tetracarboxylic diimide (PDI-OMe)**



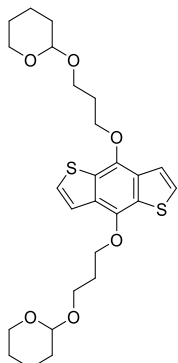
Under argon, PDI-Diol (400 mg, 0.5596 mmol) and K<sub>2</sub>CO<sub>3</sub> (309.4 mg, 2.2383 mmol) were stirred in Dry DMF (10 mL) at 80 °C for 1 h. Next, MeI (0.4 mL, 6.4257 mmol) was added and the reaction was left stirring at 60 °C for 12 h. After cooling to room temperature, the reaction mixture was poured into water (~150 mL) and filtered. The solids were then sonicated in MeOH and collected by filtration again. Next, the crude was purified via silica column chromatography using DCM and EtOAc (slow column first using 100% DCM and then 1-2% EtOAc). The product eluted with 2% EtOAc, concentrated *in vacuo*, sonicated in MeOH, and collected by filtration to afford a red solid material (160 mg, 0.2154 mmol, 38%).



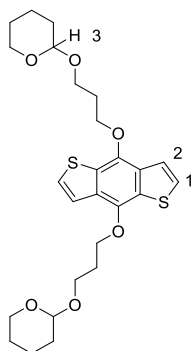
**<sup>1</sup>H NMR** (400 MHz, CDCl<sub>3</sub>) δ 8.75 (d,  $J$  = 7.9 Hz, 4H, #1), 8.68 (d,  $J$  = 8.1 Hz, 4H, #2), 7.43 (d,  $J$  = 8.5 Hz, 2H, #3), 7.23 (d,  $J$  = 5.1 Hz, 2H, #4), 7.05 (d,  $J$  = 8.7 Hz, 2H, #5), 3.79 (s, 6H, #6), 1.66 (q,  $J$  = 7.4 Hz, 4H, #7), 1.31 (s, 12H, #8), 0.78 (t,  $J$  = 7.3 Hz, 6H, #9). **HRMS** (ASAP-TOF): Calculated for C<sub>48</sub>H<sub>42</sub>N<sub>2</sub>O<sub>6</sub><sup>+</sup>: 742.3043. Found  $m/z$ : 742.3062 [M]<sup>+</sup>. **<sup>13</sup>C NMR{H}** (176 MHz, CDCl<sub>3</sub>) δ 163.39, 163.37, 152.74, 152.70, 142.41, 142.40, 134.98, 134.94, 131.85, 131.81, 130.13, 130.09, 127.87, 127.84, 127.82, 127.75, 126.86, 126.82, 123.87, 123.26, 111.62, 111.58,

56.03, 56.01, 37.58, 37.23, 28.60, 28.59, 9.37. **Anal. Calcd.** for C<sub>48</sub>H<sub>42</sub>N<sub>2</sub>O<sub>6</sub>: C, 77.61; H, 5.70; N, 3.77; O, 12.92. Found: C, 76.76; H, 5.50; N, 3.65. (average of two runs).

**4,8-bis(2-((oxy)propoxy)tetrahydro-2H-pyran)benzo[1,2-b:4,5-b']dithiophene (BDT-THP)**



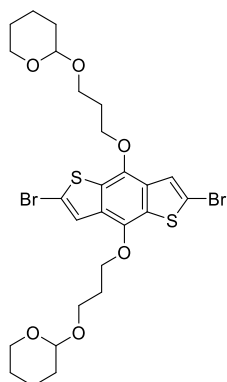
Benzo[1,2-b:4,5-b']dithiophene-4,8-dione (500 mg, 2.27 mmol), zinc powder (390 mg, 5.90 mmol), sodium hydroxide pellets (1.36 g, 34.30 mmol) and TBABr (380 mg, 0.70 mmol) were combined in a round-bottomed flask, which was subsequently evacuated and backfilled with argon 5 times. Next, degassed water (7 mL) was added to the mixture under argon, leading to a yellow suspension (a slight condensation can be observed on the flask walls). Next, the mixture was refluxed for 1.5 h. This first resulted in a colour change to a deep red suspension and later the mixture became biphasic (dark brown upper layer, faint orange/yellow bottom layer). Then, 2-(3-Bromopropoxy)tetrahydro-2H-pyran (2.08 g, 9.32 mmol) was added in one portion to the mixture, causing the reaction to turn black in colour. The reaction mixture was left refluxing overnight (the dark colour slowly dissipates, and the mixture becomes biphasic again). Next, the mixture was cooled to room temperature, diluted with water and extracted with DCM (2 x). The combined organic layer was then dried over MgSO<sub>4</sub> and the solvent was removed under reduced pressure. The THP-protected product was obtained as a transparent, slightly yellow oil (1.13 g, 2.23 mmol, 98% crude) and used as a crude in the subsequent reaction.



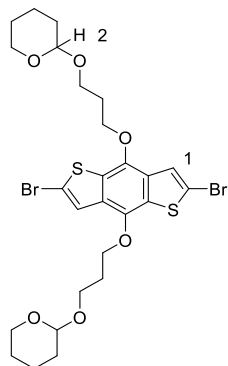
**<sup>1</sup>H NMR** (400 MHz, CDCl<sub>3</sub>) δ 7.51 (d, *J* = 5.5 Hz, 2H, #1), 7.36 (d, *J* = 5.5 Hz, 2H, #2), 4.68 – 4.62 (m, 2H, #3), 4.45 – 4.37 (m, 4H), 4.03 (dt, *J* = 9.8, 6.2 Hz, 2H), 3.87 (ddd, *J* = 11.1, 8.0, 3.2 Hz, 2H), 3.72 (dt, *J* = 9.8, 6.4 Hz, 2H), 3.55 – 3.46 (m, 2H), 2.21 – 2.11 (m, 4H), 1.88 – 1.79 (m,

2H), 1.77 – 1.68 (m, 2H), 1.62 – 1.54 (m, 8H). **HRMS** (ASAP-TOF): Calculated for  $C_{26}H_{34}O_6^{23}Na_1^{32}S_2^+$ : 529.1689. Found  $m/z$ : 529.1686 [M+Na]<sup>+</sup>.

**2,6-dibromo(4,8-bis(2-((oxy)propoxy)tetrahydro-2H-pyran))benzo[1,2-b:4,5-b']dithiophene (Br<sub>2</sub>-BDT-THP)**



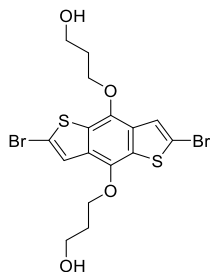
Under argon at -10 °C, n-BuLi (2 mL, 3.2000 mmol) was added dropwise into a solution of **BDT-THP** (600 mg, 1.1842 mmol) in anhydrous THF (8 mL). The mixture changed colour going from transparent to yellow, green and eventually blue/purple. After addition of n-BuLi, the mixture became thicker and more THF (2 mL) was added to keep the mixture stirring. It was stirred at room temperature for 30 minutes, after which a solution of CBr<sub>4</sub> (1.3352 mg, 4.0262 mmol) in anhydrous THF (1.2 mL) was added in one portion. The reaction mixture was left stirring overnight at room temperature. Next, the reaction mixture was washed with water and brine and re-extracted with diethyl ether (2 x). The combined organic layers were concentrated *in vacuo* and absorbed on silica and a very small amount of K<sub>2</sub>CO<sub>3</sub>. The crude was purified with silica column chromatography using hexane and DCM (stepwise column; from hexane to 25%, 50% and finally 100% DCM). The product was eluted in the first few fractions, which were concentrated *in vacuo* to afford the product as a transparent oil (307 mg, 0.4618 mmol, 39%). The product was used in the subsequent reaction without further purification.



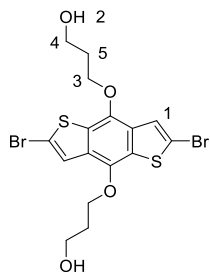
**<sup>1</sup>H NMR** (400 MHz, CDCl<sub>3</sub>) δ 7.50 (s, 2 H, #1), 4.68 – 4.63 (m, 2H, #2), 4.32 (ddd,  $J$  = 8.9, 6.1, 2.9 Hz, 4H), 4.02 (dt,  $J$  = 9.9, 6.0 Hz, 2H), 3.89 (ddd,  $J$  = 11.0, 7.4, 3.5 Hz, 2H), 3.71 – 3.64 (m,

2H), 3.56 – 3.50 (m, 2H), 2.19 – 2.11 (m, 4H), 1.85 (dt,  $J$  = 9.8, 5.7 Hz, 2H), 1.76 (ddd,  $J$  = 12.3, 7.6, 4.4 Hz, 2H), 1.66 – 1.55 (m, 8H). **HRMS** (ASAP-TOF): Calculated for  $C_{26}H_{33}Br_2O_6S_2^+$ : 663.0085. Found  $m/z$ : 663.0052 [M+H]<sup>+</sup>.

**2,6-dibromo(4,8-bis((oxy)propan-1-ol)tetrahydro-2H-pyran)benzo[1,2-b:4,5-b']dithiophene (Br<sub>2</sub>-BDT-OH)**

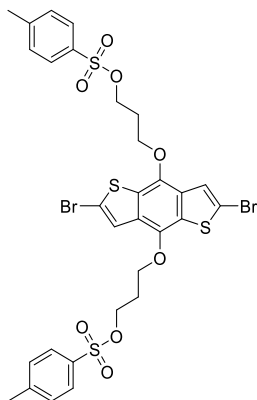


Under argon, Conc. HCl (2 drops) was added to a solution of **Br<sub>2</sub>-BDT-THP** (1.34 g, 2.0106 mmol) and PPTS (1.40 g, 5.5710 mmol) in a mixture of ethanol (50 mL) and CHCl<sub>3</sub> (10 mL). The solution was heated to 60 °C and left stirring for 12 h. Next, the reaction mixture was concentrated *in vacuo* and absorbed onto silica. The crude was purified with silica column chromatography using hexane, DCM and EtOAc (gradual column going very quickly from hexane to 50% and later 100% DCM, and then stepwise to 5%, 10% and 30% EtOAc. The solvents contained a small percentage of Et<sub>3</sub>N during column). The product fraction eluted with 30% EtOAc and was concentrated *in vacuo*. Next, it was sonicated in DCM and filtered while cold to afford the product as a white/beige solid (585 mg, 1.1793 mmol, 59%).

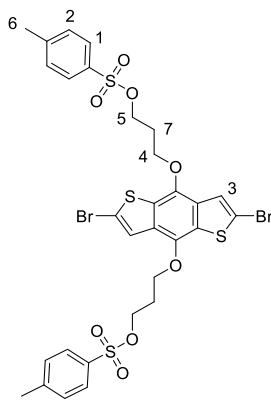


**<sup>1</sup>H NMR** (400 MHz, DMSO) δ 7.77 (s, 2H, #1), 4.61 (s, 2H, #2), 4.30 (t,  $J$  = 6.3 Hz, 4H, #3), 3.64 (m, 4H, #4), 1.91 (p,  $J$  = 6.2 Hz, 4H, #5). **<sup>13</sup>C NMR{H}** (101 MHz, DMSO) δ 142.09, 130.80, 130.00, 123.63, 114.87, 71.14, 57.12, 33.10. **HRMS** (ASAP-TOF): Calculated for  $C_{16}H_{16}O_4Br_2^{32}S_2^+$ : 493.8857. Found  $m/z$ : 493.8877 [M]<sup>+</sup>. Structure confirmed by **X-ray crystallography** (crystals were grown in an NMR tube by slow evaporation from a chloroform solution).

**2,6-dibromo(4,8-bis(oxy)propyl(*p*-toluenesulfonate))benzo[1,2-*b*:4,5-*b'*]dithiophene  
(Br<sub>2</sub>-BDT-OTs)**

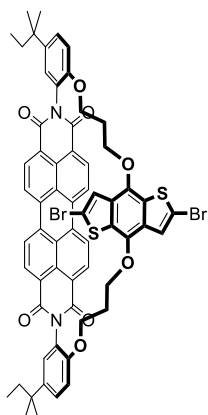


Under argon at -10 °C, degassed Et<sub>3</sub>N (0.16 mL, 1.1587 mmol) was added dropwise into a mixture of **Br<sub>2</sub>-BDT-OH** (360 mg, 0.7256 mmol) and *p*-TsCl (318 mg, 1.6685 mmol) in anhydrous DCM (6 mL). The mixture allowed to warm to room temperature and sonicated for 2 minutes, after which it was heated for 12 h at 50 °C (the reaction mixture goes into solution after ~ 1 h). Next, the reaction mixture was concentrated *in vacuo* and absorbed onto silica. The crude was purified with silica column chromatography using hexane and DCM as solvents (stepwise column going from hexane to 50%, 70% and finally 100% DCM). The product fractions were concentrated *in vacuo*, sonicated in MeOH and collected by filtration affording the product as white/beige solids (389 mg, 0.4833 mmol, 67%).



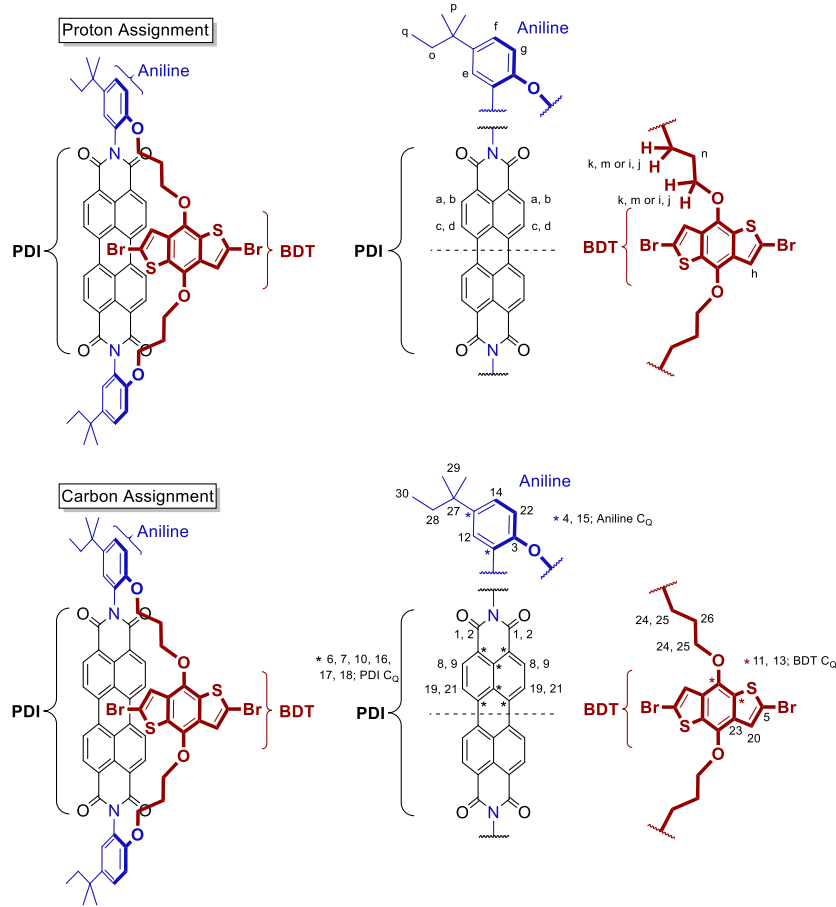
*R<sub>f</sub>* = 0.68 (DCM). **<sup>1</sup>H NMR** (500 MHz, CDCl<sub>3</sub>) δ 7.86 – 7.83 (m, 4H, #1), 7.37 (s, 2H, #2), 7.36 (dd, *J* = 8.6, 0.6 Hz, 4H, #3), 4.37 (t, *J* = 6.0 Hz, 4H, #4), 4.26 (t, *J* = 5.9 Hz, 4H, #5), 2.45 (s, 6H, #6), 2.21 (dd, *J* = 12.0, 6.0 Hz, 4H, #7). **<sup>13</sup>C NMR{H}** (126 MHz, CDCl<sub>3</sub>) δ 145.11, 142.08, 132.98, 131.17, 130.60, 130.08, 128.07, 123.01, 115.54, 69.31, 66.88, 30.10, 21.83. **HRMS** (ASAP-TOF): Calculated for C<sub>30</sub>H<sub>29</sub>Br<sub>2</sub>O<sub>8</sub>S<sub>4</sub><sup>+</sup>: 802.9107. Found *m/z*: 802.9112 [M+H]<sup>+</sup>. **Anal. Calcd.** for C<sub>30</sub>H<sub>28</sub>Br<sub>2</sub>O<sub>8</sub>S<sub>4</sub>: C, 44.78; H, 3.51; Br, 19.86; O, 15.91; S, 15.94. Found: C, 44.51; H, 3.39; N, <0.2. (average of two runs).

### Through-Space Monomer 1 (TS-M1)

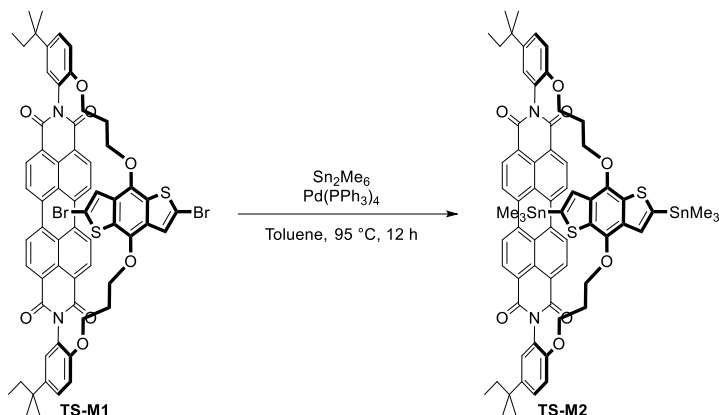


Under argon,  $\text{K}_2\text{CO}_3$  (280.3 mg, 2.0280 mmol) was added in one portion to a stirring solution of PDI-Diol (271.6 mg, 0.3800 mmol) and  $\text{Br}_2\text{-BDT-OTs}$  (327.0 mg, 0.4078 mmol) in anhydrous DMF (140 mL). Next, the mixture was heated to 80 °C and left stirring for 48 h. The reaction mixture was concentrated *in vacuo*, absorbed onto a minimal amount of silica, and purified on silica column chromatography using hexane and DCM (stepwise column going from hexane to 50%, 80% and finally 100% DCM). The product fractions were concentrated *in vacuo*. Next it was sonicated in MeOH and collected by filtration to afford the product as a dark red/pink solid (249.0 mg, 0.2124 mmol, 56%).

**$^1\text{H NMR}$**  (500 MHz,  $\text{CDCl}_3$ )  $\delta$  8.66 (d,  $J = 7.9$  Hz, 2H, #a), 8.60 (d,  $J = 7.9$  Hz, 2H, #b), 8.32 (d,  $J = 8.2$  Hz, 2H, #c), 8.23 (d,  $J = 8.2$  Hz, 2H, #d), 7.46 (d,  $J = 2.4$  Hz, 2H, #e), 7.43 (dd,  $J = 8.5$ , 2.4 Hz, 2H, #f), 7.06 (d,  $J = 8.5$  Hz, 2H, #g), 6.55 (s, 2H, #h), 4.09 (dt,  $J = 5.9$ , 4.9 Hz, 2H, #i), 4.03 (ddd,  $J = 9.5$ , 7.2, 4.3 Hz, 2H, #j), 3.76 (dt,  $J = 8.8$ , 6.4 Hz, 2H, #k), 3.67 (dt,  $J = 8.8$ , 6.4 Hz, 2H, #l), 2.01 – 1.88 (m, 4H, #m), 1.72 (q,  $J = 7.4$  Hz, 4H, #n), 1.37 (s, 12H, #o), 0.82 (t,  $J = 7.4$  Hz, 6H, #p).  **$^{13}\text{C NMR}\{\text{H}\}$**  (126 MHz,  $\text{CDCl}_3$ )  $\delta$  164.35 (#1), 164.28 (#2), 151.28 (#3), 143.69 (#4, Aniline C<sub>Q</sub>), 141.48 (#5), 134.24 (#6, PDI C<sub>Q</sub>), 134.07 (#7, PDI C<sub>Q</sub>), 131.71 (#8), 131.16 (#9), 129.78 (#10, PDI C<sub>Q</sub>), 129.05 (#11, BDT C<sub>Q</sub>), 128.27 (#12), 128.06 (#13, BDT C<sub>Q</sub>), 127.79 (#14), 126.15 (#15, Aniline C<sub>Q</sub>), 126.00 (#16, PDI C<sub>Q</sub>), 123.57 (#17, PDI C<sub>Q</sub>), 123.25 (#18, PDI C<sub>Q</sub>), 122.85 (#19), 122.77 (#20), 122.24 (#21), 115.08 (#22), 114.39 (#23), 71.06 (#24), 67.70 (#25), 37.79 (#26), 37.32 (#27), 31.48 (#28), 28.66 (#29), 9.37 (#30). **HRMS** (ASAP-TOF): Calculated for  $\text{C}_{62}\text{H}_{50}\text{N}_2\text{O}_8\text{Br}_2^{32}\text{S}_2^+$ : 1172.1375. Found  $m/z$ : 1172.1366 [M]<sup>+</sup>.



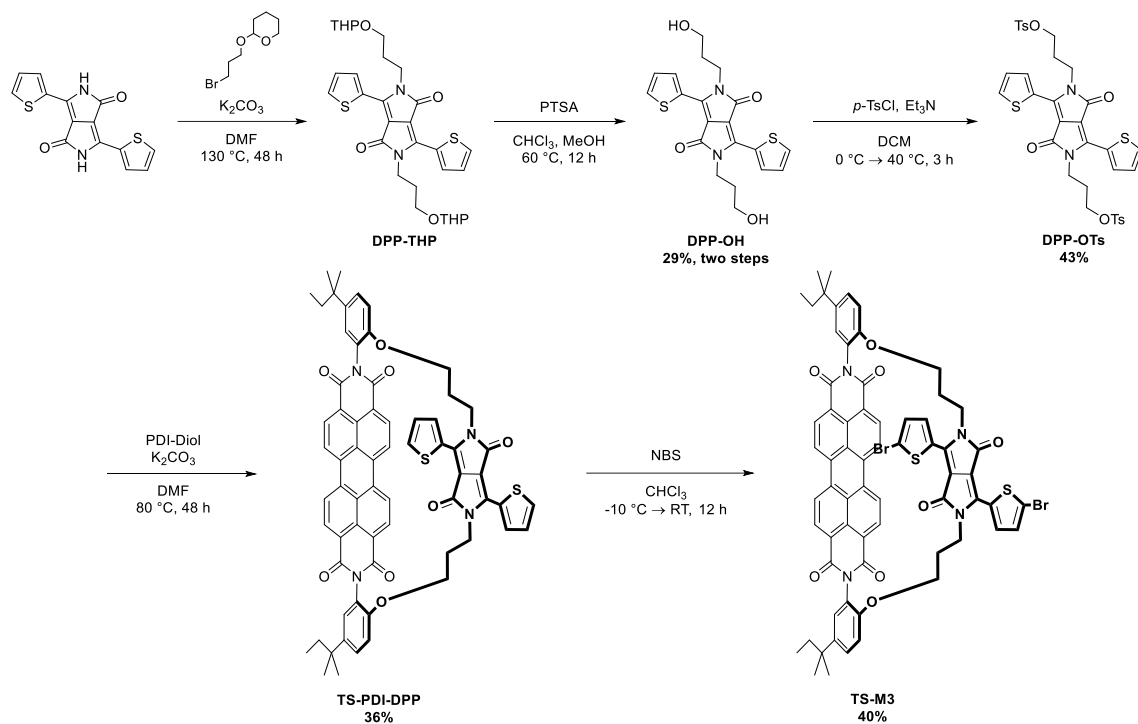
### Synthesis of Through-Space Monomer 2 (TS-M2)



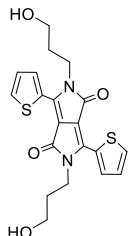
To a microwave vial under argon, dry toluene (12 mL) was added to a mixture of TS-M1 (130 mg, 0.1106 mmol),  $\text{Pd}(\text{PPh}_3)_4$  (12.8 mg, 0.0111 mmol) and hexamethylditin (300 mg, 0.9157 mmol). The reaction mixture was heated to  $95^\circ\text{C}$  and left stirring for 12 h. After cooling the mixture to room temperature, it was poured into stirring MeOH (300 mL) and water (100 mL). The resulting red solids were collected by filtration. Next, the solids were sonicated in hexane and collected by filtration (wash with 50 mL hexane). The crude product (~90% pure by NMR) was obtained as a red solid (98 mg, 0.0730 mmol, 66%) and used in the next step without further purification.

**$^1\text{H NMR}$**  (400 MHz,  $\text{CDCl}_3$ )  $\delta$  8.54 (d,  $J = 7.5$  Hz, 2H), 8.49 (d,  $J = 7.7$  Hz, 2H), 8.13 (d,  $J = 8.0$  Hz, 2H), 8.07 (d,  $J = 7.9$  Hz, 2H), 7.49 – 7.42 (m, 4H), 7.13 (d,  $J = 8.5$  Hz, 2H), 6.74 (s, 2H), 4.06 (t,  $J = 5.1$  Hz, 4H), 3.89 – 3.70 (m, 4H), 1.99 (dd,  $J = 11.7, 5.8$  Hz, 4H), 1.73 (q,  $J = 7.0$  Hz, 4H), 1.38 (s, 12H), 0.83 (t,  $J = 7.3$  Hz, 6H), 0.50 (s+d, 18H). **HRMS** (ASAP-TOF): Calculated for  $\text{C}_{68}\text{H}_{69}\text{N}_2\text{O}_8\text{S}_2\text{Sn}_2^+$ : 1343.2528. Found  $m/z$ : 1343.2479 [ $\text{M}+\text{H}]^+$ .

### Synthesis of Through-Space Monomer 3 (TS-M3)



**2,5-bis(2-(oxy)propan-1-ol)-3,6-di(thiophen-2-yl)pyrrolo[3,4-c]pyrrole-1,4-dione (DPP-OH)**

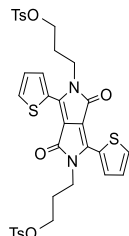


Under argon, a mixture of DPP (1.00 g, 3.3294 mmol),  $K_2CO_3$  (1.40 g, 10.1295 mmol), 2-(3-Bromopropoxy)tetrahydro-2H-pyran (1.69 mL, 10.000 mmol) and dry DMF (20 mL) were stirred at  $130\text{ }^\circ C$  for 48 h. The reaction mixture was concentrated *in vacuo*. Water was added to the residue and it was extracted with DCM (3x) and washed with brine (2x). Next, it was dried over  $MgSO_4$  and concentrated *in vacuo*. Next, the crude THP-protected product (1.00 g, 1.7101 mmol) and PTSA (1.00 g, 5.8072 mmol) were dissolved into  $CHCl_3$  (20 mL) and MeOH (30 mL) and the reaction was left stirring at  $45\text{ }^\circ C$  for 4 h under air. The reaction mixture was extracted with DCM (3x) and washed with 1M HCl (4x). The combined organic layer was dried over  $MgSO_4$  and concentrated *in vacuo*. The sticky residue was solidified by adding hexane and decanting the liquid (3 x 100 mL). The last step was repeated for diethyl ether (2 x 100 mL). The solids were collected by filtration using a 1:1 mixture of ethyl acetate and diethyl ether. Next, the crude product was purified by trituration from acetonitrile (the solids were dissolved in 500 mL boiling

acetonitrile. Charcoal was added, and the solution was filtered through celite. The solution was then reduced to 100 mL and left cooling to room temperature overnight, allowing solid product to crash out). The product was obtained as a dark pink/red coloured solid (402 mg, 0.9655 mmol, 29%).

**<sup>1</sup>H NMR** (700 MHz, DMSO) δ 8.78 (d, *J* = 3.3 Hz, 2H), 8.10 (d, *J* = 4.7 Hz, 2H), 7.44 – 7.35 (dd, *J* = 4.7 Hz, 3.3 Hz, 2H), 4.61 (t, *J* = 5.1 Hz, 2H), 4.10 – 4.02 (t, 4H), 3.50 (dd, *J* = 11.5, 6.0 Hz, 4H), 1.86 – 1.74 (p, 4H). **<sup>13</sup>C NMR** (176 MHz, DMSO) δ 160.86 (C=O), 139.77 (C<sub>Q</sub>), 134.90 (CH), 133.36 (CH), 129.63 (C<sub>Q</sub>), 129.09 (CH), 107.09 (C<sub>Q</sub>), 58.89 (CH<sub>2</sub>), 39.75 (CH<sub>2</sub>), 33.10(CH<sub>2</sub>). **HRMS** (ASAP-TOF): Calculated for C<sub>20</sub>H<sub>21</sub>N<sub>2</sub>O<sub>4</sub>S<sub>2</sub><sup>+</sup>: 417.0943. Found *m/z*: 417.0953 [M+H]<sup>+</sup>. **Anal. Calcd.** for C<sub>20</sub>H<sub>20</sub>N<sub>2</sub>O<sub>4</sub>S<sub>2</sub>: C, 57.67; H, 4.84; N, 6.73; O, 15.36; S, 15.39. Found: C, 56.34; H, 4.89; N, 6.26. (average of two runs).

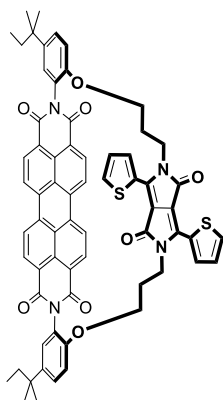
**2,5-bis(2-(oxy)propyl(*p*-toluenesulfonate))-3,6-di(thiophen-2-yl)pyrrolo[3,4-c]pyrrole-1,4-dione (DPP-OTs)**



Under argon, Et<sub>3</sub>N (0.485 mL) was added dropwise to a mixture of DPP-OH (350 mg, 0.8403 mmol) and *p*-TsCl (352 mg, 1.8487 mmol) in dry DCM (20 mL) and it was stirred for 1 h at room temperature and 3 h at 40 °C. The reaction mixture was extracted with DCM (3x) and washed with water (1x), 1M HCl (1x) and brine (2x). The combined organic layers were dried over MgSO<sub>4</sub> and concentrated *in vacuo*. The product was further purified via silica column chromatography (using 5% EtOAc in DCM) and the resulting solids were sonicated in methanol to afford the product as a dark red solid (262 mg, 0.3613 mmol, 43% yield).

**<sup>1</sup>H NMR** (600 MHz, CDCl<sub>3</sub>) δ 8.77 (dd, *J* = 3.9, 1.1 Hz, 2H), 7.78 (d, *J* = 8.3 Hz, 4H), 7.66 (dd, *J* = 5.0, 1.1 Hz, 2H), 7.31 (d, *J* = 8.0 Hz, 4H), 7.29 (dd, *J* = 5.0, 3.9 Hz, 2H), 4.16 (t, *J* = 6.2 Hz, 4H), 4.15 – 4.12 (t, 4H), 2.43 (s, 6H), 2.15 – 2.09 (m, 4H). **<sup>13</sup>C NMR{H}** (176 MHz, CDCl<sub>3</sub>) δ 161.37, 145.04, 139.91, 135.36, 133.01, 131.32, 130.03, 129.37, 128.96, 128.08, 107.78, 68.02, 39.18, 29.48, 21.82. **HRMS** (ASAP-TOF): Calculated for C<sub>34</sub>H<sub>33</sub>N<sub>2</sub>O<sub>8</sub>S<sub>4</sub><sup>+</sup>: 725.1120. Found *m/z*: 725.1085 [M+H]<sup>+</sup>. **Anal. Calcd.** for C<sub>34</sub>H<sub>32</sub>N<sub>2</sub>O<sub>8</sub>S<sub>4</sub>: C, 55.29; H, 4.26; N, 3.73. (average of two runs).

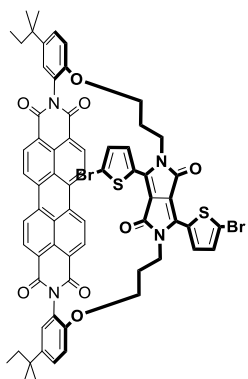
### TS-PDI-DPP



Under argon,  $\text{K}_2\text{CO}_3$  (259.3 mg, 1.8760 mmol) was added in one portion to a stirring solution of PDI-Diol (165 mg, 0.2308 mmol) and DPP-OTs (170 mg, 0.2345 mmol) in anhydrous DMF (40 mL). Next, the mixture was heated to 80 °C and left stirring for 48 h. The reaction mixture was concentrated *in vacuo*. DCM (~30 mL) and water (~30 mL) were added to the residue and it was extracted with DCM (3x) and washed with brine (1x). The combined organic layer was dried over  $\text{MgSO}_4$  and concentrated *in vacuo*. The solids were absorbed onto a minimal amount of silica and purified via silica column chromatography (100% hexane → 100% DCM → 20% EtOAc) to afford the product as a dark red/pink solid (90 mg, mmol, 36% yield).

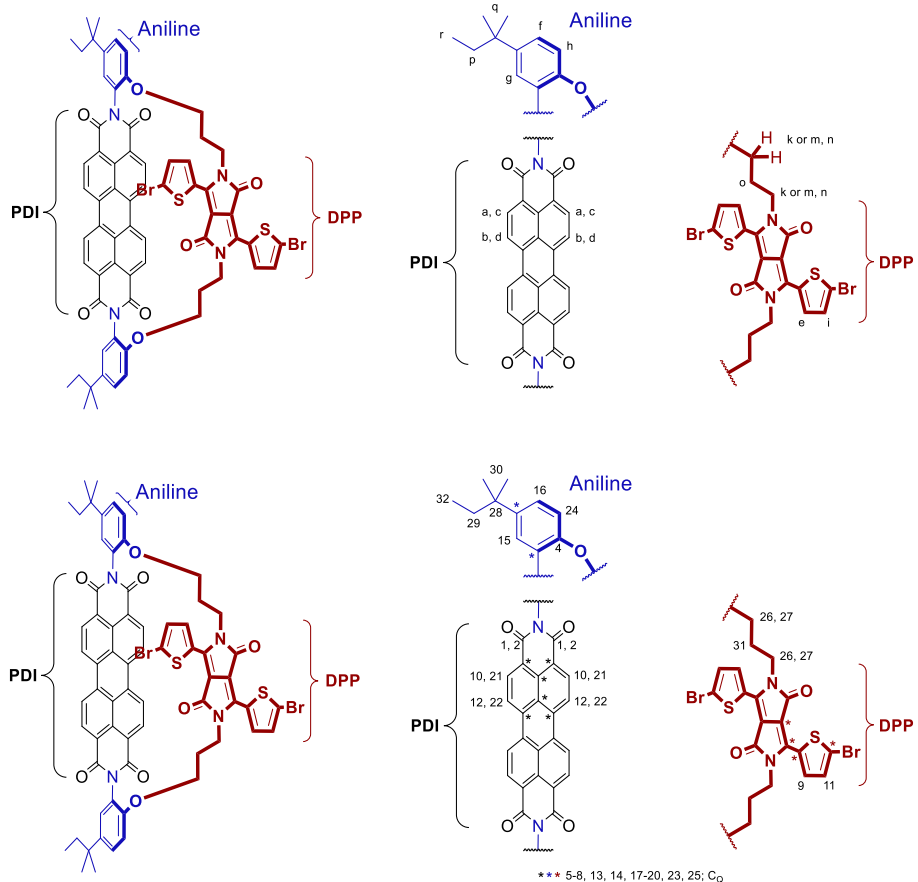
**$^1\text{H NMR}$**  (400 MHz,  $\text{CDCl}_3$ )  $\delta$  8.78 (d,  $J$  = 8.0 Hz, 2H), 8.46 (d,  $J$  = 8.2 Hz, 2H), 8.33 (dd,  $J$  = 3.9, 1.0 Hz, 2H), 8.20 (d,  $J$  = 8.0 Hz, 2H), 8.12 (d,  $J$  = 8.2 Hz, 2H), 7.56 (dd,  $J$  = 5.0, 1.0 Hz, 2H), 7.47 – 7.41 (m, 4H), 7.21 (dd,  $J$  = 4.9, 4.0 Hz, 2H), 7.15 (d,  $J$  = 8.3 Hz, 2H), 4.15 – 4.00 (m, 4H), 3.42 – 3.28 (m, 2H), 3.25 – 3.10 (m, 2H), 1.93 (dt,  $J$  = 14.3, 5.7 Hz, 4H), 1.71 (q,  $J$  = 7.4 Hz, 4H), 1.37 (s, 12H), 0.81 (t,  $J$  = 7.4 Hz, 6H).  **$^{13}\text{C NMR}\{\text{H}\}$**  (176 MHz,  $\text{CDCl}_3$ )  $\delta$  164.02, 163.98, 160.79, 151.54, 144.52, 139.33, 134.53, 134.46, 134.38, 132.13, 131.18, 131.06, 129.78, 129.37, 128.69, 128.36, 127.96, 126.41, 126.26, 124.06, 123.52, 123.26, 122.57, 116.90, 106.86, 68.78, 41.57, 37.84, 37.25, 28.64, 28.63, 28.39, 9.38. **HRMS** (ASAP-TOF): Calculated for  $\text{C}_{66}\text{H}_{53}\text{N}_4\text{O}_8\text{S}_2^+$ : 1093.3305. Found  $m/z$ : 1093.3303 [M]<sup>+</sup>. **Anal. Calcd.** for  $\text{C}_{66}\text{H}_{54}\text{N}_4\text{O}_8\text{S}_2$ : C, 72.38; H, 4.97; N, 5.12; O, 11.69; S, 5.85. Found: C, 71.21; H, 4.79; N, 5.04. (average of two runs).

### Through-Space Monomer 3 (TS-M3)



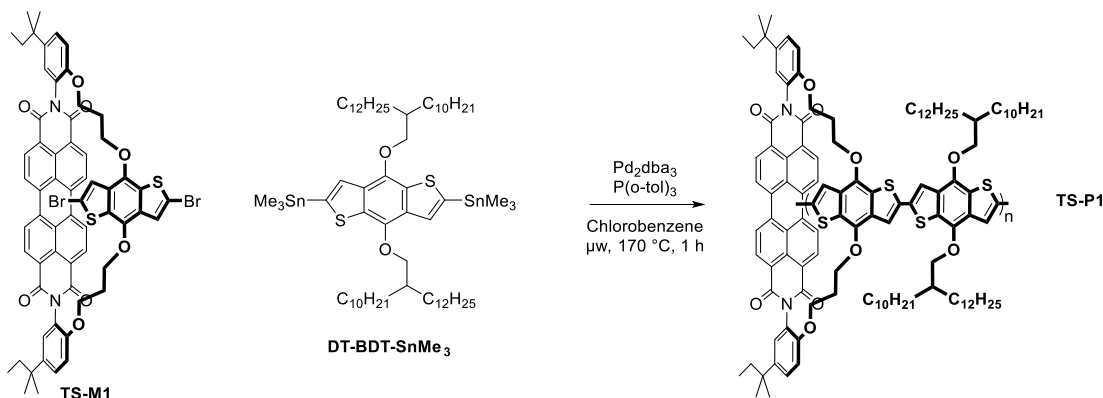
Under air, at -10 °C, NBS (101 mg, 0.5680 mmol) was added portionwise over 1 h to a solution of TS-PDI-DPP (293 mg, 0.2675 mmol) in CHCl<sub>3</sub> (7 mL). The salt/ice bath was removed, and the reaction was left stirring for 12 h at room temperature. The reaction was quenched using a sodium thiosulfate solution and extracted (2x) with DCM. Next, the organic layer was dried over MgSO<sub>4</sub> and concentrated *in vacuo*. The crude product was purified via silica column chromatography (100% hexane → 100% DCM → 3% EtOAc). The product fractions were combined and concentrated *in vacuo*. The resulting solids were sonicated in hexane and collected by filtration. Next, it was further purified using silica column chromatography for a second time (100% DCM → 0.5% Acetone). The product fractions were combined and concentrated *in vacuo*. The less pure fractions containing product were sonicated separately in hot acetone and collected by filtration. Both parts were then combined to afford a dark pink/red coloured solid product (133 mg, 0.1061 mmol, 40% yield).

**<sup>1</sup>H NMR** (500 MHz, CDCl<sub>3</sub>) δ 8.76 (d, *J* = 8.0 Hz, 2H, #a), 8.45 (d, *J* = 8.2 Hz, 2H, #b), 8.37 (d, *J* = 8.0 Hz, 2H, #c), 8.21 (d, *J* = 8.2 Hz, 2H, #d), 7.95 (d, *J* = 4.2 Hz, 2H, #e), 7.49 – 7.41 (dd, *J* = 8.7, 2.4 Hz, 2H, #f; d, 2H, #g), 7.12 (dd, *J* = 8.7, 0.9 Hz, 2H, #h; d, 2H, #i), 4.15 – 3.99 (m, 4H, #k), 3.41 (ddd, *J* = 14.6, 12.6, 4.9 Hz, 2H, #m), 3.09 (ddd, *J* = 14.7, 12.3, 5.0 Hz, 2H, #n), 2.03 – 1.77 (p, 4H, #o), 1.71 (q, *J* = 7.4 Hz, 4H, #p), 1.37 (s, 12H, #q), 0.82 (t, *J* = 7.4 Hz, 6H, #r). **<sup>13</sup>C NMR{H}** (126 MHz, CDCl<sub>3</sub>) δ 163.93 (#1, C=O), 163.90 (#2, C=O), 160.42 (#3, C=O), 151.42 (#4), 144.31 (#5, C<sub>Q</sub>), 138.00 (#6, C<sub>Q</sub>), 134.60 (#7, C<sub>Q</sub>), 134.56 (#8, C<sub>Q</sub>), 133.94 (#9), 132.04 (#10), 131.71 (#11), 131.11 (#12), 130.80 (#13, C<sub>Q</sub>), 129.93 (#14, C<sub>Q</sub>), 128.34 (#15), 127.95 (#16), 126.39 (#17, C<sub>Q</sub>), 126.02 (#18, C<sub>Q</sub>), 124.06 (#19, C<sub>Q</sub>), 123.76 (#20, C<sub>Q</sub>), 123.30 (#21), 122.50 (#22), 119.87 (#23, C<sub>Q</sub>), 116.09 (#24), 107.00 (#25, C<sub>Q</sub>), 67.97 (#26), 41.46 (#27), 37.82 (#28), 37.25 (#29), 28.62 (#30), 28.41 (#31), 9.40 (#32). **HRMS** (ASAP-TOF): Calculated for C<sub>66</sub>H<sub>53</sub>N<sub>4</sub>O<sub>8</sub>S<sub>2</sub>Br<sub>2</sub><sup>+</sup>: 1251.1672. Found *m/z*: 1251.1686 [M+H]<sup>+</sup>.



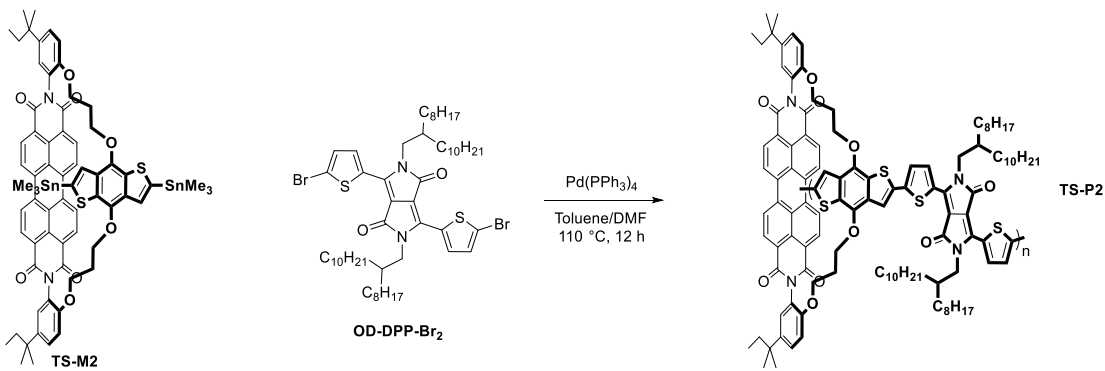
## Synthesis of Through-Space Polymers

### TS-P1



Under argon, dry chlorobenzene (2.0 mL) was added to a mixture of TS-M1 (100.0 mg, 0.0851 mmol), DT-BDT-SnMe<sub>3</sub> (95.4 mg, 0.0851 mmol), Pd<sub>2</sub>dba<sub>3</sub> (1.6 mg, 0.0017 mmol) and P(o-tol)<sub>3</sub> (2.1 mg, 0.0068 mmol), and it was stirred under microwave irradiation at 100 °C for 1 min., 120 °C for 5 min., 140 °C for 5 min., and finally 170 °C for 1 h. After cooling down, the reaction mixture was precipitated into stirring methanol (~100 mL) giving small red flakes of polymer. The crude polymer was purified with soxhlet extractions using acetone, hexane, heptane, ethyl acetate and finally chloroform. The chloroform fraction was re-precipitated into stirring methanol and collected by filtration to afford the desired polymer as a dark red/orange plastic (148.4 mg, 0.0777 mmol, 91%). Mn = 14.8 kDa, Mw = 48.8 kDa, PDI = 3.30.

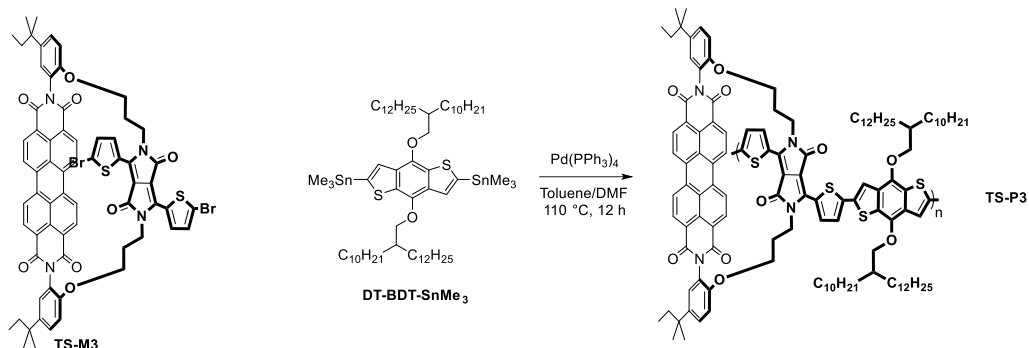
### TS-P2



Under argon, dry toluene (1.35 mL) and dry DMF (0.12 mL) were added to a mixture of TS-M2 (80.0 mg, 0.0599 mmol), OD-DPP-Br<sub>2</sub> (95.4 mg, 0.0599 mmol) and Pd(PPh<sub>3</sub>)<sub>4</sub> (1.6 mg, 0.0014 mmol), and it was stirred at 110 °C for 12 h. After cooling down, the reaction mixture was precipitated into stirring methanol (~100 mL) giving small purple-blue flakes of polymer. The crude polymer was purified with soxhlet extractions using acetone, hexane, heptane, ethyl acetate, 1,2-dimethoxyethane and finally chloroform. The chloroform fraction was re-precipitated into

stirring methanol and collected by filtration to afford the desired polymer as a dark blue/purple plastic (71.5 mg, 0.0381 mmol, 64%). Mn = 11.2 kDa, Mw = 31.7 kDa, PDI = 2.83.

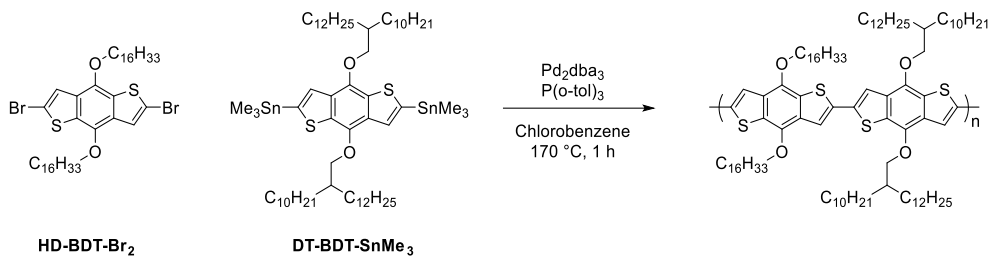
### TS-P3



Under argon, dry toluene (1.35 mL) and dry DMF (0.12 mL) were added to a mixture of TS-M3 (80.0 mg, 0.0638 mmol), DT-BDT-SnMe<sub>3</sub> (78.0 mg, 0.0638 mmol) and Pd(PPh<sub>3</sub>)<sub>4</sub> (1.6 mg, 0.0014 mmol), and it was stirred at 110 °C for 12 h. After cooling down, the reaction mixture was precipitated into stirring methanol (~100 mL) giving green flakes of polymer. The crude polymer was purified with soxhlet extractions using acetone, hexane and finally chloroform. The chloroform fraction was re-precipitated into stirring methanol and collected by filtration to afford the desired polymer as a green plastic (112.0 mg, 0.0563 mmol, 88%). Mn = 99.0 kDa, Mw = 2746.0 kDa, PDI = 27.75.

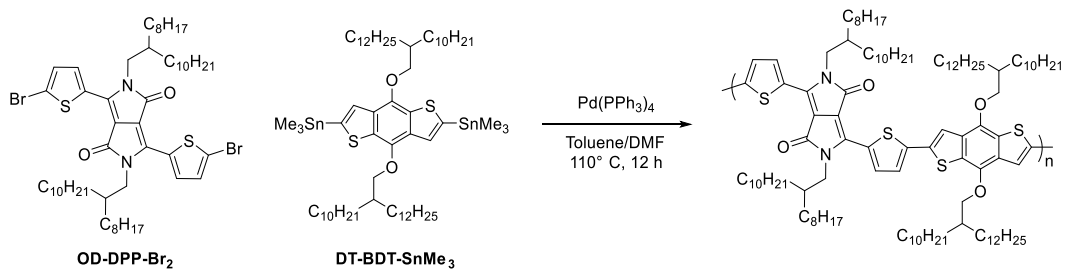
## Synthesis of Reference Polymers

### Ref-P1 Synthesis



Under argon, dry chlorobenzene (1.8 mL) was added to a mixture of HD-BDT-Br<sub>2</sub> (65.0 mg, 0.07841 mmol), DT-BDT-SnMe<sub>3</sub> (95.8 mg, 0.07841 mmol), Pd<sub>2</sub>dba<sub>3</sub> (1.5 mg, 0.0016 mmol) and P(o-tol)<sub>3</sub> (1.9 mg, 0.0031 mmol), and it was stirred under microwave irradiation at 100 °C for 1 min., 120 °C for 5 min., 140 °C for 5 min., and finally 170 °C for 1 h. After cooling down, the reaction mixture was precipitated into stirring methanol (~100 mL) giving orange flakes of polymer. The crude polymer was purified with soxhlet extractions using acetone and finally hexane and chloroform. The combined hexane and chloroform fraction was re-precipitated into stirring methanol and collected by filtration to afford the desired polymer as a dark red/orange plastic (126.3 mg, 0.0699 mmol, 89%). Mn = 63.1 kDa, Mw = 232.5 kDa, PDI = 3.68.

### Ref-P2 Synthesis



Under argon, dry toluene (2.25 mL) and dry DMF (0.2 mL) were added to a mixture of OD-DPP-Br<sub>2</sub> (100.0 mg, 0.0981 mmol), DT-BDT-SnMe<sub>3</sub> (119.8 mg, 0.0981 mmol) and Pd(PPh<sub>3</sub>)<sub>4</sub> (2.68 mg, 0.0023 mmol), and it was stirred in an oil bath at 110 °C for 12 h. After cooling down, the reaction mixture was precipitated into stirring methanol (~100 mL) giving green-blue flakes of polymer. The crude polymer was purified with soxhlet extractions using acetone, ethyl acetate and finally hexane. The hexane fraction was re-precipitated into stirring methanol and collected by filtration to afford the desired polymer as a sticky green-blue plastic (151.5 mg, 0.0863 mmol, 88%). Mn = 58.2 kDa, Mw = 220.3 kDa, PDI = 3.78.

## References

- (1) Swager, T. M. 50th Anniversary Perspective: Conducting/Semiconducting Conjugated Polymers. A Personal Perspective on the Past and the Future. *Macromolecules* **2017**, *50* (13), 4867–4886.
- (2) Hubbert, M. K. Energy from Fossil Fuels. *Science* **1949**, *109* (2823), 103–109.
- (3) Schiermeier, Q.; Tollefson, J.; Scully, T.; Witze, A.; Morton, O. Energy Alternatives: Electricity without Carbon. *Nat. News* **2008**, *454* (7206), 816–823.
- (4) Facchetti, A.  $\pi$ -Conjugated Polymers for Organic Electronics and Photovoltaic Cell Applications. *Chem. Mater.* **2010**, *23* (3), 733–758.
- (5) Oh, J. Y.; Rondeau-Gagné, S.; Chiu, Y.-C.; Chortos, A.; Lissel, F.; Wang, G.-J. N.; Schroeder, B. C.; Kurosawa, T.; Lopez, J.; Katsumata, T. Intrinsically Stretchable and Healable Semiconducting Polymer for Organic Transistors. *Nature* **2016**, *539* (7629), 411–415.
- (6) Lund, A.; van der Velden, N. M.; Persson, N.-K.; Hamed, M. M.; Müller, C. Electrically Conducting Fibres for E-Textiles: An Open Playground for Conjugated Polymers and Carbon Nanomaterials. *Mater. Sci. Eng. R Reports* **2018**, *126*, 1–29.
- (7) Oh, J. Y.; Bao, Z. Second Skin Enabled by Advanced Electronics. *Adv. Sci.* **2019**, *6* (11), 1900186.
- (8) Zhang, X.; Bauerle, P.; Aida, T.; Skabara, P.; Kagan, C. Organic Electronics for a Better Tomorrow: Innovation, Accessibility, Sustainability. *A White Pap. from Chem. Sci. Soc. Summit 2012*.
- (9) Heeger, A. J.; MacDiarmid, A. G.; Shirakawa, H. The Nobel Prize in Chemistry, 2000: Conductive Polymers. *Stock. Sweden R. Swedish Acad. Sci.* **2000**, 1–16.
- (10) Günes, S.; Neugebauer, H.; Sariciftci, N. S. Conjugated Polymer-Based Organic Solar Cells. *Chem. Rev.* **2007**, *107* (4), 1324–1338.
- (11) Guo, X.; Baumgarten, M.; Müllen, K. Designing  $\pi$ -Conjugated Polymers for Organic Electronics. *Prog. Polym. Sci.* **2013**, *38* (12), 1832–1908.
- (12) Tessler, N.; Denton, G. J.; Friend, R. H. Lasing from Conjugated-Polymer Microcavities. *Nature* **1996**, *382* (6593), 695.
- (13) Scherf, U.; Riechel, S.; Lemmer, U.; Mahrt, R. F. Conjugated Polymers: Lasing and Stimulated Emission. *Curr. Opin. Solid State Mater. Sci.* **2001**, *5* (2–3), 143–154.
- (14) Peet, J.; Kim, J. Y.; Coates, N. E.; Ma, W. L.; Moses, D.; Heeger, A. J.; Bazan, G. C. Efficiency Enhancement in Low-Bandgap Polymer Solar Cells by Processing with Alkane Dithiols. *Nat. Mater.* **2007**, *6* (7), 497.
- (15) Roncali, J. Molecular Engineering of the Band Gap of  $\Pi$ -conjugated Systems: Facing Technological Applications. *Macromol. Rapid Commun.* **2007**, *28* (17), 1761–1775.
- (16) Li, G.; Chang, W. H.; Yang, Y. Low-Bandgap Conjugated Polymers Enabling Solution-Processable Tandem Solar Cells. *Nat. Rev. Mater.* **2017**, *2* (17043), 1–13. <https://doi.org/10.1038/natrevmats.2017.43>.
- (17) Shirakawa, H. The Discovery of Polyacetylene Film: The Dawning of an Era of Conducting Polymers (Nobel Lecture). *Angew. Chemie Int. Ed.* **2001**, *40* (14), 2574–2580.
- (18) Cheng, Y.-J.; Yang, S.-H.; Hsu, C.-S. Synthesis of Conjugated Polymers for Organic Solar Cell Applications. *Chem. Rev.* **2009**, *109* (11), 5868–5923.
- (19) Liu, C.; Wang, K.; Gong, X.; Heeger, A. J. Low Bandgap Semiconducting Polymers for Polymeric Photovoltaics. *Chem. Soc. Rev.* **2016**, *45* (17), 4825–4846.
- (20) Xu, T.; Yu, L. How to Design Low Bandgap Polymers for Highly Efficient Organic Solar Cells. *Mater. today* **2014**, *17* (1), 11–15.
- (21) Bredas, J.-L. Relationship between Band Gap and Bond Length Alteration in Organic Conjugated Polymers. *J. Chem. Phys.* **1985**, *82* (8), 3808–3811.
- (22) Brédas, J. L.; Heeger, A. J. Influence of Donor and Acceptor Substituents on the Electronic Characteristics of Poly (Paraphenylene Vinylene) and Poly (Paraphenylene). *Chem. Phys. Lett.* **1994**, *217* (5–6), 507–512.
- (23) Brisset, H.; Thobie-Gautier, C.; Gorgues, A.; Jubault, M.; Roncali, J. Novel Narrow Bandgap Polymers from Sp 3 Carbon-Bridged Bithienyls: Poly (4, 4-Ethylenedioxy-4 H-

- Cyclopenta [2, 1-b; 3, 4-B'] Dithiophene). *J. Chem. Soc. Chem. Commun.* **1994**, No. 11, 1305–1306.
- (24) Roncali, J.; Thobie-Gautier, C.; Elandaloussi, E. H.; Frère, P. Control of the Bandgap of Conducting Polymers by Rigidification of the  $\pi$ -Conjugated System. *J. Chem. Soc. Chem. Commun.* **1994**, No. 19, 2249–2250.
- (25) Blanchard, P.; Brisset, H.; Illien, B.; Riou, A.; Roncali, J. Bridged Dithienylethylenes as Precursors of Small Bandgap Electrogenerated Conjugated Polymers. *J. Org. Chem.* **1997**, 62 (8), 2401–2408.
- (26) Blanchard, P.; Brisset, H.; Riou, A.; Hierle, R.; Roncali, J. Bridged 1, 6-Dithienylhexa-1, 3, 5-Trienes as Highly Photoluminescent and Stable Thiophene-Based  $\pi$ -Conjugated Systems. *J. Org. Chem.* **1998**, 63 (23), 8310–8319.
- (27) Huang, H.; Yang, L.; Facchetti, A.; Marks, T. J. Organic and Polymeric Semiconductors Enhanced by Noncovalent Conformational Locks. *Chem. Rev.* **2017**, 117 (15), 10291–10318.
- (28) Jackson, N. E.; Savoie, B. M.; Kohlstedt, K. L.; Olvera de la Cruz, M.; Schatz, G. C.; Chen, L. X.; Ratner, M. A. Controlling Conformations of Conjugated Polymers and Small Molecules: The Role of Nonbonding Interactions. *J. Am. Chem. Soc.* **2013**, 135 (28), 10475–10483.
- (29) Conboy, G.; Spencer, H. J.; Angioni, E.; Kanibolotsky, A. L.; Findlay, N. J.; Coles, S. J.; Wilson, C.; Pitak, M. B.; Risko, C.; Coropceanu, V. To Bend or Not to Bend—Are Heteroatom Interactions within Conjugated Molecules Effective in Dictating Conformation and Planarity? *Mater. Horizons* **2016**, 3 (4), 333–339.
- (30) Roncali, J.; Blanchard, P.; Frère, P. 3, 4-Ethylenedioxythiophene (EDOT) as a Versatile Building Block for Advanced Functional  $\pi$ -Conjugated Systems. *J. Mater. Chem.* **2005**, 15 (16), 1589–1610.
- (31) Li, X.; Liu, X.; Sun, P.; Feng, Y.; Shan, H.; Wu, X.; Xu, J.; Huang, C.; Chen, Z.-K.; Xu, Z.-X. Effect of Fluorination on N-Type Conjugated Polymers for All-Polymer Solar Cells. *RSC Adv.* **2017**, 7 (28), 17076–17084.
- (32) Zhu, C.; Mu, A. U.; Wang, C.; Ji, X.; Fang, L. Synthesis and Solution Processing of a Rigid Polymer Enabled by Active Manipulation of Intramolecular Hydrogen Bonds. *ACS Macro Lett.* **2018**, 7 (7), 801–806.
- (33) McEntee, G. J.; Skabara, P. J.; Vilela, F.; Tierney, S.; Samuel, I. D. W.; Gambino, S.; Coles, S. J.; Hursthouse, M. B.; Harrington, R. W.; Clegg, W. Synthesis and Electropolymerization of Hexadecyl Functionalized Bithiophene and Thieno [3, 2-b] Thiophene End-Capped with EDOT and EDTT Units. *Chem. Mater.* **2010**, 22 (9), 3000–3008.
- (34) Spencer, H. J.; Skabara, P. J.; Giles, M.; McCulloch, I.; Coles, S. J.; Hursthouse, M. B. The First Direct Experimental Comparison between the Hugely Contrasting Properties of PEDOT and the All-Sulfur Analogue PEDTT by Analogy with Well-Defined EDTT–EDOT Copolymers. *J. Mater. Chem.* **2005**, 15 (45), 4783–4792.
- (35) Guo, X.; Kim, F. S.; Jenekhe, S. A.; Watson, M. D. Phthalimide-Based Polymers for High Performance Organic Thin-Film Transistors. *J. Am. Chem. Soc.* **2009**, 131 (21), 7206–7207.
- (36) Liao, Q.; Yang, K.; Chen, J.; Koh, C. W.; Tang, Y.; Su, M.; Wang, Y.; Yang, Y.; Feng, X.; He, Z. Backbone Coplanarity Tuning of 1, 4-Di (3-Alkoxy-2-Thienyl)-2, 5-Difluorophenylene-Based Wide Bandgap Polymers for Efficient Organic Solar Cells Processed from Nonhalogenated Solvent. *ACS Appl. Mater. Interfaces* **2019**, 11 (34), 31119–31128.
- (37) Chen, J.; Yan, Z.; Tang, L.; Uddin, M. A.; Yu, J.; Zhou, X.; Yang, K.; Tang, Y.; Shin, T. J.; Woo, H. Y. 1, 4-Di (3-Alkoxy-2-Thienyl)-2, 5-Difluorophenylene: A Building Block Enabling High-Performance Polymer Semiconductors with Increased Open-Circuit Voltages. *Macromolecules* **2018**, 51 (14), 5352–5363.
- (38) Huang, J.; Guo, H.; Uddin, M. A.; Yu, J.; Woo, H. Y.; Guo, X. Fluorinated Head-to-Head Dialkoxybithiophene: A New Electron-Donating Building Block for High-Performance Polymer Semiconductors. *Adv. Electron. Mater.* **2018**, 4 (3), 1700519.

- (39) Guo, X.; Liao, Q.; Manley, E. F.; Wu, Z.; Wang, Y.; Wang, W.; Yang, T.; Shin, Y.-E.; Cheng, X.; Liang, Y. Materials Design via Optimized Intramolecular Noncovalent Interactions for High-Performance Organic Semiconductors. *Chem. Mater.* **2016**, 28 (7), 2449–2460.
- (40) Zhu, C.; Fang, L. Locking the Coplanar Conformation of  $\pi$ -Conjugated Molecules and Macromolecules Using Dynamic Noncovalent Bonds. *Macromol. Rapid Commun.* **2018**, 39 (2), 1700241.
- (41) Zhu, C.; Kalin, A. J.; Fang, L. Covalent and Noncovalent Approaches to Rigid Coplanar  $\pi$ -Conjugated Molecules and Macromolecules. *Acc. Chem. Res.* **2019**, 52 (4), 1089–1100.
- (42) Nguyen, T. L.; Choi, H.; Ko, S.-J.; Uddin, M. A.; Walker, B.; Yum, S.; Jeong, J.-E.; Yun, M. H.; Shin, T. J.; Hwang, S. Semi-Crystalline Photovoltaic Polymers with Efficiency Exceeding 9% in A~300 Nm Thick Conventional Single-Cell Device. *Energy Environ. Sci.* **2014**, 7 (9), 3040–3051.
- (43) Pomerantz, M. Planar 2, 2'-Bithiophenes with 3, 3'-and 3, 3', 4, 4'-Substituents. A Computational Study. *Tetrahedron Lett.* **2003**, 44 (8), 1563–1565.
- (44) Sadki, S.; Schottland, P.; Brodie, N.; Sabouraud, G. The Mechanisms of Pyrrole Electropolymerization. *Chem. Soc. Rev.* **2000**, 29 (5), 283–293.
- (45) Roncali, J. Conjugated Poly(Thiophenes): Synthesis, Functionalization, and Applications. *Chem. Rev.* **1992**, 92 (4), 711–738.
- (46) Toshima, N.; Hara, S. Direct Synthesis of Conducting Polymers from Simple Monomers. *Prog. Polym. Sci.* **1995**, 20 (1), 155–183.
- (47) Cheng, Y.-J.; Luh, T.-Y. Synthesizing Optoelectronic Heteroaromatic Conjugated Polymers by Cross-Coupling Reactions. *J. Organomet. Chem.* **2004**, 689 (24), 4137–4148.
- (48) Bäckvall, J. E. Palladium-Catalyzed Cross Couplings in Organic Synthesis. *Sci. Backgr. Nobel Prize Chem. 2010* **2010**.
- (49) Tamao, K.; Sumitani, K.; Kumada, M. Selective Carbon–Carbon Bond Formation by Cross-Coupling of Grignard Reagents with Organic Halides. Catalysis by Nickel–Phosphine Complexes. *J. Am. Chem. Soc.* **1972**, 94 (12), 4374–4376.
- (50) Oestreich, M. *The Mizoroki-Heck Reaction*; John Wiley & Sons, 2009.
- (51) Jagtap, S. Heck Reaction—State of the Art. *Catalysts* **2017**, 7 (9), 267.
- (52) Knowles, J. P.; Whiting, A. The Heck–Mizoroki Cross-Coupling Reaction: A Mechanistic Perspective. *Org. Biomol. Chem.* **2007**, 5 (1), 31–44.
- (53) Negishi, E.; Hu, Q.; Huang, Z.; Qian, M.; Wang, G.; Brown, H. Palladium-Catalyzed Alkenylation by the Negishi Coupling. *Aldrichim. Acta* **2005**, 38, 71–87.
- (54) Stille, J. K. The Palladium-catalyzed Cross-coupling Reactions of Organotin Reagents with Organic Electrophiles [New Synthetic Methods (58)]. *Angew. Chemie Int. Ed. English* **1986**, 25 (6), 508–524.
- (55) Miyaura, N.; Suzuki, A. Palladium-Catalyzed Cross-Coupling Reactions of Organoboron Compounds. *Chem. Rev.* **1995**, 95 (7), 2457–2483.
- (56) Sonogashira, K. Development of Pd–Cu Catalyzed Cross-Coupling of Terminal Acetylenes with Sp<sub>2</sub>-Carbon Halides. *J. Organomet. Chem.* **2002**, 653 (1–2), 46–49.
- (57) Yamamoto, T.; Morita, A.; Miyazaki, Y.; Maruyama, T.; Wakayama, H.; Zhou, Z. H.; Nakamura, Y.; Kanbara, T.; Sasaki, S.; Kubota, K. Preparation of  $\pi$ -Conjugated Poly(Thiophene-2, 5-Diyl), Poly(p-Phenylenes), and Related Polymers Using Zerovalent Nickel Complexes. Linear Structure and Properties of the  $\pi$ -Conjugated Polymers. *Macromolecules* **1992**, 25 (4), 1214–1223.
- (58) McCullough, R. D.; Lowe, R. D.; Jayaraman, M.; Anderson, D. L. Design, Synthesis, and Control of Conducting Polymer Architectures: Structurally Homogeneous Poly(3-Alkylthiophenes). *J. Org. Chem.* **1993**, 58 (4), 904–912.
- (59) Leclerc, M.; Morin, J.-F. *Design and Synthesis of Conjugated Polymers*; John Wiley & Sons, 2010.
- (60) Xu, S.; Kim, E. H.; Wei, A.; Negishi, E. Pd-and Ni-Catalyzed Cross-Coupling Reactions in the Synthesis of Organic Electronic Materials. *Sci. Technol. Adv. Mater.* **2014**, 15 (4), 44201.
- (61) Chen, T.-A.; Wu, X.; Rieke, R. D. Regiocontrolled Synthesis of Poly(3-Alkylthiophenes)

- Mediated by Rieke Zinc: Their Characterization and Solid-State Properties. *J. Am. Chem. Soc.* **1995**, *117* (1), 233–244.
- (62) Maior, R. M. S.; Hinkelmann, K.; Eckert, H.; Wudl, F. Synthesis and Characterization of Two Regiochemically Defined Poly (Dialkylbithiophenes): A Comparative Study. *Macromolecules* **1990**, *23* (5), 1268–1279.
- (63) Chen, T.-A.; Rieke, R. D. Polyalkylthiophenes with the Smallest Bandgap and the Highest Intrinsic Conductivity. *Synth. Met.* **1993**, *60* (2), 175–177.
- (64) Chen, T. A.; O'Brien, R. A.; Rieke, R. D. Use of Highly Reactive Zinc Leads to a New, Facile Synthesis for Polyarylenes. *Macromolecules* **1993**, *26* (13), 3462–3463.
- (65) Wu, X.; Chen, T.-A.; Rieke, R. D. Synthesis of Regioregular Head-to-Tail Poly [3-(Alkylthio) Thiophenes]. A Highly Electroconductive Polymer. *Macromolecules* **1995**, *28* (6), 2101–2102.
- (66) Huo, S.; Mroz, R.; Carroll, J. Negishi Coupling in the Synthesis of Advanced Electronic, Optical, Electrochemical, and Magnetic Materials. *Org. Chem. Front.* **2015**, *2* (4), 416–445.
- (67) Loewe, R. S.; Khersonsky, S. M.; McCullough, R. D. A Simple Method to Prepare Head-to-tail Coupled, Regioregular Poly (3-alkylthiophenes) Using Grignard Metathesis. *Adv. Mater.* **1999**, *11* (3), 250–253.
- (68) Loewe, R. S.; Ewbank, P. C.; Liu, J.; Zhai, L.; McCullough, R. D. Regioregular, Head-to-Tail Coupled Poly (3-Alkylthiophenes) Made Easy by the GRIM Method: Investigation of the Reaction and the Origin of Regioselectivity. *Macromolecules* **2001**, *34* (13), 4324–4333.
- (69) Yokoyama, A.; Miyakoshi, R.; Yokozawa, T. Chain-Growth Polymerization for Poly (3-Hexylthiophene) with a Defined Molecular Weight and a Low Polydispersity. *Macromolecules* **2004**, *37* (4), 1169–1171.
- (70) Bhatt, M. P.; Magurudeniya, H. D.; Sista, P.; Sheina, E. E.; Jeffries-EL, M.; Janesko, B. G.; McCullough, R. D.; Stefan, M. C. Role of the Transition Metal in Grignard Metathesis Polymerization (GRIM) of 3-Hexylthiophene. *J. Mater. Chem. A* **2013**, *1* (41), 12841–12849.
- (71) Tkachov, R.; Senkovskyy, V.; Komber, H.; Sommer, J.-U.; Kiriy, A. Random Catalyst Walking along Polymerized Poly (3-Hexylthiophene) Chains in Kumada Catalyst-Transfer Polycondensation. *J. Am. Chem. Soc.* **2010**, *132* (22), 7803–7810.
- (72) Senkovskyy, V.; Khanduyeva, N.; Komber, H.; Oertel, U.; Stamm, M.; Kuckling, D.; Kiriy, A. Conductive Polymer Brushes of Regioregular Head-to-Tail Poly (3-Alkylthiophenes) via Catalyst-Transfer Surface-Initiated Polycondensation. *J. Am. Chem. Soc.* **2007**, *129* (20), 6626–6632.
- (73) Osaka, I.; McCullough, R. D. Advances in Molecular Design and Synthesis of Regioregular Polythiophenes. *Acc. Chem. Res.* **2008**, *41* (9), 1202–1214.
- (74) Sheina, E. E.; Liu, J.; Iovu, M. C.; Laird, D. W.; McCullough, R. D. Chain Growth Mechanism for Regioregular Nickel-Initiated Cross-Coupling Polymerizations. *Macromolecules* **2004**, *37* (10), 3526–3528.
- (75) Iovu, M. C.; Sheina, E. E.; Gil, R. R.; McCullough, R. D. Experimental Evidence for the Quasi-“Living” Nature of the Grignard Metathesis Method for the Synthesis of Regioregular Poly (3-Alkylthiophenes). *Macromolecules* **2005**, *38* (21), 8649–8656.
- (76) Jeffries-EL, M.; Sauvé, G.; McCullough, R. D. In-situ End-group Functionalization of Regioregular Poly (3-alkylthiophene) Using the Grignard Metathesis Polymerization Method. *Adv. Mater.* **2004**, *16* (12), 1017–1019.
- (77) Jeffries-El, M.; Sauve, G.; McCullough, R. D. Facile Synthesis of End-Functionalized Regioregular Poly (3-Alkylthiophene)s via Modified Grignard Metathesis Reaction. *Macromolecules* **2005**, *38* (25), 10346–10352.
- (78) Miyakoshi, R.; Yokoyama, A.; Yokozawa, T. Catalyst-Transfer Polycondensation. Mechanism of Ni-Catalyzed Chain-Growth Polymerization Leading to Well-Defined Poly (3-Hexylthiophene). *J. Am. Chem. Soc.* **2005**, *127* (49), 17542–17547.
- (79) Miyakoshi, R.; Yokoyama, A.; Yokozawa, T. Synthesis of Poly (3-hexylthiophene) with a Narrower Polydispersity. *Macromol. Rapid Commun.* **2004**, *25* (19), 1663–1666.

- (80) Zhang, R.; Li, B.; Iovu, M. C.; Jeffries-el, M.; Sauvé, G.; Cooper, J.; Jia, S.; Tristram-Nagle, S.; Smilgies, D. M.; Lambeth, D. N. Nanostructure Dependence of Field-Effect Mobility in Regioregular Poly (3-Hexylthiophene) Thin Film Field Effect Transistors. *J. Am. Chem. Soc.* **2006**, *128* (11), 3480–3481.
- (81) Yamamoto, T.; Wakabayashi, S.; Osakada, K. Mechanism of C–C Coupling Reactions of Aromatic Halides, Promoted by Ni (COD) 2 in the Presence of 2, 2'-Bipyridine and PPh<sub>3</sub>, to Give Biaryls. *J. Organomet. Chem.* **1992**, *428* (1–2), 223–237.
- (82) Yamamoto, T.; Koizumi, T. Synthesis of  $\pi$ -Conjugated Polymers Bearing Electronic and Optical Functionalities by Organometallic Polycondensations and Their Chemical Properties. *Polymer (Guildf.)*. **2007**, *48* (19), 5449–5472.
- (83) Li, J.; Dierschke, F.; Wu, J.; Grimsdale, A. C.; Müllen, K. Poly (2, 7-Carbazole) and Perylene Tetracarboxydiimide: A Promising Donor/Acceptor Pair for Polymer Solar Cells. *J. Mater. Chem.* **2006**, *16* (1), 96–100.
- (84) Heck, R. F. Acylation, Methylation, and Carboxyalkylation of Olefins by Group VIII Metal Derivatives. *J. Am. Chem. Soc.* **1968**, *90* (20), 5518–5526.
- (85) Beletskaya, I. P.; Cheprakov, A. V. The Heck Reaction as a Sharpening Stone of Palladium Catalysis. *Chem. Rev.* **2000**, *100* (8), 3009–3066.
- (86) Nicolaou, K. C.; Bulger, P. G.; Sarlah, D. Palladium-catalyzed Cross-coupling Reactions in Total Synthesis. *Angew. Chemie Int. Ed.* **2005**, *44* (29), 4442–4489.
- (87) Crisp, G. T. Variations on a Theme—Recent Developments on the Mechanism of the Heck Reaction and Their Implications for Synthesis. *Chem. Soc. Rev.* **1998**, *27* (6), 427–436.
- (88) Huo, L.; He, C.; Han, M.; Zhou, E.; Li, Y. Alternating Copolymers of Electron-rich Arylamine and Electron-deficient 2, 1, 3-benzothiadiazole: Synthesis, Characterization and Photovoltaic Properties. *J. Polym. Sci. Part A Polym. Chem.* **2007**, *45* (17), 3861–3871.
- (89) Leclerc, M.; Morin, J.-F. *Synthetic Methods for Conjugated Polymer and Carbon Materials*; John Wiley & Sons, 2017.
- (90) Wilson, J. N.; Waybright, S. M.; McAlpine, K.; Bunz, U. H. F. Acetylene Gas: A Reagent in the Synthesis of High Molecular Weight Poly (p-Phenylenethynylene)s Utilizing Very Low Catalyst Loadings. *Macromolecules* **2002**, *35* (10), 3799–3800.
- (91) Carsten, B.; He, F.; Son, H. J.; Xu, T.; Yu, L. Stille Polycondensation for Synthesis of Functional Materials. *Chem. Rev.* **2011**, *111* (3), 1493–1528.
- (92) Casado, A. L.; Espinet, P. On the Configuration Resulting from Oxidative Addition of RX to Pd (PPh<sub>3</sub>) 4 and the Mechanism of the Cis-to-Trans Isomerization of [PdRX (PPh<sub>3</sub>) 2] Complexes (R= Aryl, X= Halide). *Organometallics* **1998**, *17* (5), 954–959.
- (93) Hou, J.; Park, M.-H.; Zhang, S.; Yao, Y.; Chen, L.-M.; Li, J.-H.; Yang, Y. Bandgap and Molecular Energy Level Control of Conjugated Polymer Photovoltaic Materials Based on Benzo [1, 2-b: 4, 5-B']Dithiophene. *Macromolecules* **2008**, *41* (16), 6012–6018.
- (94) Miyaura, N.; Yamada, K.; Suzuki, A. A New Stereospecific Cross-Coupling by the Palladium-Catalyzed Reaction of 1-Alkenylboranes with 1-Alkenyl or 1-Alkynyl Halides. *Tetrahedron Lett.* **1979**, *20* (36), 3437–3440.
- (95) Liu, C.-L.; Tsai, J.-H.; Lee, W.-Y.; Chen, W.-C.; Jenekhe, S. A. New Didecyloxyphenylene–Acceptor Alternating Conjugated Copolymers: Synthesis, Properties, and Optoelectronic Device Applications. *Macromolecules* **2008**, *41* (19), 6952–6959.
- (96) Swinehart, D. F. The Beer-Lambert Law. *J. Chem. Educ.* **1962**, *39* (7), 333.
- (97) Sauer, M.; Hofkens, J.; Enderlein, J. Basic Principles of Fluorescence Spectroscopy. *Handb. Fluoresc. Spectrosc. imaging from single Mol. to ensembles* **2011**, 1–30.
- (98) Zhokhavets, U.; Erb, T.; Gobsch, G.; Al-Ibrahim, M.; Ambacher, O. Relation between Absorption and Crystallinity of Poly (3-Hexylthiophene)/Fullerene Films for Plastic Solar Cells. *Chem. Phys. Lett.* **2006**, *418* (4–6), 347–350.
- (99) Petty, M. C. *Organic and Molecular Electronics: From Principles to Practice*; John Wiley & Sons, 2019.
- (100) Herschel, J. F. W. IV. Ἀμόρφων a, No. I.—on a Case of Superficial Colour Presented by a Homogeneous Liquid Internally Colourless. *Philos. Trans. R. Soc. London* **1845**, No.

- 135, 143–145.
- (101) Congrave, D. Synthesis and Photophysical Properties of New Di-and Mononuclear Phosphorescent Iridium (III) Complexes. Durham University 2018.
- (102) Eisfeld, A.; Briggs, J. S. The J-and H-Bands of Organic Dye Aggregates. *Chem. Phys.* **2006**, 324 (2–3), 376–384.
- (103) Spano, F. C.; Silva, C. H-and J-Aggregate Behavior in Polymeric Semiconductors. *Annu. Rev. Phys. Chem.* **2014**, 65, 477–500.
- (104) Baghgar, M.; Labastide, J. A.; Bokel, F.; Hayward, R. C.; Barnes, M. D. Effect of Polymer Chain Folding on the Transition from H-to J-Aggregate Behavior in P3HT Nanofibers. *J. Phys. Chem. C* **2014**, 118 (4), 2229–2235.
- (105) Uddin, M. G.; Azam, A. A Novel Oligo-DNA Probe Carrying Non-Nucleosidic Silylated Pyrene Derivatives: Synthesis and Excimer Forming Ability. *Am. J. Biochem. Mol. Biol.* **2013**, 3 (1), 175–181.
- (106) Leventis, A.; Royakkers, J.; Rapidis, A. G.; Goodeal, N.; Corpinot, M. K.; Frost, J. M.; Bučar, D.-K. K.; Blunt, M. O.; Cacialli, F.; Bronstein, H. Highly Luminescent Encapsulated Narrow Bandgap Polymers Based on Diketopyrrolopyrrole. *J. Am. Chem. Soc.* **2018**, 140 (5), 1622–1626. <https://doi.org/10.1021/jacs.7b13447>.
- (107) Yersin, H.; Rausch, A. F.; Czerwieniec, R.; Hofbeck, T.; Fischer, T. The Triplet State of Organo-Transition Metal Compounds. Triplet Harvesting and Singlet Harvesting for Efficient OLEDs. *Coord. Chem. Rev.* **2011**, 255 (21–22), 2622–2652.
- (108) van Eersel, H. Device Physics of Organic Light-Emitting Diodes: Interplay between Charges and Excitons. Technische Universiteit Eindhoven 2015.
- (109) Tang, C. W.; VanSlyke, S. A. Organic Electroluminescent Diodes. *Appl. Phys. Lett.* **1987**, 51 (12), 913–915.
- (110) Burroughes, J. H.; Bradley, D. D. C.; Brown, A. R.; Marks, R. N.; Mackay, K.; Friend, R. H.; Burns, P. L.; Holmes, A. B. Light-Emitting Diodes Based on Conjugated Polymers. *Nature* **1990**, 347 (6293), 539.
- (111) Moratti, S. C.; Bradley, D. D. C.; Cervini, R.; Friend, R. H.; Greenham, N. C.; Holmes, A. B. Light-Emitting Polymer LEDs. In *Advanced Photonics Materials for Information Technology*; International Society for Optics and Photonics, 1994; Vol. 2144, pp 108–114.
- (112) Brown, T. M.; Kim, J.-S.; Friend, R. H.; Cacialli, F.; Daik, R.; Feast, W. J. Built-in Field Electroabsorption Spectroscopy of Polymer Light-Emitting Diodes Incorporating a Doped Poly(3,4-Ethylene Dioxothiophene) Hole Injection Layer. *Appl. Phys. Lett.* **1999**, 75 (12), 1679–1681.
- (113) Hung, L. S.; Chen, C. H. Recent Progress of Molecular Organic Electroluminescent Materials and Devices. *Mater. Sci. Eng. R Reports* **2002**, 39 (5–6), 143–222.
- (114) Halls, J. J. M.; Walsh, C. A.; Greenham, N. C.; Marseglia, E. A.; Friend, R. H.; Moratti, S. C.; Holmes, A. B. Efficient Photodiodes from Interpenetrating Polymer Networks. *Nature* **1995**, 376 (6540), 498–500.
- (115) Piliego, C.; Loi, M. A. Charge Transfer State in Highly Efficient Polymer–Fullerene Bulk Heterojunction Solar Cells. *J. Mater. Chem.* **2012**, 22 (10), 4141–4150.
- (116) Yan, C.; Barlow, S.; Wang, Z.; Yan, H.; Jen, A. K.-Y.; Marder, S. R.; Zhan, X. Non-Fullerene Acceptors for Organic Solar Cells. *Nat. Rev. Mater.* **2018**, 3 (3), 1–19.
- (117) Liu, X.; Rand, B. P.; Forrest, S. R. Engineering Charge-Transfer States for Efficient, Low-Energy-Loss Organic Photovoltaics. *Trends Chem.* **2019**, 1 (9), 815–829.
- (118) Blom, P. W. M.; Mihailescu, V. D.; Koster, L. J. A.; Markov, D. E. Device Physics of Polymer: Fullerene Bulk Heterojunction Solar Cells. *Adv. Mater.* **2007**, 19 (12), 1551–1566.
- (119) Li, S.; Li, C.-Z.; Shi, M.; Chen, H. New Phase for Organic Solar Cell Research: Emergence of Y-Series Electron Acceptors and Their Perspectives. *ACS Energy Lett.* **2020**, 5 (5), 1554–1567.
- (120) Wilson, J. S.; Chawdhury, N.; Al-Mandhary, M. R. A.; Younus, M.; Khan, M. S.; Raithby, P. R.; Köhler, A.; Friend, R. H. The Energy Gap Law for Triplet States in Pt-Containing Conjugated Polymers and Monomers. *J. Am. Chem. Soc.* **2001**, 123 (38), 9412–9417.
- (121) Zampetti, A.; Minotto, A.; Squeo, B. M.; Gregoriou, V. G.; Allard, S.; Scherf, U.;

- Chochos, C. L.; Cacialli, F. Highly Efficient Solid-State Near-Infrared Organic Light-Emitting Diodes Incorporating ADA Dyes Based on  $\alpha$ ,  $\beta$ -Unsubstituted “BODIPY” Moieties. *Sci. Rep.* **2017**, *7* (1), 1611.
- (122) Dimitrov, S. D.; Schroeder, B. C.; Nielsen, C. B.; Bronstein, H.; Fei, Z.; McCulloch, I.; Heeney, M.; Durrant, J. R. Singlet Exciton Lifetimes in Conjugated Polymer Films for Organic Solar Cells. *Polymers (Basel)*. **2016**, *8* (1). <https://doi.org/10.3390/polym8010014>.
- (123) Hu, Z.; Willard, A. P.; Ono, R. J.; Bielawski, C. W.; Rossky, P. J.; Bout, D. A. Vanden. An Insight into Non-Emissive Excited States in Conjugated Polymers. *Nat. Commun.* **2015**, *6*, 8246.
- (124) Frampton, M. J.; Anderson, H. L. Insulated Molecular Wires. *Angew. Chemie Int. Ed.* **2007**, *46* (7), 1028–1064.
- (125) Sugiyasu, K.; Honsho, Y.; Harrison, R. M.; Sato, A.; Yasuda, T.; Seki, S.; Takeuchi, M. A Self-Threading Polythiophene: Defect-Free Insulated Molecular Wires Endowed with Long Effective Conjugation Length. *J. Am. Chem. Soc.* **2010**, *132* (42), 14754–14756. <https://doi.org/10.1021/ja107444m>.
- (126) Pan, C.; Sugiyasu, K.; Wakayama, Y.; Sato, A.; Takeuchi, M. Thermoplastic Fluorescent Conjugated Polymers: Benefits of Preventing  $\pi$ - $\pi$  Stacking. *Angew. Chemie - Int. Ed.* **2013**, *52* (41), 10775–10779. <https://doi.org/10.1002/anie.201305728>.
- (127) Pan, C.; Zhao, C.; Takeuchi, M.; Sugiyasu, K. Conjugated Oligomers and Polymers Sheathed with Designer Side Chains. *Chem. - An Asian J.* **2015**, *10* (9), 1820–1835. <https://doi.org/10.1002/asia.201500452>.
- (128) Xue, M.; Yang, Y.; Chi, X.; Yan, X.; Huang, F. Development of Pseudorotaxanes and Rotaxanes: From Synthesis to Stimuli-Responsive Motions to Applications. *Chem. Rev.* **2015**, *115* (15), 7398–7501.
- (129) Lagrost, C.; Ching, K. I. C.; Lacroix, J.-C.; Aeiyach, S.; Jouini, M.; Lacaze, P.-C.; Tanguy, J. Host–Guest Complexation: A Convenient Route to Polybithiophene Composites by Electrosynthesis in Aqueous Media. Synthesis and Characterization of a New Material Containing Cyclodextrins. *J. Mater. Chem.* **1999**, *9* (10), 2351–2358.
- (130) Takashima, Y.; Oizumi, Y.; Sakamoto, K.; Miyauchi, M.; Kamitori, S.; Harada, A. Crystal Structure of the Complex of  $\beta$ -Cyclodextrin with Bithiophene and Their Oxidative Polymerization in Water. *Macromolecules* **2004**, *37* (11), 3962–3964.
- (131) Hapiot, P.; Lagrost, C.; Aeiyach, S.; Jouini, M.; Lacroix, J.-C. Oxidative Coupling of Small Oligothiophenes and Oligopyrroles in Water in the Presence of Cyclodextrin. Flash Photolysis Investigations. *J. Phys. Chem. B* **2002**, *106* (14), 3622–3628.
- (132) van den Boogaard, M.; Bonnet, G.; van’t Hof, P.; Wang, Y.; Brochon, C.; van Hutten, P.; Lapp, A.; Hadzioannou, G. Synthesis of Insulated Single-Chain Semiconducting Polymers Based on Polythiophene, Polyfluorene, and  $\beta$ -Cyclodextrin. *Chem. Mater.* **2004**, *16* (23), 4383–4385.
- (133) Stanier, C. A.; O’Connell, M. J.; Clegg, W.; Anderson, H. L. Synthesis of Fluorescent Stilbene and Tolan Rotaxanes by Suzuki Coupling. *Chem. Commun.* **2001**, No. 5, 493–494.
- (134) Terao, J.; Tang, A.; Michels, J. J.; Krivokapic, A.; Anderson, H. L. Synthesis of Poly (Para-Phenylenevinylene) Rotaxanes by Aqueous Suzuki Coupling. *Chem. Commun.* **2004**, No. 1, 56–57.
- (135) Cacialli, F.; Wilson, J. S.; Michels, J. J.; Daniel, C.; Silva, C.; Friend, R. H.; Severin, N.; Samori, P.; Rabe, J. P.; O’Connell, M. J. Cyclodextrin-Threaded Conjugated Polyrotaxanes as Insulated Molecular Wires with Reduced Interstrand Interactions. *Nat. Mater.* **2002**, *1* (3), 160–164.
- (136) Terao, J.; Tsuda, S.; Tanaka, Y.; Okoshi, K.; Fujihara, T.; Tsuji, Y.; Kambe, N. Synthesis of Organic-Soluble Conjugated Polyrotaxanes by Polymerization of Linked Rotaxanes. *J. Am. Chem. Soc.* **2009**, *131* (44), 16004–16005.
- (137) Terao, J.; Tanaka, Y.; Tsuda, S.; Kambe, N.; Taniguchi, M.; Kawai, T.; Saeki, A.; Seki, S. Insulated Molecular Wire with Highly Conductive  $\pi$ -Conjugated Polymer Core. *J. Am. Chem. Soc.* **2009**, *131* (50), 18046–18047.

- (138) Terao, J.; Wadahama, A.; Matono, A.; Tada, T.; Watanabe, S.; Seki, S.; Fujihara, T.; Tsuji, Y. Design Principle for Increasing Charge Mobility of  $\pi$ -Conjugated Polymers Using Regularly Localized Molecular Orbitals. *Nat. Commun.* **2013**, *4* (1), 1–9.
- (139) Ikeda, T.; Higuchi, M.; Kurth, D. G. From Thiophene [2] Rotaxane to Polythiophene Polyrotaxane. *J. Am. Chem. Soc.* **2009**, *131* (26), 9158–9159.
- (140) Laursen, B. W.; Nygaard, S.; Jeppesen, J. O.; Stoddart, J. F. Counterion-Induced Translational Isomerism in a Bistable [2] Rotaxane. *Org. Lett.* **2004**, *6* (23), 4167–4170.
- (141) Ikeda, T.; Higuchi, M. Electrochromic Properties of Polythiophene Polyrotaxane Film. *Langmuir* **2011**, *27* (7), 4184–4189.
- (142) Ferguson, S. B.; Sanford, E. M.; Seward, E. M.; Diederich, F. Cyclophane-Arene Inclusion Complexation in Protic Solvents: Solvent Effects versus Electron Donor-Acceptor Interactions. *J. Am. Chem. Soc.* **1991**, *113* (14), 5410–5419.
- (143) Diederich, F. Cyclophanes (Monographs in Supramolecular Chemistry)(Ed.: JF Stoddart), RSC, Cambridge, UK, 1991, Chapter 7; b) DB Smithrud, F. Diederich. *J. Am. Chem. Soc.* **1990**, *112*, 339–343.
- (144) Anderson, S.; Aplin, R. T.; Claridge, T. D. W.; Goodson III, T.; Maciel, A. C.; Rumbles, G.; Ryan, J. F.; Anderson, H. L. An Approach to Insulated Molecular Wires: Synthesis of Water-Soluble Conjugated Rotaxanes. *J. Chem. Soc. Perkin Trans. I* **1998**, No. 15, 2383–2398.
- (145) Dietrich-Buchecker, C. O.; Sauvage, J. P.; Kern, J. M. Templated Synthesis of Interlocked Macroyclic Ligands: The Catenands. *J. Am. Chem. Soc.* **1984**, *106* (10), 3043–3045.
- (146) Zhu, S. S.; Carroll, P. J.; Swager, T. M. Conducting Polymetallorotaxanes: A Supramolecular Approach to Transition Metal Ion Sensors. *J. Am. Chem. Soc.* **1996**, *118* (36), 8713–8714.
- (147) Zhu, S. S.; Swager, T. M. Conducting Polymetallorotaxanes: Metal Ion Mediated Enhancements in Conductivity and Charge Localization. *J. Am. Chem. Soc.* **1997**, *119* (51), 12568–12577.
- (148) Lewis, J. E. M.; Winn, J.; Cera, L.; Goldup, S. M. Iterative Synthesis of Oligo [n] Rotaxanes in Excellent Yield. *J. Am. Chem. Soc.* **2016**, *138* (50), 16329–16336.
- (149) Movsisyan, L. D.; Franz, M.; Hampel, F.; Thompson, A. L.; Tykwienski, R. R.; Anderson, H. L. Polyyne Rotaxanes: Stabilization by Encapsulation. *J. Am. Chem. Soc.* **2016**, *138* (4), 1366–1376.
- (150) Woltering, S. L.; Gawel, P.; Christensen, K. E.; Thompson, A. L.; Anderson, H. L. Photochemical Unmasking of Polyyne Rotaxanes. *J. Am. Chem. Soc.* **2020**, *142* (31), 13523–13532.
- (151) Schlüter, A.-D.; Löffler, M.; Enkelmann, V. Synthesis of a Fully Unsaturated All-Carbon Ladder Polymer. *Nature* **1994**, *368* (6474), 831.
- (152) Fiesel, R.; Huber, J.; Scherf, U. Synthesis of an Optically Active Poly (Para-phenylene) Ladder Polymer. *Angew. Chemie Int. Ed. English* **1996**, *35* (18), 2111–2113.
- (153) Fu, D.-K.; Xu, B.; Swager, T. M. Alternating Poly (Pyridyl Vinylene Phenylene Vinylene) s: Synthesis and Solid State Organizations. *Tetrahedron* **1997**, *53* (45), 15487–15494.
- (154) Chiavarone, L.; Di Terlizzi, M.; Scamarcio, G.; Babudri, F.; Farinola, G. M.; Naso, F. Strong Reduction of Interchain Interaction by Bridged Chain Substitution in Luminescent Phenylenevinylene Thin Films. *Appl. Phys. Lett.* **1999**, *75* (14), 2053–2055.
- (155) Morgan, B. P.; Gilliard Jr, R. J.; Loungani, R. S.; Smith, R. C. Poly (P-phenylene Ethynylene) Incorporating Sterically Enshrouding M-Terphenyl Oxacyclophane Canopies. *Macromol. Rapid Commun.* **2009**, *30* (16), 1399–1405.
- (156) Giovannitti, A.; Nielsen, C. B.; Rivnay, J.; Kirkus, M.; Harkin, D. J.; White, A. J. P.; Sirringhaus, H.; Malliaras, G. G.; McCulloch, I. Sodium and Potassium Ion Selective Conjugated Polymers for Optical Ion Detection in Solution and Solid State. *Adv. Funct. Mater.* **2016**, *26* (4), 514–523.
- (157) McDearmon, B.; Lim, E.; Lee, I.-H.; Kozycz, L. M.; O'Hara, K.; Robledo, P. I.; Venkatesan, N. R.; Chabinyc, M. L.; Hawker, C. J. Effects of Side-Chain Topology on Aggregation of Conjugated Polymers. *Macromolecules* **2018**, *51* (7), 2580–2590.
- (158) Chaudhuri, S.; Mohanan, M.; Willems, A. V.; Bertke, J. A.; Gavvalapalli, N.  $\beta$ -Strand

- Inspired Bifacial  $\pi$ -Conjugated Polymers. *Chem. Sci.* **2019**, *10*, 5976–5982.
- (159) Ikeda, T.; Lintuluoto, J. M.; Aratani, N.; Yoon, Z. S.; Kim, D.; Osuka, A. Synthesis of Doubly Strapped Meso–Meso-Linked Porphyrin Arrays and Triply Linked Conjugated Porphyrin Tapes. *European J. Org. Chem.* **2006**, *2006* (14), 3193–3204.
- (160) Sugiyasu, K.; Takeuchi, M. Conducting Polymer Networks Cross-Linked by “Isolated” Functional Dyes: Design, Synthesis, and Electrochemical Polymerization of Doubly Strapped Light-Harvesting Porphyrin/Oligothiophene Monomers. *Chem. Eur. J.* **2009**, *15* (26), 6350–6362.
- (161) Becker, K.; Lagoudakis, P. G.; Gaefke, G.; Höger, S.; Lupton, J. M. Exciton Accumulation in  $\Pi$ -Conjugated Wires Encapsulated by Light-Harvesting Macrocycles. *Angew. Chemie Int. Ed.* **2007**, *46* (19), 3450–3455.
- (162) Sun, C.; Mróz, M. M.; Smirnov, J. R. C.; Lüer, L.; Hermida-Merino, D.; Zhao, C.; Takeuchi, M.; Sugiyasu, K.; Cabanillas-González, J. Amplified Spontaneous Emission in Insulated Polythiophenes. *J. Mater. Chem. C* **2018**, *6* (24), 6591–6596.
- (163) Shomura, R.; Sugiyasu, K.; Yasuda, T.; Sato, A.; Takeuchi, M. Electrochemical Generation and Spectroscopic Characterization of Charge Carriers within Isolated Planar Polythiophene. *Macromolecules* **2012**, *45* (9), 3759–3771.
- (164) Tumbleston, J. R.; Collins, B. A.; Yang, L.; Stuart, A. C.; Gann, E.; Ma, W.; You, W.; Ade, H. The Influence of Molecular Orientation on Organic Bulk Heterojunction Solar Cells. *Nat. Photonics* **2014**, *8* (5), 385.
- (165) Graham, K. R.; Cabanetos, C.; Jahnke, J. P.; Idso, M. N.; El Labban, A.; Ngongang Ndjawa, G. O.; Heumueller, T.; Vandewal, K.; Salleo, A.; Chmelka, B. F.; Amassian, A.; Beaujuge, P. M.; McGhee, M. D. Importance of the Donor: Fullerene Intermolecular Arrangement for High-Efficiency Organic Photovoltaics. *J. Am. Chem. Soc.* **2014**, *136* (27), 9608–9618.
- (166) Hao, Z.; Iqbal, A. Some Aspects of Organic Pigments. *Chem. Soc. Rev.* **1997**, *26* (3), 203–213.
- (167) Wallquist, O.; Lenz, R. 20 Years of DPP Pigments—Future Perspectives. In *Macromolecular Symposia*; Wiley Online Library, 2002; Vol. 187, pp 617–630.
- (168) Qu, S.; Tian, H. Diketopyrrolopyrrole (DPP)-Based Materials for Organic Photovoltaics. *Chem. Commun.* **2012**, *48* (25), 3039–3051. <https://doi.org/10.1039/C2CC17886A>.
- (169) Bronstein, H.; Chen, Z.; Ashraf, R. S.; Zhang, W.; Du, J.; Durrant, J. R.; Shakya Tuladhar, P.; Song, K.; Watkins, S. E.; Geerts, Y. Thieno [3, 2-b] Thiophene–Diketopyrrolopyrrole-Containing Polymers for High-Performance Organic Field-Effect Transistors and Organic Photovoltaic Devices. *J. Am. Chem. Soc.* **2011**, *133* (10), 3272–3275.
- (170) Li, W.; Hendriks, K. H.; Wienk, M. M.; Janssen, R. A. J. Diketopyrrolopyrrole Polymers for Organic Solar Cells. *Acc. Chem. Res.* **2016**, *49* (1), 78–85.
- (171) Sassi, M.; Buccheri, N.; Rooney, M.; Botta, C.; Bruni, F.; Giovanella, U.; Brovelli, S.; Beverina, L. Near-Infrared Roll-off-Free Electroluminescence from Highly Stable Diketopyrrolopyrrole Light Emitting Diodes. *Sci. Rep.* **2016**, *6*, 34096.
- (172) Yi, Z.; Wang, S.; Liu, Y. Design of High-mobility Diketopyrrolopyrrole-based  $\Pi$ -conjugated Copolymers for Organic Thin-film Transistors. *Adv. Mater.* **2015**, *27* (24), 3589–3606.
- (173) Zhang, G.; Wang, L.; Cai, X.; Zhang, L.; Yu, J.; Wang, A. A New Diketopyrrolopyrrole (DPP) Derivative Bearing Boronate Group as Fluorescent Probe for Fluoride Ion. *Dye. Pigment.* **2013**, *98* (2), 232–237.
- (174) Kaur, M.; Choi, D. H. Diketopyrrolopyrrole: Brilliant Red Pigment Dye-Based Fluorescent Probes and Their Applications. *Chem. Soc. Rev.* **2015**, *44* (1), 58–77.
- (175) Fukuda, M.; Kodama, K.; Yamamoto, H.; Mito, K. Evaluation of New Organic Pigments as Laser-Active Media for a Solid-State Dye Laser. *Dye. Pigment.* **2004**, *63* (2), 115–125.
- (176) Royakkers, J.; Minotto, A.; Congrave, D. G.; Zeng, W.; Hassan, A.; Leventis, A.; Caciali, F.; Bronstein, H. Suppressing Solid-State Quenching in Red-Emitting Conjugated Polymers. *Chem. Mater.* **2020**, *32* (23), 10140–10145.
- (177) Naik, M. A.; Patil, S. Diketopyrrolopyrrole-based Conjugated Polymers and Small Molecules for Organic Ambipolar Transistors and Solar Cells. *J. Polym. Sci. Part A*

*Polym. Chem.* **2013**, *51* (20), 4241–4260.

- (178) Tieke, B.; Rabindranath, A. R.; Zhang, K.; Zhu, Y. Conjugated Polymers Containing Diketopyrrolopyrrole Units in the Main Chain. *Beilstein J. Org. Chem.* **2010**, *6* (1), 830–845.
- (179) Vala, M.; Krajčovič, J.; Luňák Jr., S.; Ouzzane, I.; Bouillon, J.-P.; Weiter, M. HOMO and LUMO Energy Levels of N, N'-Dinitrophenyl-Substituted Polar Diketopyrrolopyrroles (DPPs). *Dye. Pigment.* **2014**, *106*, 136–142.
- (180) Yue, W.; Suraru, S.; Bialas, D.; Müller, M.; Würthner, F. Synthesis and Properties of a New Class of Fully Conjugated Azahexacene Analogues. *Angew. Chemie Int. Ed.* **2014**, *53* (24), 6159–6162.
- (181) Riggs, R. L.; Morton, C. J. H.; Slawin, A. M. Z.; Smith, D. M.; Westwood, N. J.; Austen, W. S. D.; Stuart, K. E. Synthetic Studies Related to Diketopyrrolopyrrole (DPP) Pigments. Part 3: Syntheses of Tri-and Tetra-Aryl DPPs. *Tetrahedron* **2005**, *61* (47), 11230–11243.
- (182) Zhang, K.; Tieke, B.; Forgie, J. C.; Vilela, F.; Parkinson, J. A.; Skabara, P. J. Cross-Linked Polymers Based on 2, 3, 5, 6-Tetra-Substituted Pyrrolo [3, 4-c] Pyrrole-1, 4 (2H, 5H)-Dione (DPP): Synthesis, Optical and Electronic Properties. *Polymer (Guildf.)* **2010**, *51* (26), 6107–6114.
- (183) Langhals, H.; Grundeit, T.; Potrawa, T.; Polborn, K. Highly Photostable Organic Fluorescent Pigments—A Simple Synthesis of N-Arylpolyrrolopyrrolediones (DPP). *Liebigs Ann.* **1996**, *1996* (5), 679–682.
- (184) Zhu, Y.; Rabindranath, A. R.; Beyerlein, T.; Tieke, B. Highly Luminescent 1, 4-Diketo-3, 6-Diphenylpyrrolo [3, 4-c] Pyrrole-(DPP-) Based Conjugated Polymers Prepared upon Suzuki Coupling. *Macromolecules* **2007**, *40* (19), 6981–6989.
- (185) Brovelli, S.; Latini, G.; Frampton, M. J.; McDonnell, S. O.; Oddy, F. E.; Fenwick, O.; Anderson, H. L.; Cacialli, F. Tuning Intrachain versus Interchain Photophysics via Control of the Threading Ratio of Conjugated Polyrotaxanes. *Nano Lett.* **2008**, *8* (12), 4546–4551.
- (186) Nielsen, C. B.; Turbiez, M.; McCulloch, I. Recent Advances in the Development of Semiconducting DPP-containing Polymers for Transistor Applications. *Adv. Mater.* **2013**, *25* (13), 1859–1880.
- (187) Guo, X.; Facchetti, A.; Marks, T. J. Imide- and Amide-Functionalized Polymer Semiconductors. *Chem. Rev.* **2014**, *114* (18), 8943–9012. <https://doi.org/10.1021/cr500225d>.
- (188) Letizia, J. A.; Salata, M. R.; Tribout, C. M.; Facchetti, A.; Ratner, M. A.; Marks, T. J. N-Channel Polymers by Design: Optimizing the Interplay of Solubilizing Substituents, Crystal Packing, and Field-Effect Transistor Characteristics in Polymeric Bithiophene-Imide Semiconductors. *J. Am. Chem. Soc.* **2008**, *130* (30), 9679–9694.
- (189) Zhan, X.; Facchetti, A.; Barlow, S.; Marks, T. J.; Ratner, M. A.; Wasielewski, M. R.; Marder, S. R. Rylene and Related Diimides for Organic Electronics. *Advanced Materials*. 2011, pp 268–284. <https://doi.org/10.1002/adma.201001402>.
- (190) Guo, X.; Tu, D.; Liu, X. Recent Advances in Rylene Diimide Polymer Acceptors for All-Polymer Solar Cells. *J. energy Chem.* **2015**, *24* (6), 675–685.
- (191) Kim, Y.; Lim, E. Development of Polymer Acceptors for Organic Photovoltaic Cells. *Polymers (Basel)* **2014**, *6* (2), 382–407.
- (192) Yan, H.; Chen, Z.; Zheng, Y.; Newman, C.; Quinn, J. R.; Dötz, F.; Kastler, M.; Facchetti, A. A High-Mobility Electron-Transporting Polymer for Printed Transistors. *Nature* **2009**, *457* (7230), 679–686. <https://doi.org/10.1038/nature07727>.
- (193) Capelli, R.; Toffanin, S.; Generali, G.; Usta, H.; Facchetti, A.; Muccini, M. Organic Light-Emitting Transistors with an Efficiency That Outperforms the Equivalent Light-Emitting Diodes. *Nat. Mater.* **2010**, *9* (6), 496.
- (194) Choi, J.; Kim, K.-H.; Yu, H.; Lee, C.; Kang, H.; Song, I.; Kim, Y.; Oh, J. H.; Kim, B. J. Importance of Electron Transport Ability in Naphthalene Diimide-Based Polymer Acceptors for High-Performance, Additive-Free, All-Polymer Solar Cells. *Chem. Mater.* **2015**, *27* (15), 5230–5237.
- (195) Xu, X.; Li, Z.; Zhang, W.; Meng, X.; Zou, X.; Di Carlo Rasi, D.; Ma, W.; Yartsev, A.; Andersson, M. R.; Janssen, R. A. J. 8.0% Efficient All-polymer Solar Cells with High

- Photovoltage of 1.1 V and Internal Quantum Efficiency near Unity. *Adv. Energy Mater.* **2018**, *8* (1), 1700908.
- (196) Sirringhaus, H. Electrons in the Fast Lane. *Nature* **2009**, *457* (7230), 667–668.
- (197) Caironi, M.; Bird, M.; Fazzi, D.; Chen, Z.; Di Pietro, R.; Newman, C.; Facchetti, A.; Sirringhaus, H. Very Low Degree of Energetic Disorder as the Origin of High Mobility in an N-channel Polymer Semiconductor. *Adv. Funct. Mater.* **2011**, *21* (17), 3371–3381.
- (198) Steyrleuthner, R.; Schubert, M.; Howard, I.; Klaumünzer, B.; Schilling, K.; Chen, Z.; Saalfrank, P.; Laquai, F.; Facchetti, A.; Neher, D. Aggregation in a High-Mobility n-Type Low-Bandgap Copolymer with Implications on Semicrystalline Morphology. *J. Am. Chem. Soc.* **2012**, *134* (44), 18303–18317.
- (199) Wu, Y.; Schneider, S.; Walter, C.; Chowdhury, A. H.; Bahrami, B.; Wu, H.-C.; Qiao, Q.; Toney, M. F.; Bao, Z. Fine-Tuning Semiconducting Polymer Self-Aggregation and Crystallinity Enables Optimal Morphology and High-Performance Printed All-Polymer Solar Cells. *J. Am. Chem. Soc.* **2019**, *142* (1), 392–406.
- (200) Mahmood, A.; Wang, J. A Review of Grazing Incidence Small-and Wide-Angle X-Ray Scattering Techniques for Exploring the Film Morphology of Organic Solar Cells. *Sol. RRL* **2020**, *4* (10), 2000337.
- (201) Lee, C.; Kang, H.; Lee, W.; Kim, T.; Kim, K.; Woo, H. Y.; Wang, C.; Kim, B. J. High-performance All-polymer Solar Cells via Side-chain Engineering of the Polymer Acceptor: The Importance of the Polymer Packing Structure and the Nanoscale Blend Morphology. *Adv. Mater.* **2015**, *27* (15), 2466–2471.
- (202) You, H.; Kim, D.; Cho, H.; Lee, C.; Chong, S.; Ahn, N. Y.; Seo, M.; Kim, J.; Kim, F. S.; Kim, B. J. Shift of the Branching Point of the Side-Chain in Naphthalenediimide (NDI)-Based Polymer for Enhanced Electron Mobility and All-Polymer Solar Cell Performance. *Adv. Funct. Mater.* **2018**, *28* (39), 1803613.
- (203) Marchetti, C.; Zyner, K. G.; Ohnmacht, S. A.; Robson, M.; Haider, S. M.; Morton, J. P.; Marsico, G.; Vo, T.; Laughlin-Toth, S.; Ahmed, A. A. Targeting Multiple Effector Pathways in Pancreatic Ductal Adenocarcinoma with a G-Quadruplex-Binding Small Molecule. *J. Med. Chem.* **2018**.
- (204) Berezin, A. A.; Sciutto, A.; Demitri, N.; Bonifazi, D. Rational Synthesis of Ab-Type n - Substituted Core-Functionalized Naphthalene Diimides (CNDIs). *Org. Lett.* **2015**, *17* (8), 1870–1873. <https://doi.org/10.1021/acs.orglett.5b00543>.
- (205) Chen, Z.; Zheng, Y.; Yan, H.; Facchetti, A. Naphthalenedicarboximide- vs Perylenedicarboximide-Based Copolymers. Synthesis and Semiconducting Properties in Bottom-Gate N-Channel Organic Transistors. *J. Am. Chem. Soc.* **2009**, *131* (1), 8–9. <https://doi.org/10.1021/ja805407g>.
- (206) Chaignon, F.; Falkenström, M.; Karlsson, S.; Blart, E.; Odobel, F.; Hammarström, L. Very Large Acceleration of the Photoinduced Electron Transfer in a Ru (Bpy) 3–Naphthalene Bisimide Dyad Bridged on the Naphthyl Core. *Chem. Commun.* **2007**, No. 1, 64–66.
- (207) Wu, W.; Wu, X.; Zhao, J.; Wu, M. Synergetic Effect of C<sup>\*</sup> N<sup>+</sup> N/C<sup>+</sup> N<sup>+</sup> N Coordination and the Arylacetylide Ligands on the Photophysical Properties of Cyclometalated Platinum Complexes. *J. Mater. Chem. C* **2015**, *3* (10), 2291–2301.
- (208) Marks, T. J.; Wasielewski, M. R.; Facchetti, A.; Jones, B. A. Naphthalene-Based Semiconductor Materials and Methods of Preparing and Use Thereof. Google Patents August 4, 2009.
- (209) Chopin, S.; Chaignon, F.; Blart, E.; Odobel, F. Syntheses and Properties of Core-Substituted Naphthalene Bisimides with Aryl Ethynyl or Cyano Groups. *J. Mater. Chem.* **2007**, *17* (39), 4139. <https://doi.org/10.1039/b704489e>.
- (210) Dawson, R. E.; Hennig, A.; Weimann, D. P.; Emery, D.; Ravikumar, V.; Montenegro, J.; Takeuchi, T.; Gabutti, S.; Mayor, M.; Mareda, J.; Schalley, C. A.; Matile, S. Experimental Evidence for the Functional Relevance of Anion-π Interactions. *Nat. Chem.* **2010**, *2* (7), 533–538. <https://doi.org/10.1038/nchem.657>.
- (211) Wang, L.; Fang, G.; Cao, D. Recent Advances of AIE-Active Conjugated Polymers: Synthesis and Application. *J. Macromol. Sci. Part A* **2014**, *51* (8), 668–681.
- (212) Qin, A.; Lam, J. W. Y.; Tang, B. Z. Luminogenic Polymers with Aggregation-Induced

- Emission Characteristics. *Prog. Polym. Sci.* **2012**, *37* (1), 182–209.
- (213) Hu, R.; Kang, Y.; Tang, B. Z. Recent Advances in AIE Polymers. *Polym. J.* **2016**, *48* (4), 359–370.
- (214) Sánchez-Ruiz, A.; Sousa-Hervés, A.; Tolosa Barrilero, J.; Navarro, A.; Garcia-Martinez, J. C. Aggregation-Induced Emission Properties in Fully  $\pi$ -Conjugated Polymers, Dendrimers, and Oligomers. *Polymers (Basel)*. **2021**, *13* (2), 213.
- (215) Chen, Y.; Liang, X.; Yang, H.; Wang, Q.; Zhou, X.; Guo, D.; Li, S.; Zhou, C.; Dong, L.; Liu, Z. Strong Near-Infrared Solid Emission and Enhanced N-Type Mobility for Poly (Naphthalene Diimide) Vinylene by a Random Polymerization Strategy. *Macromolecules* **2019**, *52* (21), 8332–8338.
- (216) Liang, X.; Tan, L.; Liu, Z.; Ma, Y.; Zhang, G.; Wang, L.; Li, S.; Dong, L.; Li, J.; Chen, W. Poly (Naphthalene Diimide) Vinylene: Solid State Red Emission and Semiconducting Properties for Transistors. *Chem. Commun.* **2017**, *53* (36), 4934–4937.
- (217) Thomas, T. H.; Harkin, D. J.; Gillett, A. J.; Lemaur, V.; Nikolka, M.; Sadhanala, A.; Richter, J. M.; Armitage, J.; Chen, H.; McCulloch, I. Short Contacts between Chains Enhancing Luminescence Quantum Yields and Carrier Mobilities in Conjugated Copolymers. *Nat. Commun.* **2019**, *10* (2614), 1–10.
- (218) Shao, H.; Seifert, J.; Romano, N. C.; Gao, M.; Helmus, J. J.; Jaroniec, C. P.; Modarelli, D. A.; Parquette, J. R. Amphiphilic Self-assembly of an N-type Nanotube. *Angew. Chemie* **2010**, *122* (42), 7854–7857.
- (219) Shao, H.; Parquette, J. R. A  $\pi$ -Conjugated Hydrogel Based on an Fmoc-Dipeptide Naphthalene Diimide Semiconductor. *Chem. Commun.* **2010**, *46* (24), 4285–4287.
- (220) Nalluri, S. K. M.; Berdugo, C.; Javid, N.; Frederix, P. W. J. M.; Ulijn, R. V. Biocatalytic Self-Assembly of Supramolecular Charge-Transfer Nanostructures Based on N-Type Semiconductor-Appended Peptides. *Angew. Chemie* **2014**, *126* (23), 5992–5997.
- (221) Basak, S.; Nandi, N.; Baral, A.; Banerjee, A. Tailor-Made Design of J-or H-Aggregated Naphthalenediimide-Based Gels and Remarkable Fluorescence Turn on/off Behaviour Depending on Solvents. *Chem. Commun.* **2015**, *51* (4), 780–783.
- (222) Mukhopadhyay, P.; Iwashita, Y.; Shirakawa, M.; Kawano, S.; Fujita, N.; Shinkai, S. Spontaneous Colorimetric Sensing of the Positional Isomers of Dihydroxynaphthalene in a 1D Organogel Matrix. *Angew. Chemie* **2006**, *118* (10), 1622–1625.
- (223) Scharber, M. C.; Sariciftci, N. S. Low Band Gap Conjugated Semiconducting Polymers. *Adv. Mater. Technol.* **2021**, *6* (4), 2000857. <https://doi.org/10.1002/admt.202000857>
- (224) Zhang, B.; Soleimaninejad, H.; Jones, D. J.; White, J. M.; Ghiggino, K. P.; Smith, T. A.; Wong, W. W. H. Highly Fluorescent Molecularly Insulated Perylene Diimides: Effect of Concentration on Photophysical Properties. *Chem. Mater.* **2017**, *29* (19), 8395–8403.
- (225) Chen, Z.; Stepanenko, V.; Dehm, V.; Prins, P.; Siebbeles, L. D. A.; Seibt, J.; Marquetand, P.; Engel, V.; Würthner, F. Photoluminescence and Conductivity of Self-Assembled  $\pi$ – $\pi$  Stacks of Perylene Bisimide Dyes. *Chem. Eur. J.* **2007**, *13* (2), 436–449.
- (226) Idé, J.; Méreau, R.; Ducasse, L.; Castet, F.; Olivier, Y.; Martinelli, N.; Cornil, J.; Beljonne, D. Supramolecular Organization and Charge Transport Properties of Self-Assembled  $\Pi$ – $\pi$  Stacks of Perylene Diimide Dyes. *J. Phys. Chem. B* **2011**, *115* (18), 5593–5603.
- (227) Würthner, F. Perylene Bisimide Dyes as Versatile Building Blocks for Functional Supramolecular Architectures. *Chem. Commun.* **2004**, No. 14, 1564–1579.
- (228) Schmidt, D.; Stolte, M.; Süß, J.; Liess, A.; Stepanenko, V.; Würthner, F. Protein-like Enwrapped Perylene Bisimide Chromophore as a Bright Microcrystalline Emitter Material. *Angew. Chemie Int. Ed.* **2019**, *58*, 13385 –13389.
- (229) Cai, Y.; Huo, L.; Sun, X.; Wei, D.; Tang, M.; Sun, Y. High Performance Organic Solar Cells Based on a Twisted Bay-Substituted Tetraphenyl Functionalized Perylenediimide Electron Acceptor. *Adv. Energy Mater.* **2015**, *5* (11), 1500032.
- (230) Chen, Z.; Debije, M. G.; Debaerdemaeker, T.; Osswald, P.; Würthner, F. Tetrachloro-substituted Perylene Bisimide Dyes as Promising N-type Organic Semiconductors: Studies on Structural, Electrochemical and Charge Transport Properties. *ChemPhysChem* **2004**, *5* (1), 137–140.
- (231) Osswald, P.; Leusser, D.; Stalke, D.; Würthner, F. Perylene Bisimide Based Macrocycles:

- Effective Probes for the Assessment of Conformational Effects on Optical Properties. *Angew. Chemie Int. Ed.* **2005**, *44* (2), 250–253.
- (232) Banal, J. L.; Soleimaninejad, H.; Jradi, F. M.; Liu, M.; White, J. M.; Blakers, A. W.; Cooper, M. W.; Jones, D. J.; Ghiggino, K. P.; Marder, S. R. Energy Migration in Organic Solar Concentrators with a Molecularly Insulated Perylene Diimide. *J. Phys. Chem. C* **2016**, *120* (24), 12952–12958.
- (233) Fujiwara, Y.; Ozawa, R.; Onuma, D.; Suzuki, K.; Yoza, K.; Kobayashi, K. Double Alkylene-Strapped Diphenylanthracene as a Photostable and Intense Solid-State Blue-Emitting Material. *J. Org. Chem.* **2013**, *78* (6), 2206–2212.
- (234) Battagliarin, G.; Li, C.; Enkelmann, V.; Müllen, K. 2, 5, 8, 11-Tetraboronic Ester Perylenediimides: A next Generation Building Block for Dye-Stuff Synthesis. *Org. Lett.* **2011**, *13* (12), 3012–3015.
- (235) Teraoka, T.; Hiroto, S.; Shinokubo, H. Iridium-Catalyzed Direct Tetraborylation of Perylene Bisimides. *Org. Lett.* **2011**, *13* (10), 2532–2535.
- (236) Walker, S. D.; Barder, T. E.; Martinelli, J. R.; Buchwald, S. L. A Rationally Designed Universal Catalyst for Suzuki–Miyaura Coupling Processes. *Angew. Chemie Int. Ed.* **2004**, *43* (14), 1871–1876.
- (237) Gómez, R.; Veldman, D.; Blanco, R.; Seoane, C.; Segura, J. L.; Janssen, R. A. J. Energy and Electron Transfer in a Poly (Fluorene-Alt-Phenylene) Bearing Perylenediimides as Pendant Electron Acceptor Groups. *Macromolecules* **2007**, *40* (8), 2760–2772.
- (238) Akimoto, S.; Ohmori, A.; Yamazaki, I. Dimer Formation and Excitation Relaxation of Perylene in Langmuir–Blodgett Films. *J. Phys. Chem. B* **1997**, *101* (19), 3753–3758.
- (239) Barford, W.; Marcus, M. Perspective: Optical Spectroscopy in  $\pi$ -Conjugated Polymers and How It Can Be Used to Determine Multiscale Polymer Structures. *J. Chem. Phys.* **2017**, *146* (13), 130902.
- (240) Panzer, F.; Bässler, H.; Köhler, A. Temperature Induced Order–Disorder Transition in Solutions of Conjugated Polymers Probed by Optical Spectroscopy. *J. Phys. Chem. Lett.* **2017**, *8* (1), 114–125.
- (241) Lakowicz, J. R. *Principles of Fluorescence Spectroscopy*; Springer Science & Business Media, 2013.
- (242) Janiak, C. A Critical Account on  $\pi$ – $\pi$  Stacking in Metal Complexes with Aromatic Nitrogen-Containing Ligands. *J. Chem. Soc. Dalton Trans.* **2000**, No. 21, 3885–3896.
- (243) Brown, K. E.; Salamant, W. A.; Shoer, L. E.; Young, R. M.; Wasielewski, M. R. Direct Observation of Ultrafast Excimer Formation in Covalent Perylenediimide Dimers Using Near-Infrared Transient Absorption Spectroscopy. *J. Phys. Chem. Lett.* **2014**, *5* (15), 2588–2593.
- (244) Schubert, A.; Settels, V.; Liu, W.; Würthner, F.; Meier, C.; Fink, R. F.; Schindlbeck, S.; Lochbrunner, S.; Engels, B.; Engel, V. Ultrafast Exciton Self-Trapping upon Geometry Deformation in Perylene-Based Molecular Aggregates. *J. Phys. Chem. Lett.* **2013**, *4* (5), 792–796.
- (245) Sung, J.; Kim, P.; Fimmel, B.; Würthner, F.; Kim, D. Direct Observation of Ultrafast Coherent Exciton Dynamics in Helical  $\pi$ -Stacks of Self-Assembled Perylene Bisimides. *Nat. Commun.* **2015**, *6*, 8646.
- (246) Sung, J.; Nowak-Królik, A.; Schlosser, F.; Fimmel, B.; Kim, W.; Kim, D.; Würthner, F. Direct Observation of Excimer-Mediated Intramolecular Electron Transfer in a Cofacially-Stacked Perylene Bisimide Pair. *J. Am. Chem. Soc.* **2016**, *138* (29), 9029–9032.
- (247) Becke, A. D. Density-Functional Exchange-Energy Approximation with Correct Asymptotic Behavior. *Phys. Rev. A* **1988**, *38* (6), 3098.
- (248) Ran, N. A.; Roland, S.; Love, J. A.; Savikhin, V.; Takacs, C. J.; Fu, Y.-T.; Li, H.; Coropceanu, V.; Liu, X.; Brédas, J.-L.; Bazan, G. C.; Toney, M. F.; Neher, D.; Nguyen, T.-Q. Impact of Interfacial Molecular Orientation on Radiative Recombination and Charge Generation Efficiency. *Nat. Commun.* **2017**, *8* (1), 79.
- (249) Jakowitz, A. C.; Böhm, M. L.; Sadhanala, A.; Huettner, S.; Rao, A.; Friend, R. H. Visualizing Excitations at Buried Heterojunctions in Organic Semiconductor Blends. *Nat. Mater.* **2017**, *16* (5), 551–557.

- (250) Sebastian, L.; Weiser, G.; Bässler, H. Charge Transfer Transitions in Solid Tetracene and Pentacene Studied by Electroabsorption. *Chem. Phys.* **1981**, *61* (1–2), 125–135.
- (251) Gélinas, S.; Rao, A.; Kumar, A.; Smith, S. L.; Chin, A. W.; Clark, J.; Van Der Poll, T. S.; Bazan, G. C.; Friend, R. H. Ultrafast Long-Range Charge Separation in Organic Semiconductor Photovoltaic Diodes. *Science* **2014**, *343* (6170), 512–516.
- (252) Park, S. H.; Roy, A.; Beaupre, S.; Cho, S.; Coates, N.; Moon, J. S.; Moses, D.; Leclerc, M.; Lee, K.; Heeger, A. J. Bulk Heterojunction Solar Cells with Internal Quantum Efficiency Approaching 100%. *Nat. Photonics* **2009**, *3* (5), 297–302.
- (253) Deotare, P. B.; Chang, W.; Hontz, E.; Congreve, D. N.; Shi, L.; Reusswig, P. D.; Modtland, B.; Bahlke, M. E.; Lee, C. K.; Willard, A. P.; Bulović, V.; Van Voorhis, T.; Baldo, M. A. Nanoscale Transport of Charge-Transfer States in Organic Donor–Acceptor Blends. *Nat. Mater.* **2015**, *14* (11), 1130–1134.
- (254) Chang, W.; Congreve, D. N.; Hontz, E.; Bahlke, M. E.; McMahon, D. P.; Reineke, S.; Wu, T. C.; Bulović, V.; Van Voorhis, T.; Baldo, M. A. Spin-Dependent Charge Transfer State Design Rules in Organic Photovoltaics. *Nat. Commun.* **2015**, *6* (6415), 1–6.
- (255) Qian, D.; Zheng, Z.; Yao, H.; Tress, W.; Hopper, T. R.; Chen, S.; Li, S.; Liu, J.; Chen, S.; Zhang, J. Design Rules for Minimizing Voltage Losses in High-Efficiency Organic Solar Cells. *Nat. Mater.* **2018**, *17* (8), 703–709.
- (256) Wang, R.; Xu, J.; Fu, L.; Zhang, C.; Li, Q.; Yao, J.; Li, X.; Sun, C.; Zhang, Z.-G.; Wang, X. Nonradiative Triplet Loss Suppressed in Organic Photovoltaic Blends with Fluorinated Nonfullerene Acceptors. *J. Am. Chem. Soc.* **2021**, *143* (11), 4359–4366.
- (257) Singh, R.; Shivanna, R.; Iosifidis, A.; Butt, H.-J.; Floudas, G.; Narayan, K. S.; Keivanidis, P. E. Charge versus Energy Transfer Effects in High-Performance Perylene Diimide Photovoltaic Blend Films. *ACS Appl. Mater. Interfaces* **2015**, *7* (44), 24876–24886.
- (258) Hartnett, P. E.; Timalsina, A.; Matte, H. S. S. R.; Zhou, N.; Guo, X.; Zhao, W.; Facchetti, A.; Chang, R. P. H.; Hersam, M. C.; Wasielewski, M. R. Slip-Stacked Perylenediimides as an Alternative Strategy for High Efficiency Nonfullerene Acceptors in Organic Photovoltaics. *J. Am. Chem. Soc.* **2014**, *136* (46), 16345–16356.
- (259) Li, S.; Liu, W.; Li, C.-Z.; Liu, F.; Zhang, Y.; Shi, M.; Chen, H.; Russell, T. P. A Simple Perylene Diimide Derivative with a Highly Twisted Geometry as an Electron Acceptor for Efficient Organic Solar Cells. *J. Mater. Chem. A* **2016**, *4* (27), 10659–10665.
- (260) Kang, T. E.; Kim, T.; Wang, C.; Yoo, S.; Kim, B. J. Poly (Benzodithiophene) Homopolymer for High-Performance Polymer Solar Cells with Open-Circuit Voltage of near 1 V: A Superior Candidate to Substitute for Poly (3-Hexylthiophene) as Wide Bandgap Polymer. *Chem. Mater.* **2015**, *27* (7), 2653–2658.
- (261) Song, X.; Gasparini, N.; Nahid, M. M.; Paletti, S. H. K.; Li, C.; Li, W.; Ade, H.; Baran, D. Efficient DPP Donor and Nonfullerene Acceptor Organic Solar Cells with High Photon-to-Current Ratio and Low Energetic Loss. *Adv. Funct. Mater.* **2019**, *29* (34), 1902441.
- (262) Zheng, B.; Huo, L.; Li, Y. Benzodithiophenedione-Based Polymers: Recent Advances in Organic Photovoltaics. *NPG Asia Mater.* **2020**, *12* (1), 1–22.
- (263) Zhao, Y.; Sakai, N.; Matile, S. Enolate Chemistry with Anion–π Interactions. *Nat. Commun.* **2014**, *5* (1), 1–5.
- (264) Langhals, H.; Ismael, R. Cyclophanes as Model Compounds for Permanent, Dynamic Aggregates–Induced Chirality with Strong CD Effects. *European J. Org. Chem.* **1998**, *1998* (9), 1915–1917.
- (265) Osaki, H.; Chou, C.; Taki, M.; Welke, K.; Yokogawa, D.; Irle, S.; Sato, Y.; Higashiyama, T.; Saito, S.; Fukazawa, A. A Macroyclic Fluorophore Dimer with Flexible Linkers: Bright Excimer Emission with a Long Fluorescence Lifetime. *Angew. Chemie* **2016**, *128* (25), 7247–7251.
- (266) Mei, C.-Y.; Liang, L.; Zhao, F.-G.; Wang, J.-T.; Yu, L.-F.; Li, Y.-X.; Li, W.-S. A Family of Donor–Acceptor Photovoltaic Polymers with Fused 4, 7-Dithienyl-2, 1, 3-Benzothiadiazole Units: Effect of Structural Fusion and Side Chains. *Macromolecules* **2013**, *46* (19), 7920–7931.
- (267) Homyak, P. D.; Tinkham, J.; Lahti, P. M.; Coughlin, E. B. Thieno [3, 4-b] Thiophene Acceptors with Alkyl, Aryl, Perfluoroalkyl, and Perfluorophenyl Pendants for Donor–

- Acceptor Low Bandgap Polymers. *Macromolecules* **2013**, *46* (22), 8873–8881.
- (268) Congrave, D. G.; Drummond, B. H.; Gray, V.; Bond, A. D.; Rao, A.; Friend, R. H.; Bronstein, H. Suppressing Aggregation Induced Quenching in Anthracene Based Conjugated Polymers. *Polym. Chem.* **2021**, *12*, 1830–1836. <https://doi.org/10.1039/D1PY00118C>.
- (269) Fernando, R.; Etheridge, F.; Muller, E.; Sauve, G. Tuning the Optical and Electrochemical Properties of Core-Substituted Naphthalenediimides with Styryl Imide Substituent. *New J. Chem.* **2015**, *39* (4), 2506–2514. <https://doi.org/10.1039/C4NJ01645A>.
- (270) Thalacker, C.; Röger, C.; Würthner, F. Synthesis and Optical and Redox Properties of Core-Substituted Naphthalene Diimide Dyes. *J. Org. Chem.* **2006**, *71* (21), 8098–8105. <https://doi.org/10.1021/jo0612269>.
- (271) Bell, T. D. M.; Yap, S.; Jani, C. H.; Bhosale, S. V.; Hofkens, J.; De Schryver, F. C.; Langford, S. J.; Ghiggino, K. P. Synthesis and Photophysics of Core-Substituted Naphthalene Diimides: Fluorophores for Single Molecule Applications. *Chem. – An Asian J.* **2009**, *4* (10), 1542–1550. <https://doi.org/10.1002/asia.200900215>.
- (272) Piyakulawat, P.; Keawprajak, A.; Chindaduang, A.; Hanusch, M.; Asawapirom, U. Synthesis and Preliminary Characterization of Novel Naphthalene Bisimide Based Copolymers. *Synth. Met.* **2009**, *159* (5–6), 467–472.
- (273) Senkovskyy, V.; Tkachov, R.; Komber, H.; Sommer, M.; Heuker, M.; Voit, B.; Huck, W. T. S.; Kataev, V.; Petr, A.; Kiriy, A. Chain-Growth Polymerization of Unusual Anion-Radical Monomers Based on Naphthalene Diimide: A New Route to Well-Defined n-Type Conjugated Copolymers. *J. Am. Chem. Soc.* **2011**, *133* (49), 19966–19970. <https://doi.org/10.1021/ja208710x>.
- (274) Woods, E. F.; Berl, A. J.; Kalow, J. A. Photocontrolled Synthesis of N-type Conjugated Polymers. *Angew. Chemie* **2020**, *132* (15), 6118–6123.

## Appendix

### Chapter II

#### Encapsulated DPP Monomer (II-4)

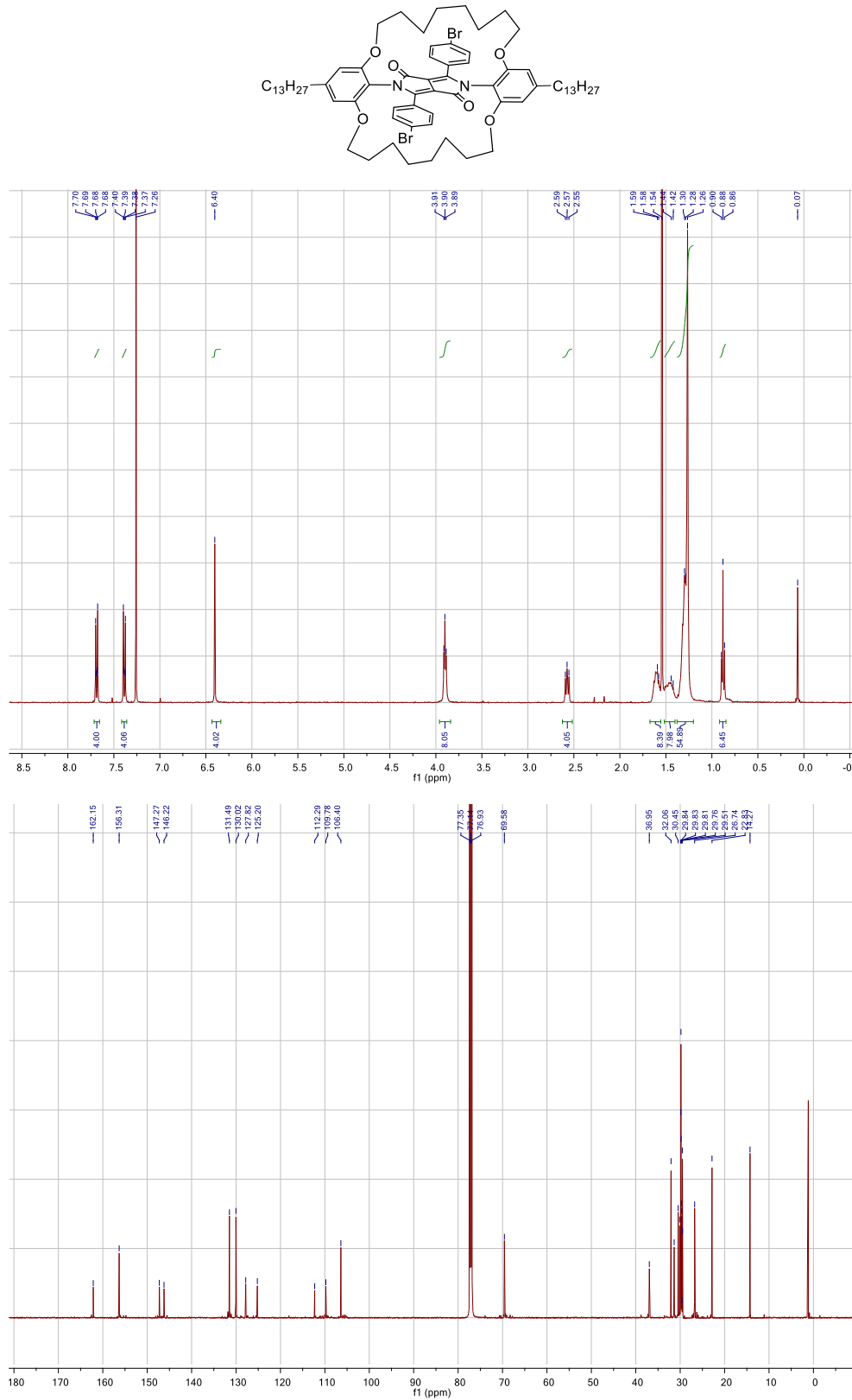


**Figure A 1.**  $^1\text{H}$  NMR (top) and  $^{13}\text{C}$  NMR{H} spectrum (bottom) of the encapsulated DPP monomer (II-4).

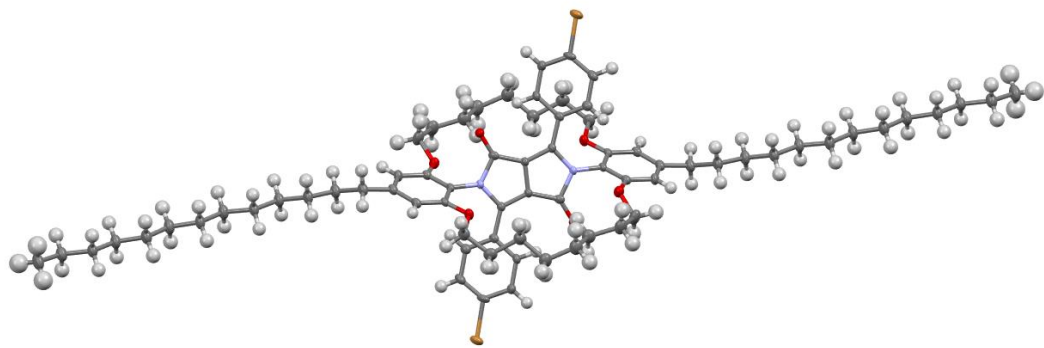


**Figure A 2.** X-ray structure of the encapsulated DPP monomer (II-4).

## Chapter III

### Br<sub>2</sub>-NDA

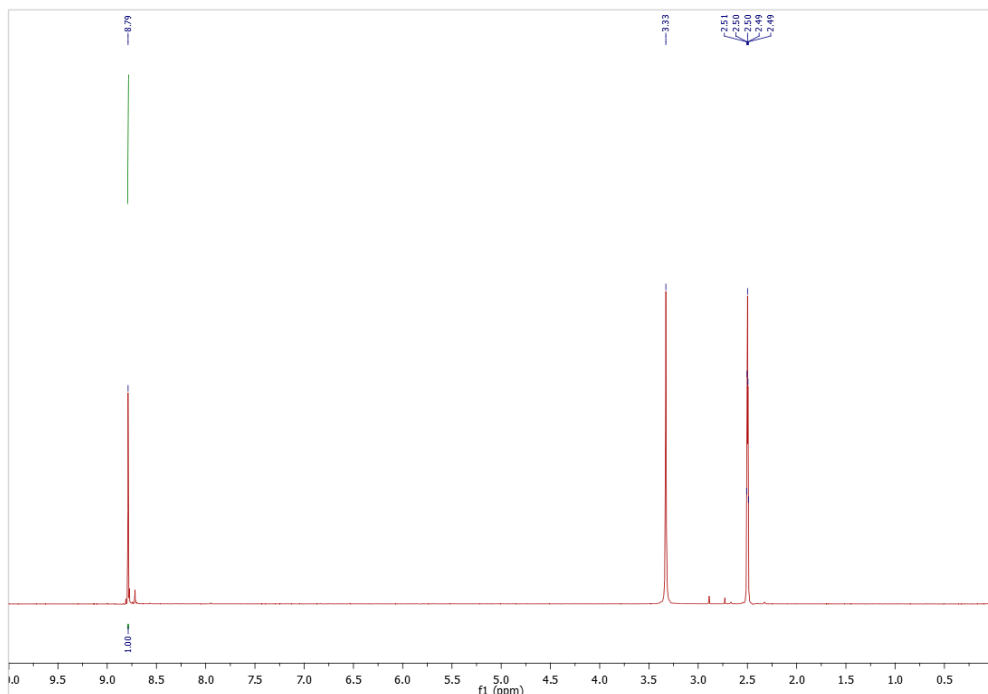
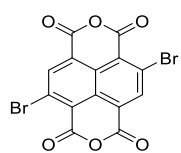


**Figure A 3.** <sup>1</sup>H NMR spectrum of Br<sub>2</sub>-NDA.

**Th<sub>2</sub>-NDA**

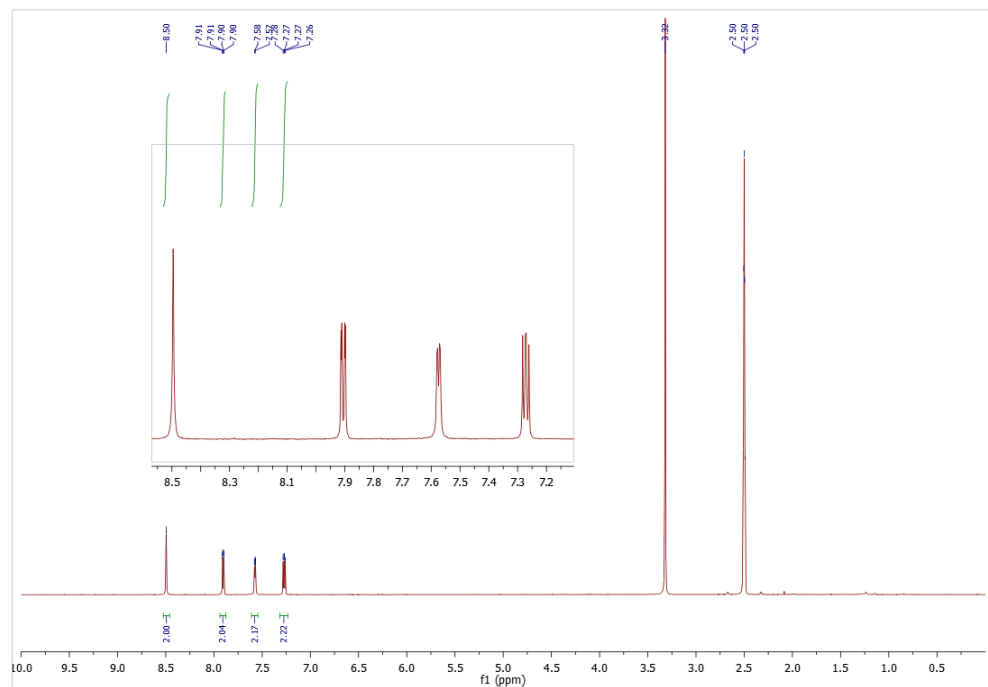
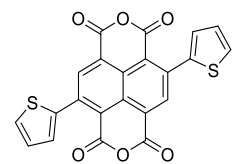


**Figure A 4.** <sup>1</sup>H NMR spectrum of Th<sub>2</sub>-NDA.

**Th<sub>2</sub>-NDI-OMe**

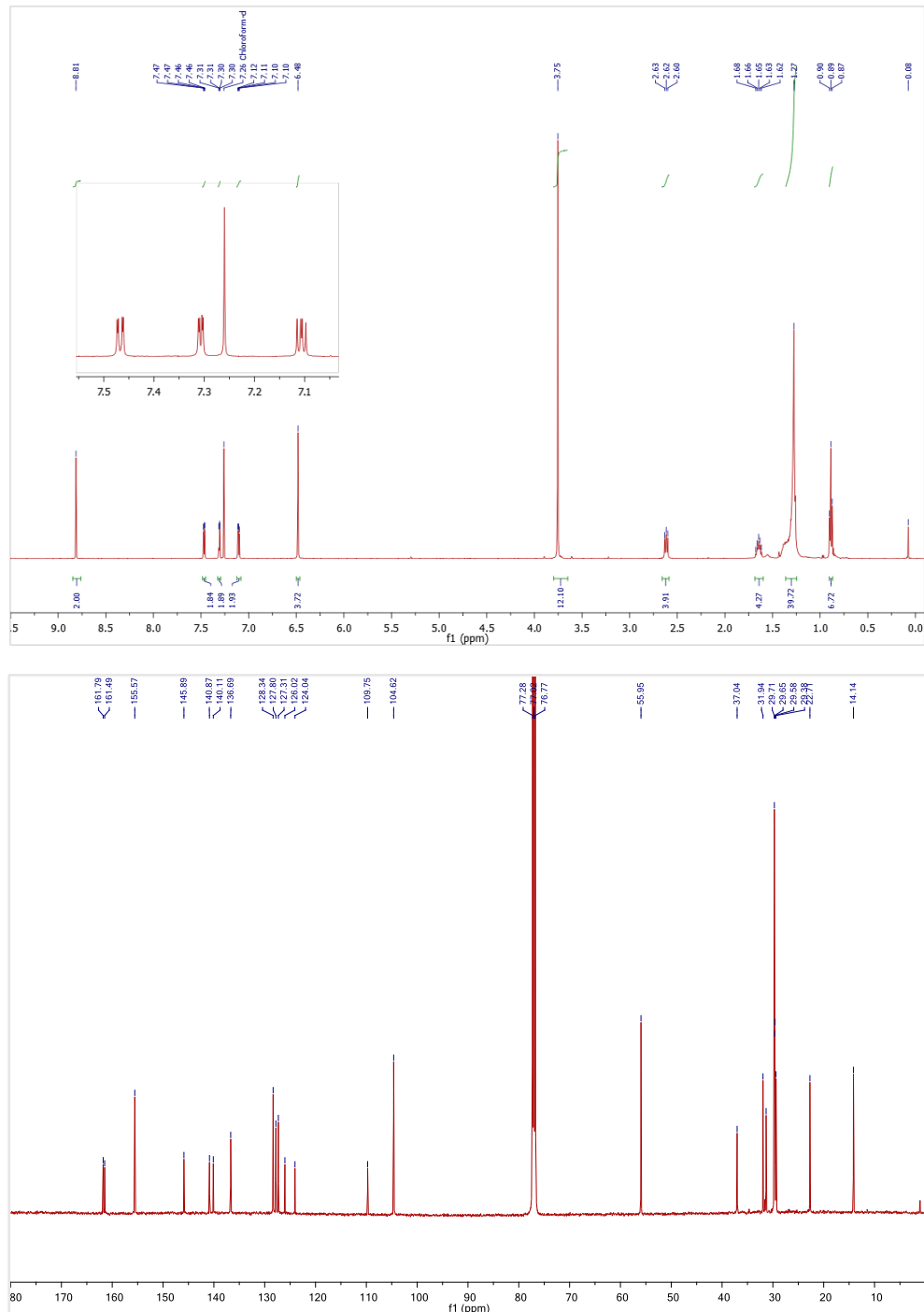
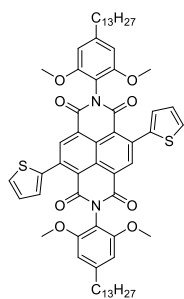


**Figure A 5.**  $^1\text{H}$  NMR (top) and  $^{13}\text{C}$  NMR{H} spectrum (bottom) of Th<sub>2</sub>-NDI-OMe.

### Th<sub>2</sub>-NDI-OH

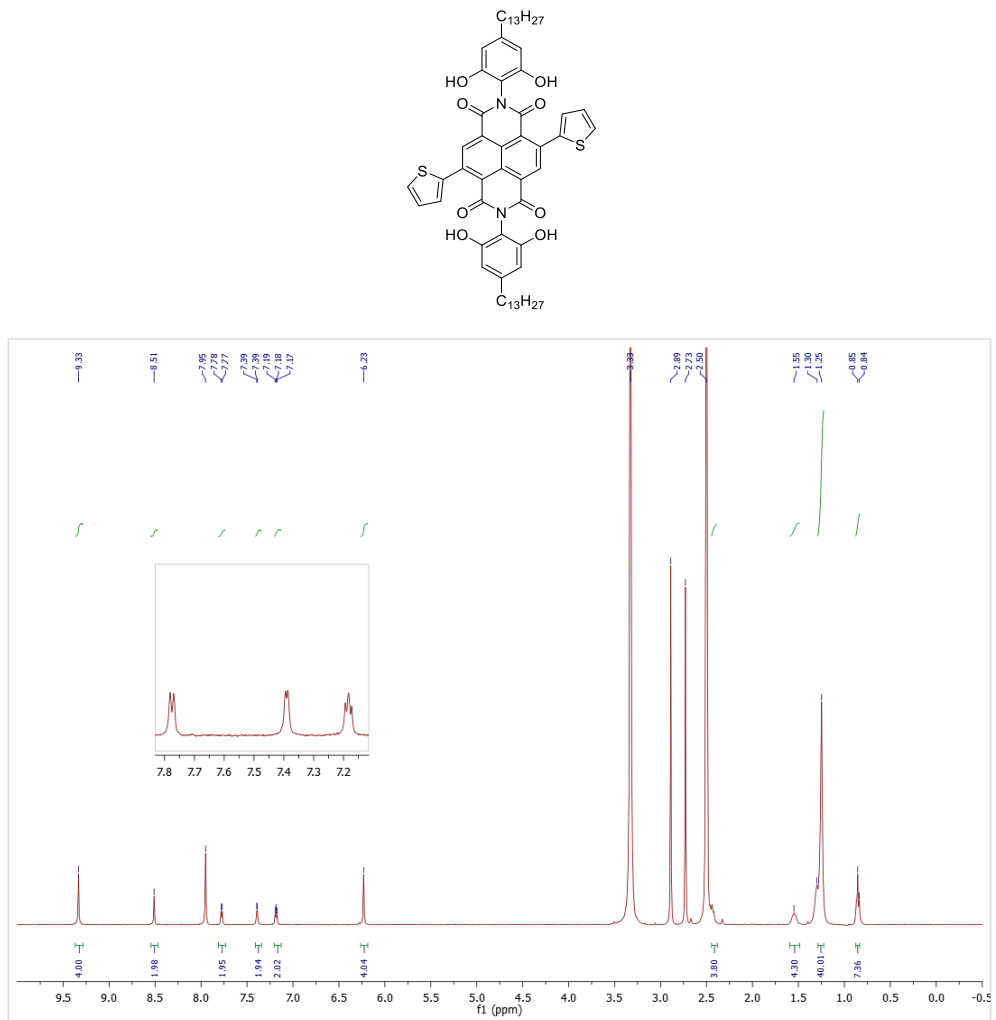


**Figure A 6.** <sup>1</sup>H NMR spectrum of Th<sub>2</sub>-NDI-OH.

**Encapsulated NDI Monomer (E-NDI-T)**

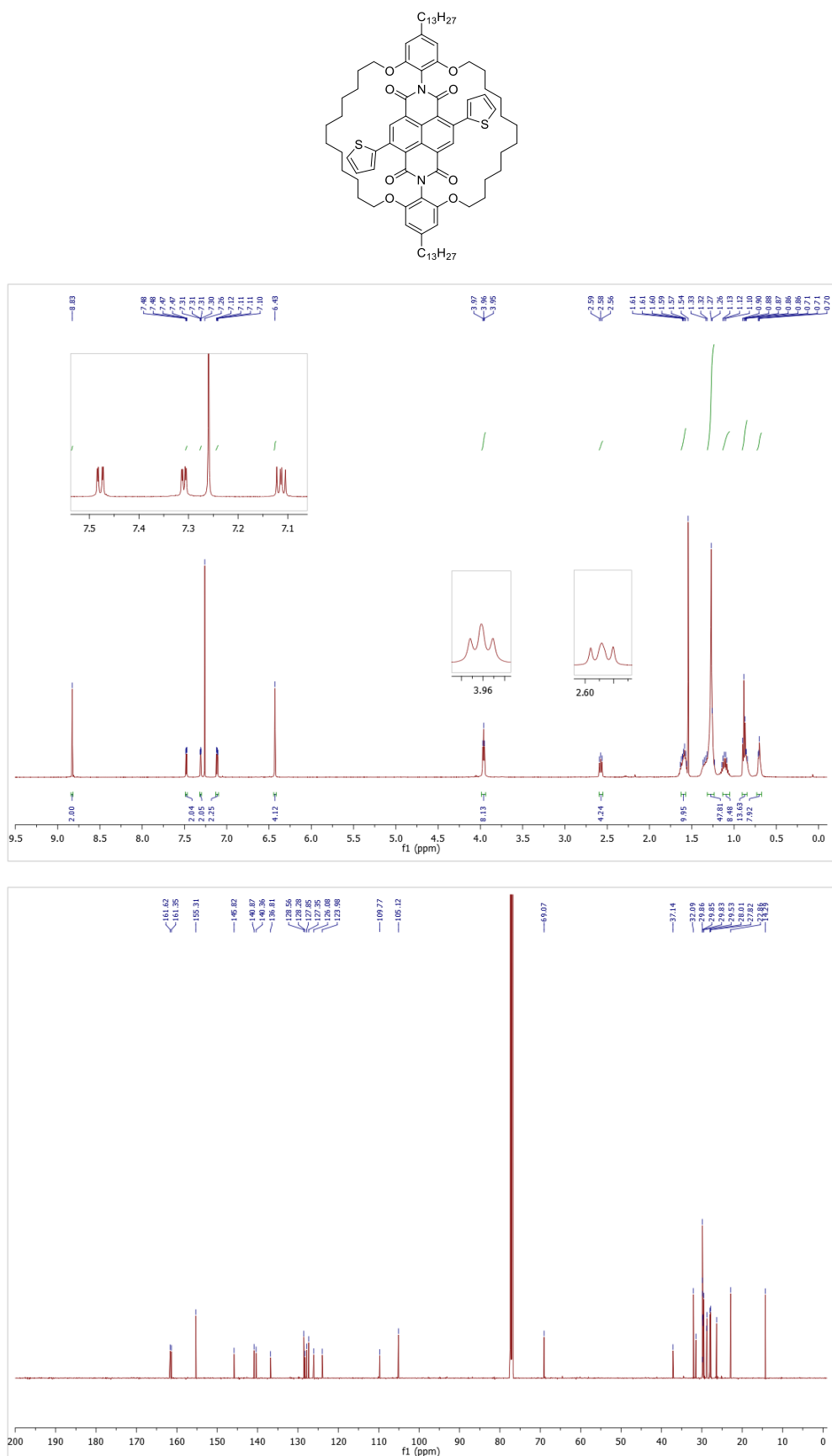


**Figure A 7.**  $^1\text{H}$  NMR (top) and  $^{13}\text{C}$  NMR{H} spectrum (bottom) of E-NDI-T.

**NBS Bromination of Encapsulated NDI Monomer (E-NDI-T)**

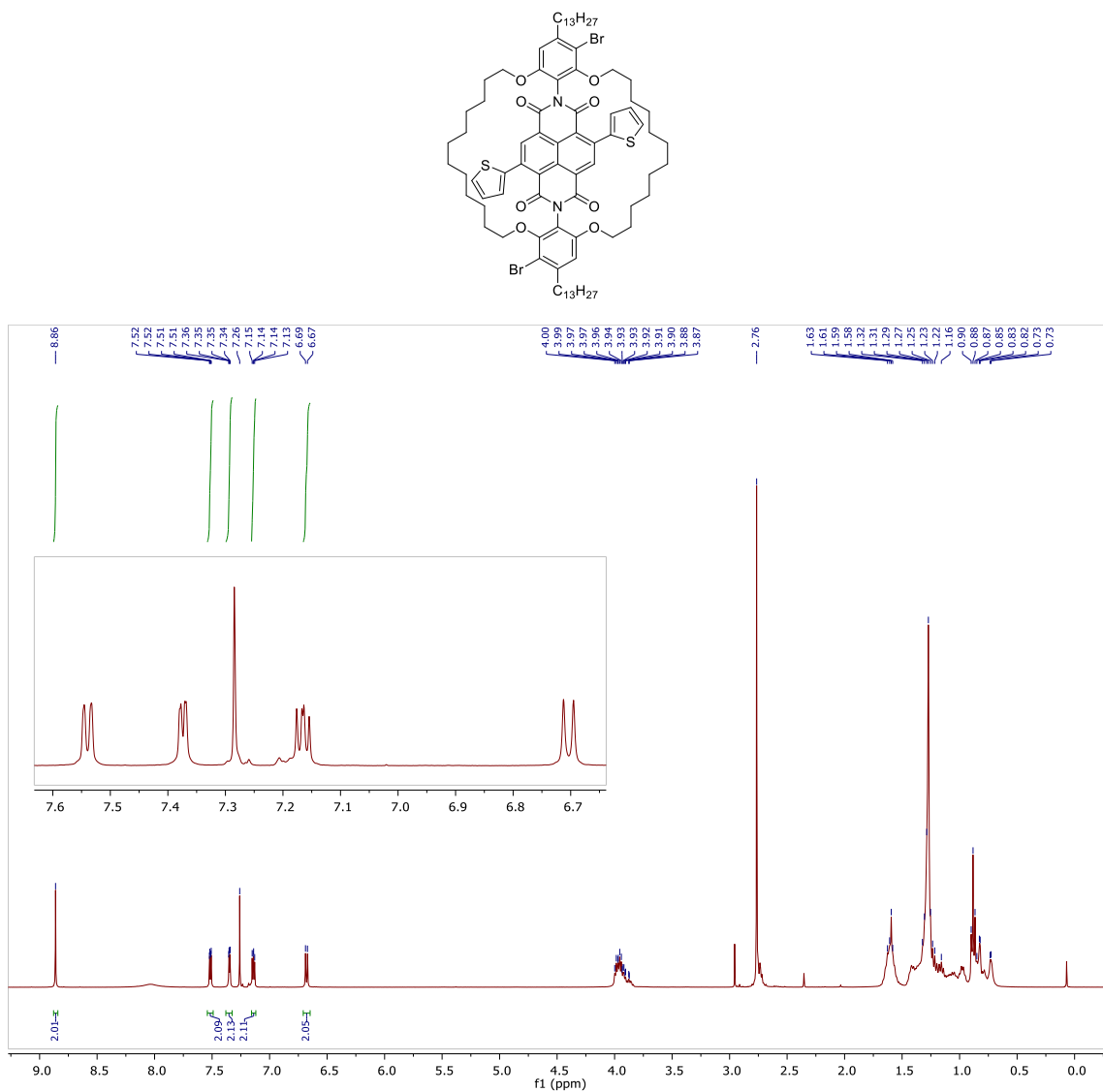


**Figure A 8.** Crude <sup>1</sup>H NMR spectrum of phenyl-brominated E-NDI-T.  
The reaction was performed in CDCl<sub>3</sub> at 60 °C for 72 hours.

**N,N'-bis(2-octyldodecyl)-2,6-dibromo-1,4,5,8-naphthalene diimide (Br<sub>2</sub>-NDI-2OD)**

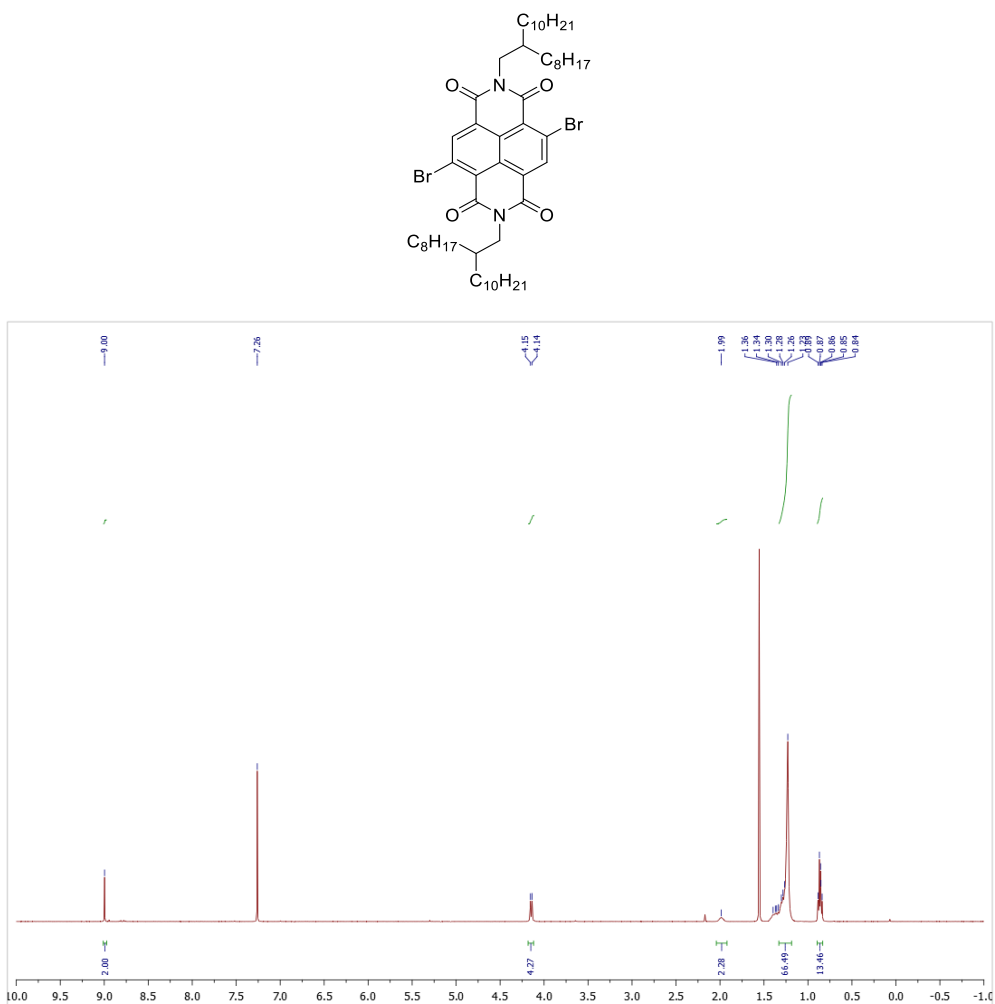


**Figure A 9.** <sup>1</sup>H NMR spectrum of Br<sub>2</sub>-NDI-2OD.

**N,N'-bis(2-octyldodecyl)-2,6-bis(thiophen-2-yl)-1,4,5,8-naphthalene diimide (Th<sub>2</sub>-NDI-2OD)**

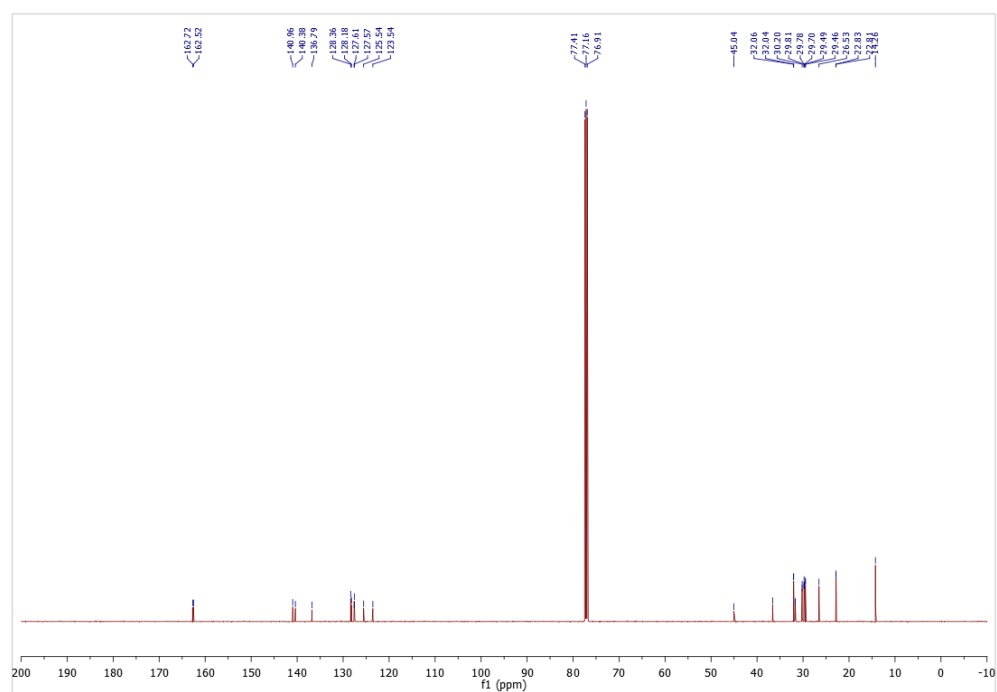
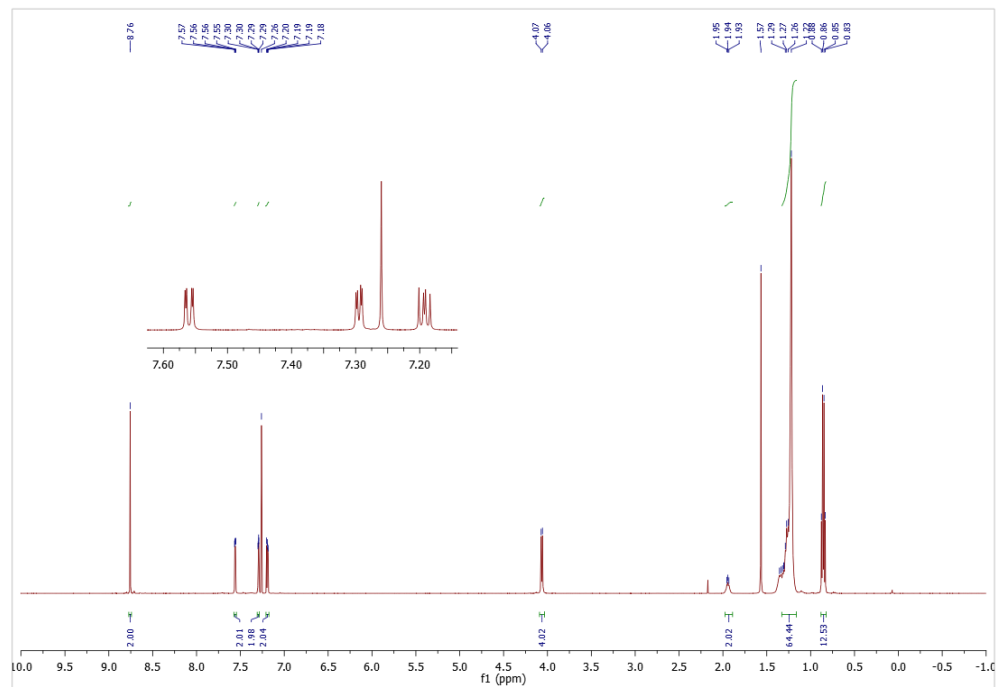
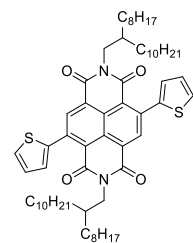


**Figure A 10.** <sup>1</sup>H NMR (top) and <sup>13</sup>C NMR{H} spectrum (bottom) of Th<sub>2</sub>-NDI-2OD.

**N,N'-bis(2-octyldodecyl)-2,6-bis(5-bromothiophen-2-yl)-1,4,5,8-naphthalene diimide  
(Br<sub>2</sub>Th<sub>2</sub>-NDI-2OD)**

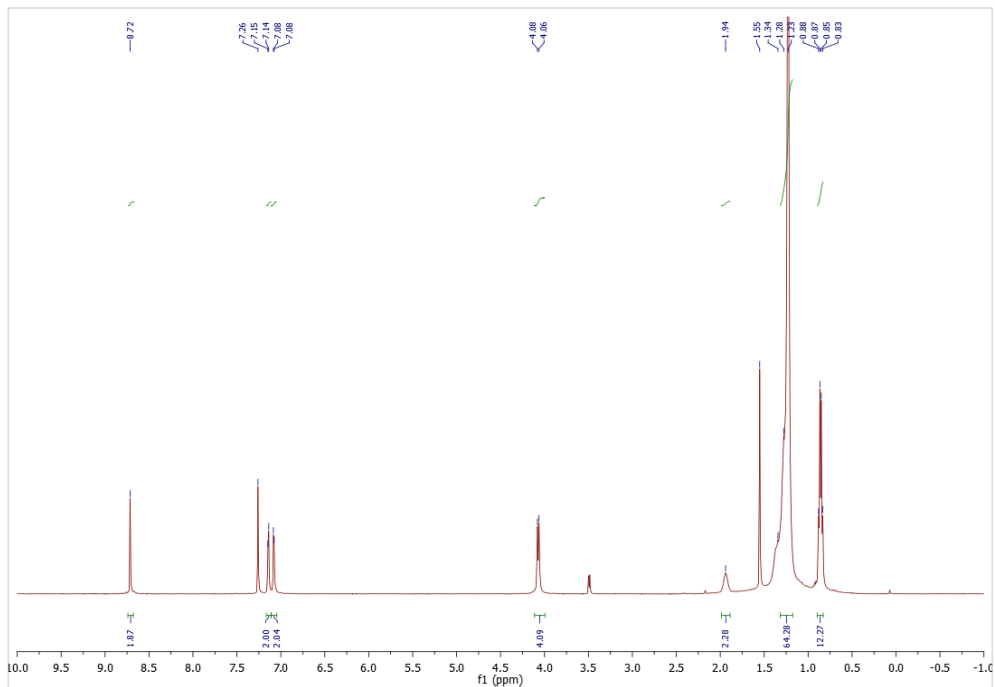
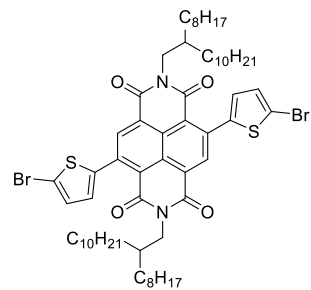


**Figure A 11.** <sup>1</sup>H NMR (top) and <sup>13</sup>C NMR{H} spectrum (bottom) of Br<sub>2</sub>Th<sub>2</sub>-NDI-2OD.

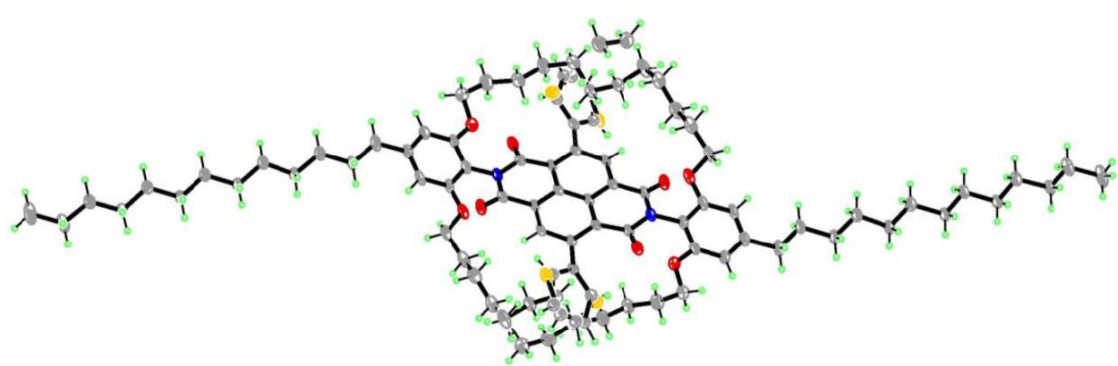


**Figure A 12.** X-ray structure of the encapsulated NDI monomer (E-NDI-T).

## Chapter IV

### N,N'-bis(2-octyldodecyl)-perylene-3,4,9,10-bis(dicarboxidamide) (PDI)

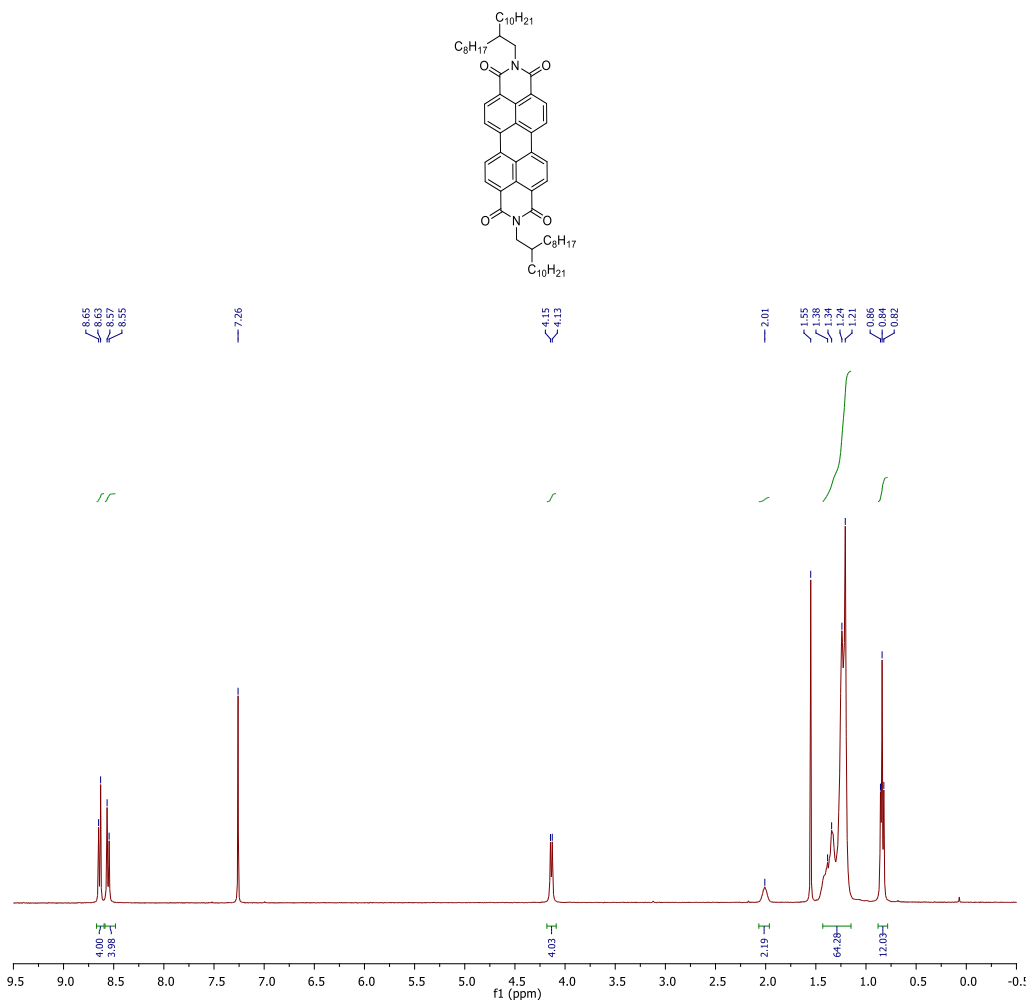
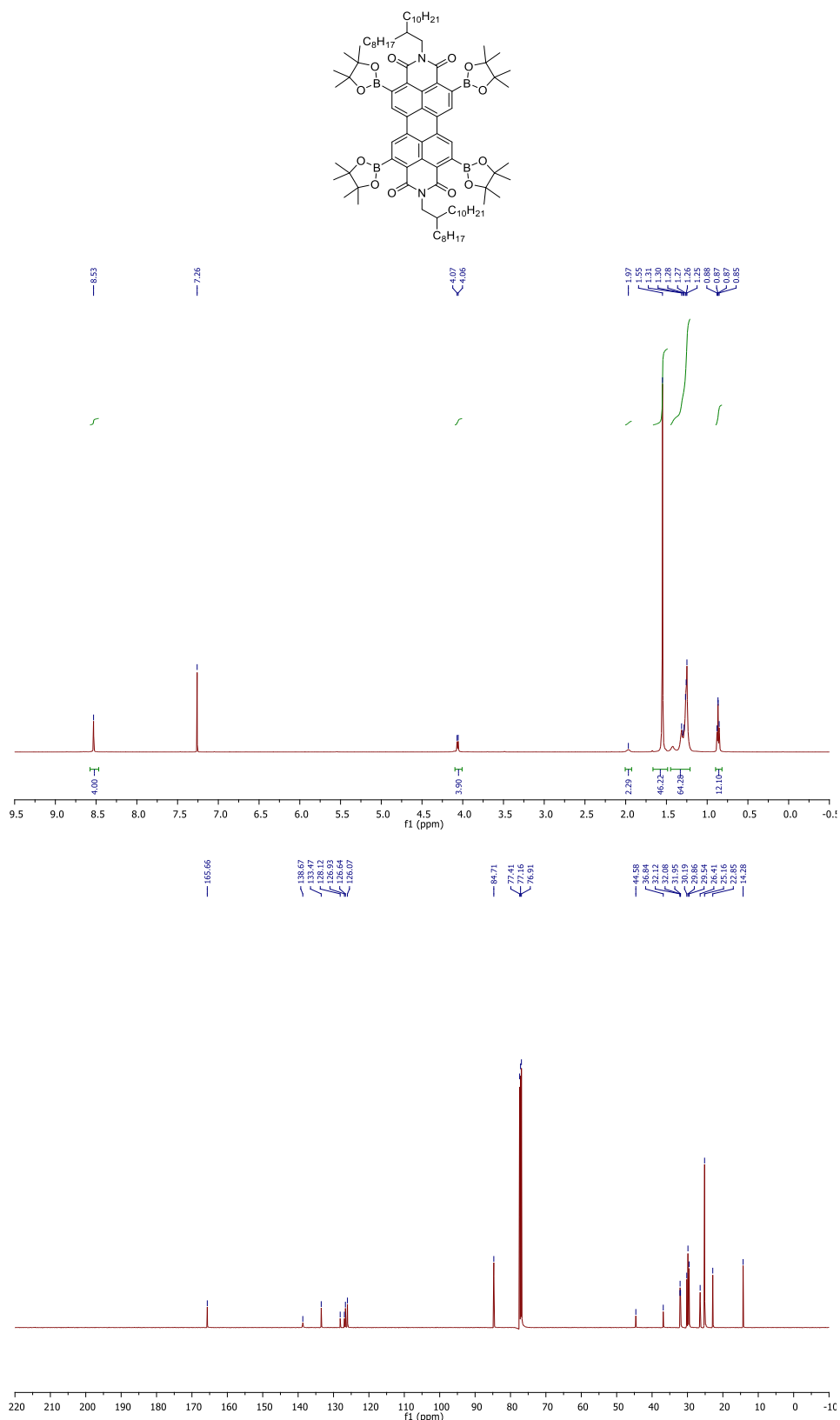


Figure A 13. <sup>1</sup>H NMR spectrum of PDI.

**N,N'-bis(2-octyldodecyl)-2,5,8,11-tetrakis(4,4,5,5-tetramethyl-1,3,2-dioxaborolan-2-yl)-perylene-3,4,9,10-tetracarboxylic acid diimide (PDI-BPin)**



**Figure A 14.** <sup>1</sup>H NMR (top) and <sup>13</sup>C NMR{H} spectrum (bottom) of PDI-BPin.

**N,N'-Bis(2-octyldodecyl)-2,5,8,11-tetrakis(2-(1,3-dimethoxybenzene))perylene-3,4,9,10-tetracarboxylic acid diimide (PDI-OMe)**

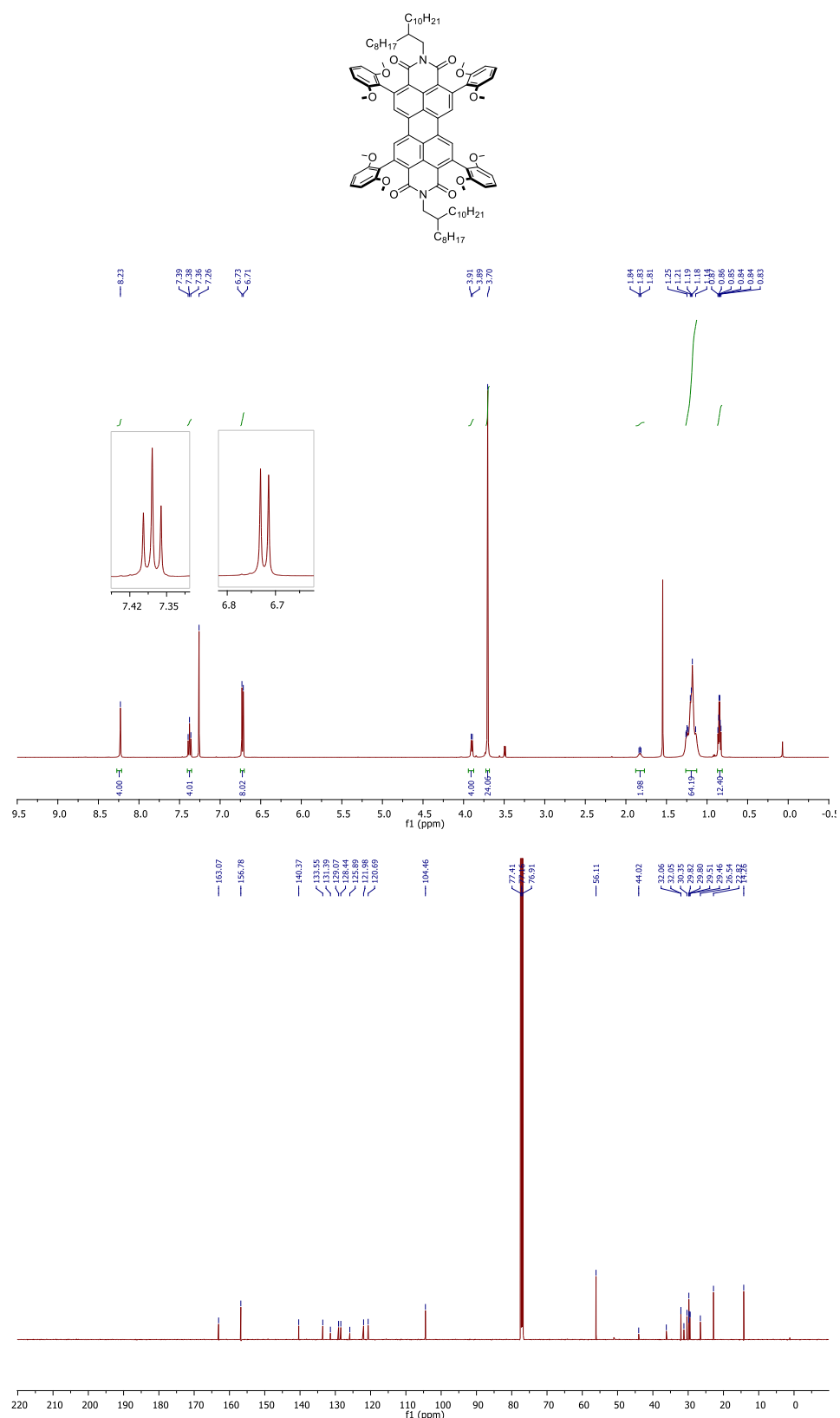


**Figure A 15.** <sup>1</sup>H NMR (top) and <sup>13</sup>C NMR{H} spectrum (bottom) of PDI-OMe.

**N,N'-Bis(2-octyldodecyl)-2,5,8,11-tetrakis(2-resorcinol)perylene-3,4,9,10-tetracarboxylic acid diimide (PDI-OH)**

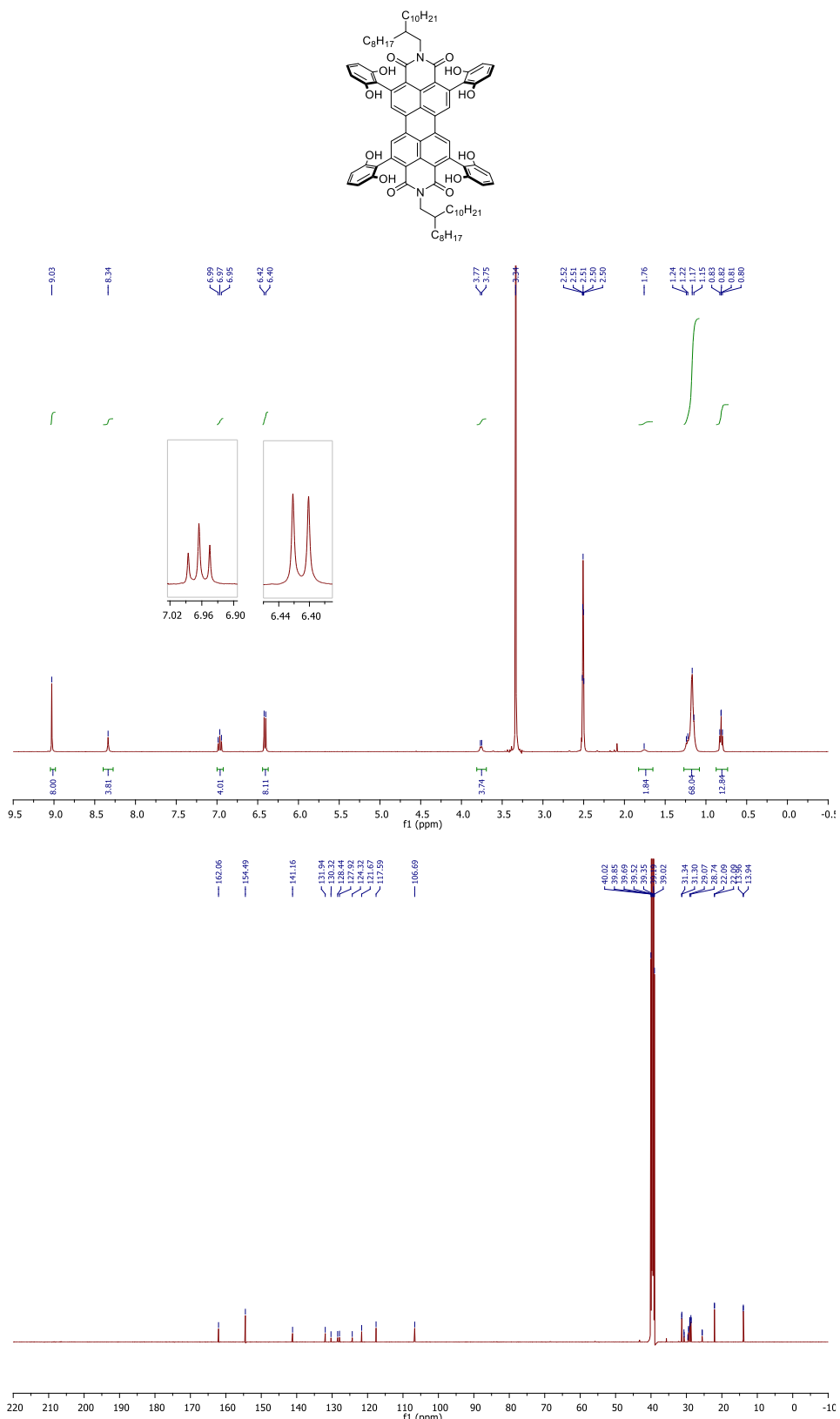


**Figure A 16.** <sup>1</sup>H NMR (top) and <sup>13</sup>C NMR{H} spectrum (bottom) of PDI-OH.

### Doubly Encapsulated PDI (PDI-Ecap)

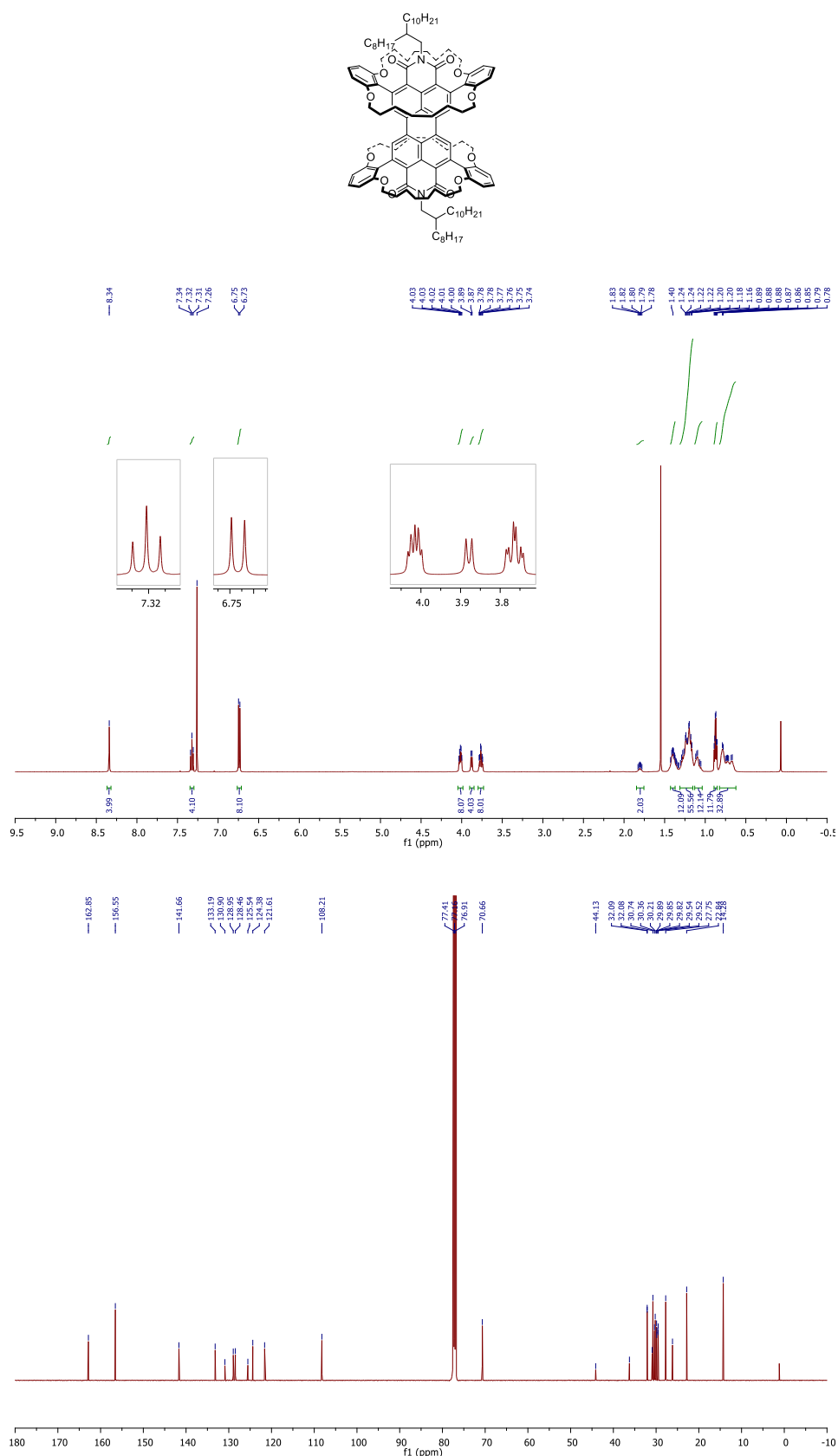


**Figure A 17.** <sup>1</sup>H NMR (top) and <sup>13</sup>C NMR{H} spectrum (bottom) of PDI-Ecap.

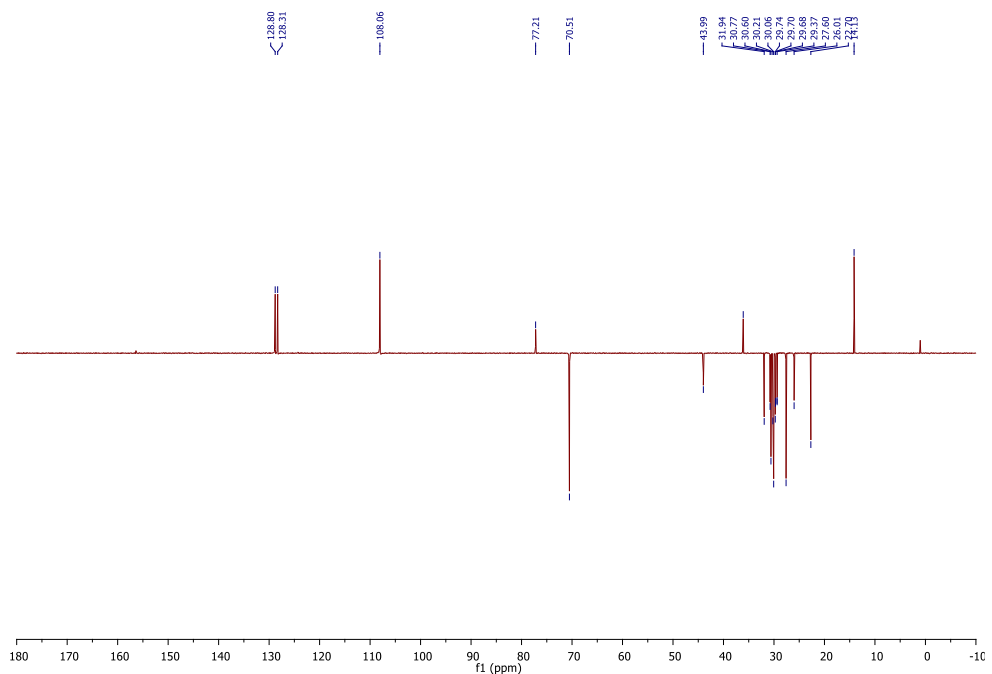


**Figure A 18.**  $^{13}\text{C}$  DEPT spectrum of PDI-Encap.

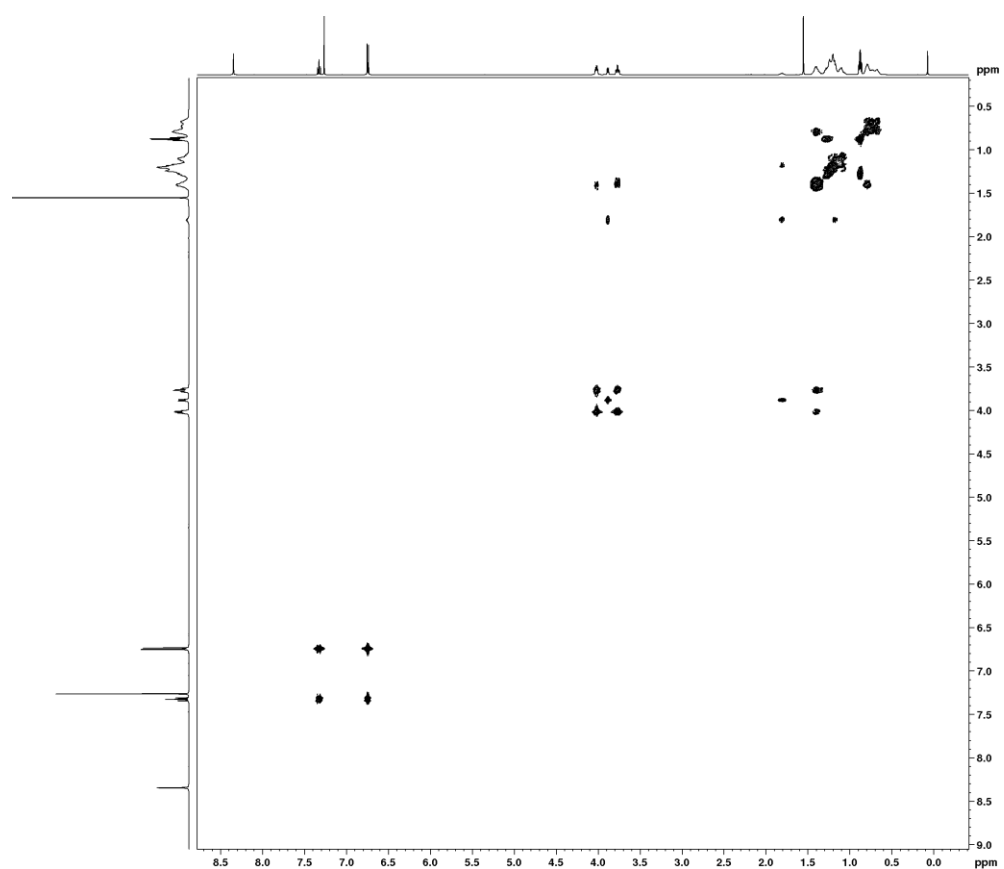


**Figure A 19.**  $^1\text{H}$ - $^1\text{H}$  COSY spectrum of PDI-Encap.

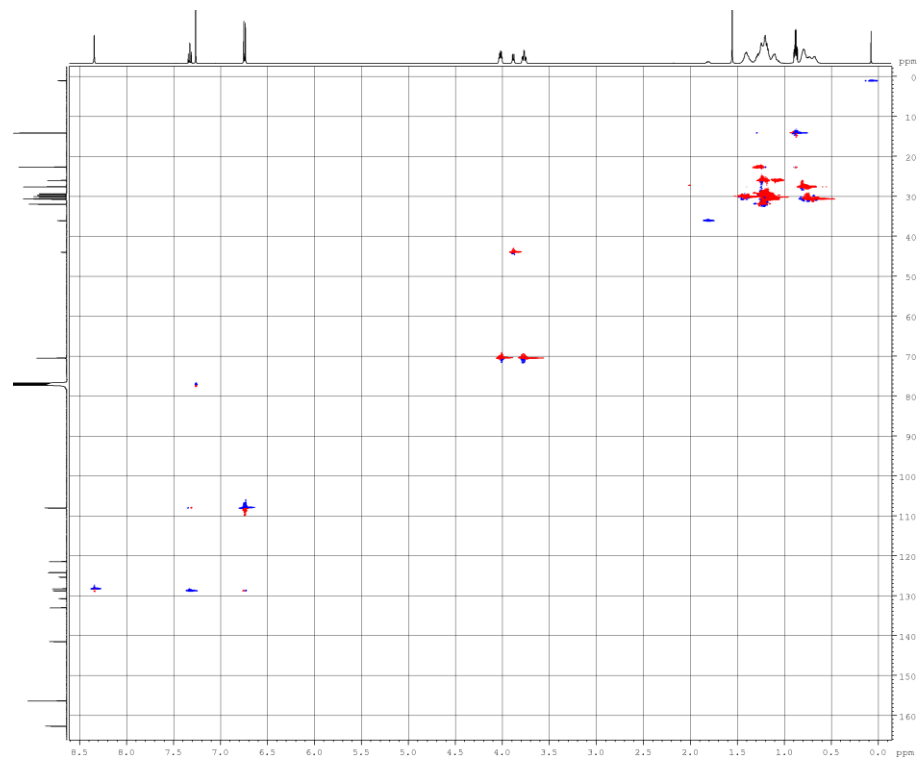


**Figure A 20.**  $^{13}\text{C}$ - $^1\text{H}$  HSQC spectrum of PDI-Encap.

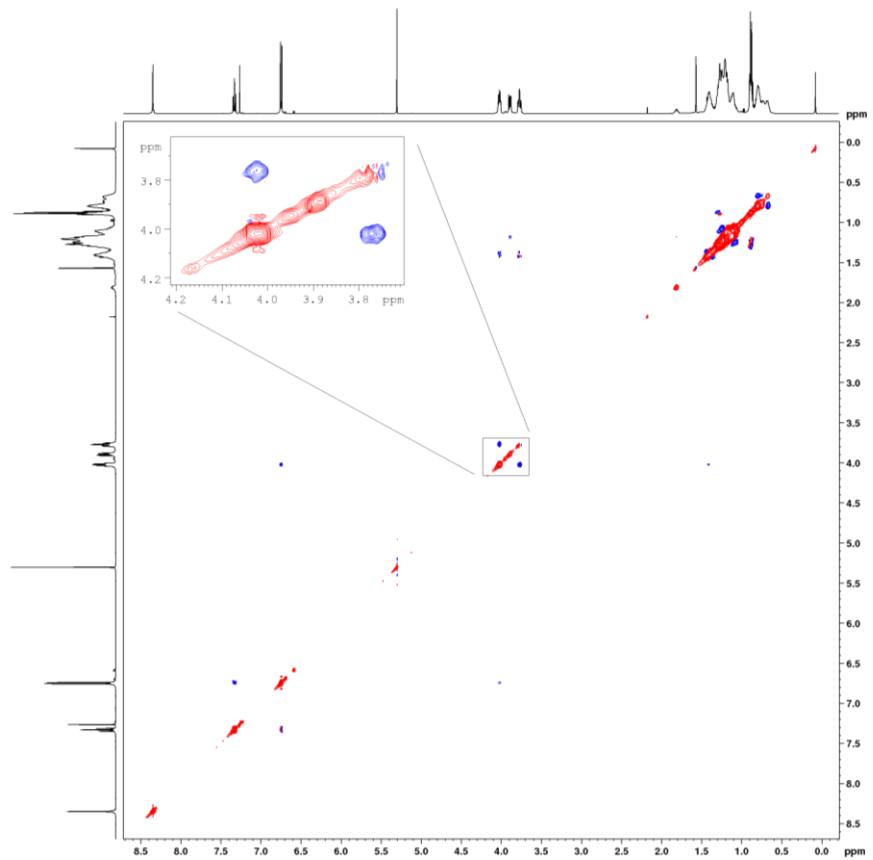


**Figure A 21.**  $^1\text{H}$ - $^1\text{H}$  ROESY spectrum of PDI-Encap.

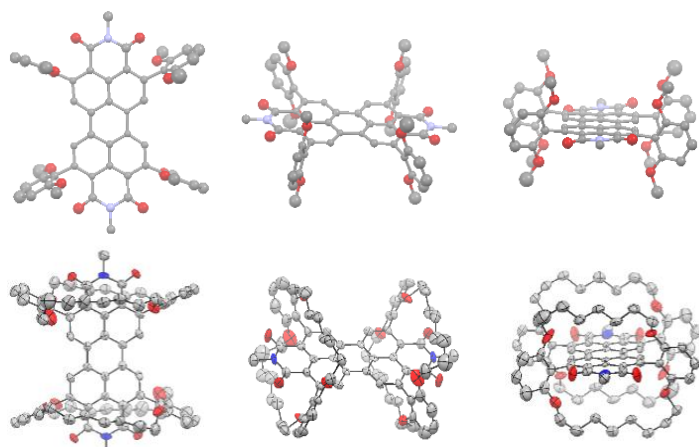


**Figure A 22.** X-ray structures of the meso compounds of PDI-OMe (top) and PDI-Encap (bottom) viewed from three different perspectives. The branched 2-octyldodecyl chains, all hydrogen atoms and solvent molecules are omitted for clarity.

## Chapter V

### 2,9-bis(2-hydroxy-5-(tert-pentyl)phenyl)perylene-3,4,9,10-tetracarboxylic diimide (PDI-Diol)

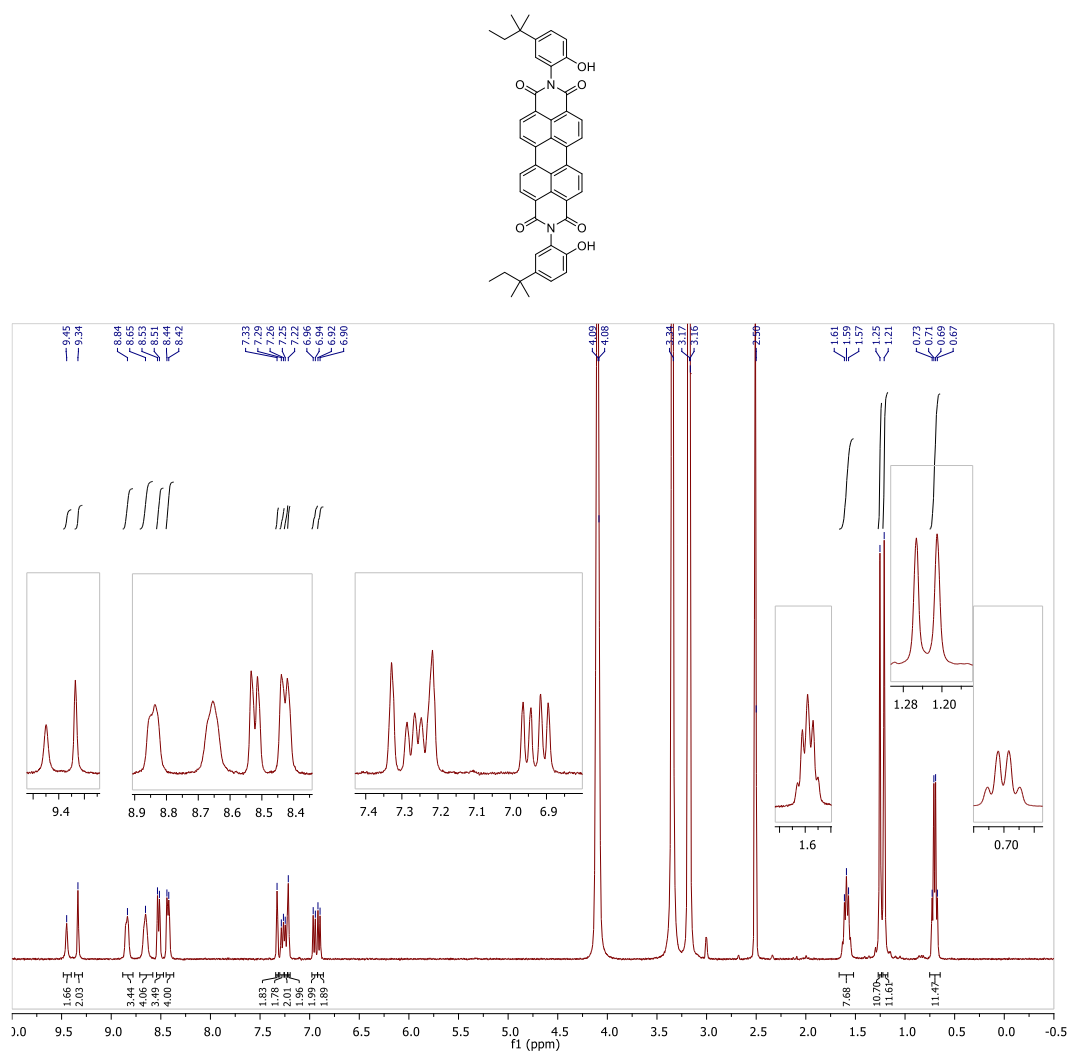


**Figure A 23.** <sup>1</sup>H NMR spectrum of PDI-Diol.

**4,8-bis(2-((oxy)propoxy)tetrahydro-2H-pyran)benzo[1,2-b:4,5-b']dithiophene (BDT-THP)**

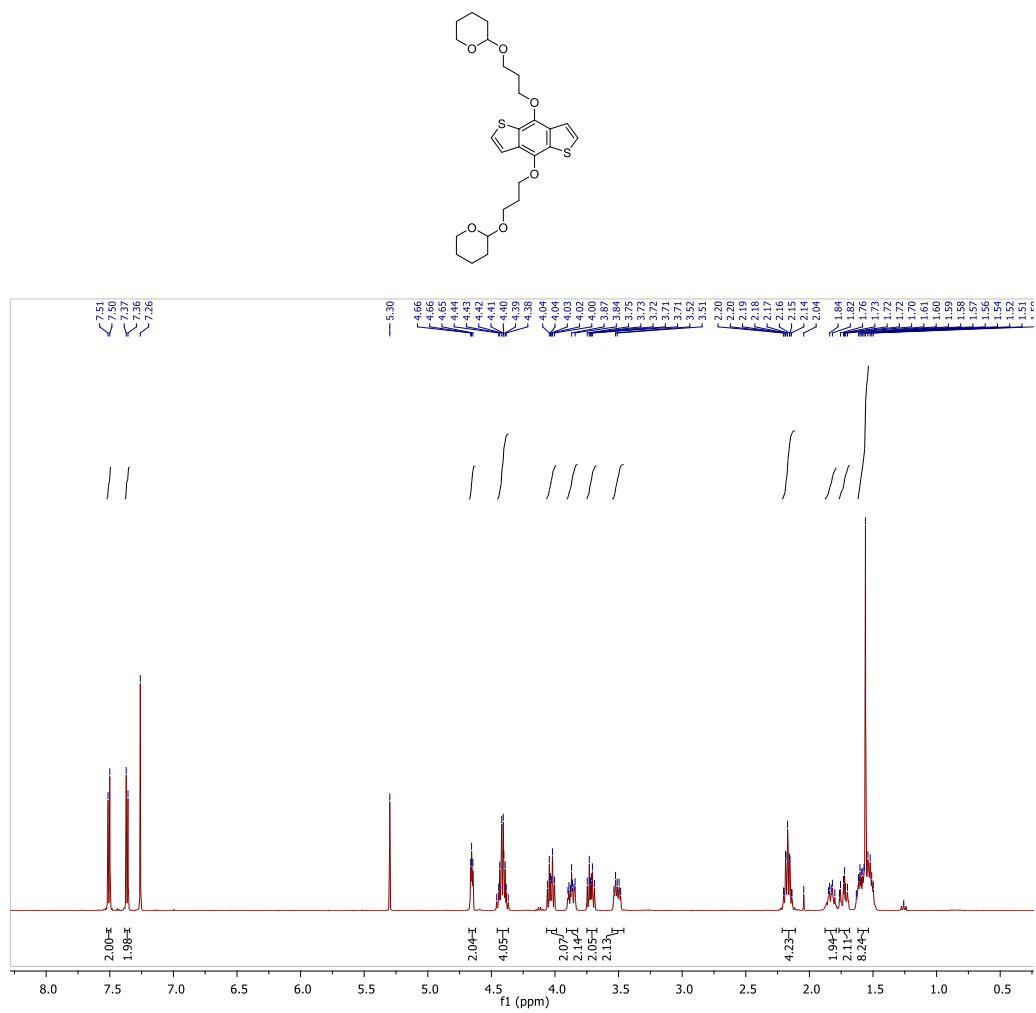


**Figure A 24.** <sup>1</sup>H NMR spectrum BDT-THP.

**2,6-dibromo(4,8-bis(2-((oxy)propoxy)tetrahydro-2H-pyran))benzo[1,2-b:4,5-b']dithiophene (Br<sub>2</sub>-BDT-THP)**

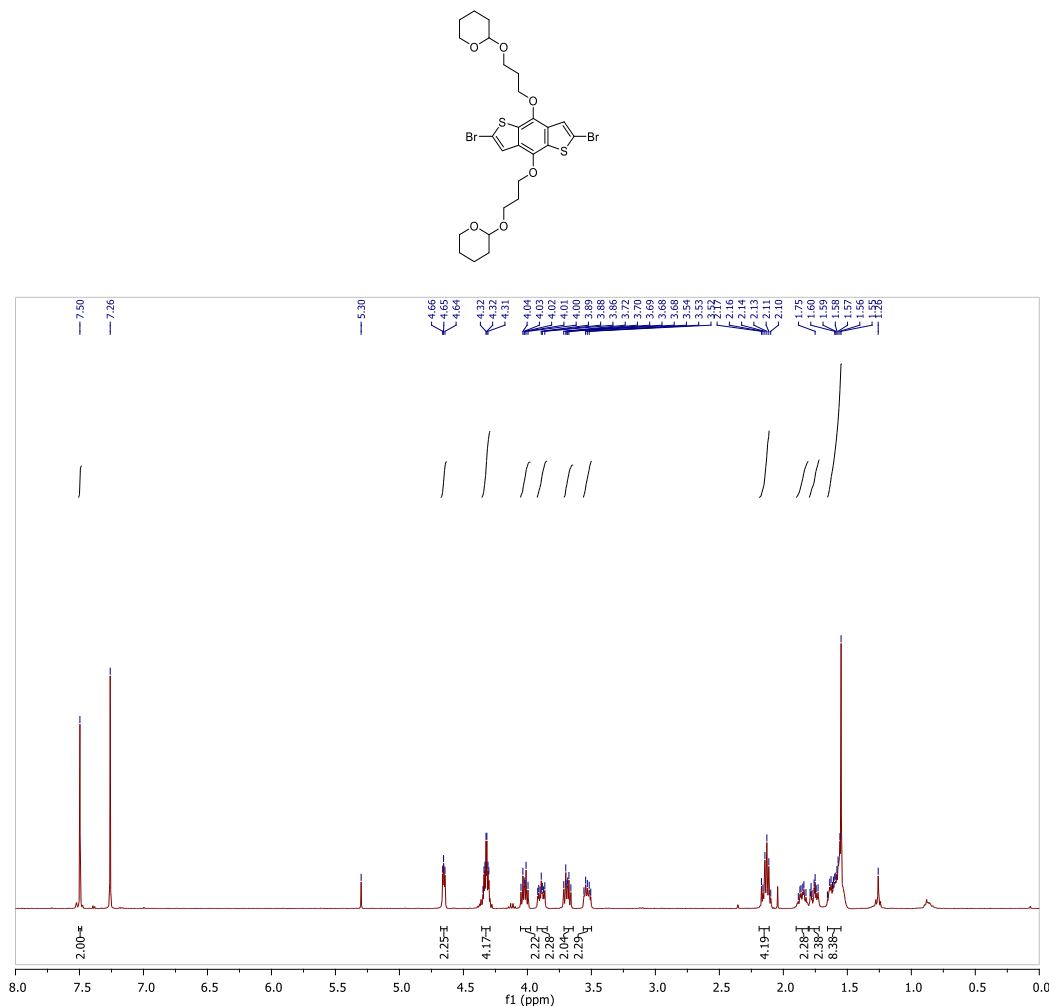


**Figure A 25. <sup>1</sup>H NMR spectrum of Br<sub>2</sub>-BDT-THP.**

**2,6-dibromo(4,8-bis((oxy)propan-1-ol)tetrahydro-2H-pyran)benzo[1,2-b:4,5-b']dithiophene (Br<sub>2</sub>-BDT-OH)**

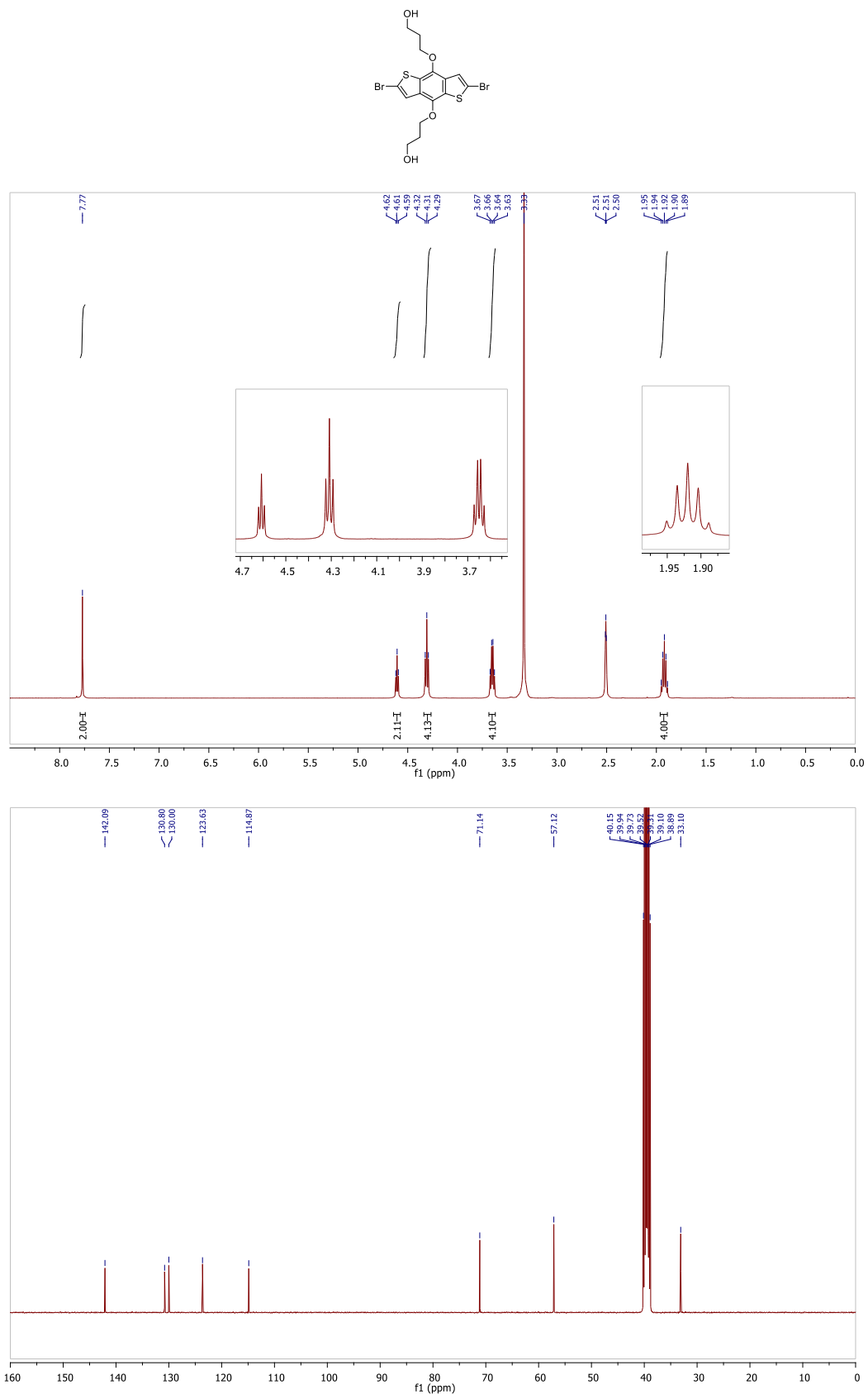


**Figure A 26.** <sup>1</sup>H NMR (top) and <sup>13</sup>C NMR{H} spectrum (bottom) of Br<sub>2</sub>-BDT-OH.

**2,6-dibromo(4,8-bis((oxy)propyl(*p*-toluenesulfonate)))benzo[1,2-*b*:4,5-*b'*]dithiophene  
(Br<sub>2</sub>-BDT-OTs)**

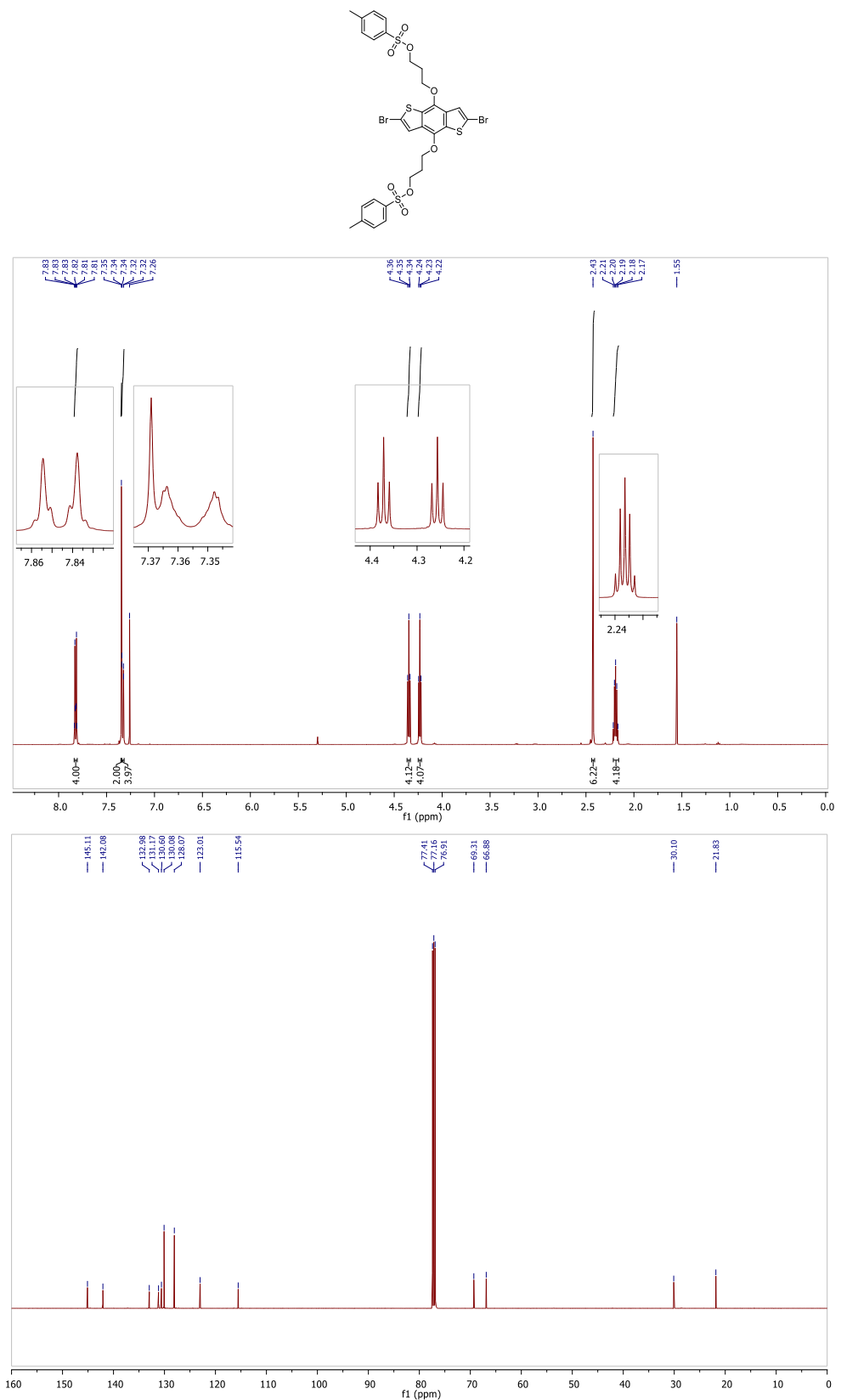


**Figure A 27.** <sup>1</sup>H NMR (top) and <sup>13</sup>C NMR{H} spectrum (bottom) of Br<sub>2</sub>-BDT-OTs.

**TS-PDI-BDT Monomer (TS-M1)**

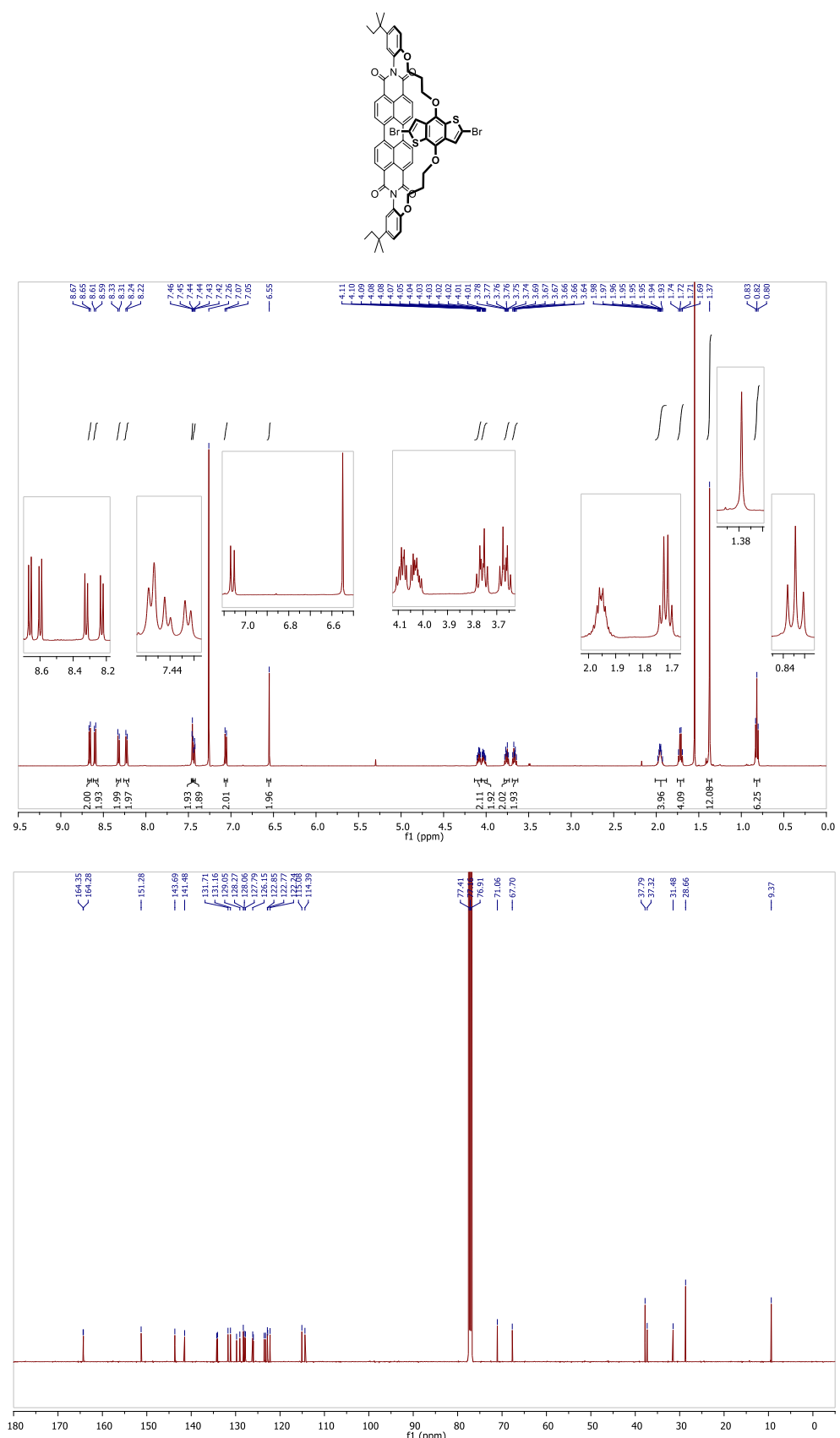


**Figure A 28.** <sup>1</sup>H NMR (top) and <sup>13</sup>C NMR{H} spectrum (bottom) of TS-M1.

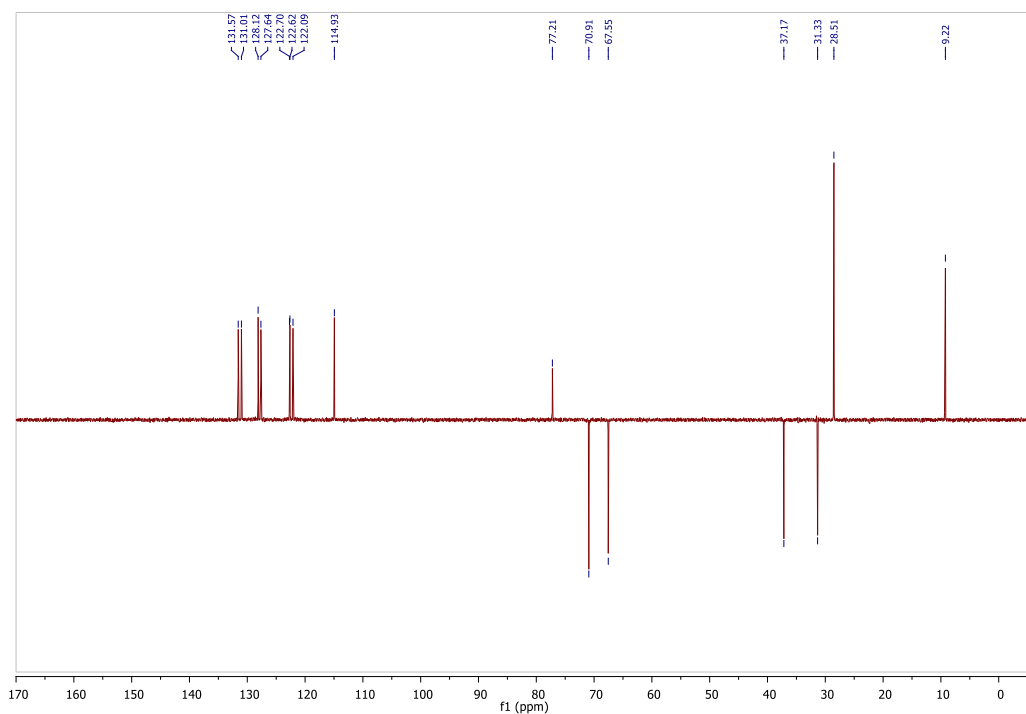


**Figure A 29.**  $^{13}\text{C}$  DEPT spectrum of TS-M1.

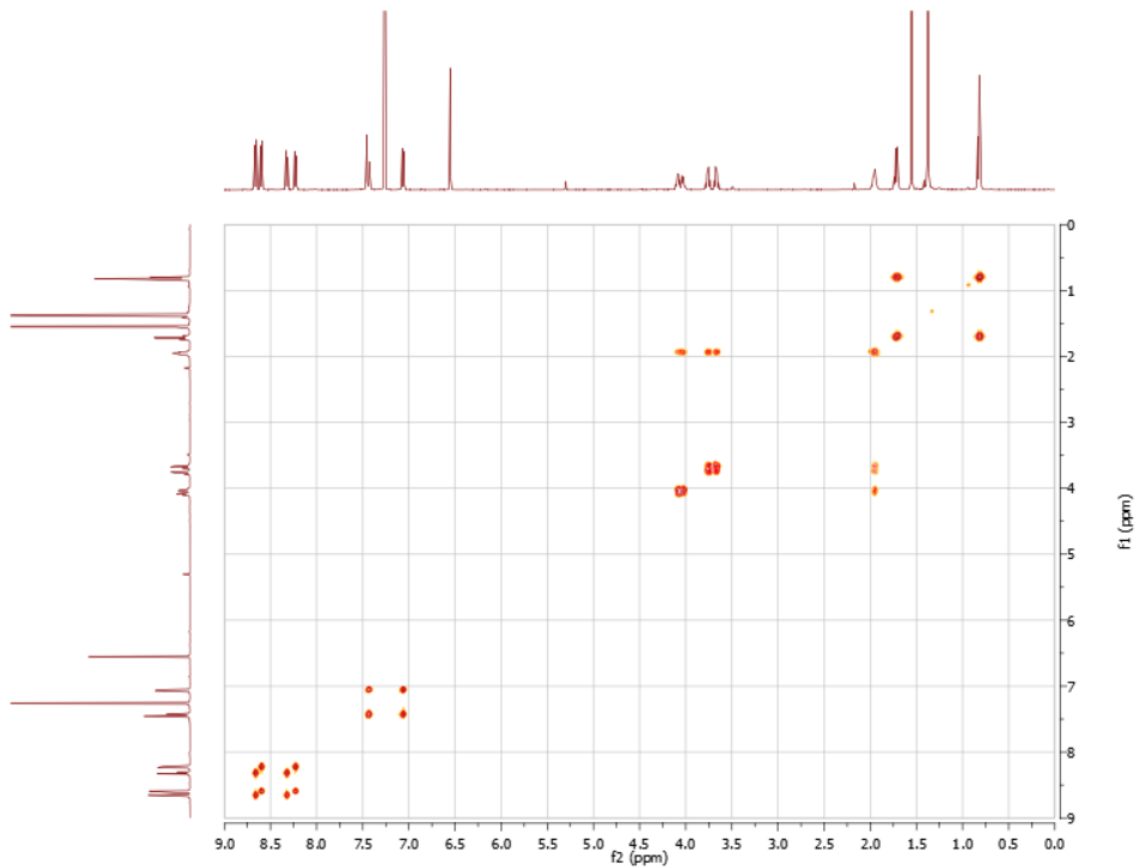


**Figure A 30.**  $^1\text{H}$ - $^1\text{H}$  COSY spectrum of TS-M1.

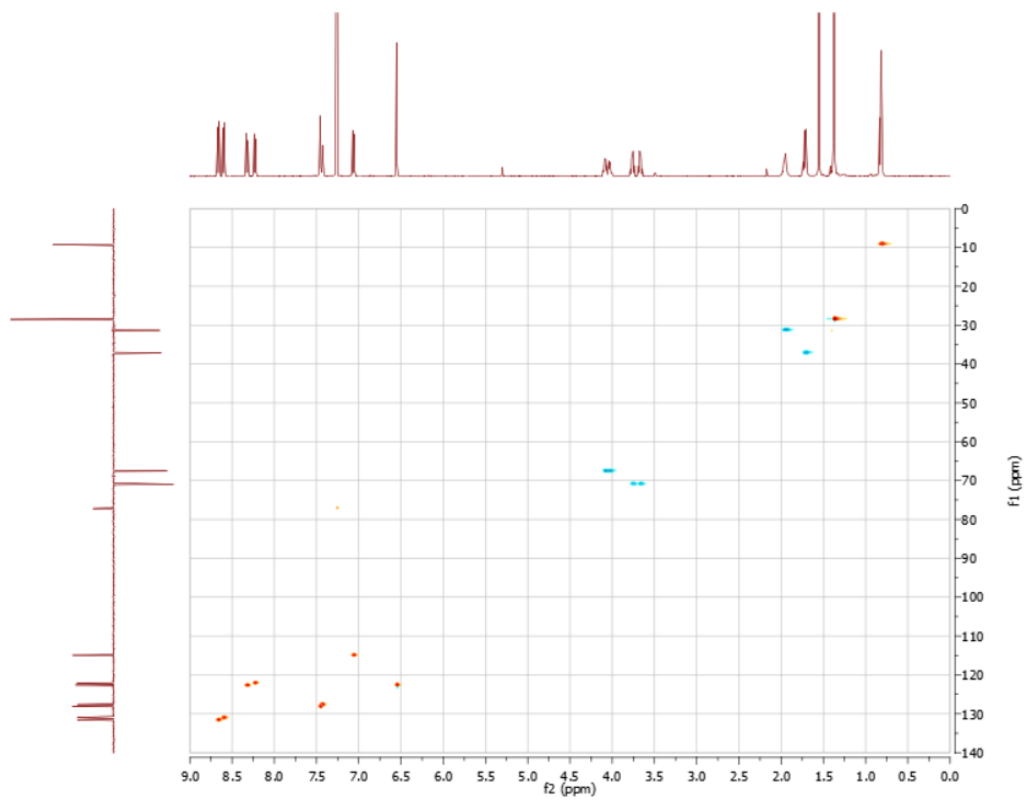


**Figure A 31.** HSQC spectrum of TS-M1, with  $^{13}\text{C}$  DEPT spectrum on y-axis.

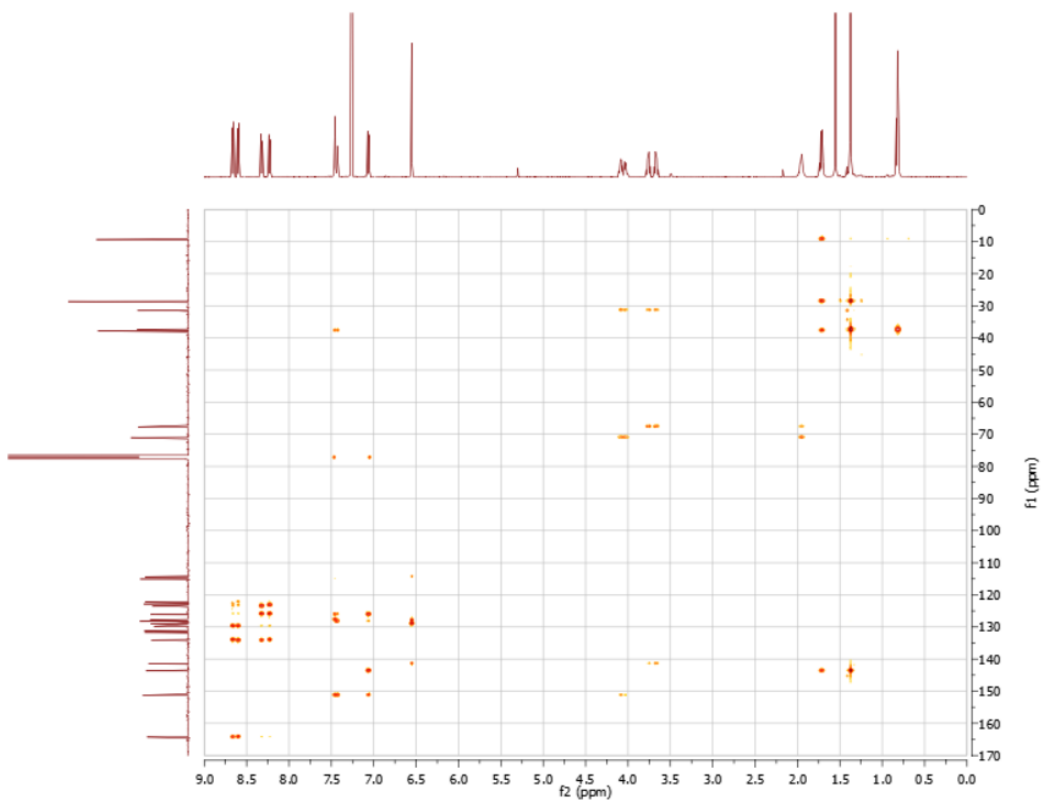


**Figure A 32.** HMBC spectrum of TS-M1.

**2,5-bis(2-(oxy)propan-1-ol)-3,6-di(thiophen-2-yl)pyrrolo[3,4-c]pyrrole-1,4-dione (DPP-OH)**

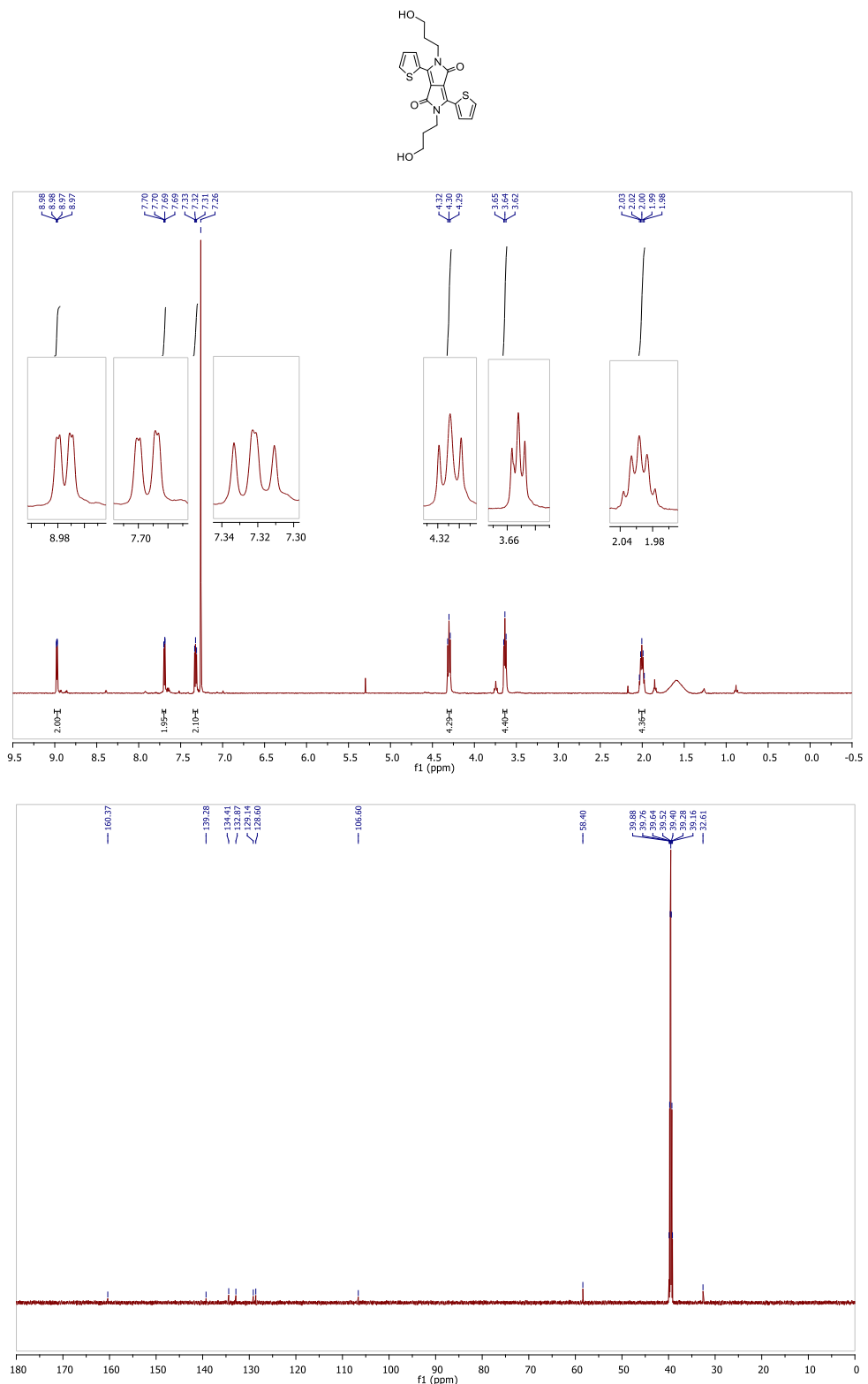


**Figure A 33.** <sup>1</sup>H NMR (top) and <sup>13</sup>C NMR{H} spectrum (bottom) of DPP-OH.

**2,5-bis(2-(oxy)propyl(*p*-toluenesulfonate))-3,6-di(thiophen-2-yl)pyrrolo[3,4-*c*]pyrrole-1,4-dione (DPP-OTs)**

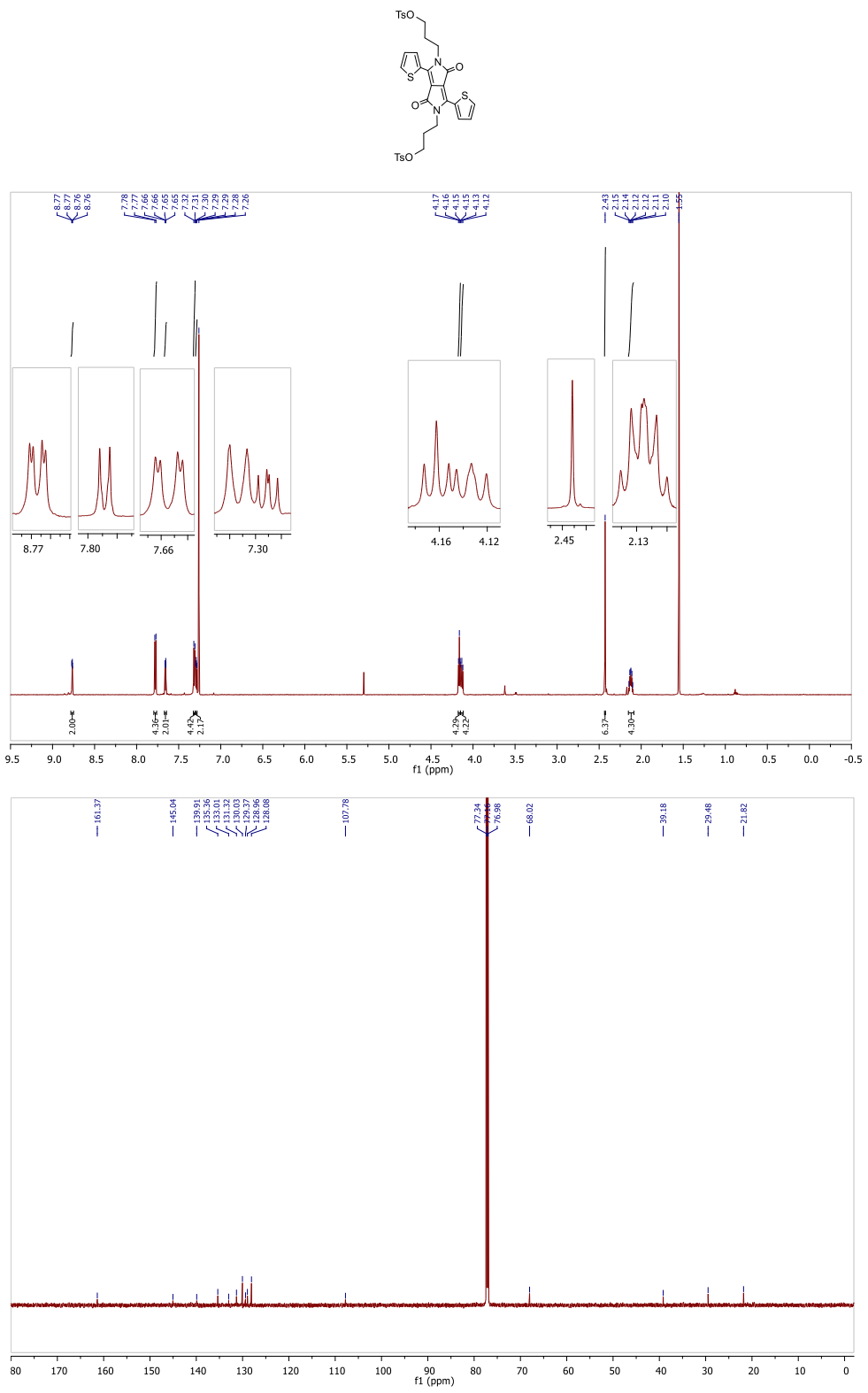


**Figure A 34.** <sup>1</sup>H NMR (top) and <sup>13</sup>C NMR{H} spectrum (bottom) of DPP-OTs.

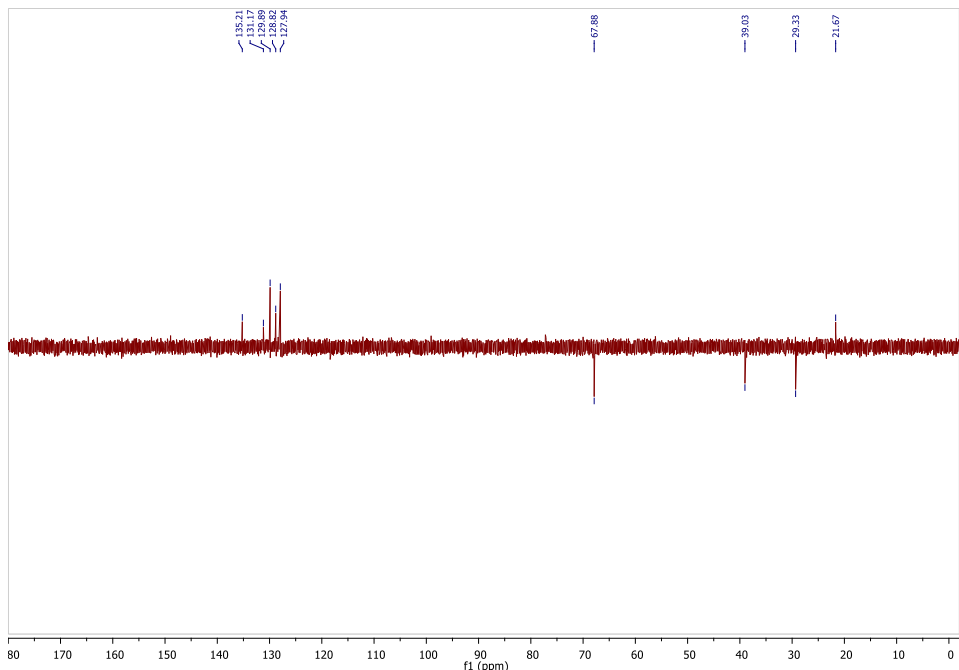


**Figure A 35.**  $^{13}\text{C}$  DEPT spectrum of DPP-OTs.

## TS-PDI-DPP

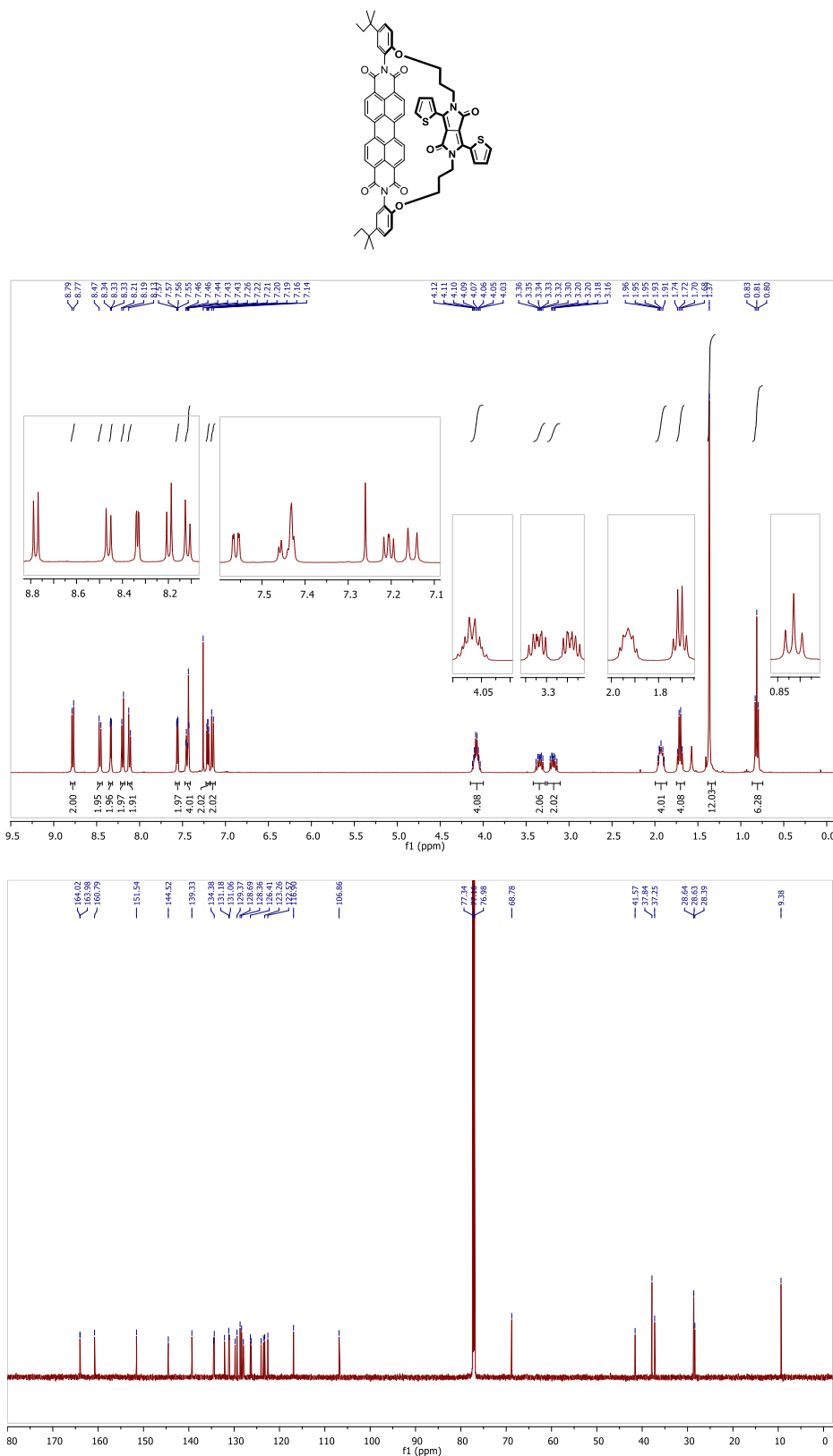


**Figure A 36.**  $^1\text{H}$  NMR (top) and  $^{13}\text{C}$  NMR{H} spectrum (bottom) of TS-PDI-DPP.

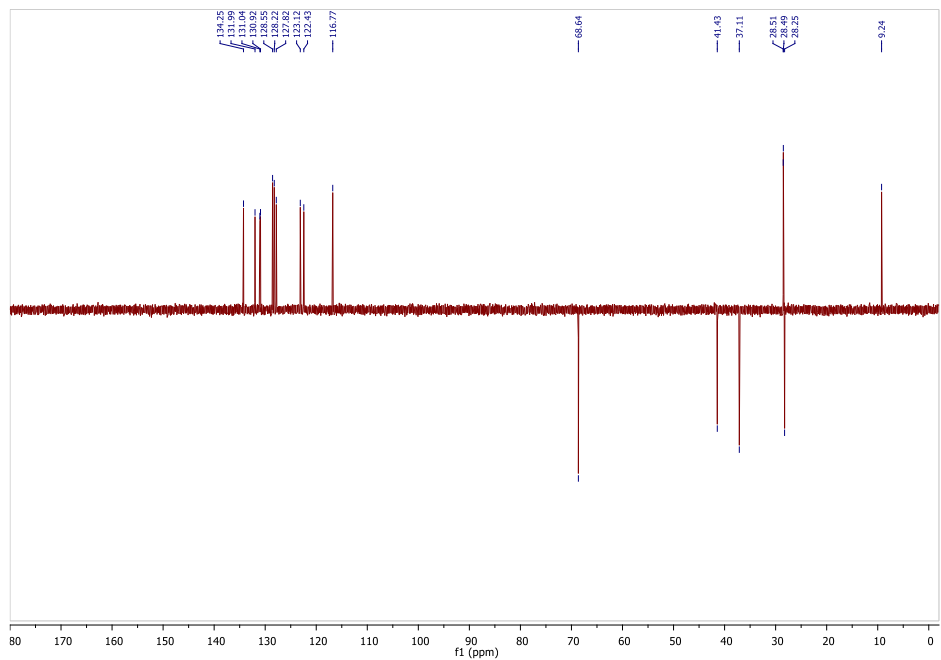


**Figure A 37.**  $^{13}\text{C}$  DEPT spectrum of TS-PDI-DPP.

**TS-PDI-DPP Monomer (TS-M2)**

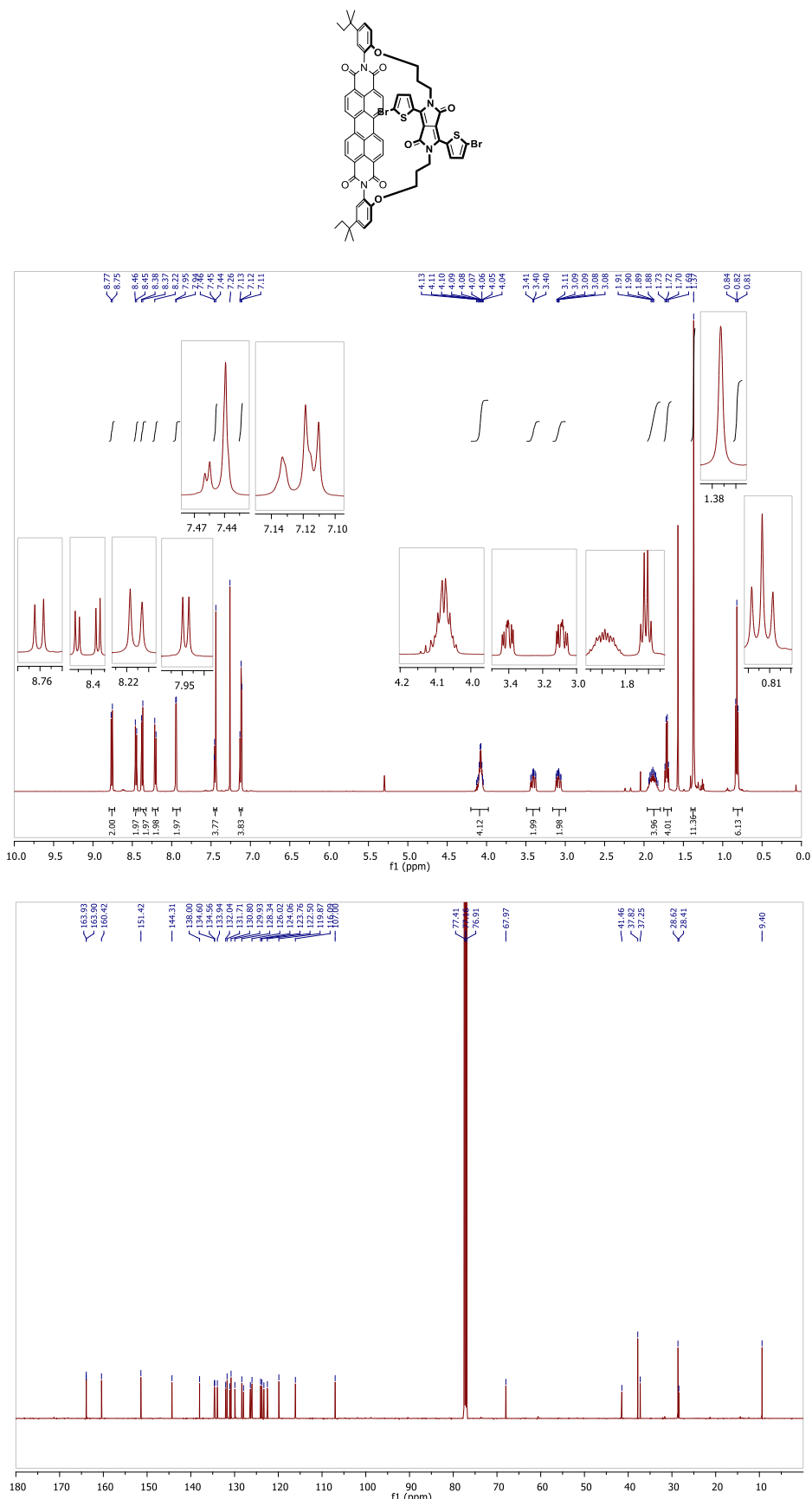


**Figure A 38.** <sup>1</sup>H NMR (top) and <sup>13</sup>C NMR{H} spectrum (bottom) of TS-M2.

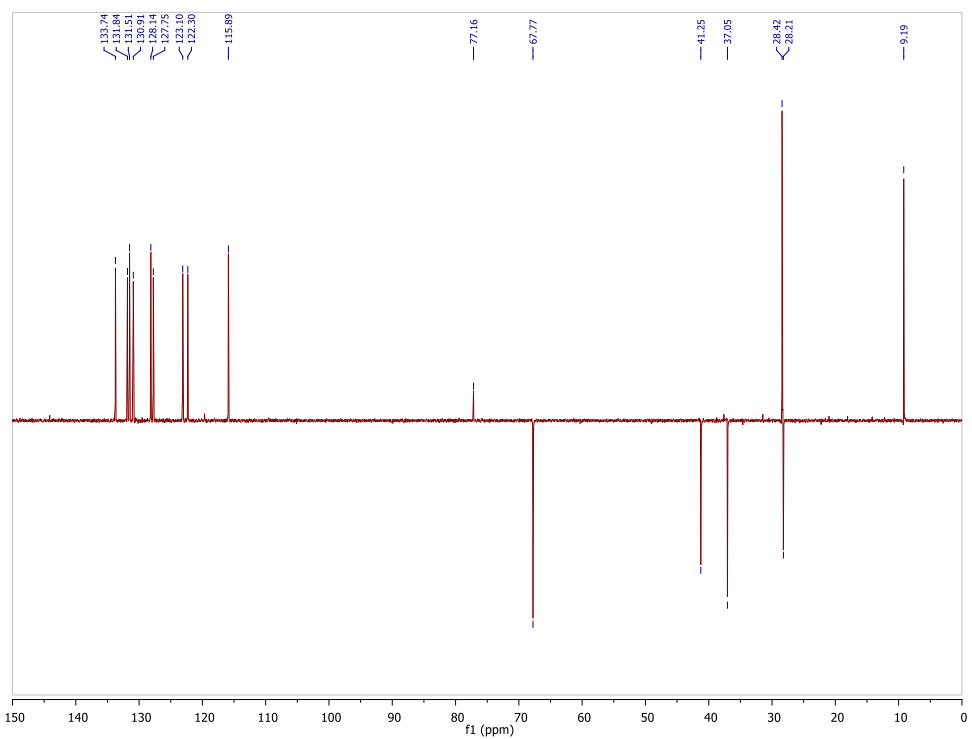


**Figure A 39.**  $^{13}\text{C}$  DEPT spectrum (bottom) of TS-M2.

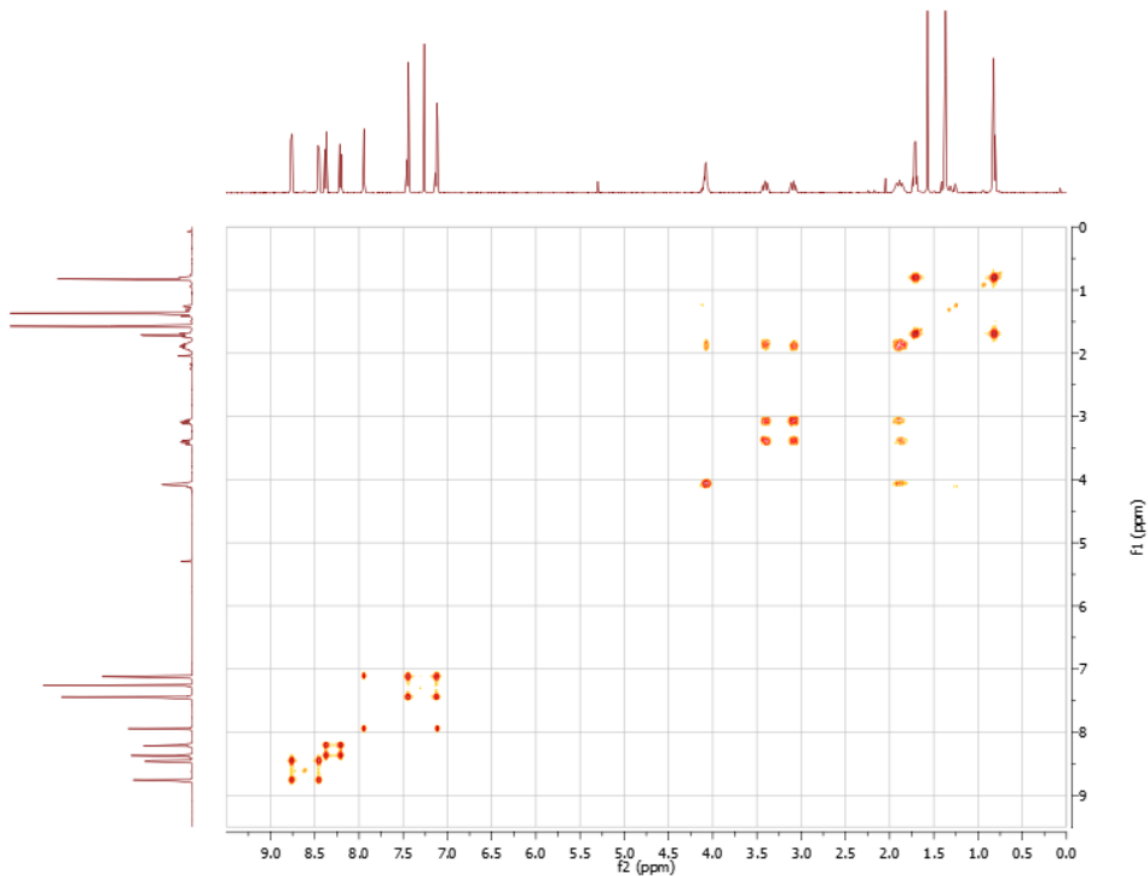


**Figure A 40.**  $^1\text{H}$ - $^1\text{H}$  COSY spectrum of TS-M2.

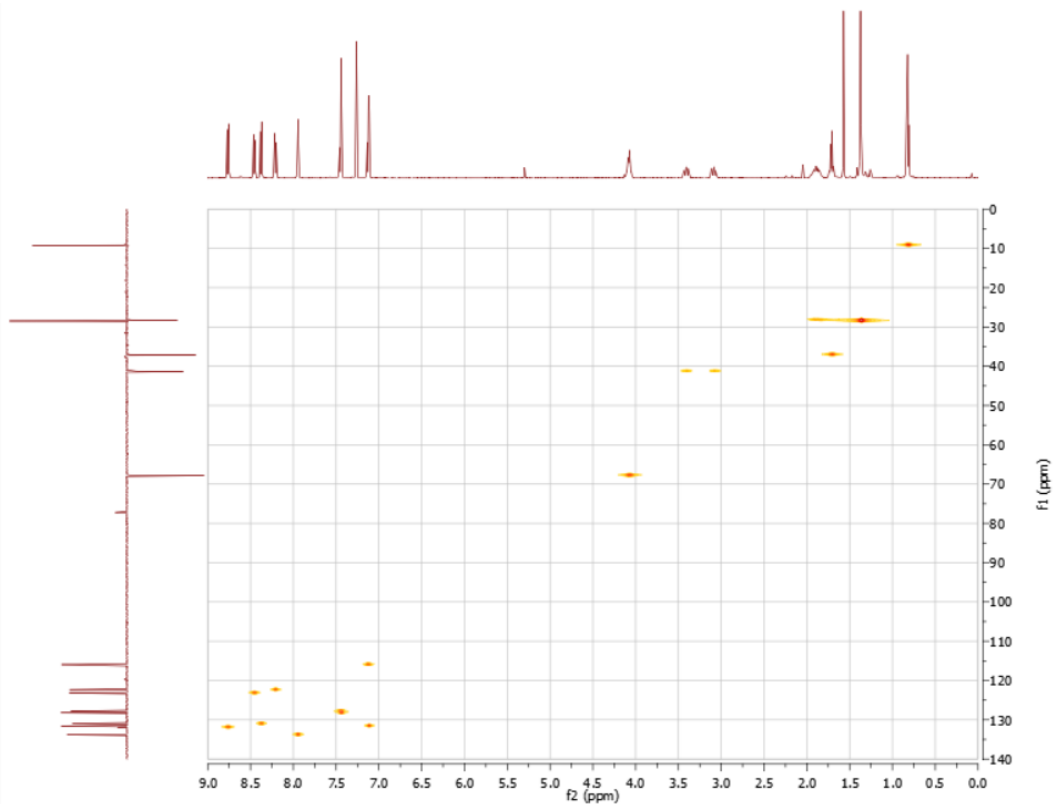


**Figure A 41.** HSQC spectrum of TS-M2, with <sup>13</sup>C DEPT spectrum on y-axis.

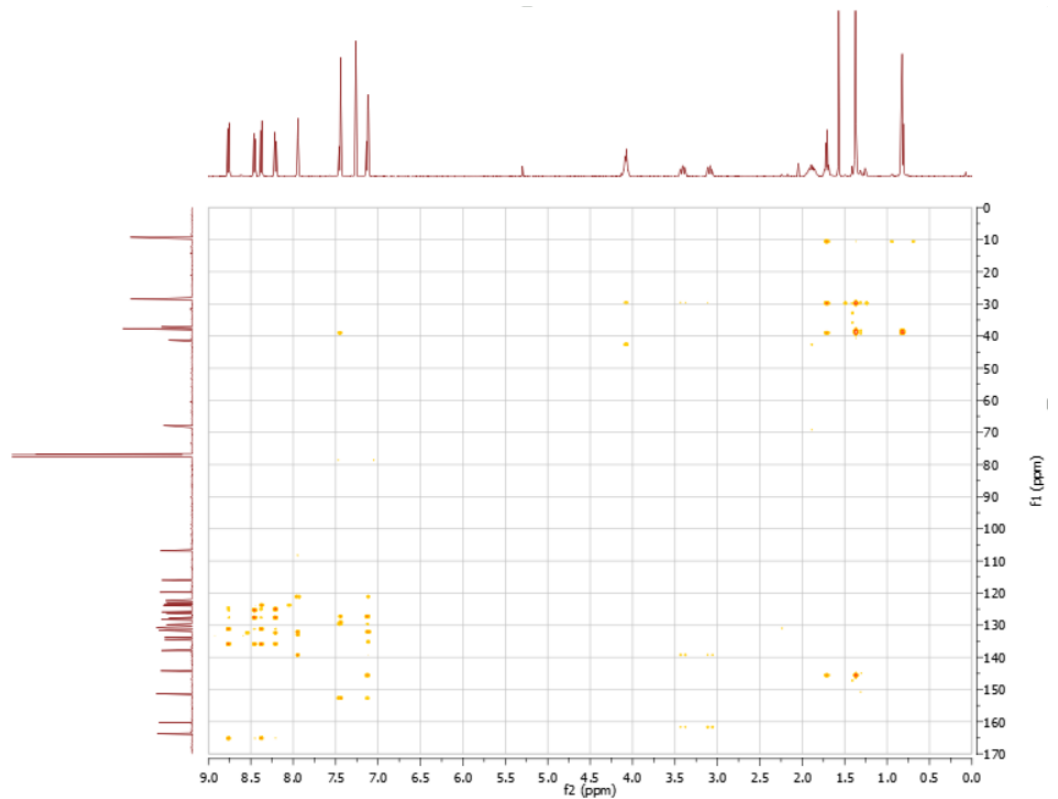


**Figure A 42.** HMBC spectrum of TS-M2.

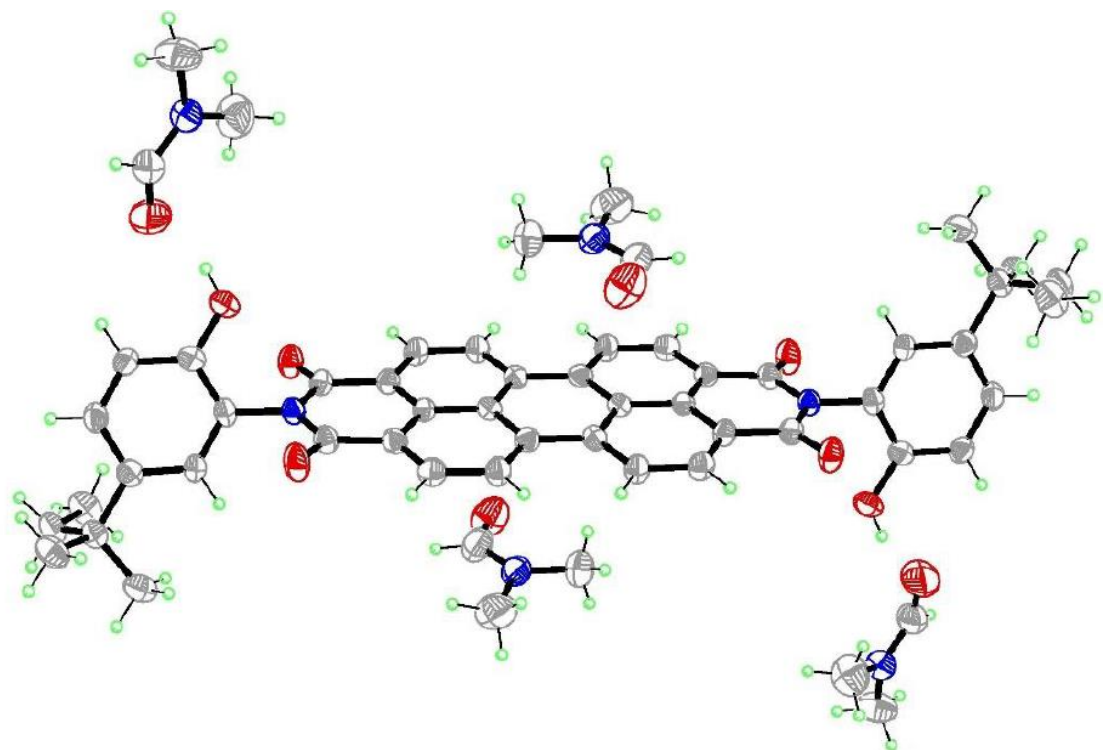


**Figure A 43.** X-ray structure of PDI-Diol.

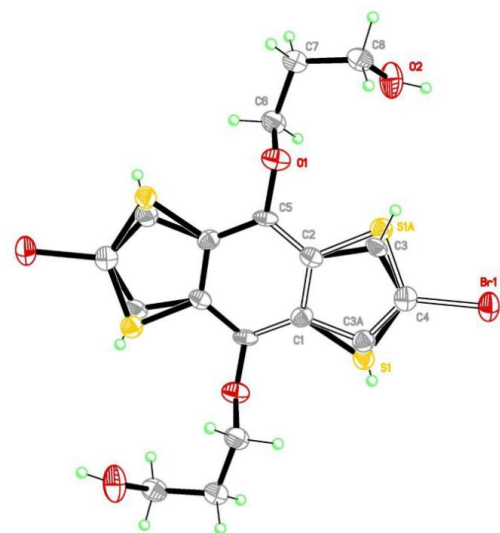


**Figure A 44.** X-ray structure of Br<sub>2</sub>-BDT-OH.